

# Quantum transport in graphene near the Dirac point



Im Fachbereich Physik  
der Freien Universität Berlin  
eingereichte

Dissertation

von

Martin Schneider

Berlin, im April 2014

- 1. Gutachter:** Prof. Dr. Piet W. Brouwer
- 2. Gutachter:** Prof. Felix von Oppen, PhD

Tag der Einreichung: 15. April 2014  
Tag der Disputation: 23. Juni 2014

## **Selbstständigkeitserklärung**

Hiermit versichere ich, dass ich in meiner Dissertation alle Hilfsmittel und Hilfen angegeben habe, und auf dieser Grundlage die Arbeit selbstständig verfasst habe. Diese Arbeit habe ich nicht schon einmal in einem früheren Promotionsverfahren eingereicht.



*Meinen Eltern gewidmet.*



# Kurzfassung

Seit der Entdeckung einer Methode, einzelne atomare Lagen von Graphit zu isolieren, hat sich Graphen, das weltweit erste zweidimensionale Material, in kürzester Zeit zu einem vielversprechenden Kandidaten für zukünftige nanoelektronische Anwendungen entwickelt. Die ungewöhnlichen elektronischen Eigenschaften dieses Materials beruhen auf einer quasi-relativistischen Dispersion, die charakteristisch für die zugrundeliegende wabenförmige Gitterstruktur von Kohlenstoffatomen ist. Diese Gitterstruktur zeigt sich zudem verantwortlich für einen zusätzlichen “Pseudospin”-Freiheitsgrad, der die Transporteigenschaften von Elektronen in erheblichem Maße beeinflusst. In der vorliegenden Arbeit werden nun einige dieser ungewöhnlichen Effekte im elektronischen Transportverhalten von Graphen näher untersucht.

Auf besonderes Interesse stößt in der Nanoelektronik die Herstellung von sogenannten “Quantenpunkten”, in welchen Elektronen auf kleinstem Raum eingesperrt werden. Ein gängiges Verfahren beruht dabei auf einer geeigneten Platzierung von metallischen Kontakten, mit denen sich Elektronen elektrostatisch einsperren lassen. Die Anwendung einer solchen Methode auf Graphen erweist sich jedoch als äußerst schwierig, in Anbetracht der Tatsache, dass die Dispersionsrelation von Graphen keine Bandlücke aufweist. Vielmehr erlaubt es der sogenannte “Klein-Tunneleffekt”, dass Elektronen in Graphen den Quantenpunkt verlassen können, wenn sie senkrecht auf dessen Oberfläche treffen. Dasselbe Argument gestattet jedoch elektrostatisches Einsperren für bestimmte Geometrien von Quantenpunkten, welche einen senkrechten Ausfall ausschließen. In dieser Arbeit werden wir zeigen, dass sich Elektronen überraschenderweise zu einem gewissen Grad auch in allgemeinen Geometrien einsperren lassen. Wir können diesen Effekt mit der “Berry-Phase” in Beziehung setzen, die aufgrund der Pseudospin-Struktur in Graphen auftritt, und Elektronen an senkrechtem Einfall auf die Oberfläche hindert. In dieser Arbeit werden wir diskutieren, wie Information über die mögliche Lokalisierung von Elektronen in Quantenpunkten in Graphen in experimentell zugänglichen Größen wie elektrischem Leitwert oder elektronischer Zustandsdichte erhalten werden kann.

Ein weiterer Teil dieser Arbeit behandelt Quanteninterferenzeffekte, welche im elektronischen Transport von ungeordneten Systemen auftreten. Insbesondere betrachten wir Systeme, in denen die Unordnung auf einer makroskopischen Skala variiert. Die elektronische Bewegung kann dann mittels klassischer Dynamik beschrieben werden, und folglich ist eine semiklassische Berechnung der Quantentransporteigenschaften möglich. Als Besonderheit machen sich Welleneffekte in solchen Systemen erst nach einer gewissen Zeit, der sogenannten Ehrenfestzeit bemerkbar. In dieser Arbeit werden wir den Einfluss der Ehrenfestzeit auf Quanteneffekte, welche von Elektron-Elektron-Wechselwirkungen herrühren, in der elektrischen Leitfähigkeit von Halbleiterstrukturen untersuchen. Desweiteren untersuchen wir Quanteneffekte im elektrischen Transport von Graphen unter semiklassischen Gesichtspunkten, wobei der Pseudospin in besonderer Weise berücksichtigt werden muss.





# Abstract

Since the discovery of a method to isolate single layers of graphite, graphene, the world's first two-dimensional material, has rapidly developed into a prospective candidate for future nanoelectronic devices. Its remarkable electronic properties arise from a quasirelativistic dispersion, that is connected to the honeycomb lattice of carbon atoms. Such lattice structure is also responsible for an additional pseudospin degree of freedom, that has crucial influence on the transport properties of electrons in graphene. The present thesis takes a closer look on some of these unusual features in electronic transport in graphene from a theoretical point of view.

Of particular interest in nanoelectronics is the fabrication of “quantum dots”, in which electrons can be confined in a small region in space. A standard procedure for the fabrication of quantum dots relies on the use of metallic gates, which allow to confine particles electrostatically. Such procedure is however highly problematic in graphene, due to the absence of a bandgap. More precisely, for graphene there is the effect of Klein tunneling, that allows the electrons to escape the dot, once they approach the surface under normal incidence. The very same argument also implies that electrostatic confinement is possible for certain shapes of the quantum dot, that exclude perpendicular incidence. In this thesis, we will show that, surprisingly, some degree of confinement also remains for the generic structure. We will relate such effect to the Berry phase, that arises due to the graphene's pseudospin structure, and prevents the electrons from strictly normal incidence. We will discuss how information about possible confinement can be revealed in experimental relevant quantities, such as conductance and density of states.

Another part of the thesis deals with quantum interference effects in the electronic transport of disordered systems. Specifically, we consider systems, that are subject to a smooth or macroscopic disorder, where the electronic motion is governed by classical dynamics, and therefore permit a semiclassical study of quantum transport. In such systems, the Ehrenfest time appears as an additional timescale, which essentially serves as a short-time threshold, below which wave effects are not operative. In this thesis, we will address the effect of such Ehrenfest time on quantum effects in the electrical conductivity of semiconductor structures, that are induced by electron-electron interactions. Furthermore, we will study quantum corrections to transport in graphene from a semiclassical point of view, where additionally the effect of the pseudospin needs to be incorporated.



# Contents

<b>Kurzfassung</b>	<b>v</b>
<b>Abstract</b>	<b>vii</b>
<b>1. Introduction</b>	<b>1</b>
1.1. Gate-defined quantum dots in graphene . . . . .	3
1.2. Semiclassical theory of quantum transport . . . . .	6
1.3. Outline of the thesis . . . . .	10
<b>2. Electronic properties of graphene</b>	<b>11</b>
2.1. The bandstructure of graphene . . . . .	11
2.2. Graphene in a magnetic field . . . . .	14
2.3. Klein tunneling . . . . .	18
2.4. Transport in clean graphene . . . . .	20
<b>3. Resonant scattering in graphene with a gate-defined chaotic quantum dot</b>	<b>25</b>
3.1. Introduction . . . . .	25
3.2. Electrostatic confinement in a gate-defined graphene quantum dot . . . . .	27
3.3. Model and method . . . . .	29
3.4. Two-terminal conductance with stadium-shaped quantum dot . . . . .	35
3.5. Conclusion . . . . .	40
<b>4. The role of the Berry phase for electrostatic confinement in graphene</b>	<b>41</b>
4.1. Bound states of a circular quantum dot with a $\pi$ -flux . . . . .	42
4.2. Two-terminal conductance . . . . .	44
4.3. Density of states . . . . .	48
4.4. Graphene quantum dot . . . . .	48
4.5. Effect of a $\pi$ -flux . . . . .	54
4.6. Conclusion . . . . .	58
<b>5. Semiclassical theory of the interaction correction to the conductance of antidot arrays</b>	<b>61</b>
5.1. Introduction . . . . .	61
5.2. Semiclassical theory of the interaction correction . . . . .	63
5.3. Interaction correction for antidot arrays . . . . .	75
5.4. Conclusion . . . . .	83
<b>6. Quantum corrections to transport in graphene: a semiclassical analysis</b>	<b>87</b>
6.1. Introduction . . . . .	87

6.2. Semiclassical Green function . . . . .	89
6.3. Diffusion coefficient and Lyapunov coefficient for a Gaussian random potential	90
6.4. Drude conductance . . . . .	94
6.5. Weak antilocalization . . . . .	95
6.6. Altshuler-Aronov correction . . . . .	98
6.7. Dephasing . . . . .	105
6.8. Conclusion . . . . .	110
<b>7. Conclusion</b>	<b>111</b>
<b>A. Appendix to Chapter 3</b>	<b>117</b>
A.1. Matrix Green Function . . . . .	117
A.2. Low- $k$ -Limit of Scattering matrix . . . . .	120
<b>B. Appendix to Chapter 4</b>	<b>123</b>
B.1. Numerical simulation of the two-terminal transport . . . . .	123
B.2. Numerical simulation of the density of states . . . . .	124
<b>C. Appendix to Chapter 5</b>	<b>127</b>
C.1. Details of the semiclassical calculation . . . . .	127
C.2. Details of the discussion . . . . .	134
<b>D. Appendix to Chapter 6</b>	<b>137</b>
D.1. Weak antilocalization . . . . .	137
D.2. Dephasing: Perturbation theory . . . . .	138
D.3. Dephasing: Loop segment . . . . .	139
<b>Bibliography</b>	<b>141</b>
<b>Acknowledgements</b>	<b>153</b>
<b>Curriculum Vitae</b>	<b>155</b>
<b>Publications</b>	<b>157</b>

# 1. Introduction

Since its first successful isolation in 2004, graphene has evolved in a truly unique fashion to a prospective material for future nanodevices, stimulating intense research activity throughout many branches of solid-state physics. Graphene is the name for a single layer of graphite and consists of carbon atoms that are arranged in a two-dimensional honeycomb lattice. While the first calculation of the bandstructure of this material dates back to 1947 [Wall 47], graphene remained for a long time a subject of purely academic interest – and no one aimed for an experimental realization of graphene, as the Mermin-Wagner theorem predicts strictly two-dimensional crystals to be unstable. It thus came as a surprise, when Geim and Novoselov reported to be able to isolate this material [Novo 04], which, together with its astonishing properties, created tremendous attraction by physicists, such that the discovery has been finally awarded with the Nobel prize in 2010.

A great part of the interest in graphene relies on its unique electronic properties, that stem from the peculiar bandstructure of the hexagonal carbon lattice. Valence and conduction band touch each other at two points in the Brillouin zone, around which the spectrum has a conical shape. This in turn means that electrons effectively behave as ultra-relativistic particles as they move through the carbon lattice, however with a velocity that is about 300 times smaller than the speed of light. The analogy with relativistic theory extends even beyond the linear dispersion, as the low-energy description of electrons in graphene is governed by the (2+1) dimensional Dirac equation for massless particles, where the spin degree of freedom is mimicked by the possibility to sit on either of the two carbon sublattices, termed as *pseudospin*. The Dirac equation aligns the pseudospin of the electrons with their direction of motion, assigning a *chirality* to the particles. The additional presence of the real spin together with the two Fermi points in the Brillouin zone (*valleys*) implies that graphene owns four copies of a Dirac cone.

The unusual electronic properties of graphene can be revealed in transport experiments. A typical setup includes a graphene nanoflake placed on an insulating substrate and connected to metallic source and drain contacts. In addition, metallic gates below or above the sample can be used to tune the chemical potential of the graphene structure, inducing a finite carrier density of electrons or holes. While the graphene samples itself can be produced in very high quality, the insulating substrate is typically prone to charged impurities, which may crucially influence the transport abilities of the nanostructure. We also mention that there is a class of alternative transport setups, which deal with freestanding (suspended) graphene.

Transport properties are highly peculiar in graphene, when the chemical potential is tuned to the Dirac point, where conductance and valence band touch. On the one hand, there are no carriers available, that mediate electric transport, as the density of states vanishes, which points towards an insulating behavior. On the other hand, a small carrier concentration would barely scatter off impurities, as the available phase space of final

electronic states reduces to zero, which would support a well-conducting behavior. The determination of the conductivity at the Dirac point is therefore quite subtle and requires a careful consideration. For a clean short-and-wide graphene sheet, theoretical studies find a finite value for the conductivity at the charge neutrality point of  $4e^2/\pi h$  [Frad 86, Ludw 94, Zieg 98, Shon 98, Twor 06, Pere 06, Kats 06a]. Experiments conducted on ultraballistic samples find a value close to that prediction, while most experiments point to somewhat larger values, which are attributed to disorder. Such disorder-enhanced conduction was confirmed by numerical studies [Bard 07, Nomu 07].<sup>1</sup> Intuitively, one may argue that disorder creates regions with a finite electron or hole concentration, which leads to an increase of the conductivity. On the other hand, disorder also magnifies the number of scattering events, so that a careful consideration of the problem is needed, to decide which effect is dominant. The intriguing feature of disorder-enhanced conductivity can be also related to the presence of a “topological term” in a field-theoretical description, that prevents the system from Anderson localization [Ostr 07].

The electronic properties of graphene are also strongly influenced by the existence of the pseudospin and the associated chiral nature of the electronic excitations in graphene. A striking manifestation is the absence of backscattering in quantum scattering processes, which is related to the phenomenon of Klein tunneling [Chei 06, Kats 06b]. Another hallmark is an unusual quantization of the Landau levels for graphene that is placed in a magnetic field. The origin of this effect lies in an additional phase that the electronic wavefunction accumulates due to chirality: Since pseudospin and orbital degree of freedoms are locked, the pseudospin winds once around its axis when the electron performs a circular motion in the magnetic field, and thereby picks up a Berry phase of  $\pi$ . The Berry phase is in turn responsible for the formation of a Landau level at zero energy - a unique feature for relativistic particles in a magnetic field. The unusual Landau level quantization can be observed in a Hall measurement, where the series of quantum Hall plateaus is shifted by  $1/2$  as compared to the standard one.<sup>2</sup> The measurement of this halfinteger quantization series provided the first direct confirmation of the relativistic nature of charge carriers in graphene [Novo 05, Zhan 05].

Even a decade after the first successful realization of graphene, there is still enormous interest in unraveling the fascinating properties of this material or “graphene-related materials” such as topological insulators or Weyl semimetals, that are also strongly influenced by the appearance of a Dirac cone. The present thesis covers various aspects of quantum transport in graphene near the Dirac point. In the first part of the thesis, we investigate the possibility to confine electrons in graphene with the help of metallic gates in a narrow region in space, a “quantum dot”. In order to define a quantum dot structure, it is essential to be able to exclude the electrons from entering the region outside of the dot. In semiconductor nanostructures, it is a well-established method to shape quantum dots with the help of gate potentials that tune the Fermi level in the bandgap outside the quantum dot. For graphene however, there is no bandgap and hence it should be impossible to fabricate quantum dots by gating. On the other hand, one may argue that the charge

---

<sup>1</sup>To be precise, this statement is valid for disorder that is smooth on the scale of the lattice constant, such that it does not couple the two valleys.

<sup>2</sup>The Hall conductance measured in units of the conductance quantum remains integer though, as graphene exhibits two Dirac cones.

carrier concentration tends to zero in regions, where the chemical potential is tuned to the Dirac point, which would favor the possibility of electrostatic confinement. These controversial viewpoints illustrate that the question, whether it is possible to confine electrons in graphene with metal gates has a nontrivial answer and deserves a careful consideration. In this thesis, we will explore under what circumstances electrostatic confinement in graphene is possible.

While the physics of graphene is highly unusual when the Fermi level lies at the Dirac point, its electronic properties resemble those of a metal, when graphene is doped away from the Dirac point, but certain features of the Dirac spectrum remain, related to the presence of the pseudospin. For weakly disordered metallic systems, it is well-known that the wave nature of electrons and the associated quantum interference effects leads to a number of manifestations in quantum transport, such as weak localization, universal conductance fluctuations, and interaction corrections. If the impurities have a range comparable to the Fermi wavelength of the electrons, the scattering process of the electrons off the impurities is quantum-diffractive, while for impurities with a range much larger than the Fermi wavelength, the scattering process can be viewed classical-deterministic. In the latter regime a description of quantum transport based on classical trajectories is amenable. This regime is distinguished from the short-range impurities by the appearance of an additional timescale, the Ehrenfest time, which essentially serves as a short-time threshold for the occurrence of quantum corrections. In this thesis, we investigate the effect of such Ehrenfest time on the interaction correction to the conductance, which will discuss first for conventional semiconductor structures. We further apply semiclassical methods to study quantum corrections in graphene. Here, the pseudospin structure enters as an additional feature, which influences the results of the quantum corrections. Besides being able to cope with a finite Ehrenfest time, the semiclassical treatment also provides an intuitive approach to address quantum corrections in electric transport.

In the following, we give an overview over the projects covered in this thesis.

## **1.1. Gate-defined quantum dots in graphene**

The possibility to confine electrons in a small region in space plays a central role in the design of future nanoelectronic devices. If the electronic motion is limited in all three spatial directions, one speaks of a “quantum dot”. The energy levels which the electron can occupy are discrete, and the system can be viewed as an “artificial atom”. Nanosystems which offer the possibility to individually address and manipulate single electrons open a way to store and process quantum information.

One way to realize such quantum dots is based on semiconductor heterostructures. For instance, GaAs/AlGaAs-heterostructures have been used to confine electrons in a two-dimensional layer. With the help of additional metal gates, it is possible to locally adjust the chemical potential. By tuning the chemical potential in the bandgap of the semiconductor, one creates regions that electrons cannot penetrate, which finally allows for confinement in all three spatial directions.

In view of the two-dimensional nature of graphene, it is tempting to adopt this idea to build graphene quantum dots. There is one big obstacle however — graphene has no

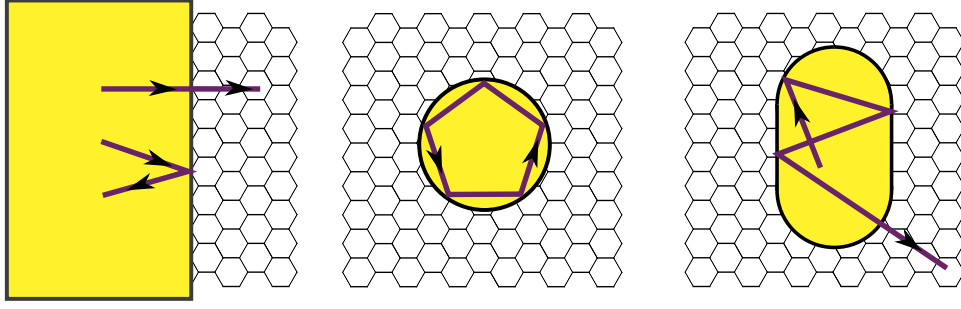


Figure 1.1.: Klein tunneling in graphene. *Left:* Transition from doped to undoped graphene sheet: electrons that hit the surface at perpendicular incidence will be transmitted, while away from normal incidence they will be reflected. *Middle:* A circular quantum dot allows for trajectories that avoid normal incidence on the surface. *Right:* In a chaotic quantum dot, sooner or later a particle will hit the surface at normal incidence and exit the dot.

bandgap, and thus it is not possible to create “forbidden regions” for the electrons. On the other hand, in a region where the chemical potential is tuned to zero, the charge carrier concentration is zero, which supports the possibility to confine electrons. The two complementary viewpoints suggest that a careful analysis is needed to solve this problem. A promising approach involves the phenomenon of Klein tunneling: Hereto, we consider an interface between a region with finite carrier concentration and a region with zero carrier concentration. As the density of states is vanishing in the undoped region, an electron that approaches the interface from the doped side will be typically reflected back. The only exception occurs at normal incidence, where the electron is transmitted with unit probability. The latter effect of course is highly problematic for possible electrostatic confinement in graphene, but it does not mean the end of the story.

In a recent article, Bardarson *et al.* [Bard 09] suggested that the answer to the question, if it is possible to confine electrons with the help of metal gates, depends very sensitively on the geometry of the quantum dot: A disc-shaped quantum dot is an example of an integrable quantum dot, for which perpendicular incidence at the surface is excluded for most of the trajectories. Hence, such a structure should support confined states in the quantum dot. On the contrary, for a geometry whose classical dynamics is chaotic, such as a stadium-shaped geometry, trajectories sooner or later approach the surface at normal incidence, and the particle can exit the dot, see Fig. 1.1.

To test this prediction based on classical considerations, Bardarson *et al.* supported their work with a numerical analysis of a circular or stadium-shaped quantum dot surrounded by a sheet of undoped graphene, that is attached to source and drain contacts. The formation of bound states is revealed as resonances in the two-terminal conductance as a function of the dot’s gate voltage. Bardarson *et al.* found sharp resonances for the disc-shaped geometry, while for the chaotic geometry only broad resonances were found, corresponding to states that have a short lifetime, which supports the classical expectation on a heuristic level.



The difference between integrable and chaotic geometry becomes most pronounced in the limit of small dot sizes in comparison to the distance between dot and leads, where the resonances become isolated. Due to numerical limitations however, the regime of isolated resonances was not accessible in Ref. [Bard 09], which prevented the authors from a closer investigation of the degree of confinement. In the mean time, Titov *et al.* proposed an extension of the so-called *matrix Green function method* to two-terminal transport in graphene [Tito 10]. With the help of this formalism, Titov *et al.* were able to determine the two-terminal conductance for graphene containing a circular quantum dot fully analytically. Inspired by this big success, we are lead to the question, if this formalism could be used to get a better understanding of the resonant structures of a chaotic quantum dot.

This question is indeed the origin of the study presented in Chapter 3, where we will introduce a combined analytical-numerical approach, built on the matrix Green function method, that allows for a detailed study of the resonances of a quantum dot of arbitrary geometry. We show, that the limit of isolated resonances can be reached very efficiently with this method, and we are able to determine the lineshape and the characteristics of the resonances, which carry signatures of the underlying chaotic geometry. We also show, that upon decreasing the ratio of dot size vs. distance to the contacts, the resonances corresponding to the regular geometry become much sharper as compared to the resonances of a chaotic quantum dot, which allows for a quantitative measure to distinguish such geometries. Quite remarkably, the amplitude of the resonances saturates at a finite value close to the conductance quantum.

### 1.1.1. The role of the Berry phase

Although the results of Chapter 3 allow for a quantitative understanding of the resonances of a chaotic quantum dot, a great puzzle remains: Why do the resonant features for a chaotic structure not disappear, even if the coupling between dot and leads shrinks to zero? A solution to the discrepancy between classical argumentation and quantum-mechanical calculation is presented in Chapter 4.

The classical reasoning presented above neglects one crucial aspect of charge carriers in graphene: As the electrons move in the quantum dot, the pseudospin adjusts to be aligned with the direction of motion. The transport of spin is accompanied with the accumulation of a quantum-mechanical phase of the electronic wave function, the Berry phase. Upon completion of a single circular motion, the pseudospin winds once around its axis, resulting in a Berry phase of  $\pi$ , which is also responsible for the unusual Landau level quantization, as discussed before. The reason, why the Berry phase crucially influences the possibility to confine electrons, becomes evident when considering the angular momentum of the electron: For graphene, orbital angular momentum and pseudospin are strongly coupled, so that only their combination is a good quantum number, which is quantized in half-integer multiples of  $\hbar$ . Thus, there is no state with zero angular momentum, that corresponds to the situation where an electron approaches the surface under normal incidence, and hence a residual confinement remains even for an arbitrary geometry of the dot.

In order to support these arguments, we consider an alternative setup, where we include

a flux tube in the quantum dot, that carries half a flux quantum. Electrons encircling this flux tube pick up an Aharonov-Bohm phase of  $\pi$ , that is precisely cancelling the effect of the Berry phase. We show, that after insertion of the flux tube, the kinematical angular momentum, relevant for classical considerations, takes on integer values, and in particular allows for a state with zero kinematical angular momentum. We show, that this state does indeed not allow for confinement by means of gate potentials.

A numerical simulation of the two-terminal transport upon inclusion of the  $\pi$ -flux then shows the desired significant difference discriminating integrable and chaotic geometries: For the circular dot, we find sharp resonances that persist in the limit of small coupling to the leads, whereas for the chaotic structure, resonances are present only for intermediate coupling, while they disappear, as the coupling goes to zero.

Besides transport measurements, valuable means to gain insight to nanoscale systems are measurements of the density of states, either locally by scanning tunneling spectroscopy, or globally, by quantum capacitive measurements. In Chapter 4, we will also discuss the signatures of confinement in graphene quantum dots in the density of states, where the existence of discrete electronic levels of the quantum dot are revealed as additional peaks in the density of states. We choose a setup, where the quantum dot surrounded by undoped graphene is attached to a circular lead. We will show, that such setup allows to access the relevant limit of weakly coupled very efficiently, and discuss how information about possible confinement can be extracted from an analysis of the density of states.

## 1.2. Semiclassical theory of quantum transport

In 1900, Paul Drude suggested a simple model to explain transport in metals [Drud 00], where he assumed that electrons behave as classical particles between successive collisions in the solid. Although treating electrons on a classical level may seem a very crude simplification, it turns out that many features of electric transport in nanosystems are successfully described with the help of a Boltzmann equation, which essentially is based on the same idea as the Drude model (see, e.g. [Ramm 98]). Despite the big significance of the Boltzmann theory for transport, we emphasize that there are also a number of phenomena in electric transport through metals, that cannot be described by treating electrons as classical particles, but rely on the wave nature of electrons and quantum interference effects.

A prominent example of such signatures of quantum effects in electric transport is *weak localization*, which results in a reduction of the conductivity compared to its classical value [Ande 79, Gork 79]. An intuitive explanation for this effect is based on electronic trajectories through the solid – quantum effects arise in this picture from interference between different trajectories [Chak 86]: We are interested in the regime of dilute disorder, where the separation between impurities is much larger than the Fermi wavelength, that describes the typical extent of an electronic wave packet. In this limit, the interference between different trajectories is typically accompanied by a large phase factor, which gets washed out upon taking the ensemble average over disorder. This observation explains the success of a description in terms of classical particles. On the other hand, there are interference terms that survive the disorder average and contribute to the ensemble-

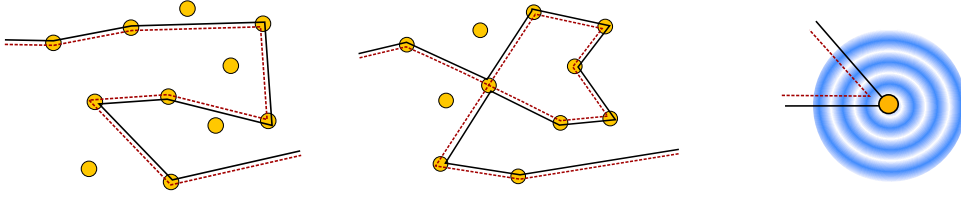


Figure 1.2.: Trajectory-based explanations for the different contributions to conductivity of a disordered metal: *Left*: Drude conductivity: trajectories are paired. *Middle*: Weak localization: trajectories contain a loop that is traversed in opposite directions. *Right*: Interaction correction: trajectories interfere upon scattering at the impurity/Friedel oscillations of the electron density.

averaged electrical conductivity. Such terms rely on the constructive interference of time-reversed trajectories, which result in an enhanced probability for the electron to return to a place it had already visited before. This effect in turn is responsible for a reduction of the conductivity, the weak localization correction (see Fig. 1.2).<sup>3</sup> Although weak localization is typically of small magnitude, it can be observed, as the application of a magnetic field destroys the interference, and restores the classical value of the conductivity, which therefore confirms the relevance of quantum effects in electric transport.

Besides weak localization, the quantum behavior of electrons manifests itself also in the *universal conductance fluctuations* [Alts 85a, Lee 85], anomalously large sample-to-sample fluctuations of the conductivity. In the presence of interaction, the value of the conductivity is additionally influenced by the *Altshuler-Aronov correction* [Alts 79, Alts 85b]. There exists an intuitive explanation also for the latter effect based on classical trajectories [Rudi 97, Zala 01]: When an impurity is placed in the solid, the charge density profile of the electrons arranges in an oscillatory fashion around the impurity, known as *Friedel oscillations*. In the interacting system, electrons may therefore not only scatter at the impurity itself but also at the Friedel oscillations created by the other electrons. The associated quantum interference is responsible for the Altshuler-Aronov correction to the conductivity (see Fig. 1.2).

Although classical trajectories have been used quite successful to understand the quantum corrections to transport in a weakly disordered system on a qualitative level, we remark that a quantitative description of those effects, that is solely based on classical trajectories, is a delicate task. The reason for this is, that the size of an impurity in typical situations is of the same order as the Fermi wavelength, that sets the extension of the electronic wave packet. Hence, the electronic wave packet will be scattered by the impurity in all directions, and a description, where the electron is following a single classical trajectory is invalidated after the first scattering event.

Recent advances in modern nanofabrication techniques however allow for the realization of systems with artificial “large scale impurities”, where the electronic motion is governed

<sup>3</sup>The effect is called weak localization, as it describes the onset of Anderson localization (or strong localization), which names the effect that a metal can turn to an insulator for sufficiently strong disorder.

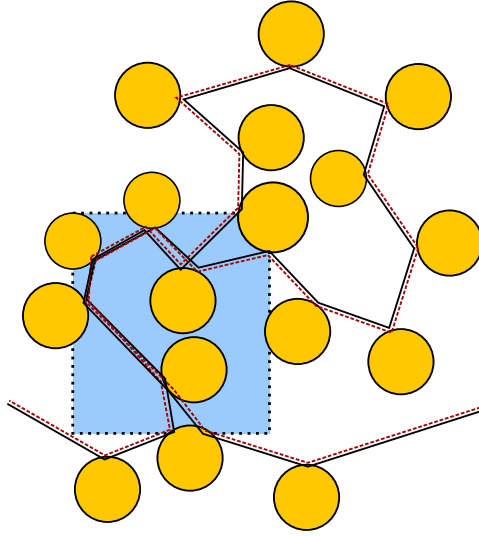


Figure 1.3.: Trajectories that contribute to weak localization in antidot arrays. Compared to the case of short-range disorder, they differ by a Lyapunov region (indicated in blue), where the pairing between trajectories is interchanged. The Lyapunov region is associated with a finite time, the Ehrenfest time  $\tau_E$ .

by classical dynamics. Such systems consist of high-mobility semiconductor structures with an additional array of antidots that is superimposed [Rouk 89, Enss 90]. The high quality of the semiconductor sample ensures, that electrons move ballistically between successive reflections off the antidots. Because the size of the antidots is much larger than the size of the electron wave packet, the antidots can be seen as “classical disorder”, and a classical description is sufficient for the scattering processes. It is an interesting question, if *quantum* effects such as weak localization are also observed in these *classical* systems. For the configurations of trajectories responsible for the weak localization, as shown in Fig. 1.2, it is crucial that impurity scattering is diffractive, as it allows the two trajectories to “split” and traverse a loop in opposite direction. For an array of irregularly placed antidots, the classical dynamics is chaotic, and two nearby trajectories separate exponentially in time, with a rate given by the Lyapunov coefficient. It is the chaotic dynamics, that allows two initially close trajectories to split up and pair with the time-reversed partner, see Fig. 1.3. Thus, weak localization also occurs in antidot arrays, however the “diffraction” of trajectories takes a finite time, set by the so-called *Ehrenfest time*  $\tau_E$ , that enters as an additional timescale in the problem [Ale 96]. If the Ehrenfest time is large (in comparison to the dwell time of the electrons in the system), one finds that the weak localization correction gets strongly suppressed, being completely absent in the strictly classical limit of infinite Ehrenfest time [Ale 96, Adag 03, Brou 07]. One may conjecture a similar suppression for all quantum effects in transport through antidot arrays. Quite surprisingly, it turns out, that the universal conductance fluctuations remain finite even in the strict classical limit [Twor 04, Jacq 04, Brou 06, Brou 07].

### 1.2.1. Semiclassical theory of the interaction correction

In Chapter 5, we study the interaction correction to the conductivity of systems where the electronic motion follows classically chaotic dynamics. Of particular interest is the effect of a finite Ehrenfest time in such systems. A first study of this problem has been carried out by Brouwer and Kupferschmidt [Brou 08], who investigated interaction corrections in a ballistic double quantum dot, where particles scatter only at the boundary of the quantum dot. The double quantum dot constitutes the simplest setup with non-zero interaction corrections, and is characterized by a long-range interaction, that is constant within each dot. It was found, that the interaction correction gets strongly suppressed, when the Ehrenfest time exceeds the dwell time or inverse temperature.

In this thesis, we considerably extend this study and construct the semiclassical theory of the interaction correction with arbitrary (short-range or long-range) interaction, and for a generic geometry. In particular, our study allows to treat the experimentally relevant example of antidot arrays.

The semiclassical approximation amounts to replace electronic propagators as a summation over all possible classical paths, that connect two points in space. Without interaction, the conductivity is expressed as a twofold sum over classical trajectories. For the interaction correction to the conductivity, one needs to sum over four classical trajectories. The challenge is to identify the configurations of trajectories that remain after disorder average, and to calculate their contribution.

Our results show a strong suppression of the interaction corrections for Ehrenfest times larger than dwell time or inverse temperature, confirming the findings of [Brou 08] also for the generic case. The sensitivity to temperature is special to the interaction correction, which has its origin in virtual processes that transfer energies larger than temperature. For the realistic case of Coulomb interaction, one has a competition between Hartree and Fock type contribution to the interaction correction (note that the Hartree contribution is absent for the double quantum dot). Interestingly, we will show, that this competition can lead to a sign change of the interaction correction as a function of Ehrenfest time.

### 1.2.2. Semiclassical theory of quantum corrections in graphene

While semiclassical methods are successfully applied for the calculation of quantum corrections in semiconductor structures with classical disorder, it is a natural task to extend these methods to describe quantum corrections to transport in graphene samples, which will be the goal of Chapter 6. The applicability of semiclassical methods is restricted to systems with “macroscopic disorder”, such as antidot arrays, where the disorder is smooth on the scale of the size of an electronic wavepacket. Besides antidot arrays, such regime can be reached in graphene samples that are placed on a substrate with high dielectric constant, such that impurities from the substrate are strongly screened, and electrons in graphene traverse a smooth disorder potential. Additionally, we require the Fermi level to lie well above or below the Dirac point, so that the electronic wavelength is sufficiently small. (We assume the Fermi level close enough to the Dirac point however, that the approximation of the linear dispersion is still valid).

The properties of graphene that is doped away from the Dirac point resemble more and more those of a metal, as the density of states is finite. However, some graphene-

specific physics remains also in this regime. The reason for this lies in the pseudospin degree of freedom, that is strongly coupled to orbital degrees of freedom. The presence of the pseudospin also calls for an extension of the semiclassical methods typically applied in systems where the spin degree of freedom plays no role. A semiclassical propagator for graphene has been derived by Carmier and Ullmo [Carm 08]. A crucial observation is that during the electronic propagation the pseudospin can be reconstructed along the classical trajectories, where it remains aligned with the momentum. Associated with the transport of the pseudospin along the trajectory is an additional phase in the semiclassical propagator, which equals the Berry phase known from spin transport.

In the past, semiclassical methods have been used to describe the effect of a finite Ehrenfest time for quantum effects in transport such as weak localization, Altshuler-Aronov correction and dephasing in conventional metals, where the spin degree of freedom is unimportant. On the other hand, the quantum corrections have been derived for graphene subject to “quantum disorder”, where the Ehrenfest time is zero. In this thesis, we will extend those works, and derive the quantum corrections to transport in graphene from a semiclassical point of view, being able to include the effect of a finite Ehrenfest time. Special attention is paid to the existence of the pseudospin, that is responsible for a change from weak localization to weak *antilocalization* in graphene, *i.e.* the conductivity is enhanced compared to its classical value, and furthermore affects the effective interaction strength that enters the interaction-induced corrections in graphene.

### 1.3. Outline of the thesis

We now outline the structure of this thesis. In Chapter 2 we introduce the reader to graphene and its special properties. Turning to the results of this thesis, we consider the possibility of electrostatic confinement in graphene, where we investigate the role of geometry (regular vs. chaotic) in Chapter 3. We then explore the role of the Berry phase for possible confinement in Chapter 4. In Chapter 5, we turn to the semiclassical theory of quantum transport, where we study the effect of a finite Ehrenfest time for the interaction correction. In Chapter 6, we consider the quantum corrections in graphene from a semiclassical point of view. We conclude our results and draw an outline for possible future research directions in Chapter 7.

## 2. Electronic properties of graphene

In this chapter, we give an introduction to the electronic properties of graphene. At the heart of all peculiar properties of graphene is the quasirelativistic bandstructure, implying that electrons that move in the two-dimensional carbon lattice behave as relativistic particles, although with an effective speed of light that is about 300 times smaller than the real speed of light. The analogy to relativistic quantum dynamics extends even beyond the linear spectrum, as the low-energy description for electrons in graphene is governed by the massless Dirac equation in 2+1 dimensions, where the “spin” degrees of freedom arise from the sublattice structure of the honeycomb lattice. The remarkable bandstructure of graphene will be introduced in Sec. 2.1.

The quasirelativistic bandstructure leads to many surprising and unconventional effects. As an illustration, we discuss the unusual Landau level quantization, that occurs when graphene is placed in a magnetic field (Sec. 2.2), and the implications on quantum tunneling (Sec. 2.3). Finally, we will show how to calculate the electric conductance for a clean graphene sample (Sec. 2.4). In this chapter, we only cover a narrow selection of the interesting electronic properties of graphene. We therefore refer the reader to the literature for a more comprehensive overview [Geim 07, Cast 09, Geim 09, Been 08, Das 11].

### 2.1. The bandstructure of graphene

Graphene is the name given to a two-dimensional material made out of carbon atoms, that are arranged in a hexagonal lattice (see Fig. 2.1). The binding between the carbon atoms is due to the  $sp^2$ -hybridization between one  $s$ -orbital and two  $p$ -orbitals, which form a  $\sigma$ -bond that binds the carbon atoms at a distance of  $a = 1.42\text{\AA}$ , and determines the unique mechanical properties. The remaining  $p_z$ -orbital is pointing perpendicular to the graphene plane. The electrons from these orbitals form a  $\pi$ -band, in turn responsible for the electronic properties of graphene. Since each carbon atom contributes one electron to the  $\pi$ -band, this  $\pi$ -band is half-filled for pristine graphene.

The first calculation of the bandstructure of graphene dates back to [Wall 47]. As the  $p_z$ -orbitals of different atoms are only weakly overlapping, a description in terms of the “tight-binding approximation” is appropriate, where terms of the Hamiltonian, which couple electrons that are more than one atom apart, are neglected. The crucial aspect of the honeycomb lattice is, that it does not satisfy the requirements for a Bravais lattice, but it rather consists of two sublattices  $A$  and  $B$ , as depicted in Fig. 2.1. We therefore make the following ansatz for the Bloch wavefunction

$$\Psi_{\mathbf{k}}(\mathbf{r}) = \psi_A(\mathbf{k}) \sum_{\mathbf{R}_A} e^{i\mathbf{k}\mathbf{R}_A} \phi(\mathbf{r} - \mathbf{R}_A) + \psi_B(\mathbf{k}) \sum_{\mathbf{R}_B} e^{i\mathbf{k}\mathbf{R}_B} \phi(\mathbf{r} - \mathbf{R}_B), \quad (2.1)$$

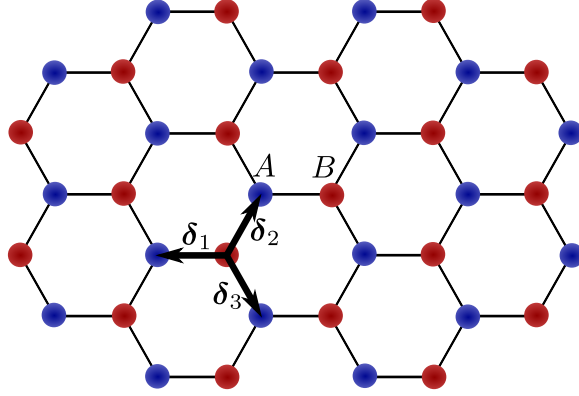


Figure 2.1.: The graphene honeycomb lattice is built from two triangular sublattices  $A$  (blue) and  $B$  (red).

where the summation extends over the lattice vectors of sublattice  $A/B$ , and  $\phi(\mathbf{r})$  denotes the wavefunction of the  $p_z$ -orbital, which is symmetric under rotation around the  $z$ -axis. The ansatz involves the two coefficients  $\psi_{A/B}(\mathbf{k})$ , which describe the amplitude of an electron to occupy sublattice  $A$  or  $B$ . After multiplication of the Schrödinger equation for the Bloch state,  $H\Psi_{\mathbf{k}}(\mathbf{r}) = \varepsilon_{\mathbf{k}}\Psi_{\mathbf{k}}(\mathbf{r})$ , by  $\phi(\mathbf{r} - \mathbf{R}_A)$  ( $\phi(\mathbf{r} - \mathbf{R}_B)$ ) and subsequent integration over the position  $\mathbf{r}$ , we can reformulate the problem as an equation for the coefficients  $\psi_{A,B}(\mathbf{k})$ . After some calculation, one obtains<sup>1</sup>

$$\begin{pmatrix} 0 & t \sum_i e^{-i\mathbf{k}\delta_i} \\ t \sum_i e^{i\mathbf{k}\delta_i} & 0 \end{pmatrix} \begin{pmatrix} \psi_A(\mathbf{k}) \\ \psi_B(\mathbf{k}) \end{pmatrix} = \varepsilon_{\mathbf{k}} \begin{pmatrix} \psi_A(\mathbf{k}) \\ \psi_B(\mathbf{k}) \end{pmatrix}. \quad (2.2)$$

The lattice Hamiltonian  $H$  contributes only the single parameter

$$t = \int d\mathbf{r} \phi(\mathbf{r} - \mathbf{R}_A) H \phi(\mathbf{r} - \mathbf{R}_A + \delta_1) \quad (2.3)$$

to the tight-binding description, where  $\mathbf{R}_A$  is an arbitrarily chosen lattice vector of sublattice  $A$ , while the lattice structure enters in the summation of the three vectors  $\delta_1 = (-a, 0)$ ,  $\delta_2 = (a/2, \sqrt{3}a/2)$ , and  $\delta_3 = (a/2, -\sqrt{3}a/2)$  that connect neighboring atoms, see Fig. 2.1.

In the notation of Eq. (2.2), the coefficients  $\psi_{A/B}$ , that describe the occupation of the different sublattices, are arranged to a spinor. Since this structure is completely unrelated to the physical spin, one terms it *pseudospin*. From Eq. (2.2), we directly obtain the dispersion of the two tight-binding bands,

$$\varepsilon_{\mathbf{k}} = \pm t \left| \sum_i e^{i\mathbf{k}\delta_i} \right|, \quad (2.4)$$

which is shown in Fig. 2.2.

---

<sup>1</sup>For the calculation, we neglected overlap-integrals consisting of orbitals that are more than one atom apart. Furthermore, we used the fact that the Hamiltonian shares the symmetry of the underlying lattice, and redefined the zero of energy.



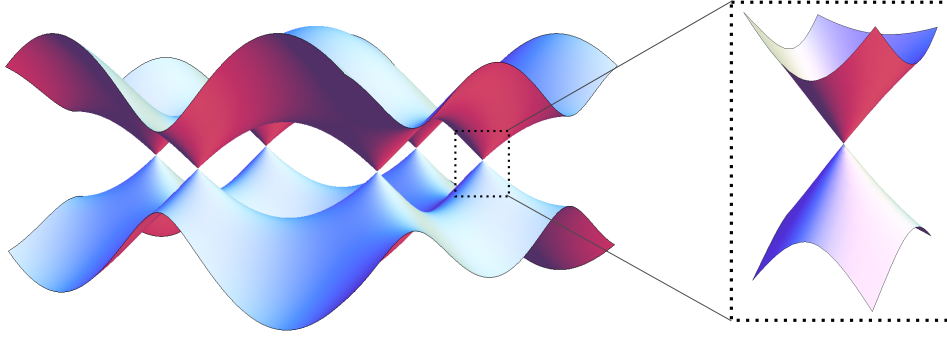


Figure 2.2.: Bandstructure of graphene: Valence and conduction band touch each other at the corners of the Brillouin zone. Around the touching points, the spectrum has a conical shape.

Quite remarkably, unlike in conventional two-dimensional systems, the set of  $\mathbf{k}$ -values which correspond to zero energy does not form a Fermi line, but rather consists of isolated Fermi points. These Fermi points are located at the corners of the hexagonal Brillouin zone of the reciprocal lattice. There are two inequivalent corners of the Brillouin zone, located at

$$\mathbf{K}_{\pm} = \pm \frac{2\pi}{3\sqrt{3}a} \begin{pmatrix} \sqrt{3} \\ 1 \end{pmatrix}. \quad (2.5)$$

These points are also called *Dirac points*, for reasons that we will discuss now.

The low-energy physics of graphene is happening close to the Dirac points, *i.e.* at wavevectors  $\mathbf{K}_{\pm} + \mathbf{k}$ , with  $|\mathbf{k}| \ll |\mathbf{K}_{\pm}|$  (Note that we redefine  $\mathbf{k}$  to be counted from the Dirac point henceforth). If we linearize in  $\mathbf{k}$  around the Dirac point  $\mathbf{K}_{+}$ , we find

$$\sum_i e^{i(\mathbf{K}_{+} + \mathbf{k})\delta_i} \simeq \frac{3a}{2} e^{i\phi} (k_x + ik_y), \quad (2.6)$$

with some phase  $\phi$ , that can be absorbed by a redefinition of the amplitudes  $\psi_{A/B}$ . We hence obtain for the effective low-energy description

$$H \begin{pmatrix} \psi_A \\ \psi_B \end{pmatrix} = \varepsilon \begin{pmatrix} \psi_A \\ \psi_B \end{pmatrix}, \quad H = \hbar v \begin{pmatrix} 0 & k_x - ik_y \\ k_x + ik_y & 0 \end{pmatrix} \equiv \hbar v \mathbf{k} \cdot \boldsymbol{\sigma}, \quad (2.7)$$

where the velocity  $v = 3at/2\hbar \approx 10^6 \text{ m/s}$ , and  $\boldsymbol{\sigma} = (\sigma_x, \sigma_y)$  names the Pauli matrices, that act on pseudospin (*i.e.* sublattice) space. The low-energy description of graphene is therefore equivalent to the massless Dirac equation in  $2 + 1$  dimensions, with an effective speed of light, that is roughly 300 times smaller than the real speed of light. The spectrum around the Dirac points is linear,

$$\varepsilon_{s,\mathbf{k}} = s\hbar v |\mathbf{k}|. \quad (2.8)$$

Here,  $s = \pm 1$  refers to the conduction and valence band, respectively. A similar description applies for electrons located close to the Dirac point  $K_-$ . We remark, that a full description

of the low energy physics takes into account electrons that reside close to either of the two Dirac points. Potential disorder may in principle allow for scattering of the electrons between the two cones, however only if it transfers a momentum of the order of  $|\mathbf{K}_\pm|$ . In this thesis, we only consider disorder that is smooth on the scale of the lattice constant, such that a description in terms of a single Dirac cone is sufficient.

We now list some properties of the Dirac equation, that are important for later use. The plane-wave solutions of the Dirac equation read

$$\psi_{s,\mathbf{k}} = \frac{1}{\sqrt{2V}} e^{i\mathbf{k}\mathbf{r}} \begin{pmatrix} 1 \\ s e^{i\theta_{\mathbf{k}}} \end{pmatrix}, \quad (2.9)$$

where  $V$  is the area of the sample, and  $\theta_{\mathbf{k}}$  is the direction of the wavevector. The plane-wave solutions are eigenstates of the helicity operator,

$$h = \frac{\mathbf{k} \cdot \boldsymbol{\sigma}}{|\mathbf{k}|}, \quad (2.10)$$

with eigenvalues  $+1$  ( $-1$ ) for electrons in the conduction (valence) band. This means, that the pseudospin is strongly coupled to the orbital degrees of freedom, as it points in the same (opposite) direction as the momentum of the particle, a property which is termed *chirality*.

Electrons described by the Dirac Hamiltonian satisfy a continuity equation

$$\partial_t \rho + \nabla \cdot \mathbf{j} = 0 \quad (2.11)$$

where the probability density  $\rho$  and the associated current  $\mathbf{j}$  are given by

$$\rho = \psi^\dagger \psi, \quad \mathbf{j} = v \psi^\dagger \boldsymbol{\sigma} \psi. \quad (2.12)$$

We remark that the velocity operator in graphene reads  $\mathbf{v} = v\boldsymbol{\sigma}$ , and does not depend on momentum, unlike for a parabolic dispersion.

In contrast to conventional two-dimensional systems, the density of states (per spin and valley) has a linear dependence on energy,

$$\nu(\varepsilon) = \frac{|\varepsilon|}{2\pi(\hbar v)^2}. \quad (2.13)$$

In particular, the density of states vanishes, as the system is tuned to the Dirac point.

## 2.2. Graphene in a magnetic field

As a first demonstration of the unconventional properties of graphene that root in the peculiar bandstructure, we consider the effect of a constant magnetic field. It is well known, that a strong magnetic field applied to a two-dimensional electron gas gives rise to well-defined quantized energies, the so-called *Landau levels* [Land 77], that are observed in magnetotransport experiments. We will see that the series of Landau levels in graphene differs crucially from the one observed in conventional semiconductor heterostructures. The standard calculation of the Landau levels proceeds by adding the vector potential

$\mathbf{A}$  for a constant magnetic field to the Hamiltonian and solve the quantum-mechanical problem by mapping it to a harmonic oscillator. We here take an alternative approach and use semiclassical arguments to determine the Landau levels, in the spirit of [Carm 08].

As a warmup, and to get confident with the semiclassical description, we start with the calculation of the Landau levels for a conventional two-dimensional electron gas with parabolic dispersion. The classical Hamilton function reads

$$H(\mathbf{p}, \mathbf{r}) = \frac{(\mathbf{p} + e\mathbf{A}(\mathbf{r}))^2}{2m}, \quad (2.14)$$

where  $e$  is the electron charge, and  $m$  is the effective mass. One proceeds by deriving the equations of motion,

$$\dot{\mathbf{r}} = \frac{\partial H}{\partial \mathbf{p}}, \quad \dot{\mathbf{p}} = -\frac{\partial H}{\partial \mathbf{r}} \quad (2.15)$$

which yield the familiar Lorentz force

$$m\ddot{\mathbf{r}} = -e\dot{\mathbf{r}} \times \mathbf{B}, \quad (2.16)$$

with the magnetic field  $\mathbf{B} = \nabla \times \mathbf{A}$ . The classical velocity is related to the canonical momentum as

$$\dot{\mathbf{r}} = \frac{1}{m} (\mathbf{p} + e\mathbf{A}). \quad (2.17)$$

The solution of these classical equations describes a cyclotronic motion of the electrons,

$$\mathbf{r} = \mathbf{r}_0 + \begin{pmatrix} R \cos \omega_c t \\ R \sin \omega_c t \end{pmatrix}, \quad (2.18)$$

where the radius and the frequency are given by

$$\omega_c = \frac{eB}{m}, \quad E = \frac{1}{2} m \omega_c^2 R^2. \quad (2.19)$$

Next, we now employ semiclassical quantization conditions,<sup>2</sup>

$$\oint \mathbf{p} d\mathbf{r} = h \left( n + \frac{1}{2} \right), \quad (2.20)$$

where the contour integral extends over a single classical orbit, whose duration we denote by  $T = 2\pi/\omega_c$ . We proceed by manipulating the left-hand side of this equation,

$$\oint \mathbf{p} d\mathbf{r} = \oint (\mathbf{p} + e\mathbf{A}) \dot{\mathbf{r}} dt - e \oint \mathbf{A} d\mathbf{r} = 2ET - eB\pi R^2 = E \frac{2\pi}{\omega_c} \quad (2.21)$$

where we used Stokes' theorem as well as Eq. (2.19). Indeed, we find the familiar Landau level quantization for a two-dimensional electron gas with parabolic dispersion.

$$E = \hbar \omega_c \left( n + \frac{1}{2} \right). \quad (2.22)$$

---

<sup>2</sup>The shift by  $\frac{1}{2}$  in the quantization condition is related to a so-called Maslov index, that appears in semiclassical theories, when the trajectories have caustics (turning points) [Gutz 90, Carm 08].

Let us now turn to the Landau levels for graphene. The calculation has to be modified, as the spectrum is now linear,

$$H(\mathbf{p}, \mathbf{r}) = v |\mathbf{p} + e\mathbf{A}(\mathbf{r})|, \quad (2.23)$$

where, for simplicity, we consider electrons from the conduction band. The velocity is no longer related to the magnitude of the momentum, but rather only to its direction, with a fixed magnitude  $v$ ,

$$\dot{\mathbf{r}} = v \frac{\mathbf{p} + e\mathbf{A}}{|\mathbf{p} + e\mathbf{A}|} = \frac{v^2}{E} (\mathbf{p} + e\mathbf{A}). \quad (2.24)$$

The Lorentz force equation now reads

$$\frac{v^2}{E} \ddot{\mathbf{r}} = -e\dot{\mathbf{r}} \times \mathbf{B}. \quad (2.25)$$

The equations of motion in graphene are hence obtained from the non-relativistic ones, if one replaces the mass using the famous relation  $E = mc^2$ , where the speed of light is replaced by  $v$ .

Like in the non-relativistic case, electrons perform cyclotronic motion in a magnetic field, but the radius and the frequency are now fixed by the equations

$$\omega_c = \frac{v^2 e B}{E}, \quad v = R\omega_c. \quad (2.26)$$

Sofar we only considered the effect of the relativistic dispersion. For an accurate description of the Landau levels however, we also have to reconcile the effect of the pseudospin. As discussed in the previous section, electrons in graphene behave as chiral particles, and they take their pseudospin with them during their motion, pointing along the momentum. As the electron performs a cyclotronic motion, the pseudospin winds once around its axis. It is known from the quantummechanical theory of angular momentum, that a  $2\pi$ -rotation of a spin leads to a  $\pi$ -phaseshift in the wavefunction, that has to be included in the quantization condition, i.e. the action integral equals now an integer multiple of the Planck constant

$$\oint \mathbf{p} d\mathbf{r} = nh. \quad (2.27)$$

When we evaluate the left-hand side of this equation, we now obtain

$$\oint \mathbf{p} d\mathbf{r} = \oint (\mathbf{p} + e\mathbf{A}) \dot{\mathbf{r}} dt - e \oint \mathbf{A} d\mathbf{r} = ET - eB\pi R^2 = \frac{\pi E^2}{v^2 e B}. \quad (2.28)$$

We then find for the quantized energies

$$E = \pm \sqrt{2n\hbar v^2 e B}, \quad (2.29)$$

where we included the  $\pm$  in the final result, in order to account for conduction and valence band. One would expect, that classical arguments supply us with good results at high energies. Quite remarkably, we obtain the correct quantum result for all the Landau levels.

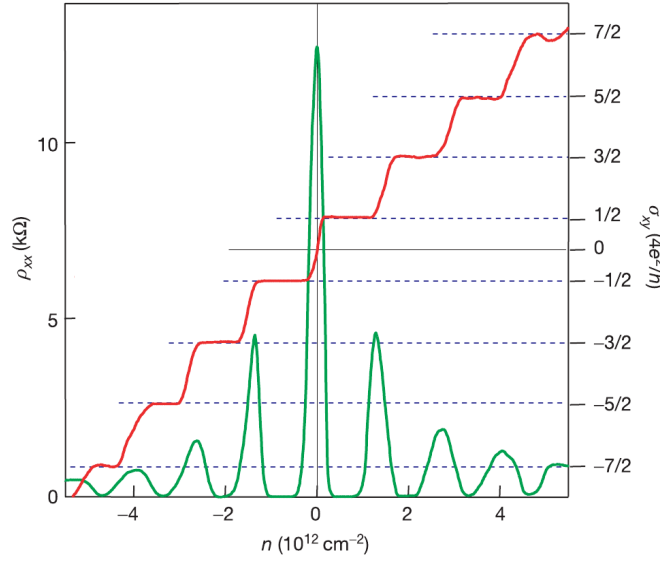


Figure 2.3.: Measurement of the Hall conductivity  $\sigma_{xy}$  and the transversal resistivity  $\rho_{xx}$  for a graphene sample exposed to a magnetic field of  $14T$ . The plateaus of the Hall conductivity demonstrate the half-integer quantization of the Landau levels in graphene. (Figure taken from [Novo 05].)

In fact, this can be understood, as the problem maps to that of a harmonic oscillator, a special kind of situation, where semiclassical quantization turns out to be exact.

Notably, we find the existence of a Landau level at zero energy in graphene, which appears as a consequence of the modified quantization condition (2.27) that arises due to the Berry phase. Thus, the existence of this zero-energy Landau level is intimately linked to the chiral nature of charge carriers in graphene. The Landau levels can be probed experimentally in a Hall bar measurement. For strong magnetic fields, the transverse conductance  $\sigma_{xy}$  as a function of energy (or density) shows plateaus with quantized values of  $e^2/h$  times the number of filled Landau levels. The existence of a Landau level at zero energy is special in that respect, as it is shared by valence and conduction band. In fact, this leads to quantized values of the transverse conductance at half-integer steps,

$$\sigma_{xy} = 4 \frac{e^2}{h} \left( n + \frac{1}{2} \right), \quad (2.30)$$

where a factor 4 accounts for spin and valley degeneracy, so that the transverse conductance is an integer multiple of  $e^2/h$ . The experimental verification of this half-integer quantization directly proved the relativistic nature of charge carriers in graphene [Novo 05, Zhan 05], see Fig. 2.3. Quite remarkably, due to the high mobility of the graphene samples, the quantum Hall effect in graphene can be observed at room temperature.

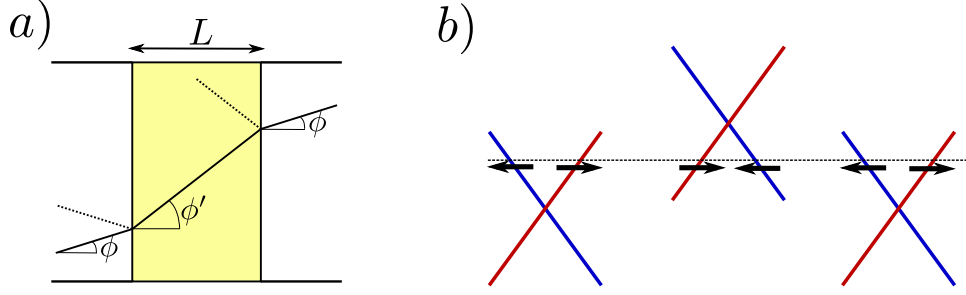


Figure 2.4.: *Left*: Schematic picture of a Dirac particle moving in a rectangular potential *Right*: Perfect transmission at normal incidence: The plot shows the Dirac spectrum for  $k_y = 0$ , which consists of two branches for right- and leftmoving states (red and blue). The dotted line indicates the Fermi level. Black arrows indicate the direction of the pseudospin, which points parallel (antiparallel) to the momentum in the conduction (valence band). The spinor of a rightmoving electron matches perfect the spinor of a rightmoving hole, so the electron is perfectly transmitted through the hole-doped region.

### 2.3. Klein tunneling

A striking manifestation of the wavenature of quantum particles is the effect, that quantum particles can penetrate classical forbidden areas, known as *quantum tunneling*. The transmission probability for this process decays exponentially with increasing height  $V_0$  of the potential barrier. In 1929, Oskar Klein studied quantum tunneling for relativistic particles, and surprisingly found that the tunneling probability becomes large again, once the potential height exceeds the electron's rest mass,  $V_0 > 2mc^2$ . This at first sight counterintuitive seeming effect can be explained with the fact that the Dirac equation allows for solutions at negative energies. Thus, while the barrier constitutes a forbidden region for positive energy states (electrons), it allows for the existence of negative energy states (positrons). Although Klein tunneling is a striking feature of relativistic quantum electrodynamic, it is of little practice relevance for electrons, as the preparation of such potential step requires gigantic electric fields. Relativistic quantum tunneling however has important consequences for the electronic properties of graphene.

We now discuss scattering processes in graphene in a rectangular potential barrier, where we follow [Cast 09]. To be specific, we consider a potential barrier of height  $V_0$  present in the strip  $0 < x < L$ . The incident particle has energy  $E$  and approaches the barrier from the left under the angle  $\phi$ . In the region I, left from the barrier, the wavefunction can be written as a sum of incident and reflected plane wave (see Eq. (2.9))

$$\psi_I(\mathbf{r}) = \frac{1}{\sqrt{2}} \begin{pmatrix} 1 \\ se^{i\phi} \end{pmatrix} e^{i(k_x x + k_y y)} + r \frac{1}{\sqrt{2}} \begin{pmatrix} 1 \\ se^{i(\pi - \phi)} \end{pmatrix} e^{i(-k_x x + k_y y)} \quad (2.31)$$

where  $s = \text{sgn}(E)$ ,  $k_F = E/s\hbar v$ ,  $k_x = k_F \cos \phi$ , and  $k_y = k_F \sin \phi$ . For the reflected part (which contains the coefficient  $r$ ), we note that the barrier inverts  $k_x$  but conserves  $k_y$ , such that the propagation angle becomes  $\phi_r = \pi - \phi$ .

In the barrier region (II), the wavefunction is of the form

$$\psi_{\text{II}}(\mathbf{r}) = a \frac{1}{\sqrt{2}} \begin{pmatrix} 1 \\ s' e^{i\phi'} \end{pmatrix} e^{i(k'_x x + k_y y)} + b \frac{1}{\sqrt{2}} \begin{pmatrix} 1 \\ s' e^{i(\pi - \phi')} \end{pmatrix} e^{i(-k'_x x + k_y y)} \quad (2.32)$$

with  $s' = \text{sgn}(E - V_0)$ . Again, the barrier does not alter the  $y$ -component of the momentum – the  $x$ -component is then fixed by the dispersion,

$$E - V_0 = s' \hbar v \sqrt{k'_x{}^2 + k_y^2}, \quad (2.33)$$

and the angle of propagation is given by  $\phi' = \arctan k_y/k'_x$ . (We assume here, that the parameters are tuned in such a way, that the incident state can propagate through the barrier, *i.e.* Eq. (2.33) can be solved for real  $k'_x$ . The opposite case will be discussed later on).

Finally, in the region right of the barrier (III), the wavefunction reads

$$\psi_{\text{III}}(\mathbf{r}) = t \frac{1}{\sqrt{2}} \begin{pmatrix} 1 \\ s e^{i\phi} \end{pmatrix} e^{i(k_x x + k_y y)}. \quad (2.34)$$

The four coefficients  $r, a, b, t$  need to be determined from matching conditions. As the Dirac equation is linear in the momentum operator, the wavefunction needs to be continuous at the potential steps at  $x = 0$  and  $x = L$ , but no restriction on the derivative of the wavefunction is imposed (unlike for non-relativistic particles with parabolic dispersion). However, as we have to match both components of the spinor at the interfaces, we obtain four equations that determine all the coefficients. We are interested in the transmission, which is found to be [Cast 09]

$$T = |t|^2 = \frac{\cos^2 \phi' \cos^2 \phi}{\cos^2 k'_x L \cos^2 \phi' \cos^2 \phi + \sin^2 k'_x L (1 - s s' \sin \phi \sin \phi')^2}. \quad (2.35)$$

We note, that  $k'_x$  also has a dependence on the angle  $\phi$ . The angle-dependence of the transmission is illustrated in Fig. 2.5

We now investigate, for which parameters the barrier becomes fully transparent, *i.e.*  $T = 1$ . We see, that this is the case, whenever  $k'_x L = n\pi$ , with integer  $n$ . This condition precisely accounts for resonant scattering, as the phase that a particle accumulates, while it traverses the barrier forth and back, is a multiple of  $2\pi$ . Such resonant scattering is well-known also from non-relativistic scattering processes. On the other hand, we find perfect transmission also for normal incidence ( $\phi = \phi' = 0$ ) independent of length and height of the potential barrier. Such effect is in striking contrast to what one is experienced from non-relativistic scattering processes. Indeed, the perfect transmission at normal incidence is a direct consequence of the chiral nature of charge carriers: Incident and reflected wave have opposite pseudospin for normal incidence; the potential barrier however conserves spin, hence no particle can be reflected. We remark, that this effect holds true even if the charge carriers in the barrier are of hole-type, while they are of electron-type outside the barrier. In this case, a normally incident electron is propagating as a hole within the barrier with 100 % efficiency, see also Fig. 2.4

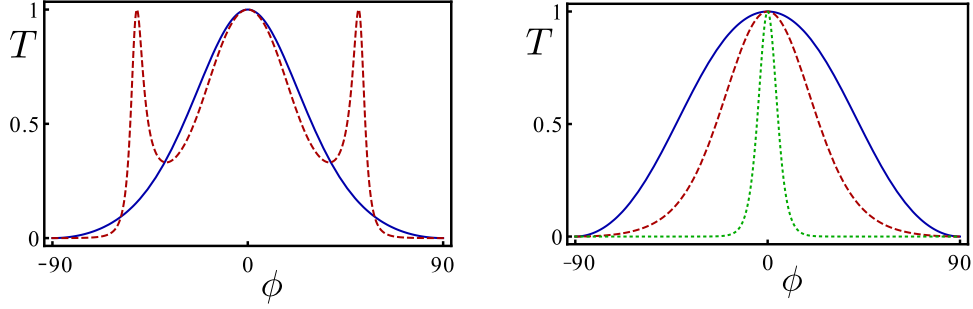


Figure 2.5.: Transmission  $T$  of the rectangular barrier as a function of the incident angle  $\phi$ . *Left:* Rectangular barrier is hole-doped while the outside regions are electron-doped, with the same carrier concentration ( $V_0 = 2E$ ). Perfect transmission is observed at normal incidence, and – depending on the parameters – at certain finite angles, the latter corresponding to resonant tunneling (blue solid curve:  $k_F L = 1$ , red dashed curve:  $k_F L = 5$ ). *Right:* Barrier is tuned to the Dirac point ( $V_0 = E$ ). Perfect transmission is always observed at normal incidence, but the transmission rapidly goes to zero away from normal incidence, as the length of the barrier is increased (blue solid curve:  $k_F L = 1$ , red dashed curve:  $k_F L = 2$ , green dotted curve:  $k_F L = 10$ ).

For the discussion so far, we assumed a situation where the incident state can propagate through the barrier. Now we also want to illustrate the opposite case. For simplicity, we consider the extreme case  $V_0 = E$ , which tunes the barrier region at the Dirac point. Then, Eq. (2.33) allows for propagating states (real  $k'_x$ ) only for normal incidence. Otherwise, the dispersion relation can only be satisfied for imaginary  $k'_x = \pm i k_y$ . The states in the barrier region are hence evanescent waves,  $\psi_{\pm}(\mathbf{r}) = \chi_{\pm} e^{\pm k_y x + i k_y y}$ , where the spinors  $\chi_{\pm}$  are determined by the Dirac equation at zero energy,  $\boldsymbol{\sigma} \cdot \nabla \psi_{\pm}(\mathbf{r}) = 0$ . We then find, that the wavefunction in the barrier region is

$$\psi_{\Pi}(\mathbf{r}) = a \begin{pmatrix} 1 \\ 0 \end{pmatrix} e^{(k_y x + i k_y y)} + b \begin{pmatrix} 0 \\ 1 \end{pmatrix} e^{(-k_y x + i k_y y)}. \quad (2.36)$$

We then obtain for the transmission through the barrier

$$T = \frac{2 \cos^2 \phi}{\cos 2\phi + \cosh 2k_y L} = \frac{2 \cos^2 \phi}{\cos 2\phi + \cosh (2k_F L \sin \phi)}. \quad (2.37)$$

Again, we find perfect transmission at normal incidence, as a consequence of the chirality of the charge carriers. The transmission however quickly drops to zero away from perpendicular incidence for long barriers, see Fig. 2.5.

## 2.4. Transport in clean graphene

Finally, we also want to study electric transport in clean graphene. To this end, we first introduce the Landauer-Büttiker formalism and then apply it to transport in graphene.



### 2.4.1. Landauer-Büttiker formalism

Transport in mesoscopic system is successfully described with the Landauer-Büttiker formalism. We consider a sample that is connected to two electron reservoirs, denoted left (L) and right (R). The Landauer formula links the conductance of the sample to its scattering matrix, more precisely to the information how well the sample allows for electrons to be transmitted from one lead to the other. We here briefly sketch the main ideas of the Landauer formula and refer to the literature for a detailed derivation (*e.g.* [Datt 95]).

We first consider the case of a perfect one-dimensional conductor. Left and right lead are kept at different chemical potentials,  $\mu_L$  and  $\mu_R$ . The occupation probability for the electrons of the lead to be in a state at a certain energy is given by the Fermi-Dirac distribution, which reads at zero temperature

$$f_i(\varepsilon) = \begin{cases} 1, & \varepsilon < \mu_i \\ 0, & \varepsilon > \mu_i \end{cases}, \quad (2.38)$$

for  $i = L, R$ . For a perfect conductor, where electrons are not backscattered, all right-moving (left-moving) electrons in the conductor originate from the left (right) lead, constituting a current

$$I = \int_0^\infty \frac{dk}{2\pi} e v_k f_L(\varepsilon_k) + \int_{-\infty}^0 \frac{dk}{2\pi} e v_k f_R(\varepsilon_k), \quad (2.39)$$

where  $k$  labels the wavenumber of the one-dimensional quantum states, and  $\varepsilon_k$  and  $v_k$  is the associated velocity. Upon using  $v_k = \frac{1}{\hbar} \frac{d\varepsilon_k}{dk}$ , we rewrite this expression as

$$I = e \int \frac{d\varepsilon}{2\pi\hbar} [f_L(\varepsilon) - f_R(\varepsilon)] = \frac{e}{h} (\mu_L - \mu_R), \quad (2.40)$$

where we made use of the explicit distribution function Eq. (2.38). With the definition of the voltage  $V = (\mu_L - \mu_R)/e$ , we find for the conductance of a perfect one-dimensional conductor  $G_0 = I/V$ ,

$$G_0 = \frac{e^2}{h}, \quad (2.41)$$

which we refer to as “conductance quantum” and whose reciprocal value corresponds to a resistance of 25.8 k $\Omega$ . We note that the conductance for the perfect one-dimensional conductor results from the net charge transport of electrons impinging from left and right lead. When the conductor is not perfect, electrons might be scattered back to the leads. It is then only the fraction  $T$  of electrons transmitted from one lead to the other, that contributes to the current

$$G = \frac{e^2}{h} T. \quad (2.42)$$

While the discussion so far applied for a strictly one-dimensional systems, it may be easily generalized to higher dimensions, where the states in the leads are characterized by an additional quantum number  $n$  resulting from the wavefunction for the transverse coordinates. These transverse degrees of freedom are also referred to as *modes* or *channels*,

and for the Landauer conductance, one needs to sum the transmission from all the channels in the left lead to all the channels in the right lead,

$$G = \frac{e^2}{h} \sum_{nm} |t_{nm}|^2 = \frac{e^2}{h} \text{Tr}(tt^\dagger). \quad (2.43)$$

Here  $t_{nm}$  is the transmission amplitude for a particle starting from mode  $m$  in the left lead to end up in the mode  $n$  in the right lead, while  $t$  denotes the corresponding matrix.

### 2.4.2. Conductance of a clean graphene sample

With the help of the Landauer-Büttiker formalism, we are now in the position to calculate the conductance of a clean graphene sheet, following the calculation presented in [Twor 06]. Our setup consists of a rectangular graphene sample of dimensions  $L \times W$ , which is in contact to metallic leads at  $x = 0$  and  $x = L$ , which strongly dope the graphene region under it. The Hamiltonian reads

$$H = v\mathbf{p} \cdot \boldsymbol{\sigma} + V(x) \quad (2.44)$$

where  $V(x)$  models the potential induced by the leads

$$V(x) = \begin{cases} V_L, & x < 0 \text{ or } x > L \\ 0, & 0 < x < L \end{cases} \quad (2.45)$$

In principle, electronic transport in graphene nanoribbons can be very sensitive to the boundary conditions, i.e. if the edges are of armchair or zigzag type. We here avoid these issues by considering a very wide sample  $W \gg L$ , so that boundary effects do not influence the value of the conductance. We then can choose periodic boundary conditions, for which the calculation is most simple: As the system is translationally invariant in the  $y$ -direction, the wavefunctions are of the form

$$\Psi_n(x, y) = \psi_n(x) \frac{1}{\sqrt{W}} e^{iq_n y} \quad (2.46)$$

with the quantized transverse momenta

$$q_n = n \frac{2\pi}{W} \quad (2.47)$$

where  $n$  is an integer number. We then solve the Dirac equation for each transverse mode in each of the three regions left lead (L), central region (C) and right lead (R). For the scattering state of a particle impinging from the left lead, we write

$$\begin{aligned} \psi_n^{(L)}(x) &= \chi_{n,k_L} e^{ik_L x} + r_n \chi_{n,-k_L} e^{-ik_L x} \\ \psi_n^{(C)}(x) &= \alpha_n \chi_{n,-k} e^{ikx} + \beta_n \chi_{n,-k} e^{-ikx} \\ \psi_n^{(R)}(x) &= t_n \chi_{n,k_L} e^{ik_L x}, \end{aligned} \quad (2.48)$$

with coefficients  $r_n, t_n, \alpha_n, \beta_n$ . Here, the wavenumbers  $k$  and  $k_L$  are found from the relativistic dispersion

$$k = \sqrt{(\varepsilon/\hbar v)^2 - q_n^2} \quad (2.49)$$

$$k_L = \sqrt{\left(\frac{\varepsilon - V_L}{\hbar v}\right)^2 - q_n^2}, \quad (2.50)$$

where  $\varepsilon$  denotes the energy of the electrons in graphene. The wavenumber  $k$  in the sample may be real or imaginary, discriminating oscillatory and evanescent modes. In the leads, we only account for propagating modes. The spinor structure of the solution reads

$$\chi_{n,k} = \frac{1}{\sqrt{2}} \begin{pmatrix} 1 \\ sz_{n,k} \end{pmatrix}, \quad z_{n,k} = \frac{k + iq_n}{\sqrt{k^2 + q_n^2}} \quad (2.51)$$

where  $s = \pm$  refers to conduction/valence band. This expression for the spinor is valid for both real and imaginary  $k$ . For real  $k$ , we have  $z_{n,k} = e^{i\theta}$ , where  $\theta$  is the polar angle of the wavevector  $(k, q_n)$ , which gives the well-known expression from Eq. (2.9). We consider the limit of highly doped leads,  $V_L \rightarrow -\infty$ , so that the spinors in the leads have a particular simple form

$$\chi_{n,\pm k_L} = \frac{1}{\sqrt{2}} \begin{pmatrix} 1 \\ \pm 1 \end{pmatrix}. \quad (2.52)$$

We can easily interpret these results, as for fixed  $q_n$  and  $V_L \rightarrow -\infty$  the electrons are mainly moving in the  $x$ -direction in the leads, and thus the spinors are eigenstates of the  $\sigma_x$  Pauli matrix.

The next step is to connect the wavefunctions at the lead-sample interfaces  $x = 0$  and  $x = L$ . As discussed in the previous Section, we demand the wavefunction to be continuous at the interfaces, but we pose no restriction on the derivative. One then obtains for the transmission

$$T_n = |t_n|^2 = \left| \frac{k}{k \cos kL + i\sqrt{k^2 + q_n^2} \sin kL} \right|^2. \quad (2.53)$$

Having determined the transmission for each channel, we can calculate the Landauer conductance

$$G = 4 \frac{e^2}{h} \sum_n T_n, \quad (2.54)$$

where a factor 4 accounts for the spin and valley degeneracy in graphene. In the short-and-wide limit  $W \gg L$ , the summation over transverse momenta can be replaced by an integration

$$\sum_n \rightarrow \frac{W}{2\pi} \int dq \quad (2.55)$$

The conductance for a short-and-wide sample as a function of energy is shown in Fig. 2.6. If we tune the energy of the charge carriers in the sample to zero, transport is mediated by evanescent modes,

$$T_n = \frac{1}{\cosh^2 q_n L}. \quad (2.56)$$

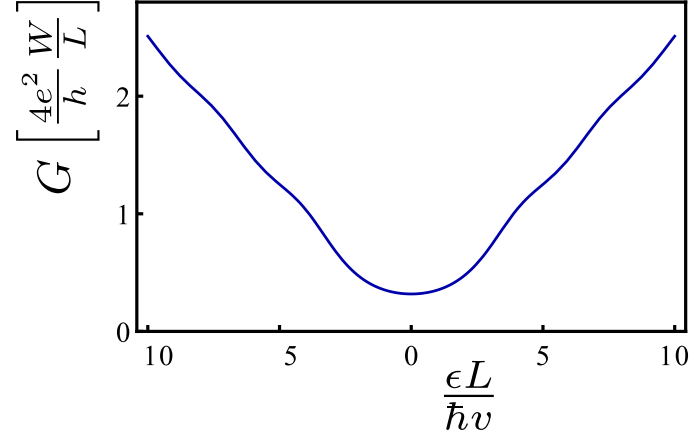


Figure 2.6.: Conductance of an undoped graphene sheet, as a function of energy.

Nevertheless, the conductivity acquires a *finite* value,

$$G = \frac{4}{\pi} \frac{e^2}{h} \frac{W}{L} \Leftrightarrow \sigma = \frac{4}{\pi} \frac{e^2}{h}. \quad (2.57)$$

As one increases the energy in the sample, more and more modes can propagate through the sample, and the conductance increases roughly linear with energy.

### 3. Resonant scattering in graphene with a gate-defined chaotic quantum dot

The successful production of high-quality nanoflakes together with the strictly two-dimensional nature of the material have made graphene to a promising candidate for future nanoelectronic devices. Of particular interest is the realization of quantum dots, where electrons are confined locally in a narrow region of the graphene sample. A well-established experimental route in the fabrication of quantum dots utilizes metallic gates nearby the sample, that repel electrons from regions outside the quantum dot. Such procedure however is problematic for graphene, in view of the Klein tunneling, that allows the electrons to escape the quantum dot, as we discussed in the previous chapter.

Recently, Bardarson, Titov and Brouwer argued that there is an exception to this statement, and for geometries, for which the Dirac equation is separable, confinement with the help of metal gates should be possible [Bard 09]. Their study was supplemented by a numerical simulation of transport, where the graphene sheet containing the quantum dot, is attached to source and drain contacts. The interesting limit, where the dot is only weakly coupled to the leads, was however not accessible with the applied numerical method. The purpose of this chapter is to study the geometry-dependence of gate-defined quantum dots in graphene, where we gain new insights by applying a recently developed method from Ref. [Tito 10].

This chapter is structured as follows: After an introduction, we briefly summarize the main findings of [Bard 09] in Section 3.2. In Section 3.3, we then explain how the method of [Tito 10] can be used to study gate-defined quantum dots of arbitrary geometries in graphene. Our results are presented in Section 3.4. We conclude in section 3.5. The Secs. 3.1, 3.3 – 3.5 of this chapter are based on the publication [Schn 11].

#### 3.1. Introduction

There are two commonly used routes in the fabrication of quantum dots, which create a spatial confinement of the electrons. One way is to mechanically carve out nanostructures (“etched quantum dots”). The other possibility relies on metallic gates, which can create forbidden regions for the electrons, when the Fermi level is shifted in the bandgap of the nanosystem. Due to the absence of a bandgap in graphene, experimentalists pursue the first possibility for the fabrication of graphene quantum dots [Bunc 05, Pono 08, Stam 08, Schn 09, Gutt 12, Jaco 12].

In a recent article [Bard 09], Bardarson, Titov and Brouwer showed that the common assertion, that it is not possible to confine electrons in graphene with metal gates, can be circumvented in certain cases. In their article, they considered a quantum dot that is surrounded by undoped graphene. As the density of states vanishes, when the Fermi level

is tuned to the Dirac point, such scenario comes closest to the “formation of a bandgap” in graphene. We learned in the previous chapter, that Klein tunneling opens a way to penetrate the surrounding. However, Klein tunneling is only effective when the electron hits the surface of the quantum dot at perpendicular incidence, while the transmission probability quickly drops to zero away from perpendicular incidence. The authors of Ref. [Bard 09] therefore argued, that confinement should be possible in graphene, when the geometry is such, that the Dirac equation is separable, and the associated classical motion is integrable. An example for such a geometry is a disc-shaped dot with a uniform potential inside the disc. Generic classical trajectories in this geometry will never hit the surface at perpendicular incidence, which renders Klein tunneling ineffective. On the other hand, in a geometry with classical chaotic dynamics, every electron eventually the surface at perpendicular incidence, and the quantum dot lacks confinement (see also Fig. 1.1 of Chapter 1).

To further investigate this reasoning based on classical arguments, the authors of Ref. [Bard 09] numerically simulated the two-terminal transport, when the quantum dot surrounded by undoped graphene is attached to source and drain contacts, see Fig. 3.1. Bound states of the quantum dot are then revealed as resonances in the two-terminal conductance. For a circular geometry, the authors indeed found a series of sharp resonances, corresponding to well-confined quantum states, while for a stadium geometry, the resonances are typically broader, indicating a lack of confinement. The difference between integrable quantum dots and non-integrable quantum dots becomes most pronounced in the limit that the distance  $L$  between the two metallic contacts becomes large, in comparison to the size of the quantum dot. However, a detailed investigation of this limit was not possible in Ref. [Bard 09] because of limitations of the numerical approach required to study the non-integrable case.

In the mean time, the problem of gate-defined quantum dots in graphene has been revisited by Titov, Ostrovsky, Gornyi, Schuessler, and Mirlin [Tito 10]. These authors adapted the matrix Green function method, originally developed by Nazarov in the context of mesoscopic superconductivity [Naza 94], to two-terminal transport in graphene. One of their main results is a relation between the two-terminal conductance of a rectangular graphene sheet containing an arbitrary “scatterer” and the scatterer’s  $T$ -matrix. A gate-defined quantum dot is a special case of such a scatterer. Using this method, Titov *et al.* were able to give an analytic expression for the conductance of an otherwise undoped graphene sheet with a disc-shaped quantum dot, reproducing the numerically obtained conductance of Bardarson *et al.* [Bard 09].

In this chapter, we want to find out what information the matrix Green function method makes available if we consider undoped graphene with a non-separable quantum dot. This requires a numerical calculation of the  $T$  matrix, since no analytical results are available for a quantum dot for which the Dirac equation is not separable. We here show that the numerical evaluation of the  $T$  matrix can be done very efficiently and that the remaining steps in the matrix Green function formalism can still be carried out analytically. In particular, once the  $T$  matrix of the quantum dot is known, the  $L$  dependence of the conductance resonances can be found without additional numerical effort. This allows us to obtain information about the constitution of the resonances deep into the regime in which resonances are separated, which could not be addressed with the generic numerical

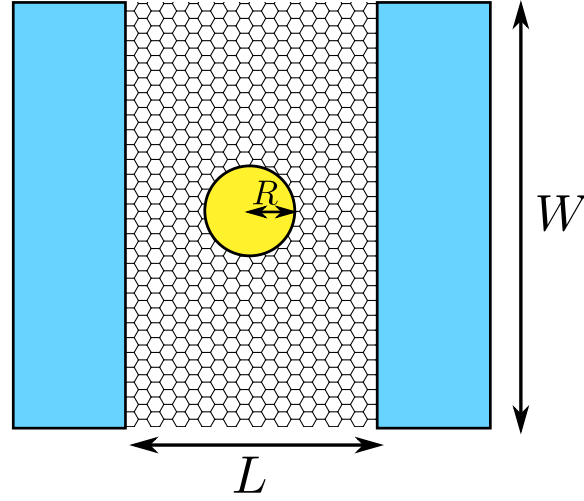


Figure 3.1.: Geometry of the two-terminal transport setup: A rectangular sample of graphene of dimensions  $L \times W$ , that contains a quantum dot of size  $R$ .

algorithm used in Ref. [Bard 09]. We apply the formalism to a stadium-shaped quantum dot. Our main result is that the resonance lineshapes are described by the Fano resonance formula in the case of the stadium-shaped (*i.e.*, non-separable) quantum dot, while they are Breit-Wigner resonances for the disc-shaped dot.

## 3.2. Electrostatic confinement in a gate-defined graphene quantum dot

Before we enter the presentation of our results, we give a brief summary of the main findings of Ref. [Bard 09], in order to keep the thesis self-contained.

### 3.2.1. Bound states of a circular quantum dot

We start by considering a circular quantum dot in a graphene sheet. For this situation, an analytic calculation of the resonant levels is possible. We thus study the Hamiltonian

$$H = v\mathbf{p} \cdot \boldsymbol{\sigma} + V(\mathbf{r}), \quad (3.1)$$

where the gate potential  $V(\mathbf{r})$  accounts for the circular quantum dot of radius  $R$ ,

$$V(\mathbf{r}) = \begin{cases} -\hbar v V_0, & r < R \\ 0, & r > R, \end{cases} \quad (3.2)$$

The constant  $V_0$  has the dimension of inverse length and we choose  $V_0 > 0$ , so that the quantum dot is electron doped. Although the potential  $V(\mathbf{r})$  is steplike in our description,

we remark, that this step is required to be smooth on the scale of the lattice constant, so that a description in terms of a single Dirac point is justified.

The radial symmetry of the problem facilitates a solution in polar coordinates  $(r, \theta)$ , for which the kinetic part of the Hamiltonian is found to be

$$v\mathbf{p} \cdot \boldsymbol{\sigma} = -i\hbar v \begin{pmatrix} 0 & \partial_- \\ \partial_+ & 0 \end{pmatrix}, \quad (3.3)$$

with the operators

$$\partial_{\pm} = e^{\pm i\theta} \left( \partial_r \pm \frac{i}{r} \partial_{\theta} \right). \quad (3.4)$$

The radial symmetry furthermore suggests to look for common eigenstates of the Hamiltonian and the angular momentum operator. As the kinetic part strongly couples orbital and pseudospin degrees of freedom, neither orbital angular momentum, nor pseudospin alone is conserved. What is conserved however, is the total angular momentum  $j_z = l_z + \frac{\hbar}{2}\sigma_z$ . We therefore seek for eigenstates of the form

$$\psi_m(\mathbf{r}) = e^{im\theta} \begin{pmatrix} e^{-i\frac{\theta}{2}} \varphi_{m,+}(r) \\ e^{i\frac{\theta}{2}} \varphi_{m,-}(r) \end{pmatrix} \quad (3.5)$$

which are eigenstates of the total angular momentum  $j_z \psi_m = m\hbar \psi_m$ , with half-integer quantum number  $m$ .

Inside the dot, for  $r < R$ , the Dirac equation yields the following coupled equations for the radial wave functions  $\varphi_{m,\pm}$ ,

$$\begin{aligned} \left( \partial_r - \left(m - \frac{1}{2}\right) \frac{1}{r} \right) \varphi_{m,+}(r) &= iV_0 \varphi_{m,-}(r), \\ \left( \partial_r + \left(m + \frac{1}{2}\right) \frac{1}{r} \right) \varphi_{m,-}(r) &= iV_0 \varphi_{m,+}(r). \end{aligned} \quad (3.6)$$

The solution of these equations read

$$\begin{aligned} \varphi_{m,+}(r) &= J_{|m-1/2|}(V_0 r) \\ \varphi_{m,-}(r) &= i \operatorname{sgn}(m) J_{|m+1/2|}(V_0 r), \end{aligned} \quad (3.7)$$

where  $J_n(x)$  is the Bessel function of  $n$ -th order. We here required the solution to be regular at the origin.

Outside the dot, the gate potential is zero, and the equations for  $\varphi_{m,\pm}$  decouple. Here, the radial wave functions behave as a power law

$$\varphi_{m,+}(r) = a_+ r^{m-1/2}, \quad \varphi_{m,-}(r) = a_- r^{-m-1/2}, \quad (3.8)$$

with coefficients  $a_{\pm}$ . We require that the wave function must not diverge for  $r \rightarrow \infty$ , which gives the constraint  $a_+ = 0$  ( $m > 0$ ) or  $a_- = 0$  ( $m < 0$ ). From continuity of the wavefunction at  $r = R$ , we then obtain the resonance condition

$$J_{|m|-1/2}(V_0 R) = 0, \quad (3.9)$$



*i.e.* we expect resonances, when the parameter  $V_0 R$  is tuned to be a root of a Bessel function. Outside the dot, one component of the spinor wavefunction is zero, while the other is decaying as

$$\psi \propto r^{-(|m|+1/2)}. \quad (3.10)$$

Interestingly, for  $|m| = 1/2$  we find a marginally non-normalizable state.

To sum up, the bound states of a disc-shaped quantum dot have been calculated, which are classified by their angular momentum. We know at which parameters resonances are expected, and how the wavefunction of a resonant state is decaying outside the dot.

### 3.2.2. Resonances in a two-terminal conductance setup

For the further studies, Bardarson *et al.* investigated numerically two-terminal transport of a quantum dot surrounded by undoped graphene and attached to source and drain contacts. In Fig. 3.2, we display their results for the conductance as a function of the dot's gate voltage, for a circular quantum dot, an example for a classical regular structure, and a stadium quantum dot, a prototypical example for a classical chaotic geometry. The analysis of the conductance can be used to detect the bound states of the quantum dot, which show up as resonant features.

For the circular quantum dot of size  $R$ , one finds that the position of the resonances in the conductance agree with roots of the integer Bessel functions, in line with the theoretical prediction, Eq. (3.9). The resonances have a definite angular momentum. Their finite width  $\Gamma$  can be estimated as  $\Gamma \sim \frac{|\psi(L)|^2 L}{|\psi(R)|^2 R}$ , where  $\psi$  denotes the wavefunction outside the dot, Eq. (3.10), and  $L$  is the distance between the leads. From this estimate, we conclude, that the width of the resonances scales as

$$\Gamma \propto (R/L)^{2|m|}. \quad (3.11)$$

Such behaviour was confirmed by the studies of [Bard 09] (data not shown here). Resonances belonging to the lowest possible angular momentum,  $|m| = \frac{1}{2}$ , gives rise to broad resonances,  $\Gamma \propto (R/L)$ , while bound states from higher angular momenta give rise to much sharper resonances. The figures also show, that the resonances for the chaotic structure are typically much broader than for the regular structure, indicating a weaker confinement. For the specific parameters of the simulation in Ref. [Bard 09] however, the resonances are still overlapping. Due to numerical limitations, it was not possible to access the regime of well-separated resonances and to carry out a detailed study of the resonances of the chaotic dot. This task will be completed in the remaining part of this chapter.

## 3.3. Model and method

We now describe, how to utilize the matrix Green function formalism in order to study transport in graphene with a gate-defined quantum dot. In addition to the calculation of the bound states of the circular dot in the previous section, our system is attached to source and drain contacts. The setup thus consists of a rectangular sample of graphene of length  $L$  and width  $W \gg L$ , described by the Hamiltonian

$$H = -i\hbar v \boldsymbol{\sigma} \cdot \boldsymbol{\nabla} + U(x) + V(\mathbf{r}). \quad (3.12)$$

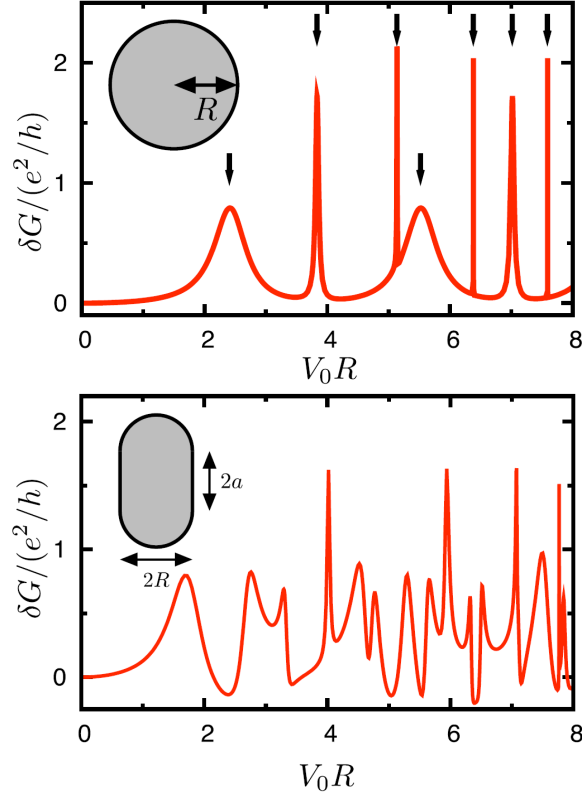


Figure 3.2.: Two-terminal conductance of an undoped graphene sheet containing an electrostatically gated region (quantum dot). *Upper panel:* Circular quantum dot; positions of the resonances agree with the theoretical prediction (indicated with arrows, parameters:  $R/L = 0.2$ ,  $W/L = 6$ ). *Lower panel:* Stadium quantum dot (parameters:  $R/L = 0.2$ ,  $W/L = 6$ ,  $2a/R = \sqrt{3}$ .) [Figures adopted from [Bard 09].]

The potential  $V(\mathbf{r})$  defines the quantum dot. It takes a constant value  $V(\mathbf{r}) = -\hbar v V_0$  inside the quantum dot, and  $V(\mathbf{r}) = 0$  outside the dot. The potential  $U(x)$  accounts for the metallic leads and is set to be  $U(x) \rightarrow -\infty$  for  $x < 0$  and  $x > L$ , whereas  $U(x) = 0$  for  $0 < x < L$ , so that the graphene sheet is tuned to the Dirac point in the region of interest.

In order to calculate the two-terminal conductance of the system, we apply Nazarov’s matrix Green function formalism [Naza 94], which has been adapted to graphene by Titov *et al.* [Tito 10]. Below, we summarize the essential elements of this method. Central object is a  $4 \times 4$  matrix Green function  $\check{G}$  with matrix structure in the pseudospin space [corresponding to the Pauli matrices  $\sigma_x$  and  $\sigma_y$  in the Dirac equation (3.12)] and the “retarded-advanced” (RA) space. The matrix Green function is defined by the equation

$$\begin{pmatrix} \varepsilon - H + i0 & -\hbar v \sigma_x \zeta \delta(x) \\ -\hbar v \sigma_x \zeta \delta(x - L) & \varepsilon - H - i0 \end{pmatrix} \check{G}(\mathbf{r}, \mathbf{r}') = \delta(\mathbf{r} - \mathbf{r}'), \quad (3.13)$$

where  $\varepsilon$  is the quasiparticle energy (set to zero in the remainder of the calculation), and

$\zeta$  is an additional parameter. Following Ref. [Tito 10], we define the generating function  $\mathcal{F}(\phi)$  as

$$\mathcal{F}(\phi) = \text{Tr} \ln \check{G}^{-1} \Big|_{\zeta=\sin(\phi/2)}, \quad (3.14)$$

where the trace operation includes summation over RA and pseudospin indices, as well as integration over spatial coordinates. The generating function  $\mathcal{F}$  contains information about the full counting statistics of two-terminal transport through the system [Naza 94]. Here, we restrict our discussion to the two-terminal conductance  $G$ , which is obtained from  $\mathcal{F}$  through the equality

$$G = -2g_0 \frac{\partial^2 \mathcal{F}}{\partial \phi^2} \Big|_{\phi=0}, \quad (3.15)$$

where  $g_0 = 4e^2/h$  is the conductance quantum in graphene.

Denoting the matrix Green function for the graphene sheet without quantum dot ( $V = 0$ ) as  $\check{G}_0$ , and writing  $\mathcal{F}_0 = \text{Tr} \ln \check{G}_0^{-1}$ , we rewrite Eq. (3.13) as

$$\begin{aligned} \delta \mathcal{F} &= \mathcal{F} - \mathcal{F}_0 \\ &= \text{Tr} \ln(1 - V \check{G}_0). \end{aligned} \quad (3.16)$$

The matrix Green function  $\check{G}_0$  for the clean system (without dot) has been calculated analytically in Ref. [Tito 10]. The explicit expression is rather lengthy and can be found in Appendix A.1. Substituting the explicit expression for  $\check{G}_0$  into Equation (3.15) then gives

$$G = \frac{g_0 W}{\pi L} + \delta G, \quad \delta G = -2g_0 \frac{\partial^2 \delta \mathcal{F}}{\partial \phi^2} \Big|_{\phi=0}, \quad (3.17)$$

where the first term corresponds to the conductivity of clean graphene [Ludw 94, Zieg 98, Pere 06, Twor 06] and the second term gives the correction from the presence of the quantum dot, which is the focus of our calculation.

The calculation of Ref. [Tito 10] proceeds by expressing  $\delta \mathcal{F}$  in terms of the  $T$  matrix of the quantum dot. Hereto, one introduces the Green function  $g$  for zero-energy quasiparticles in an infinite sample (*i.e.*, with  $V = U = 0$ ),

$$g(\mathbf{r}, \mathbf{r}') = -\frac{i}{2\pi\hbar v} \frac{\boldsymbol{\sigma} \cdot (\mathbf{r} - \mathbf{r}')}{|\mathbf{r} - \mathbf{r}'|^2}, \quad (3.18)$$

as well as the function

$$\check{G}_{\text{reg}} = \check{G}_0 - g, \quad (3.19)$$

which, being a difference of two Green functions, is regular if the spatial arguments coincide. With the standard Born series for the  $T$  matrix [Mess 61],

$$T = (1 - Vg)^{-1}V, \quad (3.20)$$

one finds [Tito 10]

$$\delta \mathcal{F} = \text{Tr} \ln(1 - T \check{G}_{\text{reg}}), \quad (3.21)$$

up to terms that do not depend on the counting field  $\phi$ . Equation (3.21) is the basis for our further investigations.

We will consider the limit that the size of the quantum dot is small in comparison to the length  $L$ . In that case, it is advantageous to expand  $\check{G}_{\text{reg}}$  around the position  $\mathbf{r}_0$  of the center of the quantum dot. After a short algebraic manipulation, which is carried out in Appendix A.1, one finds that one may replace the operators  $T$  and  $\check{G}_{\text{reg}}$  in Eq. (3.21) by matrices with elements  $T^{\mu\nu}$  and  $G_{\text{reg}}^{\mu\nu}$ , with  $\mu, \nu = 0, 1, 2, \dots$  and

$$G_{\text{reg}}^{\mu\nu} = \left. \frac{\partial^\mu}{\partial x^\mu} \frac{\partial^\nu}{\partial x'^\nu} \check{G}_{\text{reg}}(\mathbf{r}, \mathbf{r}') \right|_{\mathbf{r}=\mathbf{r}'=\mathbf{r}_0}, \quad (3.22)$$

$$T^{\mu\nu} = \frac{1}{\mu! \nu!} \int d^2 \mathbf{r} d^2 \mathbf{r}' [(x - x_0) - i\sigma_z(y - y_0)]^\mu \times T(\mathbf{r}, \mathbf{r}') [(x' - x_0) + i\sigma_z(y' - y_0)]^\nu. \quad (3.23)$$

Note that each element  $G_{\text{reg}}^{\mu\nu}$  is a  $4 \times 4$ -matrix with non-trivial operation on pseudospin and RA degrees of freedom, whereas  $T^{\mu\nu}$  acts in pseudospin space only and leaves the RA space untouched. With this replacement, the trace in Eq. (3.21) is taken over the matrix indices  $\mu$  or  $\nu$ , the pseudospin degrees of freedom, and the RA degrees of freedom.

Essentially, the matrix  $T^{\mu\nu}$  is the  $T$  matrix in a partial-wave expansion. In graphene, the partial wave expansion involves waves of angular momentum  $\sigma(\mu + 1/2)$ , with  $\sigma = \pm 1$  a pseudospin index and  $\mu = 0, 1, 2, \dots$  the index of the matrix  $T^{\mu\nu}$ . The corresponding basis functions  $\psi_{k,\mu,\sigma}(\mathbf{r})$  are defined at a finite energy  $\varepsilon = \hbar v k$  only, where, for definiteness, we choose  $k > 0$ . They are the solutions of the Dirac equation  $H\psi_{k,\mu,\sigma}(\mathbf{r}) = \varepsilon\psi_{k,\mu,\sigma}(\mathbf{r})$  in the absence of the potentials  $U$  and  $V$ . With the matrix notation  $\Psi_{k\mu} = (\psi_{k,\mu,+1}, \psi_{k,\mu,-1})$ , one has

$$\Psi_{k\mu}(\mathbf{r}) = \sqrt{\frac{k}{4\pi}} \begin{pmatrix} e^{i\mu\theta} J_\mu(kr) & ie^{-i(\mu+1)\theta} J_{\mu+1}(kr) \\ ie^{i(\mu+1)\theta} J_{\mu+1}(kr) & e^{-i\mu\theta} J_\mu(kr) \end{pmatrix}, \quad (3.24)$$

where  $J_\nu$  is a Bessel function and we used polar coordinates  $(r, \theta)$ . Denoting the  $T$  matrix in the partial-wave basis by  $T_{\mu\nu}(k)$ , one then finds that

$$T^{\mu\nu} = \lim_{k \rightarrow 0} \frac{2^{\mu+\nu+2}\pi}{k^{\mu+\nu+1}} T_{\mu\nu}(k), \quad (3.25)$$

where we again refer to appendix A.1 for details. In our discussion below, we will refer to the mode indices  $\mu, \nu = 0, 1, 2, \dots$  as  $s, p, d, \dots$ .

It remains to describe a method to calculate the  $T$ -matrix  $T_{\mu\nu}(k)$  for a specific quantum dot potential  $V(\mathbf{r})$ . This is done through by first relating  $T$  to the scattering matrix  $S_{\mu\nu}(k)$  in the partial-wave basis,

$$S_{\mu\nu}(k) = \delta_{\mu\nu} - 2\pi i T_{\mu\nu}(k). \quad (3.26)$$

The scattering matrix  $S_{\mu\nu}(k)$  relates the coefficients of incoming  $(-)$  and outgoing  $(+)$  parts of the basis functions (3.24) at energy  $\varepsilon = \hbar v k$ . Again using the shorthand notation  $\Psi_{k\mu}^{(\pm)} = (\psi_{k,\mu,+1}^{(\pm)}, \psi_{k,\mu,-1}^{(\pm)})$ , these are

$$\Psi_{k\mu}^{(\pm)}(\mathbf{r}) = \sqrt{\frac{k}{4\pi}} \begin{pmatrix} e^{i\mu\theta} H_\mu^{(\pm)}(kr) & ie^{-i(\mu+1)\theta} H_{\mu+1}^{(\pm)}(kr) \\ ie^{i(\mu+1)\theta} H_{\mu+1}^{(\pm)}(kr) & e^{-i\mu\theta} H_\mu^{(\pm)}(kr) \end{pmatrix}, \quad (3.27)$$

where the  $H_\mu^{(\pm)} = J_\mu \pm iY_\mu$  are Hankel functions of the first (+) and second kind (-), respectively. The scattering matrix  $S_{\mu\nu}(k)$  is then defined through the asymptotic form of the solution of the Dirac equation  $H\psi_k(\mathbf{r}) = \hbar vk\psi_k(\mathbf{r})$  for  $r \rightarrow \infty$ , which takes the general form

$$\psi_k(\mathbf{r}) = \sum_{\mu} \left( \Psi_{k\mu}^{(+)}(\mathbf{r}) a_{k\mu} + \Psi_{k\mu}^{(-)}(\mathbf{r}) b_{k\mu} \right), \quad (3.28)$$

with, in  $2 \times 2$  matrix notation,

$$a_{k\mu} = \sum_{\nu} S_{\mu\nu}(k) b_{k\nu}. \quad (3.29)$$

To find  $S_{\mu\nu}(k)$ , we employ a variation of a method commonly applied to rectangular strips of disordered graphene [Bard 07]. Hereto, we divide the graphene sheet in circular slices  $a_{j-1} < r < a_j$ ,  $j = 1, \dots, N$ , with  $a_0 = 0$  and  $a_N$  so large that  $V(\mathbf{r}) = 0$  for  $r > a_N$ . We then obtain the scattering matrix  $S(k)$  by solving two auxiliary scattering problems first.

In the first auxiliary problem, we set the potential  $V$  to zero everywhere, except in the circular slice  $a_{j-1} < r < a_j$ . In this case, the wavefunctions can be expanded in incoming and outgoing partial waves for  $r < a_{j-1}$  as well as for  $r > a_j$ . The general solution of the Dirac equation in the regions  $r < a_{j-1}$  and  $r > a_j$  can be characterized by means of two reflection matrices  $\rho_j$  and  $\rho'_j$  and two transmission matrices  $\tau_j$  and  $\tau'_j$ , such that  $\rho$  relates the coefficients of outgoing partial waves on the exterior to the coefficients of incoming partial waves on the exterior etc. If  $\delta a = a_j - a_{j-1}$  is sufficiently small, these matrices can be calculated in the first-order Born approximation. Writing  $\rho_{\mu\nu} = \delta\rho_{\mu\nu}$ ,  $\rho'_{\mu\nu} = \delta\rho'_{\mu\nu}$ ,  $\tau_{\mu\nu} = \delta\tau_{\mu\nu}$ , and  $\tau'_{\mu\nu} = \delta\tau'_{\mu\nu}$ , this calculation gives

$$\begin{aligned} \delta\rho_{\mu\nu} &= -\frac{i\pi}{2\hbar v} \int_{a_{j-1} < r < a_j} d\mathbf{r} \Psi_{k\mu}^{(+)}(\mathbf{r})^\dagger U(\mathbf{r}) \Psi_{k\nu}^{(-)}(\mathbf{r}), \\ \delta\tau_{\mu\nu} &= -\frac{i\pi}{2\hbar v} \int_{a_{j-1} < r < a_j} d\mathbf{r} \Psi_{k\mu}^{(-)}(\mathbf{r})^\dagger U(\mathbf{r}) \Psi_{k\nu}^{(-)}(\mathbf{r}), \\ \delta\rho'_{\mu\nu} &= -\frac{i\pi}{2\hbar v} \int_{a_{j-1} < r < a_j} d\mathbf{r} \Psi_{k\mu}^{(-)}(\mathbf{r})^\dagger U(\mathbf{r}) \Psi_{k\nu}^{(+)}(\mathbf{r}), \\ \delta\tau'_{\mu\nu} &= -\frac{i\pi}{2\hbar v} \int_{a_{j-1} < r < a_j} d\mathbf{r} \Psi_{k\mu}^{(+)}(\mathbf{r})^\dagger U(\mathbf{r}) \Psi_{k\nu}^{(+)}(\mathbf{r}), \end{aligned}$$

up to corrections of higher order in  $\delta a$ .

In the second auxiliary problem, we set  $V$  to zero for  $r > a_j$  only. Defining  $S_j(k)$  to be the scattering matrix for this situation, we obtain the recursion relation

$$S_j(k) = \rho_j + \tau'_j (1 - S_{j-1}(k) \rho'_j)^{-1} S_{j-1}(k) \tau_j. \quad (3.30)$$

Together with the initial condition  $S_0 = 1$  and the equality  $S_N = S$  this leads to the desired solution.

Unitarity implies the relations  $\delta\rho'_j = -\delta\rho_j^\dagger$ ,  $\delta\tau_j = -\delta\tau_j^\dagger$ , and  $\delta\tau'_j = -\delta\tau_j^{\prime\dagger}$ . Consistent with the Born approximation, we may rewrite the recursion relation (3.30) as

$$S_j(k) = S_{j-1}(k) [1 + i\delta h_j], \quad (3.31)$$

where

$$\begin{aligned} i\delta h_j &= S_{j-1}^\dagger(k)\delta\rho_j + \delta\rho'_j S_{j-1}(k) \\ &+ S_{j-1}^\dagger(k)\delta\tau'_j S_{j-1}(k) + \delta\tau_j \end{aligned} \quad (3.32)$$

is a hermitian matrix.

Although this concludes our formal description of the method, there are a few issues regarding the numerical implementation that we also need to discuss:

(i) — For the final result, we have to take the low- $k$  limit of the scattering matrix  $S(k)$ , which, at first sight, may be problematic because the Hankel functions appearing in the Born approximation for the matrices  $\delta\rho$ ,  $\delta\rho'$ ,  $\delta\tau$ , and  $\delta\tau'$  diverge in this limit. However, this problem can easily be circumvented by shifting the potential  $V(\mathbf{r}) \rightarrow V(\mathbf{r}) + \hbar v k'$  for  $r < a_N$ , while at the same time increasing the quasiparticle energy according to  $k \rightarrow k + k'$ . This means that we transfer contributions between the free propagation and the perturbation. We then solve the scattering problem inside the disc starting from “free” Dirac fermions with energy  $\hbar v(k + k')$ , which remains finite in the limit  $k \rightarrow 0$ . The wavefunction outside the disc, where free electrons have momentum  $k$ , can be found by matching to the wave function inside the disc, and contains the information of the scattering matrix we need.

For the low- $k$ -expansion of the scattering matrix, we then find an expression of the form

$$S_{\mu\nu}(k) = \delta_{\mu\nu} + S'_{\mu\nu}(k')k^{\mu+\nu+1} + \mathcal{O}(k^{\mu+\nu+2}), \quad (3.33)$$

where  $S'(k')$  depends on  $a_N$ ,  $k'$ , and the scattering matrix  $S_N(k')$  obtained for the modified problem where we have replaced  $k$  by  $k' + k$  and safely can take the limit  $k \rightarrow 0$ . A detailed derivation is given in Appendix A.2. Note, that the expansion in Eq. (3.33) gives us precisely that order in  $k$ , that we need in order to obtain the matrix  $T^{\mu\nu}$  in Eq. (3.25).

The wavenumber  $k'$  of the quasiparticles can be chosen arbitrarily, and we have verified that the result of our calculations do not depend on the choice of  $k'$ . However, one may exploit this freedom for a wise choice of  $k'$ . It should be not too small, because otherwise the Hankel functions in the spherical incoming and outgoing waves become too large, indicating the fact that particles are repelled from the origin and therefore the Born approximation loses its applicability. On the other hand, if the wave vector  $k'$  is chosen too large, the effective potential  $V + \hbar k'v$  gets large, too, and the thickness  $\delta a$  of the slices has to be decreased.

(ii) — It is sufficient to choose the radius  $a_0$  of the first slice such, that  $V(\mathbf{r})$  is uniform for  $r < a_0$ . For this situation an exact solution is available.

(iii) — In order to guarantee numerical stability during multiplication of scattering matrices, we change Eq. (3.31) to

$$S_j(k) = S_{j-1}(k) \left(1 + i\frac{\delta h_j}{2}\right) \left(1 - i\frac{\delta h_j}{2}\right)^{-1}, \quad (3.34)$$

which is valid up to corrections beyond the accuracy of Born approximation, but ensures that the scattering matrices remain unitary at all times.

(iv) — In the calculation of the scattering matrix, we keep a total of  $M$  modes. After the calculation of the full scattering matrix  $S$ , we then further truncate the scattering

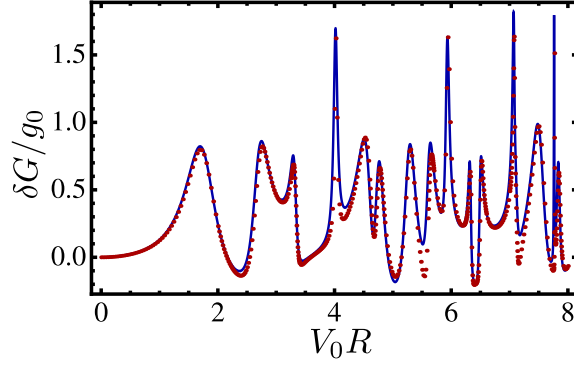


Figure 3.3.: Conductance versus gate voltage  $V_0$  for an undoped graphene sheet with a gate-defined stadium-shaped quantum dot. The parameters of the numerical calculation are  $2a/R = \sqrt{3}$  and  $L/R = 5$ . The curves correspond to the numerical calculation using the method of Sec. 3.3, with contributions to the  $T$  matrix up to  $d$ -wave (blue, solid), and to a direct numerical solution of the Dirac equation (red, points; data taken from Ref. [Bard 09]).

matrix upon calculation of the determinant in Eq. (3.21), keeping matrix elements  $S^{\mu\nu}$  with  $\mu, \nu = 0, 1, \dots, M'$  only. Keeping a large number of modes  $M$  in the calculation of the scattering matrix is important in order to properly resolve the dynamics inside the quantum dot. The number of modes  $M'$  required for the calculation of the conductance depends on the ratio of the size  $L$  of the graphene sheet and the size of the quantum dot, and can be kept small if this ratio is large. The numerical calculation of the conductance has converged, when the result does no longer change upon increasing  $M$ ,  $M'$  or  $N$ . For the results of the conductance shown here, we kept channels up to  $d$ -wave ( $M' = 2$ ) only, which we found to be sufficient for the parameters chosen in our calculation.

## 3.4. Two-terminal conductance with stadium-shaped quantum dot

### 3.4.1. Two-terminal conductance

As a nontrivial application of the formalism laid out in the previous Section, we have calculated the two-terminal conductance of a stadium-shaped quantum dot in an otherwise undoped graphene sheet. The quantum dot is placed halfway between the contacts. It is characterized by the radius  $R$  of the circular pieces and the length  $2a$  of the linear segment. The gate voltage  $V(\mathbf{r}) = -\hbar v V_0$  for  $\mathbf{r}$  inside the quantum dot, and  $V(\mathbf{r}) = 0$  otherwise. In our calculations, we have included contributions up to  $d$ -wave in the  $T$  matrix, whereas as many modes were used for the calculation of the scattering matrix  $S$  as were necessary to reach convergence. (See the discussion at the end of the previous section.)

In Fig. 3.3, we show the two-terminal conductance as a function of the gate voltage  $V_0$ . The conductance exhibits several resonances due to the formation of quasi-bound states

in the stadium. The parameters for the data in this figure are chosen to be the same as in Ref. [Bard 09], so that the results can be compared. The excellent agreement between both curves concerns the position as well as the shape of the resonances. We attribute small deviations in the resonance heights to corrections from higher angular momentum that were not taken into account in the calculations. Such corrections disappear upon increasing the ratio of system size vs. dot size  $L/R$  (see discussion below).

The effect of inclusion of successive angular momentum channels in the  $T$  matrix (while keeping essentially all angular momentum channels in the calculation of the scattering matrix  $S$ ) is illustrated in Fig. 3.4, where, in the upper panel, we show a close-up of the data of Fig. 3.3 with one, two, and three angular momentum channels included in the final step of the calculation (i.e. with truncation at  $M' = 0, 1, 2$ ). This figure clearly demonstrates that each resonance has contributions from more than one angular mode, as is to be expected for a chaotic quantum dot. In particular, we find that all resonances have a non-vanishing  $s$ -wave contribution, so that the resonance position can be extracted from the  $s$ -wave channel solely. For the data shown in Fig. 3.3, one needs to include the  $p$ -wave contribution in order to obtain the correct resonance shape. The effect of the  $d$ -wave contribution is small, which we find remarkable, because the ratio of dot size  $2(R + a)$  versus contact size  $L$  is  $\approx 0.75$ , which is not small in comparison to unity. The lower panel of Fig. 3.4 shows conductance data for  $M' = 0, 1, 2$ , showing that the convergence with respect to  $M'$  quickly improves upon increasing  $L/R$ .

We conclude, that most information about the resonances that is relevant for transport at large or moderately large  $L/R$  is encoded in the contributions from small angular momentum, and is therefore stored in a small set of parameters. That fact is a strong indication of the power of the method employed here, in comparison to a direct simulation of the Dirac equation.

#### 3.4.2. Lineshape

The main advantage of the present method over the direct numerical solution of the Dirac equation is that it allows one to extend the conductance calculations to the regime  $L \gg R$ : The complete dependence on the length  $L$  is encoded on the Green function  $\tilde{G}_{\text{reg}}$ , which is known analytically. It is only in the regime  $L \gg R$  that resonances are well separated and can be characterized individually. The calculations of Ref. [Bard 09], on the other hand, were limited to the regime  $L \leq 5R$ , where resonances were still strongly overlapping. (Reference [Bard 09] also considered the case  $L \approx 8R$  for  $W = L$ . However, in that case the conductance is strongly influenced by the finite width  $W$  of the graphene sheet.)

In Fig. 3.5 we show how the first and second resonance behaves upon increasing the contact size  $L$  at fixed dot size  $R$ . The plots illustrate that the resonance width shrinks, while the height saturates. The asymmetry of the line shape disappears in the limit  $L/R \rightarrow \infty$ , consistent with the expectation that  $s$ -wave scattering dominates if  $L \gg R$ . Similar behaviour is found for the other resonances.

In order to quantitatively analyze the lineshapes, we note that each resonance is characterized by a divergence of the  $T$  matrix. With a suitable parameterization of these divergencies an explicit expression for the resonance lineshape can be obtained. Hereto we introduce the dimensionless variable  $\epsilon = V_0 R$ . Then, close to a divergence at  $\tilde{\epsilon}_0$ , the



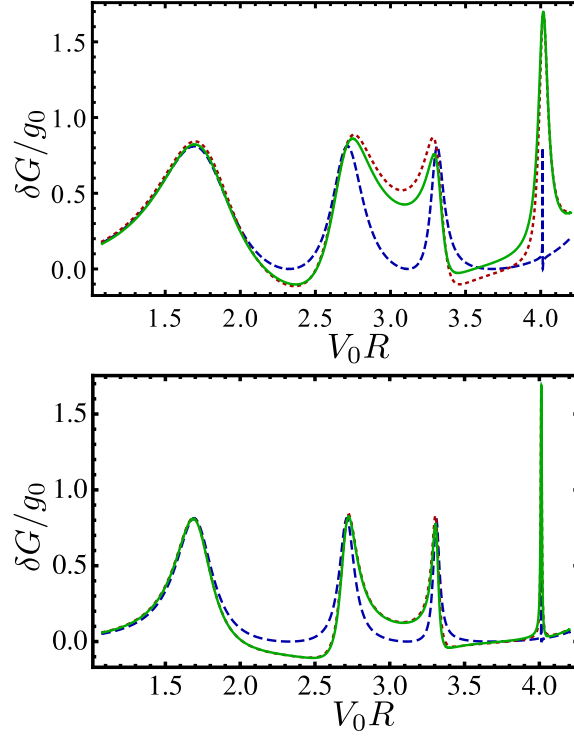


Figure 3.4.: First four conductance resonances: The conductance has been calculated using Eq. (3.21) with the  $T$  matrix truncated after the  $s$ -wave (blue, dashed),  $p$ -wave (red, dotted), and  $d$ -wave angular-momentum channel (green, solid), corresponding to  $M' = 0, 1, 2$ , respectively. In the upper panel, we set  $L/R = 5$ , while in the lower panel,  $L/R = 10$ . The ratio  $a/R$  remains the same as in Fig. 3.3.

divergent part of  $T^{\mu\nu}$  is of the form

$$T^{\mu\nu}(\epsilon) \simeq \frac{R^{\mu\nu}}{\epsilon - \tilde{\epsilon}_0}, \quad (3.35)$$

where the matrix  $R^{\mu\nu}$  contains the information about the resonance shape. The matrix elements  $R^{\mu\nu}$  are related by hermiticity,  $R^{\mu\nu} = (R^{\nu\mu})^\dagger$  and time-reversal symmetry,  $R^{\mu\nu} = \sigma_y (R^{\nu\mu})^T \sigma_y$ . Moreover, for the specific problem we consider here, inversion symmetry and reflection symmetry impose further constraints on  $R$ , which allow us to parameterize the matrix as

$$R = \begin{pmatrix} l_s \sigma_0 & i l_{sp} \sigma_x & l_{sd} \sigma_0 \\ -i l_{sp} \sigma_x & l_p \sigma_0 & i l_{pd} \sigma_x \\ l_{sd} \sigma_0 & -i l_{pd} \sigma_x & l_d \sigma_0 \end{pmatrix}, \quad (3.36)$$

where  $\sigma_0$  is the  $2 \times 2$  unit matrix. Due to Kramers degeneracy,  $R$  can be decomposed into two identical submatrices, which, for a generic resonance, are of unit rank. (In a chaotic quantum dot level repulsion ensures that this condition is always fulfilled.) This gives the

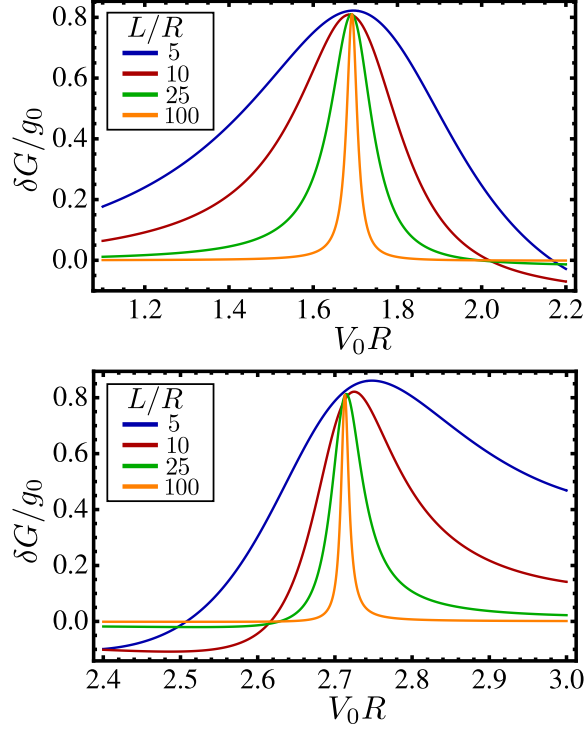


Figure 3.5.: Dependence of the first and second resonance on the ratio of dot size versus system size  $R/L$ .

additional constraints

$$l_{sp}^2 = l_s l_p, \quad l_{sd}^2 = l_s l_d, \quad l_{pd}^2 = l_p l_d \quad (3.37)$$

on the parameters in Eq. (3.36). Note, that  $l_s$ ,  $l_p$ , and  $l_d$  have the dimension of a length, length<sup>3</sup>, and length<sup>5</sup>, respectively.

Substituting Eq. (3.36) into Eq. (3.21) and making use of the condition (3.37), we find that the line shapes are described by the Fano resonance formula [Fano 61]

$$G = G_{\text{nr}} \frac{|2(\epsilon - \epsilon_0) + q\Gamma|^2}{4(\epsilon - \epsilon_0)^2 + \Gamma^2} \quad (3.38)$$

Here,  $G_{\text{nr}}$  is the non-resonant conductance,  $\Gamma$  is the resonance width,  $\epsilon_0$  is the resonance position, and  $q$  is the complex ‘‘Fano parameter’’. After subtracting the background conductance  $G_{\text{nr}}$ , we rewrite Eq. (3.38) as

$$\delta G = g_0 \frac{\beta + 4\alpha(\epsilon - \epsilon_0)}{4(\epsilon - \epsilon_0)^2 + \Gamma^2}, \quad (3.39)$$

where  $\beta = (G_{\text{nr}}/g_0)(|q|^2 - 1)\Gamma^2$  and  $\alpha = (G_{\text{nr}}/g_0)\text{Re } q$ . For  $\alpha = 0$  the resonance has a Breit-Wigner shape; Non-zero  $\alpha$  is responsible for an asymmetry in the lineshape. When

we express the resonance parameters through the entries of  $R$ , we also use  $\sigma_{sp} = \text{sign}(l_{sp})$  etc., which is not fixed by Eq. (3.37):

$$\epsilon_0 = \tilde{\epsilon}_0 + \frac{\pi\sqrt{l_s l_p} \sigma_{sp}}{24L^2} - \frac{7\pi^3\sqrt{l_p l_d} \sigma_{pd}}{960L^4}, \quad (3.40)$$

$$\Gamma = \left| \frac{l_s}{2L} + \frac{\pi^2 l_p}{8L^3} + \frac{\pi^2 \sqrt{l_s l_d} \sigma_{sd}}{4L^3} + \frac{5\pi^4 l_d}{32L^5} \right|, \quad (3.41)$$

$$\begin{aligned} \beta = & \frac{2l_s^2}{\pi^2 L^2} + \frac{2l_p l_s}{3L^4} + \frac{8\sqrt{l_s^3 l_d} \sigma_{sd}}{3L^4} + \frac{19l_p^2 \pi^2}{72L^6} \\ & + \frac{481l_d l_s \pi^2}{180L^6} + \frac{17l_p \sqrt{l_s l_d} \sigma_{sd} \pi^2}{18L^6} + \frac{61l_d l_p \pi^4}{90L^8}, \\ & + \frac{251\sqrt{l_s l_d^3} \sigma_{sd} \pi^4}{180L^8} + \frac{13549l_d^2 \pi^6}{28800L^{10}} \end{aligned} \quad (3.42)$$

$$\alpha = -\frac{2\sqrt{l_s l_p} \sigma_{sp}}{\pi L^2} + \frac{\pi\sqrt{l_p l_d} \sigma_{pd}}{2L^4}. \quad (3.43)$$

Note, that the shift  $\epsilon_0 - \tilde{\epsilon}_0$  of the resonance position, as well as the asymmetry  $\alpha$  is absent, if the resonance consists of a single angular momentum component only.

Now consider the situation, where we fix the product  $V_0 R$  of the gate voltage quantum dot and the quantum dot size — *i.e.*, we look at a fixed resonance — and increase the length  $L$  of the graphene sheet. Then, as long as  $l_s \neq 0$ , at sufficiently large  $L$ , the conductance will be determined by its  $s$ -wave contribution, so that the resonance line shape reduces to the Breit-Wigner form. In this limit, the height for  $\delta G$  approaches the constant universal value  $8g_0/\pi^2$ , and the width scales as  $\Gamma = l_s/2L$ , as was found previously by Titov *et al.* [Tito 10].

### 3.4.3. Comparison Disc - Stadium

We now summarize the main qualitative difference in the conductance resonances for stadium-shaped quantum dots, which have been considered numerically here and in Ref. [Bard 09], and disc-shaped dots, which were considered analytically in Ref. [Tito 10] and numerically in Ref. [Bard 09]. The main difference, which is illustrated in Fig. 3.4, is that generic resonances for the stadium dot have contributions from more than one angular momentum channel. This means that the resonance lineshape changes from a Fano shape for moderate ratios  $L/R$  to a Breit-Wigner lineshape for large  $L/R$ , as seen in Fig. 3.5. In the limit  $L/R \rightarrow \infty$  of isolated resonances, the height of the conductance resonances takes the universal value  $8g_0/\pi^2$ , whereas the width of all resonances scales proportional to  $R/L$ . Though we considered a stadium-shaped dot only, we believe, that the features found here are generic and shared by all chaotic dots.

This is to be contrasted to the situation of a circular quantum dot, where different angular momentum channels do not mix, and the resonances are of pure type ( $s$ -wave,  $p$ -wave, ...). The resonance lineshape is always of Breit-Wigner form and approaches a constant height upon taking the limit  $L/R \rightarrow \infty$ . The asymptotic resonance height depends on the angular momentum channel, with a height  $8g_0/\pi^2$  for  $s$ -wave resonances

( $l = 0$ ) and  $\lesssim 2g_0$  for higher angular-momentum channels ( $l \geq 1$ ). The resonance width depends on the angular momentum channel,  $\Gamma \propto (R/L)^{2l+1}$ .

We close this comparison with a comment on the results of Ref. [Bard 09]. There it was found that the resonance height of the chaotic dot goes to zero upon taking the limit of large  $L/R$ . This observation referred to a setup with aspect ratio  $W/L = 1$  and periodic boundary conditions along the transverse direction. For aspect ratio  $W \ll L$ , only the mode with zero transverse momentum substantially contributes to transport [Twor 06]. Therefore,  $s$ -wave scattering does not affect the conductance, resulting the observed suppressed height of  $s$ -wave conductance resonances. We verified that the same phenomenon occurs in our calculations, by evaluating the regularized Green function  $\check{G}_{\text{reg}}$  for finite width. This explains, why the resonances in Ref. [Bard 09] completely disappear in the limit of large  $L/R$ , while in our investigation for aspect ratio  $W \gg L$  the height of the resonances remains finite.

### 3.5. Conclusion

In this chapter, we investigated the resonances of the conductance of a graphene sheet with a chaotic quantum dot. Using a numerical implementation of the matrix Green function method of Ref. [Tito 10], we were able to study the behaviour of the resonances in the limit of well-separated resonances. This essential limit could not be reached in the original treatment of the problem [Bard 09].

As was proposed in Ref. [Bard 09], the resonances of the chaotic dot behave significantly different compared to the case when the gated region is circular. While the circular geometry does not allow for mode mixing, so that all resonances are Breit-Wigner resonances with a well-defined angular momentum, in the stadium dot, due to its non-integrable dynamics, all resonances have contributions from all scattering channels. The presence of mixed angular-momentum modes is responsible for an asymmetry of the line shape, described by the Fano resonance formula. In the limit of very well separated resonances, corresponding to the limit in which the size  $R$  of the quantum dot is much smaller than the distance  $L$  between the metallic contacts, for the chaotic quantum dot all resonances are dominated by the lowest ( $s$ -wave) angular momentum component, and recover the Breit-Wigner form. In contrast, for the disc-shaped dot, parametrically narrower resonances for higher angular momentum channels ( $p$ -wave,  $d$ -wave, etc.) persist in the limit of large  $L/R$ . This establishes a clear signature that distinguishes regular and chaotic dynamics of gate-defined quantum dots from the conductance resonances.

## 4. The role of the Berry phase for electrostatic confinement in graphene

In the previous chapter, we studied the two-terminal conductance of a gate-defined quantum dot surrounded by undoped graphene, which is attached to source and drain contacts. We learned, how the lineshape of the resonant features of the conductance reveals information about the constitution of the resonant level of the quantum dot and about the degree of confinement. The resonances of a regular and a chaotic dot are distinguished in the limit of small coupling between dot and leads, where the resonances of a chaotic dot become narrower in a linear dependence on the ratio dot size vs. distance to the leads  $R/L$  upon decreasing the coupling to the leads, while a regular dot has resonant levels that become narrower in a higher power in  $R/L$ , indicating a better confinement. Remarkably, the resonant structures for the chaotic dot remain at a finite height close to the conductance quantum even for arbitrarily small coupling between dot and leads.

It remains to find an explanation, why the resonances of the chaotic dot persist even for weak coupling, which seems to contradict the naive classical expectation. We will resolve this issue in the present chapter. The classical arguments invoked to predict the kind of structures that should support confinement did not take into account one crucial aspect for graphene: The Berry phase, that the electronic wavefunction accumulates in the presence of the graphene pseudospin. As the latter is strongly linked to the particle's momentum, upon a circular motion the pseudospin winds once around its axis, accumulating a Berry phase of  $\pi$ . Such Berry phase is of great importance, as a consequence also the electron's angular momentum is quantized in half-integer multiples of  $\hbar$ , and thus the lowest possible angular momentum is  $\hbar/2$ .

In the present chapter, we investigate how the Berry phase affects the formation of resonant levels in a gate-defined quantum dot in graphene. To isolate the effect of the Berry phase, we introduce a flux tube to the system, that contains precisely half a flux quantum. Electrons encircling the flux tube collect an Aharonov-Bohm phase of  $\pi$ , precisely cancelling the effect of the Berry phase. The kinematic angular momentum, which is relevant for the classical considerations, is shifted to integer values in the presence of the  $\pi$ -flux, and therefore allows for a state with zero angular momentum. This state is shown to be unable to accommodate bound states. As a consequence we find that chaotic dots cannot support resonant states in the presence of  $\pi$ -flux, and bound states therefore appear solely in regular structures. Thus, we can identify the Berry phase as the cause of the discrepancy between classical expectation and the quantum-mechanical outcome.

Besides measuring the conductance, experimental probes of the density of states provide a valuable tool in the study of nanosystems. In this chapter, we will further discuss, how information about resonant states in a gate-defined quantum dot in graphene can be obtained from evaluations of the density of states. We will explore the role of geometry and

the Berry phase on electrostatic confinement also with an alternative approach considering the density of states, which allows for a very efficient study of the limit of dots that are weakly coupled to the leads.

The present chapter is arranged as follows: In Sec. 4.1, we revisit the calculation from the previous chapter for the resonant levels of a disc-shaped quantum dot in the presence of a  $\pi$ -flux, and show the emergence of a channel that cannot bind resonant states. We then study the two-terminal conductance for a regular and a chaotic shaped quantum dot in the presence of a flux tube in Sec. 4.2. We turn to a calculation for the density of states in Sec. 4.3. Here, we start with a calculation of the density of states for a circular quantum dot, which can be done analytically, and compare the findings with the density of states for a chaotic dot in Sec. 4.4. We contrast the situation with the inclusion of a  $\pi$ -flux in Sec. 4.5. We conclude our results in Sec. 4.6.

The present chapter is based on the publications [Hein 13] (Sec. 4.1, 4.2 & 4.6 ) and [Schn 14a] (Sec. 4.3–4.6). The results of Secs. 4.1 & 4.2 also appear in the diploma thesis of Julia Heinel, that was written under my co-supervision in the AG Brouwer at FU Berlin.

## 4.1. Bound states of a circular quantum dot with a $\pi$ -flux

We return to the problem of a circular quantum dot as discussed in Sec. 3.2.1 in the previous chapter, where we now include a magnetic flux tube. The Hamiltonian, that we consider, thus reads

$$H = v(\mathbf{p} + e\mathbf{A}) \cdot \boldsymbol{\sigma} + V(\mathbf{r}), \quad (4.1)$$

with the gate potential  $V(\mathbf{r})$  for a circular dot of radius  $R$

$$V(\mathbf{r}) = \begin{cases} -\hbar v V_0, & r < R \\ 0, & r > R. \end{cases} \quad (4.2)$$

The vector potential corresponding to the magnetic flux line is

$$\mathbf{A}(\mathbf{r}) = \frac{h}{e} \frac{\Phi}{2\pi r} \hat{\mathbf{e}}_\theta, \quad (4.3)$$

where  $\hat{\mathbf{e}}_\theta$  is the unit vector for the azimuthal angle, and  $\Phi$  is the magnetic flux measured in units of the flux quantum  $h/e$ . For our study, we consider the cases  $\Phi = 0$  (no flux tube) or  $\Phi = 1/2$  (flux tube containing half a flux quantum). We remark, that we assume, that the spatial extension of the flux line is large in comparison to the lattice constant, such that it does not couple the two valleys. On the other hand, the flux line is required to be much smaller than the dot size, hence Eq. (4.3) is the appropriate description for the vector potential.

In polar coordinates, the kinetic part of the Hamiltonian then reads

$$v(\mathbf{p} + e\mathbf{A}) \cdot \boldsymbol{\sigma} = -i\hbar v \begin{pmatrix} 0 & D_- \\ D_+ & 0 \end{pmatrix}, \quad (4.4)$$

where we defined the operators

$$D_\pm = e^{\pm i\theta} \left( \partial_r \pm \frac{i}{r} \partial_\theta \mp \frac{\Phi}{r} \right). \quad (4.5)$$

With our choice of the vector potential, the Hamiltonian is invariant under rotation, hence we can look for eigenstates of the total angular momentum  $j_z = l_z + \frac{\hbar}{2}\sigma_z$ . They have the form

$$\psi_m(\mathbf{r}) = e^{im\theta} \begin{pmatrix} e^{-i\frac{\theta}{2}} \varphi_{m,+}(r) \\ e^{i\frac{\theta}{2}} \varphi_{m,-}(r) \end{pmatrix}, \quad (4.6)$$

where  $m = \pm 1/2, \pm 3/2, \dots$ . Inside the dot, for  $r < R$ , the radial wave functions  $\varphi_{m,\pm}$  are determined by the coupled equations

$$\begin{aligned} (\partial_r - (m - \frac{1}{2})\frac{1}{r} - \frac{1}{r}\Phi) \varphi_{m,+}(r) &= iV_0 \varphi_{m,-}(r), \\ (\partial_r + (m + \frac{1}{2})\frac{1}{r} + \frac{1}{r}\Phi) \varphi_{m,-}(r) &= iV_0 \varphi_{m,+}(r). \end{aligned} \quad (4.7)$$

Outside the dot the equations decouple, and the radial wave functions show a power law behavior

$$\varphi_{m,+}(r) = a_+ r^{m-1/2+\Phi}, \quad \varphi_{m,-}(r) = a_- r^{-m-1/2-\Phi}, \quad (4.8)$$

with coefficients  $a_{\pm}$ .

We note, that the results obtained sofar agree with the calculation for the bound states of a circular dot without flux tube, upon replacing  $\Phi = 0$ . Now we consider a disc-shaped quantum dot with a flux tube carrying half a flux quantum ( $\Phi = 1/2$ ) — a “ $\pi$ -flux” — at its center. The results take a form similar to those without flux tube if we consider the kinematical orbital angular momentum,

$$l_{z,\text{kin}} = [\mathbf{r} \times (\mathbf{p} + e\mathbf{A})]_z, \quad (4.9)$$

instead of the canonical angular momentum. With the inclusion of a  $\pi$ -flux, we then find  $l_{z,\text{kin}} = l_z + \frac{\hbar}{2}$ . The wavefunctions from Eq. (4.6) are then eigenstates of  $j_{z,\text{kin}}$  with eigenvalue  $\mu\hbar$ , where  $\mu = m + 1/2$ , *i.e.* the kinematical angular momentum takes on *integer* values. For  $\mu \neq 0$  the calculation for the bound states proceeds in the same way as without flux, and we find that the resonance condition is given by

$$J_{|\mu|-1/2}(V_0 R) = 0. \quad (4.10)$$

Thus, bound states appear now at roots of half-integer Bessel functions. Outside the dot, the wavefunction decays proportional to  $r^{-(|\mu|+1/2)}$ . We conclude that, if the dot and the surrounding undoped graphene layer are contacted to source and drain reservoirs, the width  $\Gamma$  of the resonances in the two-terminal conductance scales as

$$\Gamma \propto \left(\frac{R}{L}\right)^{2|\mu|}. \quad (4.11)$$

The state with zero kinematical angular momentum ( $\mu = 0$ ) however is special: First of all, inside the dot, the wavefunction is of the form

$$\psi(\mathbf{r}) = b_1 \begin{pmatrix} e^{-i\theta} J_{1/2}(V_0 r) \\ iY_{1/2}(V_0 r) \end{pmatrix} + b_2 \begin{pmatrix} e^{-i\theta} Y_{1/2}(V_0 r) \\ -iJ_{1/2}(V_0 r) \end{pmatrix}. \quad (4.12)$$

Recalling that the half-integer Bessel functions take the simple form  $J_{1/2}(x) = \sqrt{2/\pi x} \sin x$ , and  $Y_{1/2}(x) = -\sqrt{2/\pi x} \cos x$ , we see that  $\psi(\mathbf{r})$  diverges as  $1/\sqrt{V_0 r}$  at the origin, and that

there is no non-trivial choice of coefficients  $b_1$  and  $b_2$  which removes this divergence. The root of this singular behavior lies in the vector potential, which is singular upon approaching the origin. The problem can be cured by regularizing the vector potential. One possibility is to let the flux  $\Phi$  have an  $r$ -dependence, such that  $\Phi = 0$  for  $r < \rho$  and  $\Phi = 1/2$  for  $r > \rho$ , *i.e.*, the flux is not located at the origin, but on a circle of radius  $\rho$ . Obviously, the problem is now well-defined at the origin, and we can take the solution from the case without flux tube,

$$\psi(\mathbf{r}) = c \begin{pmatrix} e^{-i\theta} J_1(V_0 r) \\ -iJ_0(V_0 r) \end{pmatrix}, \quad (4.13)$$

where  $c$  is a complex constant. We then match the wavefunctions from Eq. (4.13) and Eq. (4.12) at  $r = \rho$ . Upon taking  $\rho \rightarrow 0$ , we get  $b_2 = 0$  as a condition for Eq. (4.12). The boundary condition at the origin ensures, that there is precisely one solution for zero angular momentum.

The  $\mu = 0$  state is also special outside the dot, where the wavefunction is proportional to  $\frac{1}{\sqrt{r}}$  in both components. Thus it has the same decay as a free circular wave in two dimensions and, hence, it does not allow for the formation of a bound state. This conclusion is independent of the choice of the regularization of the wavefunction near  $r = 0$ .

Summarizing: Without flux tube, the bound states are labeled by the angular momentum quantum number  $m$ , which takes half-integer values. For  $|m| = 1/2$  one has a “quasi-bound state”, because the corresponding wavefunction is marginally non-normalizable. With a  $\pi$  flux tube, the bound states are labeled by the kinematic angular momentum quantum number  $\mu$ , which takes integer values. There is no bound state for  $\mu = 0$ .

## 4.2. Two-terminal conductance

We now attach metallic source and drain contacts to the undoped graphene layer that surrounds the quantum dot. Schematically, this setup has been shown in Fig. 3.1. We then calculate the two-terminal conductance, where bound states of the dot show up as resonant features as a function of the gate voltage  $V_0$ .

The contacts are included by the addition of an additional potential  $U_{\text{leads}}$  with [Twor 06]

$$U_{\text{leads}} = \begin{cases} 0 & \text{if } -L/2 < x < L/2, \\ \infty & \text{if } x < -L/2 \text{ or } x > L/2. \end{cases} \quad (4.14)$$

We apply periodic boundary conditions in the  $y$  direction, with period  $W$ . For the vector potential  $\mathbf{A}$  we take a different gauge than in Sec. 4.1,

$$\mathbf{A}(\mathbf{r}) = \frac{h\Phi}{e} \delta(x) \mathbf{e}_x \times \begin{cases} 0 & \text{if } 0 < y < W/2, \\ 1 & \text{if } -W/2 < y < 0, \end{cases} \quad (4.15)$$

where  $\mathbf{e}_x$  is the unit vector in the  $x$  direction. With this choice of the vector potential there are two flux tubes: one, at  $y = 0$ , located in the quantum dot, and one, at  $y = W/2$ , located outside the quantum dot. The second flux tube is necessary to implement the periodic boundary conditions. It does not affect the conductance resonances in the limit



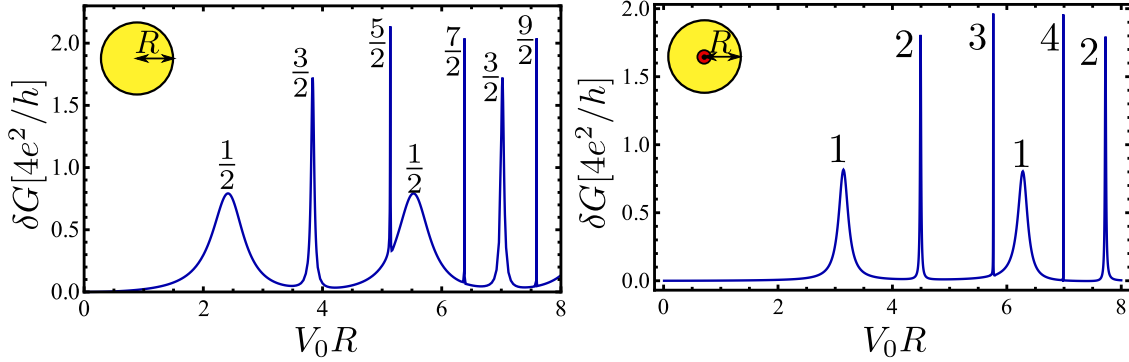


Figure 4.1.: Two-terminal conductance of a graphene sheet containing a disc-shaped quantum dot without (left) and with (right)  $\pi$ -flux tube. Model parameters are  $R/L = 0.2$  and  $W/L = 6$ . Without flux tube, resonances have definite angular momentum, with quantum number  $|m|$  indicated at each resonance [data taken from Ref. [Bard 09]]. Without flux tube, resonances are labeled by the kinematic angular momentum quantum number  $|\mu|$ . No resonance is found for  $\mu = 0$ .

that the sample width  $W$  is much larger than the distance  $L$  between source and drain contacts.

The numerical calculation of the two-terminal conductance follows the method of Ref. [Bard 07]. Details specific to the presence of the flux tube are discussed in Appendix B.1. The conductance can be written as

$$G = G_0 + \delta G, \quad G_0 = \frac{4e^2}{\pi h} \frac{W}{L}, \quad (4.16)$$

where  $G_0$  refers to the conductance of an undoped graphene sheet in the absence of a quantum dot [Twor 06]. We now compare results for the conductance change  $\delta G$  for quantum dots with and without flux tube. We give results for a disc-shaped quantum dot, as a prototype of a quantum dot with integrable dynamics, and a stadium-shaped quantum dot, the prototype of a dot with chaotic dynamics.

#### 4.2.1. Disc-shaped dot

The two-terminal conductance for the case of a disc-shaped quantum dot without and with flux tube is shown in Fig. 4.1 (we repeat the figure for the case without flux tube here, which was already shown in Fig. 3.2 in the previous chapter, so that the reader can easily compare both situations). The figure shows pronounced resonances as a function of the gate voltage  $V_0$ , with positions that agree with the ones calculated Sec. 3.2.1 and Sec. 4.1. Without flux tube, the resonances are labeled by the quantum number  $|m| = 1/2, 3/2, 5/2, \dots$ . Their width scales  $\propto (R/L)^{2|m|}$  as the coupling to the leads is decreased (data not shown), as discussed in Sec. 4.1. With flux tube, the resonances are labeled by the kinematic angular momentum quantum number  $|\mu| = 1, 2, 3, \dots$ . There are no

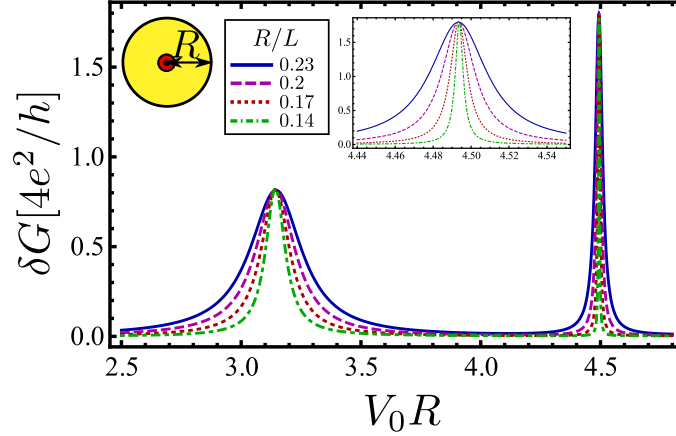


Figure 4.2.: First two resonances for a disc-shaped quantum dot with  $\pi$ -flux tube, for different coupling strengths to the leads. Calculations are performed for  $W/L = 8$  and various  $R/L$ , as indicated in the figure. The second resonance is shown enlarged in the inset.

resonances for  $\mu = 0$ . Upon decreasing the coupling to the leads, the resonances become narrower but retain their height, see Fig. 4.2, and the scaling of the resonance width with the ratio  $R/L$  is consistent with Eq. (4.11) (data not shown).

#### 4.2.2. Stadium-shaped dot

As a prototypical example of a chaotic quantum dot, we consider a stadium-shaped quantum dot. Here the potential  $V(\mathbf{r}) = -\hbar v V_0$  for positions  $\mathbf{r}$  inside the stadium and  $V(\mathbf{r}) = 0$  otherwise. Without magnetic flux, the two-terminal conductance shows resonances, which, in the limit of small  $R/L$ , all behave as the  $|m| = 1/2$ -type resonances of the disc-shaped dot, *i.e.*, their height remains finite, whereas the resonance width scales proportional to  $R/L$ , as discussed in the previous chapter. The numerical data shown in the left panels of Figs. 4.3 and 4.4 clearly reveal these resonances, although the asymptotic scaling of the resonance width and resonance height with  $R/L$  is somewhat obscured by transient contributions for moderate  $R/L$  that originate from higher-angular-momentum contributions to the resonances, as mentioned in the previous chapter.

The conductance trace for a stadium-shaped quantum dot with a flux tube carrying half a flux quantum is shown in the right panels of Figs. 4.3 and 4.4. In order to break inversion symmetry, the stadium is placed asymmetrically with respect to the flux tube, see the inset of Fig. 4.3. The differences with the case of the disc-shaped quantum dot and with the case without a flux tube are significant. We find that the conductance depends on the gate voltage  $V_0$  for finite  $R/L$ , but the widths of the “resonances” is independent of the coupling to the leads, which is set by the ratio  $R/L$ , whereas the height decreases upon decreasing  $R/L$ . This agrees with the expectation that, since all states in the stadium have a  $\mu = 0$  component, a stadium dot should not support any (quasi)bound states. While for intermediate values of  $R/L$  contributions from higher angular momentum channels still

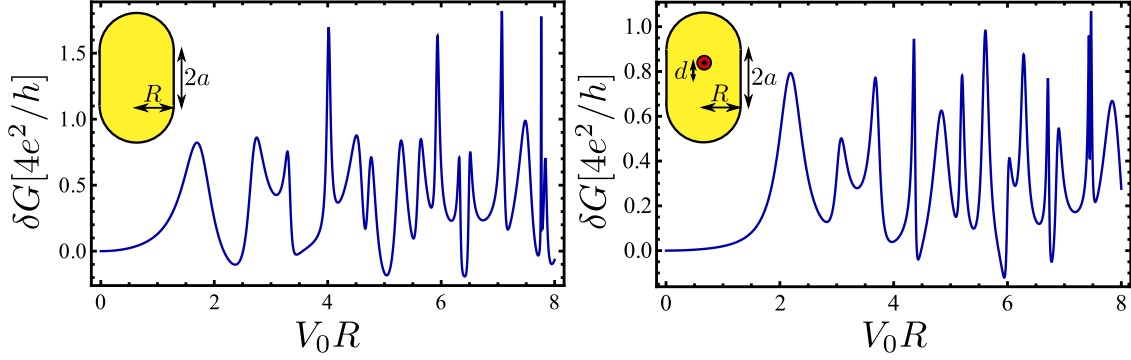


Figure 4.3.: Two-terminal conductance of a graphene sheet containing a stadium-shaped quantum dot without (left) and with (right) a  $\pi$ -flux. Parameters for the calculation are  $R/L = 0.2$ ,  $W/L = 12$ ,  $a/R = \sqrt{3}/2$ ,  $d = 2a/3$ . The figure for the case without flux tube has been also presented in Fig. 3.3.

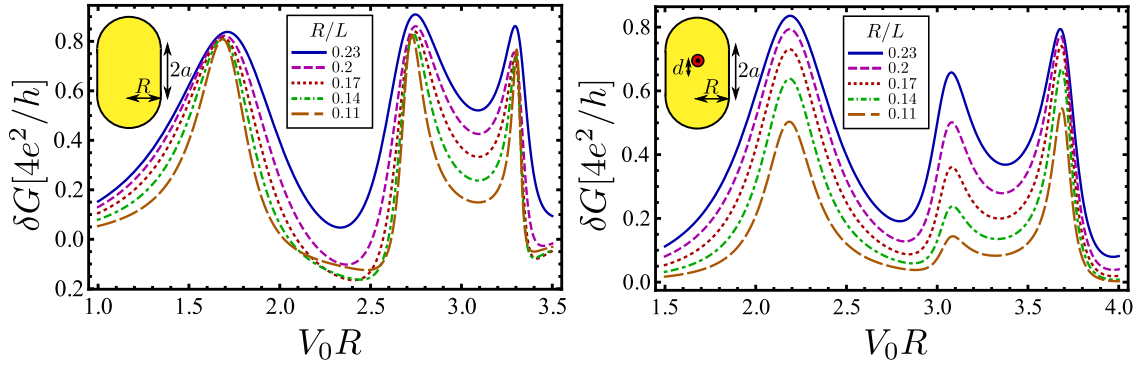


Figure 4.4.: Behavior of the first three quasi resonances of the stadium-shaped quantum dot without (left) and with (right)  $\pi$ -flux upon changing the coupling to the leads  $R/L$ . The other parameters are the same as in Fig. 4.3.

give rise to broad “quasi-resonances”, in the limit  $R/L \rightarrow 0$ , only the  $\mu = 0$  channel is relevant, and the conductance becomes featureless as a function of  $V_0$ .

We remark that, if the flux tube would be placed exactly in the middle of the stadium, inversion symmetry would split the resonances into two groups, resulting from even and odd  $\mu$ . The “even” resonances have a finite  $\mu = 0$  component and disappear upon taking the limit  $R/L \rightarrow 0$ . The “odd” resonances survive in this limit, with a finite resonance height and a resonance width  $\Gamma \propto (R/L)^2$  (data not shown). We also note, that for a disc-shaped dot with a flux tube located away from the center, integrability is broken, and the resulting conductance has features that are characteristic for a chaotic dot (data not shown).

### 4.3. Density of states

While the previous studies were focused on the signatures of confinement in the two-terminal conductance, we now want to extend and complement these studies by investigating how information about confinement is revealed in the density of states or, equivalently, the quantum capacitance of the quantum dot. Density of states measurements provide a valuable experimental technique in the study of nanosystems, and have been also widely used in the context of graphene. One way to gain information is by local probes such as scanning tunneling spectroscopy or scanable single-electron transistors, that give access to the local density of states or the local compressibility of the system, see, *e.g.*, Refs. [Ishi 07, Li 07, Mart 08]. Other works also employ capacitive measurements, that extend to the analysis of the total compressibility of the system, see, *e.g.* Refs. [Gian 09, Xia 09, Dros 10, Pono 10, Stol 11]. Similar to the study of two-terminal conductance, where the resonant tunneling between dot and leads opens an additional conducting channel and leads to a resonant feature, for the density of states, the presence of well-quantized states in the quantum dot leads to an additional peak structure.

A second motivation to study the density of states, rather than the two-terminal conductance, is of a more technical nature: The theoretical formalism to compute the two-terminal conductance is quite involved, and is not easily adapted to include the  $\pi$  flux tube that was used to bring out the role of the Berry phase. For this reason, the study of the previous Section performed a direct numerical simulation of the quantum dot structure, which does not allow one to go to the limit of very narrow resonances. On the other hand, measurement of the density of states involves only one contact (in addition to the electrostatic gate) and can be described theoretically without breaking the rotational symmetry. As we show below, this allows for a considerable simplification of the analysis, making it possible to reach the narrow-resonance limit with a  $\pi$  flux line, too.

The setup that we study consists of a gate-defined quantum dot surrounded by undoped graphene, and connected to a ring-shaped metallic contact at distance  $L$  from the center of the quantum dot, shown schematically in Fig. 4.5b. An unambiguous identification of bound states requires the limit of large  $L$ , in which the dot is well separated from the metallic contact. It is for this limit that the method presented in this chapter proves to be particularly effective. Although the rotational symmetry of the leads is chosen primarily for technical reasons, we note that it has no consequence for the qualitative  $L$ -dependence of the resonances (which can be seen, *e.g.*, by comparing the results of the remainder of this chapter with that of Ch. 3), but also that ring-shaped contacts for graphene can be fabricated in principle [Boot 08], whereas local gating of suspended graphene has also been demonstrated recently [Grus 13, Rick 13].

### 4.4. Graphene quantum dot

Our setup consists of a gate-defined graphene quantum dot, surrounded by an intrinsic graphene layer, which is connected to a ring-shaped metallic contact. The electronic wavefunction satisfies the two-dimensional Dirac equation

$$H\psi_\varepsilon = \varepsilon\psi_\varepsilon, \quad H = v\mathbf{p} \cdot \boldsymbol{\sigma} + V(\mathbf{r}), \quad (4.17)$$

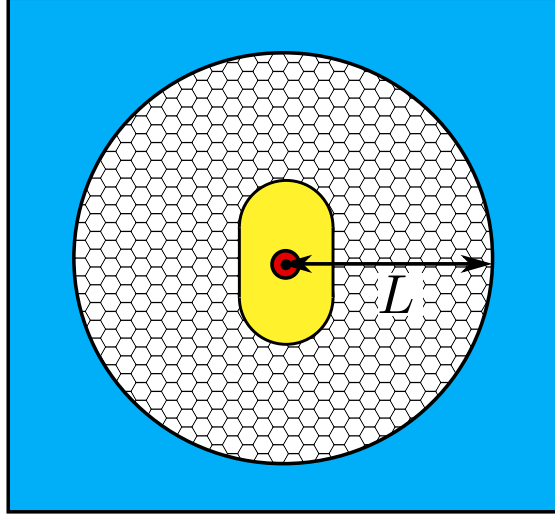


Figure 4.5.: The setup: A quantum dot (yellow) surrounded by undoped graphene, that is attached to a circular lead (blue) at distance  $L$  from the origin. We also investigate the situation with the presence of a magnetic flux tube (red), that contains half a flux quantum.

where  $\varepsilon$  is the energy of the quasiparticle. We take the gate potential to be of the form

$$V(\mathbf{r}) = \begin{cases} -\hbar v V_0, & \mathbf{r} \in \mathcal{R} \\ -\hbar v V_\infty, & r > L, \\ 0, & \text{else,} \end{cases} \quad (4.18)$$

where, for definiteness, we choose the parameters  $V_0$  and  $V_\infty$  to be positive, such that dot and lead region are electron-doped. The region  $\mathcal{R}$  denotes the area of the dot. For a circular dot  $\mathcal{R}$  consists of all coordinates  $\mathbf{r}$  with  $r < R$ ,  $R$  being the dot radius. The ring-shaped metallic contact for  $r > L$  is modelled by taking the limit  $V_\infty \rightarrow \infty$ . While our choice of a piecewise uniform potential considerably simplifies the calculations, it is not necessary for the existence of bound states [Down 11, Mkhi 12], and our general conclusions will remain valid in the more general case of a central potential  $V(r)$ .

Scattering states can be defined in the ring-shaped ideal contact, see Eq. (4.23) below. In order to calculate the density of states, we use the relation between the local density of states  $\nu(\mathbf{r}, \varepsilon)$  and the derivative of the scattering matrix  $\mathcal{S}(\varepsilon)$  with respect to the potential  $V(\mathbf{r})$  at position  $\mathbf{r}$  [Lang 61, Butt 93, Butt 94],

$$\nu(\mathbf{r}, \varepsilon) = -\frac{1}{2\pi i} \text{tr} \mathcal{S}^\dagger \frac{\delta \mathcal{S}}{\delta V(\mathbf{r})}. \quad (4.19)$$

The total density of states of the dot is then obtained by integration over the region

$r < L$ ,<sup>1</sup>

$$\nu_{\text{dot}}(\varepsilon) = -\frac{1}{2\pi i} \int_{r < L} d\mathbf{r} \text{tr} \mathcal{S}^\dagger \frac{\delta \mathcal{S}}{\delta V(\mathbf{r})}. \quad (4.20)$$

The density of states  $\nu_{\text{dot}}$  is defined as the density of states per spin and valley. The expression (4.20) is related to the Wigner-Smith time delay [Wign 55, Smit 60]. It is also related to the dot's capacitance [Butt 00], which can be measured from the current response to an alternating bias on the ring-shaped metallic contact, at fixed value of the gate voltage  $V_0$ .

The calculation of the density of states  $\nu_{\text{dot}}$  at zero energy as a function of the dot potential  $V_0$  requires to solve the Dirac equation (4.17) at small, but finite energy  $\varepsilon$ . Dealing with a finite energy also in the region between dot and lead goes beyond previous studies that addressed the two-terminal conductance, see [Bard 09, Tito 10] and the previous part of this thesis.

#### 4.4.1. Circular quantum dot

We begin our discussion with a circular quantum dot, where the region  $\mathcal{R}$  equals a disc of radius  $R$  centered at the origin. In this case the angular momentum  $j_z = (\mathbf{r} \times \mathbf{p})_z + \frac{\hbar}{2}\sigma_z$  is conserved, and the solutions of the Dirac equation (4.17) can be labeled by the angular momentum  $m\hbar$ , where  $m$  is half-integer as a consequence of the pseudospin degree of freedom for graphene. Writing Hamiltonian (4.17) in polar coordinates (see also Sec. 3.2.1),

$$H = -i\hbar v \begin{pmatrix} 0 & \partial_- \\ \partial_+ & 0 \end{pmatrix} + V(r), \quad (4.21)$$

with the operators

$$\partial_{\pm} = e^{\pm i\theta} (\partial_r \pm i \frac{1}{r} \partial_\theta), \quad (4.22)$$

we solve the Dirac equation  $H\psi_\varepsilon = \varepsilon\psi_\varepsilon$  in the three regions  $0 < r < R$ ,  $R < r < L$  and  $r > L$  in which the potential  $V$  is constant. In each region, we obtain two linearly independent solutions,

$$\psi_{k,m}^{(\pm)}(\mathbf{r}) = e^{im\theta} \sqrt{\frac{k}{8v}} \begin{pmatrix} e^{-i\theta/2} H_{|m-1/2|}^{(\pm)}(kr) \\ i \text{sgn}(m) e^{i\theta/2} H_{|m+1/2|}^{(\pm)}(kr) \end{pmatrix}, \quad (4.23)$$

which describe incoming (−) or outgoing (+) circular waves of wavenumber  $k = (\varepsilon - V)/\hbar v$  in the conduction band, normalized to unit flux. (Without loss of generality we assume that the energy  $\varepsilon$  is positive; We checked that our final results remain valid for negative  $\varepsilon$ .) Further, the  $H_n^{(\pm)}$  are Hankel functions of the first (+) and second kind (−), respectively. The Hankel functions are related to the Bessel (Neumann) function  $J_n$  ( $Y_n$ ) as  $H_n^{(\pm)} = J_n \pm iY_n$ .

---

<sup>1</sup>The functional derivative  $\delta\mathcal{S}/\delta V(\mathbf{r}')$  can be obtained by changing the potential  $V(\mathbf{r})$  by  $v_0\delta(\mathbf{r} - \mathbf{r}')$  and taking the derivative of the scattering matrix with respect to  $v_0$ . In practice, for the calculation of the density of states integrated over a certain region, one shifts the potential  $V(\mathbf{r})$  by a constant  $v_0$  within the specific region, and takes the derivative of the scattering matrix with respect to  $v_0$ .

The precise value of the wavenumber  $k$  is different for the three regions in which the solutions (4.23) apply. For  $r < R$  one has  $k \equiv k_0 = \varepsilon/\hbar v + V_0$ ; for  $R < r < L$  one has  $k = \varepsilon/\hbar v$ , and for  $r > L$  one has  $k \equiv k_\infty = \varepsilon/\hbar v + V_\infty$ . For  $r > L$  the wavefunction can be written as a linear combination of the two solutions of Eq. (4.23),

$$\psi_{\varepsilon,m}(\mathbf{r}) = a_m(\varepsilon)\psi_{k_\infty,m}^{(-)}(\mathbf{r}) + b_m(\varepsilon)\psi_{k_\infty,m}^{(+)}(\mathbf{r}). \quad (4.24)$$

The coefficients  $a_m(\varepsilon)$  and  $b_m(\varepsilon)$  can be determined using continuity of the wavefunction at  $r = L$  and  $r = R$ , as well as regularity at  $r = 0$ . They define the scattering matrix  $\mathcal{S}_{mn}(\varepsilon) = \mathcal{S}_m(\varepsilon)\delta_{m,n}$  through the relation

$$b_m(\varepsilon) = \mathcal{S}_m(\varepsilon)a_m(\varepsilon). \quad (4.25)$$

The scattering matrix  $\mathcal{S}$  is then used to calculate the density of states, see Eq. (4.20).

To simplify the further analysis, we consider the limit of a highly doped lead  $k_\infty L \gg 1$ . In this regime, we make use of the asymptotic behavior of the Hankel functions for large arguments,  $H_n^{(\pm)}(x) \approx (2/\pi x)^{1/2} e^{\pm i(x - n\frac{\pi}{2} - \frac{\pi}{4})}$  for the wavefunction in the lead region  $r > L$ . The smallness of the energy  $\varepsilon$  furthermore allows to expand in the wavenumber  $k$  in the region  $R < r < L$  corresponding to the undoped layer separating the quantum dot from the lead. One then finds

$$\mathcal{S}_m(\varepsilon) = e^{-2ik_\infty L + i|m|\pi} \left[ \mathcal{S}_m^{(0)} + kL\mathcal{S}_m^{(1)} + \mathcal{O}(\varepsilon^2) \right], \quad (4.26)$$

where  $k$  is the wavenumber in the region  $R < r < L$ ,

$$\mathcal{S}_m^{(0)} = \frac{L^{2|m|} + i\mathcal{J}_m R^{2|m|}}{L^{2|m|} - i\mathcal{J}_m R^{2|m|}}, \quad (4.27)$$

and

$$\mathcal{S}_m^{(1)} = -\frac{2i}{2|m| - 1} \mathcal{S}_m^{(0)} + \frac{8i|m|L^{4|m|} + 2i[(2|m| + 1)\mathcal{J}_m^2 - (2|m| - 1)]R^{2|m|+1}L^{2|m|-1}}{(4|m|^2 - 1)(L^{2|m|} - i\mathcal{J}_m R^{2|m|})^2} \quad (4.28)$$

if  $|m| \neq 1/2$ , whereas

$$\mathcal{S}_{\pm 1/2}^{(1)} = \frac{i(L^2 - R^2) + 2i\mathcal{J}_{\frac{1}{2}}^2 R^2 \log(L/R)}{(L - i\mathcal{J}_{\frac{1}{2}} R)^2}. \quad (4.29)$$

In Eqs. (4.27)–(4.29) we used the abbreviation

$$\mathcal{J}_m = \frac{J_{|m|+1/2}(k_0 R)}{J_{|m|-1/2}(k_0 R)}. \quad (4.30)$$

We now use Eq. (4.20) to calculate the density of states  $\nu_{\text{dot}}$  at zero energy,

$$\nu_{\text{dot}} = \frac{1}{2\pi i \hbar v} \sum_m \mathcal{S}_m^{(0)*} \left[ \frac{\partial \mathcal{S}_m^{(0)}}{\partial V_0} + L\mathcal{S}_m^{(1)} \right]. \quad (4.31)$$

The first term in Eq. (4.31) represents the integral of the local density of states inside the quantum dot region  $r < R$ ; the second term is the integral of the local density of states in the undoped layer that separates the dot and the metallic contact.

Let us now analyse the density of states as a function of the gate voltage  $V_0$ . In the limit  $R \ll L$  (weak coupling to the ring-shaped contact), the DOS exhibits isolated resonances at gate voltages  $V_0 = V'_0$  satisfying the condition

$$J_{|m|-1/2}(V'_0 R) = 0. \quad (4.32)$$

Close to resonance, we have that  $\mathcal{J}_m \approx -1/[R(V_0 - V'_0)]$ , and the density of states has a Lorentzian dependence on  $V_0$ . For a generic resonance with  $|m| \neq 1/2$  the zero-energy density of states has the form

$$\nu_{\text{dot}} = \frac{4R|m|}{\pi\hbar v(2|m| - 1)} \frac{\Gamma}{4R^2(V_0 - V'_0)^2 + \Gamma^2}, \quad (4.33)$$

where the dimensionless resonance width is given by

$$\Gamma = 2(R/L)^{2|m|}. \quad (4.34)$$

Resonances are well separated if  $R \ll L$ . In the lowest angular momentum channel  $|m| = 1/2$  the expression for the density of states reads

$$\nu_{\text{dot}} = \frac{2R}{\pi\hbar v} \left(1 + \log \frac{L}{R}\right) \frac{\Gamma}{4R^2(V_0 - V'_0)^2 + \Gamma^2}, \quad (4.35)$$

with  $\Gamma = 2R/L$ . We remark that the position of the resonances, as well as the scaling of the width agree with the results for the two-terminal conductance, where  $L$  is the distance between source and drain.

We note, that the resonant part of  $\nu_{\text{dot}}$  that comes from the first term in Eq. (4.31) integrates to  $1/\hbar v$ , when integrated over  $V_0$ , corresponding to a  $2\pi$  shift of the scattering phase upon tuning  $V_0$  through a resonance. The second term in Eq. (4.31) gives an additional contribution to the density of states, whose weight decays for higher angular momentum. Remarkably, in the lowest angular momentum channel, this additional contribution has a large factor  $\log(L/R)$  factor in the prefactor. We relate the presence of this large factor to the fact, that the bound states of the lowest angular momentum have only a slow decay  $\propto 1/r$ , such that the wavefunction is marginally non-normalizable, see Sec. 3.2.1.

We show a plot of the density of states for a circular quantum dot as a function of the gate voltage in Fig. 4.6. As discussed, the DOS exhibits resonant peaks, that can be labelled according to their angular momentum channel, and the position is given by Eq. 4.32. The higher the angular momentum, the sharper the resonances, consistent with the scaling of the width Eq. (4.34).

#### 4.4.2. Chaotic quantum dot

We now extend our analysis to a quantum dot of arbitrary geometry. For the generic situation, the scattering matrix is no longer diagonal in the angular momentum basis and



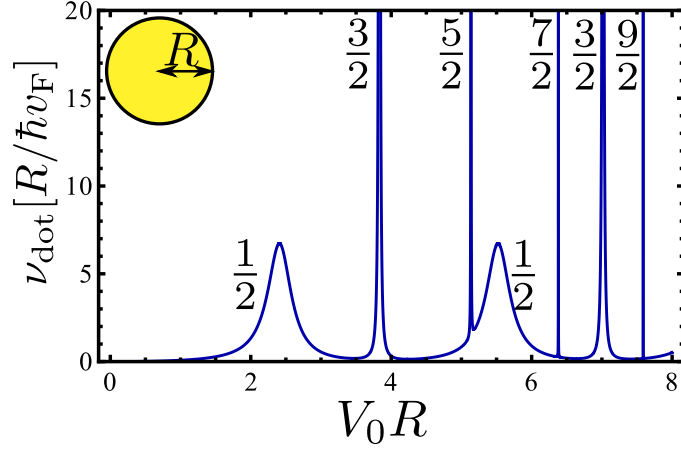


Figure 4.6.: Density of states for a circular quantum dot. Resonances are labelled according to their angular momentum  $|m|$  ( $R/L = 0.2$ ).

an analytical solution is no longer available. We pursue a numerical approach for the calculation of the scattering matrix instead.

Our numerical method follows the calculation of the scattering matrix in Ch. 3. The problem is broken up into thin circular slices, for which the scattering effect is weak and may be captured in Born approximation. The scattering matrix of the full system is then obtained by subsequent concatenation of the scattering matrices of the slices. A difference with Ch. 3 is that we have to calculate the scattering matrix at a finite energy or potential in order to evaluate Eq. (4.20). Since the quantum dot has a finite size, the numerical evaluation is necessary up to a distance  $\tilde{R}$  away from the origin only. (For the geometry shown in Fig. 4.7, one has  $\tilde{R} = R + a$ ). For  $\tilde{R} < r < L$  the analytical calculations outlined above can be used. We refer to Appendix B.2 for further details of the numerical implementation.

As a prototypical example of a chaotic dot, we now investigate the density of states for a stadium-shaped quantum dot. In Fig. 4.7, we show the result of a calculation of the density of states as a function of the gate voltage  $V_0$ . We find a series of resonances of similar width. The width is comparable to that of the broadest resonances for the circular dot, in agreement with the general expectation that confinement is suppressed in chaotic dots.

To further analyze the situation, we zoom in on the first resonance and investigate its dependence on the strength of the dot-lead coupling  $R/L$ , see Fig. 4.8. We extract height and width of the resonance by fitting to a Lorentzian,

$$\nu_{\text{dot}} = \frac{2RA}{\hbar\pi v} \frac{\Gamma}{4R^2(V_0 - V_0')^2 + \Gamma^2}, \quad (4.36)$$

where  $V_0'$  is the resonance position. For the chaotic structure, we expect the resonant states to be composed as a mixture of all angular momentum channels. In the limit of large  $L/R$  we expect that the lowest possible angular momentum channel  $|m| = \frac{1}{2}$  is dominant. The

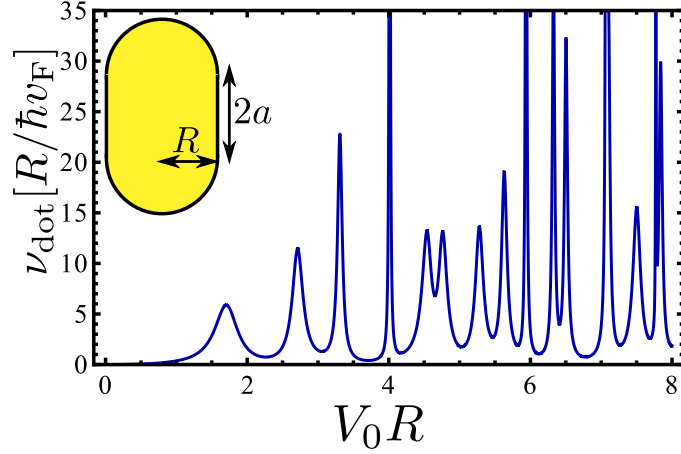


Figure 4.7.: Density of states for a stadium quantum dot. ( $R/L = 0.2$ ,  $2a/R = \sqrt{3}$ .)

behavior of the resonances should then resemble those of a  $|m| = \frac{1}{2}$ -resonance of a circular dot, *i.e.*, we expect width and amplitude to scale as

$$\Gamma = a \frac{R}{L}, \quad (4.37)$$

$$\mathcal{A} = b + c \log \frac{L}{R}, \quad (4.38)$$

with coefficients  $a$ ,  $b$ , and  $c$  of order unity. The numerical study indeed verifies this assertion, as can be seen from the inset of Fig. 4.8. We further checked, that the other resonances of Fig. 4.7 show the same behavior for sufficiently small values of  $R/L$ , although the onset of the asymptotic small- $R/L$  behavior and the precise values of the numerical coefficients  $a$ ,  $b$ , and  $c$  vary from resonance to resonance. We attribute these variations to the different constitutions of the resonances, indicating the relative weight of the  $|m| = \frac{1}{2}$  channel for a certain resonance in comparison to higher angular-momentum channels. We further verified, that the position of the resonances agrees with the ones obtained in a calculation of the conductance (Ch. 3).

To summarize: For a regular quantum dot, we find signatures of well-confined states, that become very sharp in the limit of weak coupling between dot and lead, as well as broad resonances with a width scaling  $\propto R/L$  upon changing the coupling to the lead. For the chaotic dot, we observe such “broad” resonances only. The results for the density of states are consistent with the results for a two-terminal conductance setup.

## 4.5. Effect of a $\pi$ -flux

The difference between regular and chaotic quantum dots in graphene becomes much more pronounced, when we introduce a magnetic flux carrying half a flux quantum. Electrons encircling this flux tube acquire an Aharonov-Bohm phase of  $\pi$ , which cancels the Berry phase that the electronic wavefunction collects via the pseudospin upon performing a

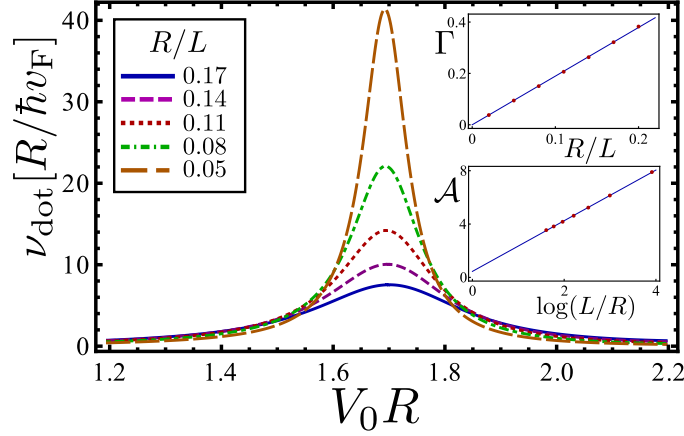


Figure 4.8.: Density of states for the first resonance, as well as resonance height  $\mathcal{A}$  and width  $\Gamma$  (insets) of the stadium dot for various values of the ratio  $R/L$ . ( $2a/R = \sqrt{3}$ .)

circular motion. The magnetic flux shifts the kinematic angular momentum to integer values, allowing for a state that cannot be confined by gate potentials.

We now analyse the density of states for a graphene quantum dot in the presence of such  $\pi$ -flux. For this, we add the vector potential

$$\mathbf{A}(\mathbf{r}) = \frac{\hbar}{e} \frac{1}{2r} \hat{\mathbf{e}}_\theta. \quad (4.39)$$

Inclusion of  $\mathbf{A}(\mathbf{r})$  into the Dirac equation amounts to making the replacement  $\partial_\pm \rightarrow D_\pm$  in Eq. (4.21), with (see also Sec. 4.1)

$$D_\pm = e^{\pm i\theta} \left( \partial_r \pm i \frac{1}{r} \partial_\theta \mp \frac{1}{2r} \right). \quad (4.40)$$

We further introduce the kinematic angular momentum,

$$j_{z,\text{kin}} = [\mathbf{r} \times (\mathbf{p} + e\mathbf{A})]_z + \frac{\hbar}{2} \sigma_z \quad (4.41)$$

For the  $\pi$ -flux (4.39), the kinematic angular momentum is related to the canonical angular momentum as  $j_{z,\text{kin}} = j_z + \hbar/2$ , and therefore is quantized in integer multiples of  $\hbar$ . We now consider the effect of a  $\pi$ -flux line on the density of states in a circular and chaotic quantum dot separately.

#### 4.5.1. Circular dot

For the circular dot the flux line is positioned in the origin, so that rotational symmetry is preserved. The calculation for the density of states proceeds in an analogous way as in the case without flux line. The presence of the flux modifies the basis wavefunctions (4.23). We label the new basis states by the integer index of the kinematic angular momentum  $\mu$ ,

$$j_{z,\text{kin}} \psi_{k,\mu}^{(\pm)} = \mu \hbar \psi_{k,\mu}^{(\pm)}. \quad (4.42)$$

For non-zero  $\mu$ , the basis states now read

$$\psi_{k,\mu}^{(\pm)}(\mathbf{r}) = \sqrt{\frac{k}{8v}} \begin{pmatrix} e^{i(\mu-1)\theta} H_{|\mu-1/2|}^{(\pm)}(kr) \\ i \operatorname{sgn}(\mu) e^{i\mu\theta} H_{|\mu+1/2|}^{(\pm)}(kr) \end{pmatrix}, \quad (4.43)$$

while for zero kinematic angular momentum, we find

$$\psi_{k,0}^{(\pm)}(\mathbf{r}) = \frac{e^{\pm ikr}}{\sqrt{4\pi r v}} \begin{pmatrix} \pm e^{-i\theta} \\ 1 \end{pmatrix}. \quad (4.44)$$

The state with zero kinematic angular momentum needs to be discussed separately, and will be responsible for the crucial difference caused by the magnetic flux. Let us discuss the states with non-zero kinematic angular momentum first, where the magnetic flux only leads to slight modifications. Indeed, one finds that the results of Eqs. (4.27)-(4.28) remain valid, provided the half-integer index  $m$  is replaced by the integer index  $\mu$ , which labels kinematic angular momentum. In particular, resonances in the density of states now appear at roots of half-integer Bessel function  $J_{|\mu|-1/2}(V_0 R) = 0$ , and the resonance width is  $\Gamma = 2(R/L)^{2|\mu|}$ .

For the case  $\mu = 0$  regularity of the wavefunction at the origin is not sufficient to determine the scattering matrix  $\mathcal{S}_0(\varepsilon)$ . This problem can be cured by a suitable regularization of the flux line. Taking a flux line of extended diameter we find the condition that the upper component of the wavefunction has to vanish at the origin (see Sec. 4.1). With this regularization the calculation of the scattering matrix  $\mathcal{S}_0(\varepsilon)$  is straightforward and has the result

$$\mathcal{S}_0 = e^{-2i(k_\infty - k_0)R} e^{-2i(k_\infty - k)(L-R)}, \quad (4.45)$$

where  $k = \varepsilon/\hbar v$  and  $k_0 = \varepsilon/\hbar v + V_0$ . This scattering matrix gives a constant, non-resonant contribution to the density of states, which will be disregarded in the considerations that follow because it is independent of the gate voltage  $V_0$ .

We show the density of states for a circular quantum dot in the presence of a flux tube in Fig. 4.9. It contains resonances originating from non-zero angular momentum channels. The position and the width of such resonances has been discussed above. The zero-angular momentum channel has no  $V_0$ -dependent contribution to the density of states. Our findings are consistent with a simulation of the two-terminal transport, concerning the position and the scaling of the width upon changing  $R/L$  of the resonances (Sec. 4.2) although the regime of small  $R/L$  could not be accessed there.

#### 4.5.2. Chaotic Dot

The numerical method described in Sec. 4.4.2 and the appendix can be easily carried over to the case with the  $\pi$ -flux, by taking the wave functions Eqs. (4.43) and (4.44) instead of Eq. (4.23). One has to pay attention to the boundary condition at the origin for the zero angular momentum channel, as discussed above.

We show the result of a calculation of the density of states of a stadium-shaped quantum dot in the presence of a flux tube in Fig. 4.10, as a function of the dot's potential. The

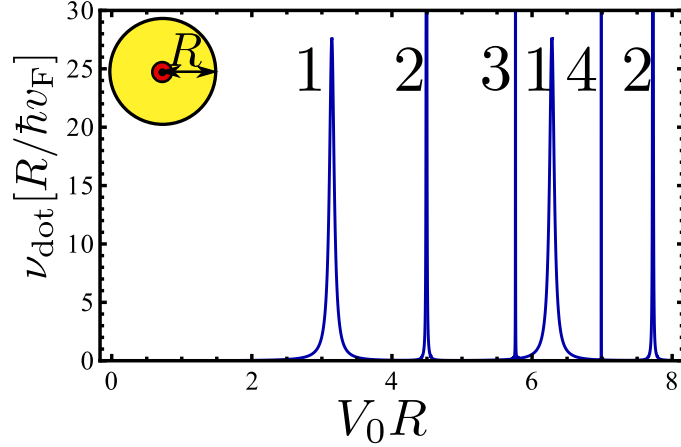


Figure 4.9.: Density of states for a circular quantum dot in the presence of a flux tube. Resonances are labelled according to their kinematic angular momentum  $|\mu|$ . ( $R/L = 0.2$ .)

flux tube is placed off-center in order to lift a twofold rotation symmetry. We observe a density of states with broad peaks, the peak widths typically being much larger than for the circular dot (compare with Fig. 4.9). The analysis can be made quantitative by considering a specific “peak” as a function of  $R/L$ , see Fig. 4.11. Remarkably, the density of states saturates in the limit  $R/L \rightarrow 0$  that corresponds to a weak coupling between the quantum dot and the ring-shaped metallic contact. This behavior is a qualitative difference with the case of a circular dot and clearly distinguishes resonances of a chaotic dot with flux from those of a regular dot or the situation without flux. We explain this feature by the special role of the zero angular momentum channel, that becomes dominant decay channel in the limit of small  $R/L$ . As this channel is not capable of binding (or backscattering) states, the density of states becomes insensitive of the distance  $L$  to the metallic contact. The transient behavior for  $R/L$  of order unity is attributed to the contribution from finite-angular-momentum channels to the resonance width, which gradually disappears if  $R/L$  becomes small.

For the specific resonance shown in Fig. 4.11, the saturation of the density of states takes place only for very small dot sizes. On the other hand, the absence of a bound state may also be inferred from an analysis of the width of the resonance-like feature as a function of  $R/L$ . Obtaining the width  $\Gamma$  from a Lorentzian fit, the inset of Fig. 4.11 shows that  $\Gamma$  approaches a finite value as  $R/L$  goes to zero, with a leading correction  $\propto (R/L)^2$ , which we attribute to a contribution from the angular momentum channel  $|\mu| = 1$ . Such behaviour is in stark contrast to the scenario without flux tube, where the width goes to zero in the limit  $R/L \rightarrow 0$ . We verified the same qualitative behavior for the other resonance-like features shown in Fig. 4.10, where the value of  $R/L$ , at which the width saturates, varies considerably for different resonances, expressing the variations of the relative contribution in the channel of zero angular momentum. We also found rough agreement in the positions of the resonances with the ones obtained in the calculation

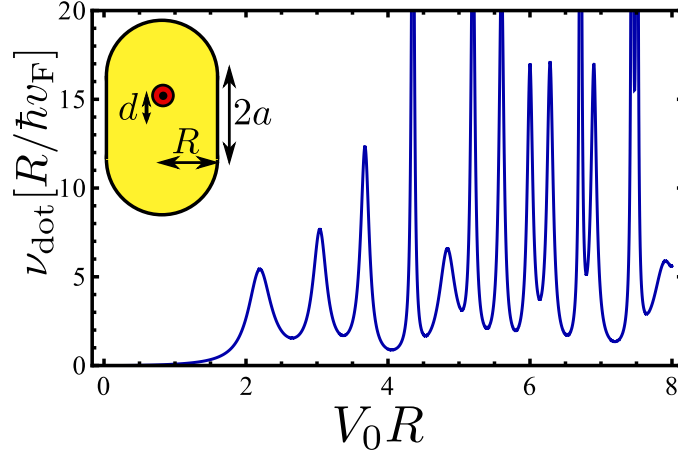


Figure 4.10.: Density of states for a stadium-shaped quantum dot in the presence of a  $\pi$ -flux tube. The flux is shifted from the center of the stadium in order to break inversion symmetry and obtain a truly chaotic structure, see also Sec. 4.2. ( $R/L = 0.2$ ,  $2a/R = \sqrt{3}$ ,  $d = 2a/3$ .)

of the conductance (Sec. 4.2), although no precise comparison is possible here, since the resonances cannot be made arbitrarily narrow upon making the dot smaller. We note, that our calculation of the density of states allows us to access for much smaller values of  $R/L$  as compared to the numerical study of the two-terminal conductance in Sec. 4.2, including access to the regime, where the lineshape of the density of states saturates.

## 4.6. Conclusion

In this Chapter we investigated the observation of Chapter 3, that the two-terminal conductance of a generic gate-defined graphene quantum dot shows resonances in the limit of a weak coupling to the leads, in spite of the naive expectation that electrons can not be confined in such a quantum dot because of Klein tunneling. We attribute this observation to the Berry phase in graphene, which quantizes angular momenta to half-integer values. With half-integer angular momenta, strict perpendicular incidence — the condition for Klein tunneling with unit probability — does not occur. As a consequence, conductance resonances exist in both integrable and chaotic geometries. The only difference between the two cases is a quantitative one: it concerns the scaling of the resonance widths with the coupling to the leads.

The Berry phase can be cancelled against an Aharonov-Bohm phase, when a flux tube containing half a flux quantum is introduced to the system. With a magnetic flux tube, we showed that the relevant angular momentum, the kinematical angular momentum, is quantized to integer values. In this case a state with zero angular momentum is possible. Such a state can not form a bound state or give rise to a conductance resonance. We showed this by an explicit calculation for the disc-shaped quantum dot in Sec. 4.1, and using numerical calculations for disc-shaped and stadium-shaped quantum dots in Sec.

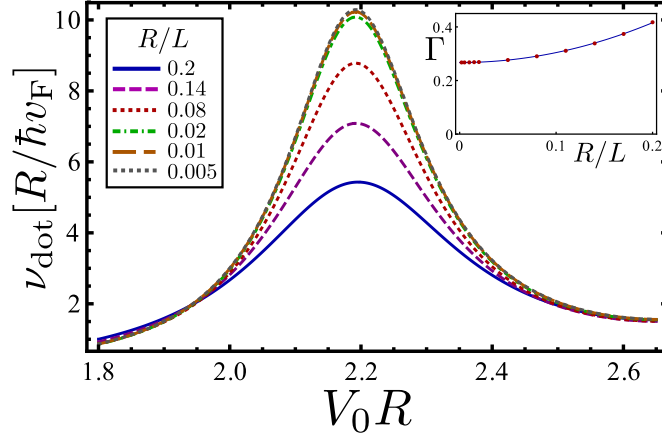


Figure 4.11.: Density of states for the first “resonance” and the corresponding resonance width (inset) of the stadium dot for various values of the ratio  $R/L$ . Both height and width of the feature saturate in the limit  $R/L \rightarrow 0$ . ( $2a/R = \sqrt{3}, d = 2a/3$ .)

4.2. Once the Aharonov-Bohm phase from the  $\pi$ -flux tube cancels the Berry phase, the results of the full quantum theory are consistent with the simple classical expectations. With a  $\pi$ -flux, there is a stark qualitative difference between conductance resonance for integrable and non-integrable quantum dots: Whereas sharp conductance resonances for the case of an integrable quantum dot continue to exist, in the limit of weak lead-dot coupling the conductance becomes featureless for a generic non-integrable quantum dot.

We further explored the density of states as an alternative signature of confinement in this chapter. As we have shown, the calculation of the density of states is significantly easier than the calculation of the two terminal conductance, which allows us to extend the analysis to quantum dots with a flux line (in order to highlight the role of the Berry phase associated with the graphene pseudospin) and to access the regime of well isolated resonances, which requires the limit that the metallic contacts are far away from the quantum dot. This limit could not be reached in numerical simulations of the two-terminal transport.

The strong influence of the geometry on the capability of the quantum dot to confine states can also be deduced from our calculation of the density of states. While both regular and chaotic dot have resonant signatures in the density of states, the scaling of the width of these features with the (linear) size  $L$  of the undoped graphene layer separating the dot and the metallic contacts allows to discern the geometries: While for the chaotic dot, all resonances have a width scaling proportional to  $1/L$ , indicating a weak confinement, for the regular dot, most of the resonances have a width that vanishes faster upon increasing  $L$ , indicating well-confined states. The difference between chaotic and integrable geometries becomes much more pronounced, when a flux tube carrying half a flux quantum is introduced to the system. In this case, in the limit of large  $L$  the lineshape for the density of states for the chaotic dot saturates — corresponding to a “resonance

width” that is independent of  $L$ . Such behavior signals the absence of confined states, in contrast to the case of a disc-shaped dot, that continues to show sharp resonances after a flux tube has been inserted.

The analysis carried out in this chapter considered the density of states integrated over the dot and the surrounding undoped graphene sheet. On the other hand, scanning tunneling microscope experiments measure a local density of states for the region covered by the tunneling tip. The formalism that we developed here can easily be extended to this kind of measurement setup. As far as a qualitative analysis of peak widths and peak positions goes, however, we expect no difference between the local density of states and the integrated density of states that was studied here.



## 5. Semiclassical theory of the interaction correction to the conductance of antidot arrays

The wave nature of electrons manifests itself in a number of signatures in the electric transport of disordered metals, such as weak localization, universal conductance fluctuations, or interaction-induced effects like the Altshuler-Aronov correction to the conductivity. The qualitative effect of these features is successfully explained on a semiclassical level, based on classical electronic trajectories through the solid, while the quantitative analysis is typically reserved to powerful field-theoretical methods, such as diagrammatic perturbation theory. In recent years however, semiclassical methods have been enormously improved, such that also a quantitative description of these quantum effects in transport is possible nowadays. The semiclassical description differs from a field-theoretical description by the appearance of an additional timescale — the so-called Ehrenfest time, which sets a minimal time below which wave effects are not operative.

Noninteracting effects as weak localization and universal conductance fluctuations have been intensively studied by semiclassical methods in past years. This chapter aims at a semiclassical description for the interaction correction to the electrical conductivity. Subsequent to an introduction, we develop the semiclassical theory for the interaction correction of a generic conductor in Sec. 5.2. We then illustrate the effects in quasi-one and two-dimensional antidot arrays, which represent experimentally relevant examples of systems that require a semiclassical approach (Sec. 5.3). We conclude our results in Sec. 5.4.

The content of this chapter is based on the publication [Schn 13].

### 5.1. Introduction

Electronic transport in weakly disordered metals is successfully described by the Boltzmann theory, in which electrons are treated as effectively classical particles moving freely between scattering events. The wave nature of electrons gives rise to a number of corrections to transport properties, such as the weak localization correction [Ande 79, Gork 79], the Altshuler-Aronov interaction correction [Alts 79, Alts 85b], or the universal conductance fluctuations [Alts 85a, Lee 85]. Weak localization results from the constructive interference of electrons propagating along time-reversed paths [Chak 86]. The physical intuition behind the interaction correction is constructive interference of electron trajectories which are scattered on impurities and Friedel oscillations of the electron density [Rudi 97, Zala 01]. These quantum corrections become increasingly important as the temperature is lowered, the effective dimensionality of the sample is reduced, or as the

disorder level is increased. They have a distinctive and universal dependence on external parameters, such as temperature or magnetic field, which makes them identifiable in experiments. In particular, the two quantum corrections to the conductivity, weak localization and the Altshuler-Aronov correction, can be distinguished by application of a magnetic field, since weak localization is suppressed by already a very small magnetic field, whereas the Altshuler-Aronov correction is not.

A “classical analog” of a disordered metal is realized in high-mobility semiconductor structures with randomly placed large antidots [Rouk 89, Enss 90]. The absence of impurities ensures that electrons move ballistically between reflections off the antidots. The reason why these systems are referred to as classical is that the size of the antidots  $a$  is much larger than the Fermi wavelength  $\lambda_F$ . As a result, not only the electron’s motion through the two-dimensional electron gas, but also the reflection off an antidot is described by classical mechanics. (In contrast, in a disordered metal, the size of impurities is comparable to  $\lambda_F$ , so that the scattering event is strongly diffractive.) For an irregular arrangement of antidots, the classical dynamics is chaotic. Nearby trajectories separate exponentially in time, the exponential separation being characterized by the Lyapunov coefficient  $\lambda$ . The chaotic dynamics is essential for the existence of quantum corrections in this system, as it magnifies the quantum uncertainty of even a minimal wavepacket up to classical dimensions within the short time

$$\tau_E = \frac{1}{\lambda} \ln(a/\lambda_F), \quad (5.1)$$

thus transforming the classical dynamics into quantum-diffractive dynamics on time scales larger than  $\tau_E$  [Ale 96]. The time  $\tau_E$  is known as the “Ehrenfest time”.

Since wave effects are not operative for times shorter than  $\tau_E$  — electrons essentially move along classical trajectories up to the Ehrenfest time —, the Ehrenfest time serves as a short-time threshold for the duration of the trajectories contributing to the quantum corrections in an antidot array. For weak localization, it was found that the correction to the conductivity is exponentially suppressed if  $\tau_E$  is larger than the dwell time  $\tau_D$ , the typical time to be transmitted through the system, or the dephasing time  $\tau_\phi$  [Ale 96, Adag 03, Brou 07, Tian 07]. In contrast, other quantum corrections, such as the universal conductance fluctuations, remain finite if  $\tau_E \gg \tau_D$  [Twor 04, Jacq 04, Brou 06, Brou 07].

The goal of this chapter is to present a theory of the Ehrenfest-time-dependence of the Altshuler-Aronov correction  $\delta G_{AA}$ . The analysis presented here significantly extends a previous calculation by Kupferschmidt and Brouwer [Brou 08], which studied the  $\tau_E$  dependence of the interaction correction to the conductance of a ballistic double quantum dot and found that  $\delta G_{AA}$  is strongly suppressed if  $\tau_E$  exceeds the dwell time  $\tau_D$  or the inverse temperature  $\hbar/T$ . The double quantum dot studied in Ref. [Brou 08] is the simplest system with nonzero Altshuler-Aronov correction to the conductance, and is characterized by a long-range interaction, which is spatially homogeneous within each dot. The theory presented here is valid for both short-range and long-range interactions and can be applied to any geometry in which the classical electron dynamics is chaotic — although we will focus our discussion on the case of an antidot array. For the general case considered here we confirm the suppression of  $\delta G_{AA}$  for  $\tau_E \gg \min(\tau_D, \hbar/T)$  and we calculate the precise functional dependence of  $\delta G_{AA}$  on  $\tau_D$  and  $T$  for finite Ehrenfest time. The explicit

dependence on temperature is characteristic for the interaction correction, which has its origin in virtual processes with an energy transfer larger than temperature.

Our calculation makes use of a semiclassical formalism that starts from the saddle-point approximation around classical trajectories for the single-particle Green function. In this way, the conductance in the absence of electron-electron interactions is written as a double sum over classical trajectories that connect source and drain reservoirs [Jala 90, Bara 93]. Weak localization and other quantum corrections to the conductance then follow from special configurations of trajectories, in which the two trajectories in the summation are piecewise paired, and proceed through “crossings” at points where the pairing is changed [Rich 02, Mull 07]. In the language of diagrammatic perturbation theory, segments where the trajectories are paired correspond to diffusons or cooperons, whereas the crossings correspond to Hikami boxes. The application to interacting electrons requires a modification of the formalism, which will be described in detail below.

Our analysis applies to a “ballistic” conductor, where the label “ballistic” is meant to specify that the electrons move along well-defined classical trajectories. In the literature, “ballistic” sometimes refers to a different limit, and several calculations of the interaction correction to the conductance have been reported for such “ballistic limits”. Whereas the original work of Altshuler and Aronov [Alts 79] addressed a disordered metal with short-range scatterers in the diffusive regime  $T\tau \ll 1$ , the theory was generalized to account for the effects of higher temperatures  $T\tau \gtrsim 1$ , a regime referred to as “ballistic” [Gold 86, Das 99, Zala 01]. The case of a smooth disorder potential, in which scattering is predominantly forward, was considered in Ref. [Gorn 04]. Another type of system, where interaction corrections appear, are networks of capacitively coupled ballistic quantum dots [Belo 03, Golu 04, Kupf 08], where, however, Ehrenfest-time-related phenomena can be neglected as long as  $\tau_E$  is much smaller than the dwell time in a single quantum dot. Interactions also affect the conductance through their effect on the weak localization correction (dephasing). Semiclassical studies of the effect of interaction-induced dephasing on weak localization can be found in Refs. [Yevt 00, Tian 07, Peti 07, Whit 08], for electronic systems and in Ref. [Hart 12] for bosonic matter waves.

## 5.2. Semiclassical theory of the interaction correction

In this section we present the semiclassical description of the interaction corrections for a conductor with a well-defined chaotic classical electron dynamics. We first review the expressions for the interaction corrections to the conductance in terms of the single-particle Green function, and then apply the semiclassical approximation methods, taking into account the finite Ehrenfest time.

### 5.2.1. Skeleton diagrams for the conductance

For definiteness, we consider a two-dimensional ballistic conductor, such as a ballistic electron gas with an antidot array, in contact with reservoirs at  $x = 0$  and  $x = L$ , see Fig. 5.1. Without interactions, we can calculate the conductance  $G$  from the Kubo formula

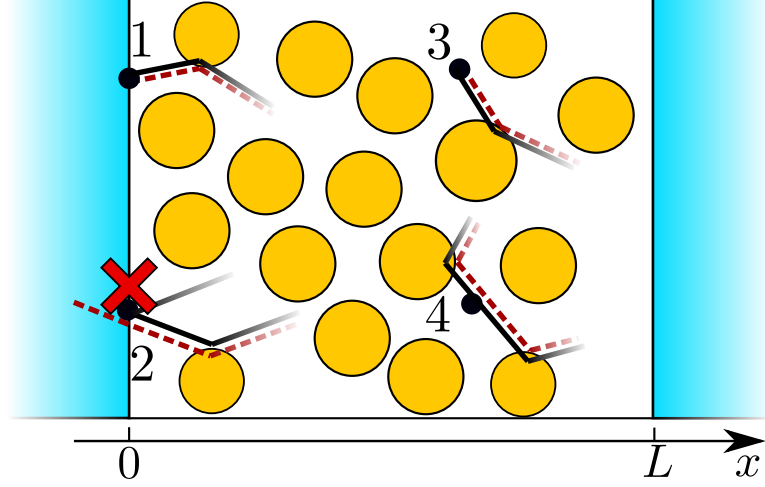


Figure 5.1.: Schematic picture of the system under consideration: A ballistic conductor, attached to ideal leads at  $x = 0$  and  $x = L$ . In the semiclassical calculation of the conductance, one retarded and one advanced Green function are attached to a current vertex located at the interface with the leads. In a semiclassical picture, these Green functions are associated with “retarded” and “advanced” classical trajectories (solid and dashed in the figure), both of which must point into the conductor (1). A current vertex combined with two Green functions of the same kind is not possible for the calculation of the conductance: after pairing, we have trajectories that go straight into the leads (2). On the contrary, for a calculation of the conductivity, the current vertex can be anywhere inside the conductor, and pairing of retarded and advanced trajectories is possible also if two Green functions of the same kind are attached to one current vertex (3 and 4).

[Akke 07],

$$G = \frac{e^2 \hbar}{\pi} \int dy \int dy' \int d\xi \left( -\frac{\partial f(\xi)}{\partial \xi} \right) [\hat{v}_x \mathcal{G}^R(\mathbf{r}, \mathbf{r}'; \xi) \hat{v}_{x'} \mathcal{G}^A(\mathbf{r}', \mathbf{r}; \xi)]_{x'=0}^{x=L}, \quad (5.2)$$

where  $f(\xi) = 1/(\exp(\xi/T) + 1)$  denotes the Fermi function,

$$\hat{v}_x = \frac{\hbar}{2mi} \left( \vec{\partial}_x - \overleftarrow{\partial}_x \right) \quad (5.3)$$

is the velocity operator, and  $\mathcal{G}^R(\mathbf{r}, \mathbf{r}'; \xi)$  and  $\mathcal{G}^A(\mathbf{r}, \mathbf{r}'; \xi)$  is the retarded and advanced single-particle Green function, respectively. Retarded and advanced Green functions are related as

$$\mathcal{G}^A(\mathbf{r}', \mathbf{r}; \xi) = \mathcal{G}^R(\mathbf{r}, \mathbf{r}'; \xi)^*. \quad (5.4)$$

To leading (first) order in the interaction strength, the interaction correction  $\delta G_{AA}$  is obtained by replacing  $\mathcal{G}^R(\mathbf{r}, \mathbf{r}'; \xi)$  by  $\mathcal{G}^R(\mathbf{r}, \mathbf{r}'; \xi) + \delta \mathcal{G}_F^R(\mathbf{r}, \mathbf{r}'; \xi) + \delta \mathcal{G}_H^R(\mathbf{r}, \mathbf{r}'; \xi)$  and expanding

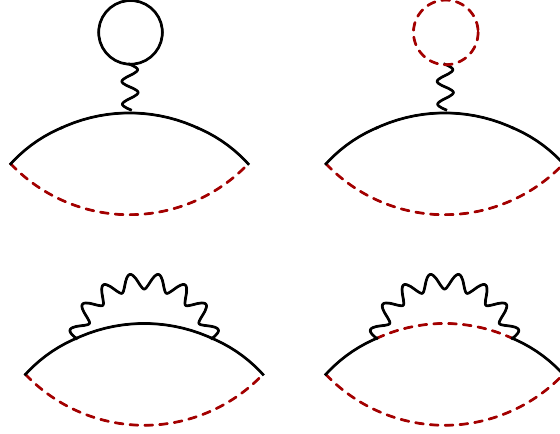


Figure 5.2.: Hartree (upper) and Fock (lower) diagrams: solid (dashed) lines represent retarded (advanced) Green functions, the wiggly line represents the interaction. Each diagram has a counterpart with retarded and advanced Green functions interchanged.

to first order in the interaction  $U$  [Alej 99, Zala 01, Brou 08], where

$$\begin{aligned} \delta\mathcal{G}_F^R(\mathbf{r}, \mathbf{r}'; \xi) &= \int \frac{d\omega}{4\pi i} \int d\mathbf{r}_1 d\mathbf{r}_2 \tanh\left(\frac{\omega - \xi}{2T}\right) \mathcal{G}^R(\mathbf{r}, \mathbf{r}_1; \xi) \mathcal{G}^R(\mathbf{r}_2, \mathbf{r}'; \xi) \\ &\times \{U^A(\mathbf{r}_1, \mathbf{r}_2; \omega) \mathcal{G}^R(\mathbf{r}_1, \mathbf{r}_2; \xi - \omega) - U^R(\mathbf{r}_1, \mathbf{r}_2; \omega) \mathcal{G}^A(\mathbf{r}_1, \mathbf{r}_2; \xi - \omega)\}, \end{aligned} \quad (5.5)$$

$$\begin{aligned} \delta\mathcal{G}_H^R(\mathbf{r}, \mathbf{r}'; \xi) &= -2 \int \frac{d\omega}{4\pi i} \int d\mathbf{r}_1 d\mathbf{r}_2 \tanh\left(\frac{\omega - \xi}{2T}\right) \mathcal{G}^R(\mathbf{r}, \mathbf{r}_1; \xi) \mathcal{G}^R(\mathbf{r}_1, \mathbf{r}'; \xi) \\ &\times \{U^A(\mathbf{r}_1, \mathbf{r}_2; 0) \mathcal{G}^R(\mathbf{r}_2, \mathbf{r}_2; \xi - \omega) - U^R(\mathbf{r}_1, \mathbf{r}_2; 0) \mathcal{G}^A(\mathbf{r}_2, \mathbf{r}_2; \xi - \omega)\}, \end{aligned} \quad (5.6)$$

and with similar expressions for the advanced functions  $\delta\mathcal{G}_F^A(\mathbf{r}', \mathbf{r}; \xi)$  and  $\delta\mathcal{G}_H^A(\mathbf{r}', \mathbf{r}; \xi)$ . In these expressions,  $U^R(\mathbf{r}_1, \mathbf{r}_2; \omega)$  and  $U^A(\mathbf{r}_1, \mathbf{r}_2; \omega)$  are the retarded and advanced interaction kernels, respectively. The interaction is taken to be zero in the leads, for  $x < 0$  and  $x > L$ . Such a structure represents the change of the single-particle Green function due to scattering off Friedel oscillations of the density matrix  $\rho(\mathbf{r}_1, \mathbf{r}_2)$  (Fock) or the density  $\rho(\mathbf{r}_2)$  (Hartree) [Zala 01]. The resulting contributions to  $\delta G_{AA}$  are represented diagrammatically as in Fig. 5.2.

We would like to emphasize that we kept here only those diagrams for which one retarded and one advanced Green function are connected to each current vertex. These are the relevant diagrams for the calculation of the conductance. This is in contrast to the calculation of the interaction correction to the conductivity  $\delta\sigma_{AA}$ , where diagrams with two Green functions of the same kind attached to the current vertex play an important role [Alts 79]. (The conductivity  $\sigma$  is expressed in a similar way as Eq. (5.2), but contains

integrals over the  $x$ -coordinates as well, rather than fixing them to the contacts at  $x = 0$  and  $x = L$ ). Although the structure of the calculation for conductance or conductivity considerably differs, the final results for these quantities are related by a geometrical factor only. In two dimensions, for a rectangular sample, one has  $G = \sigma \frac{W}{L}$ , where  $W$  is the width of the system.

The difference between the conductance calculation and the conductivity calculation is readily seen in the semiclassical language. In that language, Green functions are associated with classical trajectories, and only terms in which “retarded” and “advanced” trajectories are paired contribute. (For more details, see below). Since the leads are assumed to be free of disorder and without electron-electron interactions, both the retarded and the advanced trajectories at the positions  $\mathbf{r}$  and  $\mathbf{r}'$  in Eq. (5.2) must point into the conductor if the conductance is calculated. On the other hand, for a current vertex in the system’s interior, pairing of advanced and retarded trajectories is still possible even if two Green functions of the same kind are attached to the current vertex, see Fig. 5.1.

The fact that different diagrams are needed for the calculation of conductance and conductivity is well known, the same is true for the Drude conductance and conductance fluctuations of a disordered metal (see Ref. [Kane 88]). For instance, for the calculation of the Drude conductivity  $\sigma_0$  in a metal with short-ranged disorder there is no need to dress the diagram with an impurity ladder, while for the classical conductance  $G_0$ , the diagram dressed with an impurity ladder, i.e., a diffuson, is most relevant. For the Drude conductivity one might argue that the distance between the current vertices is of the order of the mean free path, since the two Green functions decay on this scale. The diffuson in turn is long-ranged, and hence needed to describe propagation from one lead to the other, as required for the conductance.

We also note that the calculation of the conductance as it is outlined here is similar to the calculation of the density-density correlation functions [Fink 83, Cast 84]. A subtle point in this regard is the existence of additional corrections in the calculation of the density-density correlation function, namely vertex corrections and the so-called wave-function renormalization. In the description developed below, both of them appear to vanish. For the density-density correlation function, in turn, vertex corrections and the wave function renormalization cancel each other, so that these corrections do not lead to a net change of the result in either case.

### 5.2.2. Semiclassical theory

The conductance  $G$  depends on the precise locations of antidots, the system boundary, and on the Fermi energy. We now employ a semiclassical analysis in order to identify those contributions to the conductance that remain after an average over the Fermi energy.

Starting point is the semiclassical expression of the Green function  $\mathcal{G}^R(\mathbf{r}, \mathbf{r}'; \xi)$  as a sum over classical trajectories  $\alpha$  from  $\mathbf{r}'$  to  $\mathbf{r}$  at energy  $\xi$  [Gutz 90],

$$\mathcal{G}^R(\mathbf{r}, \mathbf{r}'; \xi) = \frac{2\pi}{(2\pi i \hbar)^{3/2}} \sum_{\alpha} A_{\alpha} e^{i\mathcal{S}_{\alpha}/\hbar}. \quad (5.7)$$

Here,  $\mathcal{S}_{\alpha}(\mathbf{r}, \mathbf{r}'; \xi)$  is the classical action corresponding to the trajectory  $\alpha$ , which has the

properties

$$\frac{\partial \mathcal{S}_\alpha}{\partial \mathbf{r}} = \mathbf{p}_\alpha, \quad \frac{\partial \mathcal{S}_\alpha}{\partial \mathbf{r}'} = -\mathbf{p}'_\alpha, \quad (5.8)$$

and

$$\frac{\partial \mathcal{S}_\alpha}{\partial \xi} = \tau_\alpha, \quad (5.9)$$

where  $\mathbf{p}_\alpha$  and  $\mathbf{p}'_\alpha$  denotes the momentum at the end and beginning of  $\alpha$ , respectively, and  $\tau_\alpha$  is the duration of the trajectory. The stability amplitude  $A_\alpha$  is given by  $A_\alpha = \sqrt{|\det(D_\alpha)|}$ , with

$$D_\alpha = \begin{pmatrix} \frac{\partial^2 \mathcal{S}_\alpha}{\partial \mathbf{r}' \partial \mathbf{r}} & \frac{\partial^2 \mathcal{S}_\alpha}{\partial \mathbf{r}' \partial \xi} \\ \frac{\partial^2 \mathcal{S}_\alpha}{\partial \xi \partial \mathbf{r}} & \frac{\partial^2 \mathcal{S}_\alpha}{\partial \xi^2} \end{pmatrix}. \quad (5.10)$$

The semiclassical Green function further contains an additional phase-shift, the so-called Maslov index [Gutz 90], which we omitted because it does not play a role in our considerations. The semiclassical expression for advanced Green function follows from Eq. (5.4).

Using the semiclassical Green function (5.7) we express the interaction correction  $\delta G_{AA}$  as a fourfold sum over classical trajectories. We refer to these trajectories as “retarded” or “advanced”, depending on the type of the Green function that they originate from. The summation over classical trajectories can be simplified for a system with chaotic classical dynamics: In this case, the classical trajectory and hence the classical action depend very sensitively on the initial conditions. On the other hand, in the semiclassical limit  $\hbar \rightarrow 0$  only configurations of trajectories with sum of the actions of the “retarded” trajectories *systematically* equal to the sum of the actions of the “advanced” trajectories up to a difference  $\Delta \mathcal{S}$  of the order of  $\hbar$  contribute substantially to the conductance. This occurs only if the “retarded” and “advanced” trajectories are piecewise paired, whereby they can exchange “partners” only at a “small-angle encounter” [Rich 02], at which two pairs meet to within a phase-space distance of order  $\hbar^{1/2}$ .

For the remaining summation over trajectories, we use a sum rule that expresses the summation over trajectories  $\alpha$  between positions  $\mathbf{r}'$  and  $\mathbf{r}$  and at energy  $\xi$  in terms of an integral over the trajectory’s duration  $t$ , the initial and final momenta  $\mathbf{p}'$  and  $\mathbf{p}$ , as well as a “trajectory density”  $\rho_\xi(\mathbf{X}' \rightarrow \mathbf{X}; t)$  between the phase-space points  $\mathbf{X}' = (\mathbf{r}', \mathbf{p}')$  and  $\mathbf{X} = (\mathbf{r}, \mathbf{p})$  [Arga 95, Arga 96],

$$\sum_{\alpha: \mathbf{r}' \rightarrow \mathbf{r}; \xi} A_\alpha^2 f(\mathbf{p}'_\alpha, \mathbf{p}_\alpha, \tau_\alpha) = \int_0^\infty dt \int d\mathbf{p}'_\xi \int d\mathbf{p}_\xi \rho_\xi(\mathbf{X}' \rightarrow \mathbf{X}; t) f(\mathbf{p}', \mathbf{p}, t), \quad (5.11)$$

see App. C.1.1 for details. Here  $f$  is an arbitrary function. The initial point in phase space  $\mathbf{X}' = (\mathbf{r}', \mathbf{p}')$ , together with the Hamilton function  $H$  uniquely determines the classical trajectory, and after a time  $t$  this trajectory has reached the phase space point  $\mathbf{X}(t) = (\mathbf{r}(\mathbf{r}', \mathbf{p}'; t), \mathbf{p}(\mathbf{r}', \mathbf{p}'; t))$ . The trajectory density

$$\begin{aligned} \rho(\mathbf{X}' \rightarrow \mathbf{X}; t) &= \delta[\mathbf{X} - \mathbf{X}(t)] \\ &= \delta[\mathbf{r} - \mathbf{r}(\mathbf{r}', \mathbf{p}'; t)] \delta[\mathbf{p} - \mathbf{p}(\mathbf{r}', \mathbf{p}'; t)] \end{aligned} \quad (5.12)$$

selects then only those phase space points which are connected by a trajectory of duration  $t$ . At fixed energy  $\xi$ , the momentum integrations are restricted to the energy shell,  $d\mathbf{p}_\xi =$

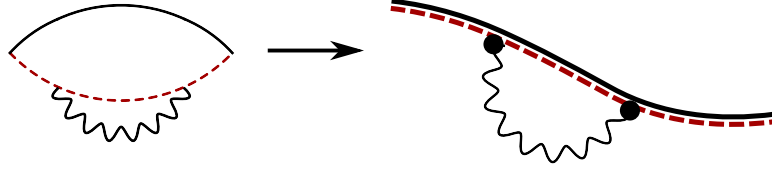


Figure 5.3.: Configuration of trajectories relevant for the first diagram to the Fock contribution.

$d\mathbf{p}\delta(\xi - H(\mathbf{p}, \mathbf{r}))$ , and for the trajectory density we may factor out the part which ensures energy conservation,

$$\rho(\mathbf{X}' \rightarrow \mathbf{X}; t) = \rho_\xi(\mathbf{X}' \rightarrow \mathbf{X}; t) \delta[H(\mathbf{X}) - H(\mathbf{X}')]. \quad (5.13)$$

The factor  $A_\alpha^2$  provides the Jacobian for this transformation.

Following the procedure outlined so far, we obtain an expression in terms of trajectory densities which, strictly speaking, is a sum of  $\delta$ -functions. We then replace the exact trajectory density  $\rho_\xi$  by a coarse-grained smooth density  $\bar{\rho}$  [Smil 92, Arga 93]. The coarse graining takes place with respect to small fluctuations of the initial and final phase space points and/or the positions of the scattering discs or the system's boundaries. In the regime  $\lambda\tau_D \gg 1$ , where the chaotic dynamics has fully developed, the classical dynamics is essentially stochastic, which justifies the coarse graining procedure. The coarse-grained trajectory density

$$\bar{\rho}_\xi(\mathbf{X}' \rightarrow \mathbf{X}; t) = P(\mathbf{X}, \mathbf{X}'; t) \quad (5.14)$$

can be identified with the probability density  $P(\mathbf{X}, \mathbf{X}'; t)$  that a particle originating at the phase space point  $\mathbf{X}' = (\mathbf{r}', \mathbf{p})$  is found at the phase space point  $\mathbf{X} = (\mathbf{r}, \mathbf{p})$  after a time  $t$ . (Since we are interested in the regime where temperature is much smaller than Fermi energy, we drop the dependence of the classical propagators on  $\xi$ .) For the case of antidot arrays, this probability density is described by a diffusion equation.

The Drude conductance is obtained by keeping only pairs of classical trajectories that connect source and drain reservoirs. Following the steps described above, we find

$$G_0 = \frac{e^2}{2\pi^2\hbar^2} \int_0^\infty dt \int dy dy' \int d\mathbf{p}_\xi d\mathbf{p}'_\xi [v_x P(\mathbf{X}, \mathbf{X}'; t) v'_x]_{x'=0}^{x=L} \quad (5.15)$$

We now turn to the semiclassical calculation for the interaction correction.

### 5.2.3. Fock contribution

We start with the Fock contribution to  $\delta G_{AA}$ , which is given by the two lower diagrams in Fig. 5.2, together with their counterparts, which are obtained by interchanging the retarded and advanced Green functions. We first consider the conductance correction



$\delta G_{AA}^{F,1}$  from the lower left diagram and its counterpart, which reads

$$\begin{aligned} \delta G_{AA}^{F,1} = & -\frac{e^2 \hbar}{\pi} \int d\xi \left( -\frac{\partial f(\xi)}{\partial \xi} \right) \int \frac{d\omega}{2\pi} \tanh \left( \frac{\omega - \xi}{2T} \right) \text{Im} \left\{ \int d\mathbf{r}_1 d\mathbf{r}_2 U^R(\mathbf{r}_1, \mathbf{r}_2; \omega) \right. \\ & \times \left. \int dy \int dy' [\hat{v}_x \mathcal{G}^R(\mathbf{r}, \mathbf{r}'; \xi) \hat{v}_{x'} \mathcal{G}^A(\mathbf{r}', \mathbf{r}_2; \xi) \mathcal{G}^A(\mathbf{r}_2, \mathbf{r}_1; \xi - \omega) \mathcal{G}^A(\mathbf{r}_1, \mathbf{r}; \xi)] \right\}_{x'=0}^{x=L}. \end{aligned} \quad (5.16)$$

After insertion of the semiclassical expression Eq. (5.7) for the Green functions, we obtain a sum over one retarded and three advanced trajectories. In the semiclassical limit, a convolution of Green functions is customarily calculated using the stationary phase approximation. For this one first needs to determine the configurations of trajectories which make the total action stationary. This results in a factor  $\propto e^{i\mathcal{S}_{\text{st}}}$ , where  $\mathcal{S}_{\text{st}}$  is obtained by inserting the stationary configuration into the total action. Integration over quadratic fluctuations around the stationary configurations then renders the prefactor. In the present case the convolution of Green functions is accompanied by the interaction propagator. One might expect, that the interaction propagator affects the stationary trajectories, such that they no longer connect to a single classical trajectory, as in the case without interaction. However for the calculation of the conductance, we need to pair the advanced trajectories with the retarded one, see Fig. 5.3. Hence, performing the integration over  $\mathbf{r}_1$  and  $\mathbf{r}_2$  in Eq. (5.16) within stationary phase approximation, we only take into account stationary configurations that connect to a single classical trajectory. The detailed calculation is carried out in Appendix C.1.2 and has the result

$$\begin{aligned} & \int d\mathbf{r}_1 d\mathbf{r}_2 \mathcal{G}^A(\mathbf{r}', \mathbf{r}_2; \xi) \mathcal{G}^A(\mathbf{r}_2, \mathbf{r}_1; \xi - \omega) \mathcal{G}^A(\mathbf{r}_1, \mathbf{r}; \xi) U^R(\mathbf{r}_1, \mathbf{r}_2; \omega) \\ = & -\frac{1}{\hbar^2} \frac{2\pi}{(-2\pi i \hbar)^{3/2}} \sum_{\alpha: \mathbf{r}' \rightarrow \mathbf{r}; \xi} A_\alpha e^{-i\mathcal{S}_\alpha/\hbar} \int_0^{\tau_\alpha} dt \int_0^t dt' U^R(\mathbf{r}_\alpha(t), \mathbf{r}_\alpha(t'); \omega) e^{i\omega(t-t')/\hbar}, \end{aligned} \quad (5.17)$$

where  $\mathbf{r}_\alpha(t)$  is the coordinate of trajectory  $\alpha$  after time  $t$ . The integration over time reflects the freedom to choose  $\mathbf{r}_1$  and  $\mathbf{r}_2$  anywhere along the trajectory  $\alpha$ ; the factor  $e^{i\omega(t-t')/\hbar}$  takes into account the action difference at different energies,  $\mathcal{S}_\alpha(\xi - \omega) = \mathcal{S}_\alpha(\xi) - \omega\tau_\alpha$  (for  $\omega \ll \xi$ ). With  $\mathbf{X}_\alpha(t) = (\mathbf{r}_\alpha(t), \mathbf{p}_\alpha(t))$  we may rewrite

$$U^R(\mathbf{r}_\alpha(t), \mathbf{r}_\alpha(t'); \omega) = \int d\mathbf{X}_1 d\mathbf{X}_2 \rho_\xi(\mathbf{X}'_\alpha \rightarrow \mathbf{X}_1; t) \rho_\xi(\mathbf{X}'_\alpha \rightarrow \mathbf{X}_2; t') U^R(\mathbf{r}_1, \mathbf{r}_2; \omega), \quad (5.18)$$

where  $d\mathbf{X} = d\mathbf{r} d\mathbf{p}_\xi$  is an integration over phase-space points on the energy shell, and  $\mathbf{X}'_\alpha = \mathbf{X}_\alpha(0)$  is the initial phase-space point of trajectory  $\alpha$ .

After inserting Eqs. (5.17) and (5.18) into Eq. (5.16), and upon applying the semiclassical approximation to the retarded Green function as well, the interaction correction  $\delta G_{AA}^{F,1}$  is expressed as a double sum over trajectories  $\alpha$  and  $\beta$  running from  $\mathbf{r}'$  to  $\mathbf{r}$ . Only diagonal terms with  $\alpha = \beta$  are systematically nonzero, so that we only keep these. Again making use of the sum rule (Eq. (5.11)) we express  $\delta G_{AA}^{F,1}$  as an integral over the two intermediate phase space points  $\mathbf{X}_1$  and  $\mathbf{X}_2$ . Before the exact trajectory densities can be replaced by

### 5. Semiclassical theory of the interaction correction to the conductance of antidot arrays

their coarse-grained versions, we split the classical trajectories into uncorrelated segments using the equality

$$\begin{aligned} & \int_0^\infty dt \int_0^t dt' \rho_\xi(\mathbf{X}_0 \rightarrow \mathbf{X}_1; t) \rho_\xi(\mathbf{X}_0 \rightarrow \mathbf{X}_2; t') \\ &= \int_0^\infty dt_1 \rho_\xi(\mathbf{X}_0 \rightarrow \mathbf{X}_2; t_1) \int_0^\infty dt_2 \rho_\xi(\mathbf{X}_2 \rightarrow \mathbf{X}_1; t_2). \end{aligned} \quad (5.19)$$

After coarse-graining, the expression for  $\delta G_{\text{AA}}^{\text{F},1}$  involves the probability densities  $P(\mathbf{X}_1 \rightarrow \mathbf{X}_2; t)$  for the chaotic classical motion. The expression can be further simplified by introducing

$$\begin{aligned} P_{\text{in}}(\mathbf{X}) &= \int dy' \int d\mathbf{p}'_\xi \int_0^\infty dt [v'_x P(\mathbf{r}', \mathbf{p}' \rightarrow \mathbf{X}; t)]_{x'=0}, \\ P_{\text{out}}(\mathbf{X}) &= \int dy \int d\mathbf{p}_\xi \int_0^\infty dt [P(\mathbf{X} \rightarrow \mathbf{r}, \mathbf{p}; t) v_x]_{x=L}, \end{aligned} \quad (5.20)$$

which express the probability that a trajectory at phase space point  $\mathbf{X}$  entered at the left contact or exits at the right contact, respectively. Using the equality

$$\int d\xi \left( -\frac{\partial f(\xi)}{\partial \xi} \right) \tanh \left( \frac{\omega - \xi}{2T} \right) = \frac{\partial}{\partial \omega} \left( \omega \coth \frac{\omega}{2T} \right) \quad (5.21)$$

we finally obtain

$$\delta G_{\text{AA}}^{\text{F},1} = \frac{e^2}{4\pi^3 \hbar^4} \int d\omega \frac{\partial}{\partial \omega} \left( \omega \coth \frac{\omega}{2T} \right) \text{Im} \left\{ \int d\mathbf{X}_1 d\mathbf{X}_2 U^{\text{R}}(\mathbf{r}_1, \mathbf{r}_2; \omega) K^1(\mathbf{X}_1, \mathbf{X}_2; \omega) \right\}, \quad (5.22)$$

where we singled out the part containing classical propagators,

$$K^1(\mathbf{X}_1, \mathbf{X}_2; \omega) = \int_0^\infty dt P_{\text{out}}(\mathbf{X}_1) P(\mathbf{X}_1, \mathbf{X}_2; t) e^{i\omega t/\hbar} P_{\text{in}}(\mathbf{X}_2). \quad (5.23)$$

We now consider the interaction correction  $\delta G_{\text{AA}}^{\text{F},2}$  that corresponds to the lower right diagram of Fig. 5.2 and its counterpart obtained by switching retarded and advanced labels,

$$\begin{aligned} \delta G_{\text{AA}}^{\text{F},2} &= -\frac{e^2 \hbar}{\pi} \int d\xi \left( -\frac{\partial f(\xi)}{\partial \xi} \right) \int \frac{d\omega}{2\pi} \tanh \left( \frac{\omega - \xi}{2T} \right) \text{Im} \left\{ \int d\mathbf{r}_1 d\mathbf{r}_2 U^{\text{R}}(\mathbf{r}_1, \mathbf{r}_2, \omega) \right. \\ &\quad \times \left. \int dy \int dy' [\hat{v}_x \mathcal{G}^{\text{R}}(\mathbf{r}, \mathbf{r}_1; \xi) \mathcal{G}^{\text{A}}(\mathbf{r}_1, \mathbf{r}_2; \xi - \omega) \mathcal{G}^{\text{R}}(\mathbf{r}_2, \mathbf{r}'; \xi) \hat{v}_{x'} \mathcal{G}^{\text{A}}(\mathbf{r}', \mathbf{r}; \xi)] \right\}_{x'=0, x=L}. \end{aligned} \quad (5.24)$$

Insertion of the semiclassical expression for the Green functions leads to a fourfold sum over two retarded trajectories (from  $\mathbf{r}'$  to  $\mathbf{r}_2$  and from  $\mathbf{r}_1$  to  $\mathbf{r}$ ), and two advanced trajectories (from  $\mathbf{r}'$  to  $\mathbf{r}$  and from  $\mathbf{r}_1$  to  $\mathbf{r}_2$ ).

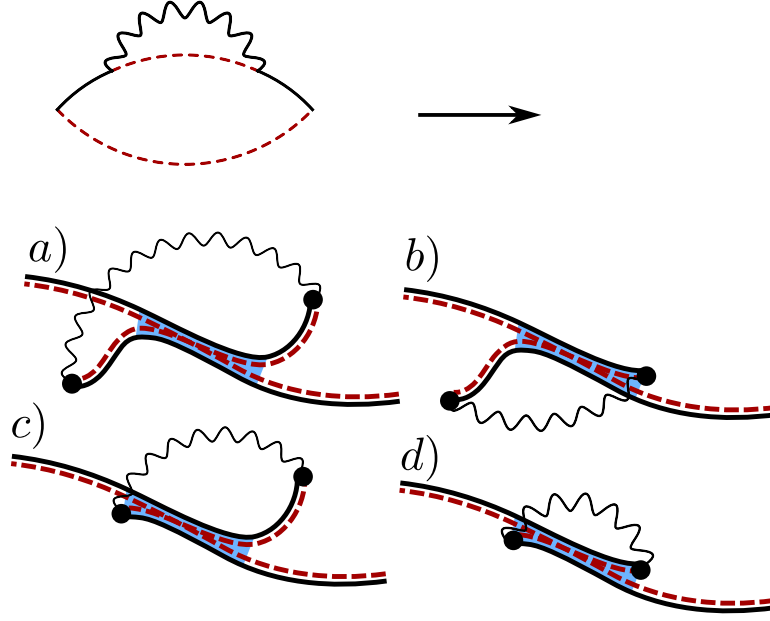


Figure 5.4.: Configurations of trajectories relevant for the second diagram to the Fock contribution. Encounter regions are indicated in blue; here the motion of all four trajectories is correlated.

Because of the specific requirements for the start and end points of the trajectories, it is not possible, to pair the trajectories one by one for their entire duration. Instead, the trajectories need to undergo a “small-angle encounter”, in which all four trajectories are close together in phase space for at least part of their length [Rich 02]. The four possible configurations of trajectories are shown in Fig. 5.4, where we take into account the possibilities that none, one, or both points  $\mathbf{r}_1$  and  $\mathbf{r}_2$  lie inside the encounter region. Their contributions to  $\delta G_{AA}$  will be denoted  $\delta G_{AA}^{\text{F},2a} - \delta G_{AA}^{\text{F},2d}$ , see Fig. 5.4.

The summation over classical trajectories with a small-angle encounter follows the procedure outlined in Refs. [Mull 07, Brou 07]. We refer the reader to appendix C.1.3 for details, and proceed with the results of that calculation. All four contributions to  $\delta G_{AA}$  have the same form as the contribution from the first diagram, see Eq. (5.22), but with different expressions for the function  $K(\mathbf{X}_1, \mathbf{X}_2; \omega)$ . For the contributions 2a–2d these

expressions read

$$K^{2a} = - \int d\mathbf{X} d\mathbf{X}' P_{\text{in}}(\mathbf{X}) P(\mathbf{X}, \mathbf{X}_1; \omega) P(\mathbf{X}_2, \mathbf{X}'; \omega) P_{\text{out}}(\mathbf{X}') \times \frac{\partial}{\partial \tau_E} \left[ P(\mathbf{X}', \mathbf{X}; \tau_E) e^{i\omega \tau_E / \hbar} \right], \quad (5.25)$$

$$K^{2b} = - \int d\mathbf{X} P_{\text{in}}(\mathbf{X}) P(\mathbf{X}, \mathbf{X}_1; \omega) P_{\text{out}}(\mathbf{X}_2) P(\mathbf{X}_2, \mathbf{X}; \tau_E) e^{i\omega \tau_E / \hbar}, \quad (5.26)$$

$$K^{2c} = - \int d\mathbf{X}' P_{\text{in}}(\mathbf{X}_1) P(\mathbf{X}_2, \mathbf{X}'; \omega) P_{\text{out}}(\mathbf{X}') P(\mathbf{X}', \mathbf{X}_1; \tau_E) e^{i\omega \tau_E / \hbar}, \quad (5.27)$$

$$K^{2d} = - \int_0^{\tau_E} dt P_{\text{in}}(\mathbf{X}_1) P(\mathbf{X}_2, \mathbf{X}_1; t) e^{i\omega t / \hbar} P_{\text{out}}(\mathbf{X}_2). \quad (5.28)$$

Here  $P(\mathbf{X}, \mathbf{X}'; \omega)$  is the Fourier transform of  $P(\mathbf{X}, \mathbf{X}'; t)$ ,

$$P(\mathbf{X}, \mathbf{X}'; \omega) = \int_0^{\infty} dt P(\mathbf{X}, \mathbf{X}'; t) e^{i\omega t / \hbar}. \quad (5.29)$$

Taken together, Eqs. (5.22), (5.23), (5.25), (5.26), (5.27), and (5.28) determine the general result for the Fock contribution to  $\delta G_{AA}$  for finite Ehrenfest time, expressed in terms of classical propagators.

Let us briefly discuss the effect of the Ehrenfest time: Interestingly, the contribution  $K^1$  does not involve a crossing and therefore shows no dependence on the Ehrenfest time. However, it is cancelled by the contribution  $K^{2d}$ , if the travel time between  $\mathbf{X}_1$  and  $\mathbf{X}_2$  is shorter than the Ehrenfest time. Thus, adding all contributions together, we indeed find, that effectively only trajectories with a duration longer than the Ehrenfest time are responsible for the interaction correction.

#### 5.2.4. Hartree contribution

The Hartree contribution to the Altshuler-Aronov correction is given by the two upper diagrams in Fig. 5.2. Proceeding as in the case of the Fock contribution, each Green function is written as a sum over classical trajectories, which must then be pairwise paired in order to give a nonvanishing contribution to the interaction correction to the conductance. The resulting configurations of classical trajectories are shown schematically in Fig. 5.5. The trajectory configurations of Fig. 5.5 are in one-to-one correspondence to those of Figs. 5.3 and 5.4 for the Fock contribution to  $\delta G_{AA}$ : The diagram of Fig. 5.5a corresponds to that of Fig. 5.3, whereas the diagrams of Fig. 5.5b–e correspond to those of Fig. 5.4a–d.

Unlike the Fock diagrams, all diagrams for the Hartree correction involve a finite-angle crossing of the trajectories, in addition to the small-angle encounter of Figs. 5.5b–e. Another important difference is that the action difference  $\Delta S$  for the Hartree case depends on the two positions  $\mathbf{r}_1$  and  $\mathbf{r}_2$  associated with the interaction vertex. Denoting the momenta involved in the finite-angle crossing of the trajectories by  $\mathbf{p}_1$  and  $\mathbf{p}_2$ , see Fig. 5.5, the action difference contributes an additional oscillating phase factor  $e^{i(\mathbf{r}_1 - \mathbf{r}_2) \cdot (\mathbf{p}_1 - \mathbf{p}_2) / \hbar}$ . (No fast oscillating phase factors are associated with the integration over  $\mathbf{r}_1$  and  $\mathbf{r}_2$  for

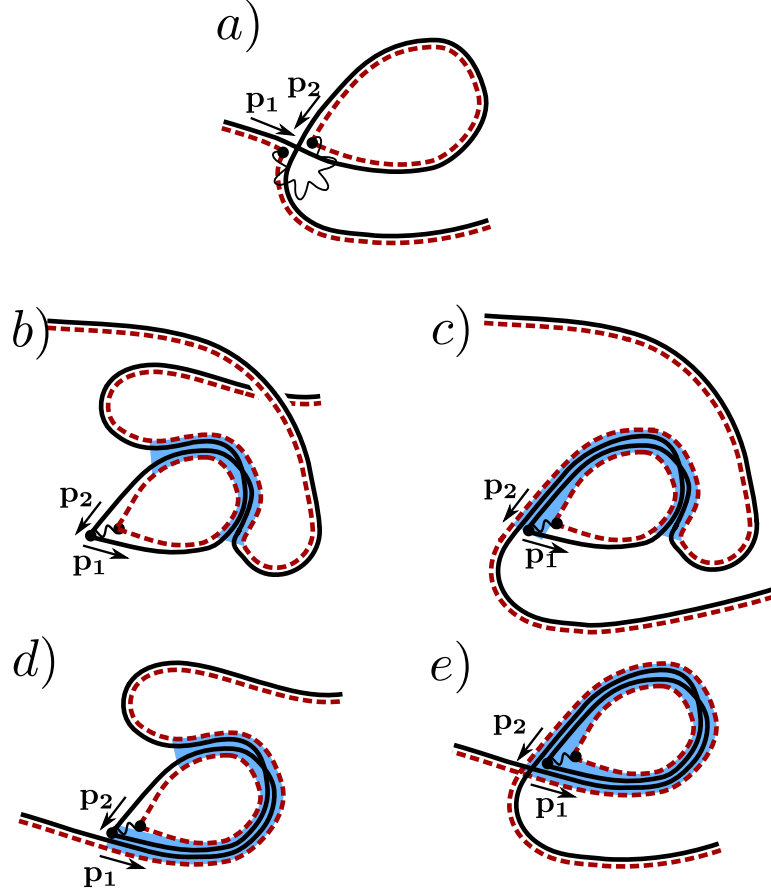


Figure 5.5.: Configurations of classical trajectories that give the Hartree contribution to the interaction correction  $\delta G_{AA}$ . The configurations in parts b–e contain a small-angle encounter, indicated in blue. All five configurations also contain a crossing of the classical trajectories. The momenta associated with the crossing are denoted  $\mathbf{p}_1$  and  $\mathbf{p}_2$ .

the Fock diagrams.) For chaotic classical motion, the directions of the momenta  $\mathbf{p}_1$  and  $\mathbf{p}_2$  are random and uncorrelated, while the magnitude  $|\mathbf{p}_1| = |\mathbf{p}_2| = p_F$  is fixed by energy conservation. As a result, only a short-range component of the interaction contributes to the Hartree correction, and one finds the same expression for  $\delta G_{AA}$  as for the Fock contribution, with the replacement [Alts 79]

$$U^R(\mathbf{r}_1 - \mathbf{r}_2; \omega) \rightarrow -2\delta(\mathbf{r}_1 - \mathbf{r}_2) \left\langle \int d\mathbf{r} e^{i\mathbf{r} \cdot (\mathbf{p}_1 - \mathbf{p}_2)/\hbar} U^R(\mathbf{r}; \omega = 0) \right\rangle_{\mathbf{p}_1, \mathbf{p}_2}, \quad (5.30)$$

where the brackets  $\langle \dots \rangle$  indicate an average over the momenta  $\mathbf{p}_1$  and  $\mathbf{p}_2$  with  $|\mathbf{p}_1| = |\mathbf{p}_2| = p_F$ . In case of a short-range interaction  $U(\mathbf{r}_1, \mathbf{r}_2) \propto \delta(\mathbf{r}_1 - \mathbf{r}_2)$ , one verifies that this replacement rule leads to  $\delta G_{AA}^H = -2\delta G_{AA}^F$ , in agreement with Eqs. (5.5) and (5.6).

Intuitively, the interaction correction associated with the trajectory configurations of Fig. 5.5 can be interpreted as the interference of electrons that follow a classical trajectory connecting source and drain contacts, and electrons that additionally scatter from Friedel oscillations [Rudi 97, Zala 01, Alei 99]. In the configuration of Fig. 5.5a the trajectory that contains the scattering from the Friedel oscillation is shorter than that of the reference trajectory, whereas it is longer in the configurations of Figs. 5.5b–e. The phase difference between the scattered trajectory and the reference trajectory is precisely compensated by the phase of the Friedel oscillation [Alei 99]. A similar interpretation applies to the Fock contribution, although here the scattering is from Friedel oscillations of the density matrix, not of the electron density itself.

### 5.2.5. Coulomb interaction

For the Coulomb interaction  $U_C(\mathbf{r}_1, \mathbf{r}_2) = e^2/|\mathbf{r}_1 - \mathbf{r}_2|$ , due to the long-range nature, it is never sufficient to deal with the first order in perturbation theory only, and effects of dynamical screening have to be included. Hence it is not sufficient to consider only diagrams with a single bare interaction line as in Fig. 5.2; instead one has to sum up a ladder of diagrams within the Random Phase Approximation (RPA). This analysis is explained in Refs. [Fink 83, Alts 83, Zala 01, Gorn 04] and it can be carried over to the semiclassical formalism without significant modifications.

For the purpose of including higher order interaction contributions, the separation into Hartree and Fock contributions is no longer meaningful. Instead, it is favorable to decompose the interaction into singlet and triplet channels. Hereto, we consider the interaction amplitude of a scattering process, where two particles with initial momenta  $\mathbf{p}_1$  ( $\mathbf{p}_2$ ) and spin  $\alpha$  ( $\gamma$ ) interact and depart with final momenta  $\mathbf{p}_1 + \mathbf{q}$  ( $\mathbf{p}_2 - \mathbf{q}$ ) and spin  $\beta$  ( $\delta$ ). Since in the semiclassical theory of transport only paired trajectories are relevant, we may restrict our analysis to the case  $|\mathbf{q}| \ll p_F$ . The classification into singlet ( $j = 0$ ) and triplet part ( $j = 1$ ) then amounts to separating the interaction amplitude according to its spin structure as

$$U_{\alpha\beta\gamma\delta} = U^{(j=0)}\delta_{\alpha\beta}\delta_{\gamma\delta} + U^{(j=1)}\sum_i \sigma_{\alpha\beta}^i \sigma_{\gamma\delta}^i, \quad (5.31)$$

where  $\sigma^i$  represents the Pauli-matrices ( $i = x, y, z$ ). To lowest order, the interaction amplitude consists of the scattering processes shown in Fig. 5.6. Here, in the left process

the interaction transfers a small momentum  $\mathbf{q}$ . Such small-angle scattering appears in the Fock contribution to the interaction correction. The spin structure of this process belongs to the singlet channel. The right process allows for large-angle scattering, which appears in the Hartree contribution to the interaction correction. This process has to be split into singlet and triplet contribution, so that we end up with

$$U_0^{(j=0)}(\mathbf{q}) = U_C(\mathbf{q}) - \frac{1}{2} \langle U_C(\mathbf{p}_1 - \mathbf{p}_2) \rangle_{|\mathbf{p}_1|=|\mathbf{p}_2|=p_F}, \quad (5.32)$$

$$U_0^{(j=1)}(\mathbf{q}) = -\frac{1}{2} \langle U_C(\mathbf{p}_1 - \mathbf{p}_2) \rangle_{|\mathbf{p}_1|=|\mathbf{p}_2|=p_F}. \quad (5.33)$$

Here we anticipated, that for a diffusive system we may average over the directions of the momenta of the electrons. To include screening, one then sums up the RPA-series in each channel,

$$U^{(j)}(\mathbf{q}, \omega) = U_0^{(j)}(\mathbf{q}) - U_0^{(j)}(\mathbf{q}) \Pi(\mathbf{q}, \omega) U^{(j)}(\mathbf{q}, \omega) \quad (5.34)$$

where the disorder-averaged polarization operator  $\Pi$  is diagonal in spin space (note, that the disorder average of the polarization operator does not involve a crossing, and therefore has no  $\tau_E$ -dependence).

The discussion so far is valid for weak interaction (i.e. interaction parameter  $r_s \ll 1$ ). For stronger interactions, one should also include Fermi liquid effects. Then the structure of the screened interaction remains the same, but the bare interaction is now expressed in terms of Fermi-liquid parameters  $F_0^{\rho, \sigma}$ ,

$$U_0^{(j=0)}(\mathbf{q}) = U_C(\mathbf{q}) + \frac{1}{2\nu} F_0^\rho, \quad U_0^{(j=1)}(\mathbf{q}) = \frac{1}{2\nu} F_0^\sigma. \quad (5.35)$$

Let's turn back to the Altshuler-Aronov correction. Applying the preceding analysis, we find that Coulomb interaction is properly included, if we calculate the Fock-type diagrams as in Fig. 5.2, where the interaction is replaced by the effective interaction

$$U(\mathbf{r}_1, \mathbf{r}_2; \omega) = U^{(j=0)}(\mathbf{r}_1, \mathbf{r}_2; \omega) + 3U^{(j=1)}(\mathbf{r}_1, \mathbf{r}_2; \omega), \quad (5.36)$$

where the factor 3 comes from the spin summation and accounts for the multiplicity of the triplet channel. The precise relation between  $U(\mathbf{r}_1, \mathbf{r}_2; \omega)$  and  $U(\mathbf{q}; \omega)$  follows from the solution of the diffusion equation and will be clarified in the next section (see Eq. (5.59)).

### 5.3. Interaction correction for antidot arrays

In the preceding Section, we developed the semiclassical theory of the interaction correction to the conductance, where we expressed our final results in terms of the classical propagator  $P(\mathbf{X}, \mathbf{X}', t)$ . The explicit expression of this classical propagator is determined by the geometry of the system under consideration. In semiclassical studies, two prototypical geometries are mainly investigated: ballistic quantum dots, where the classical chaotic motion results from reflections at the boundary of the dot, and antidot arrays, where the placement of artificial macroscopic scatterers leads to a chaotic dynamics. For a single ballistic quantum dot, the interaction correction vanishes. The simplest example of a

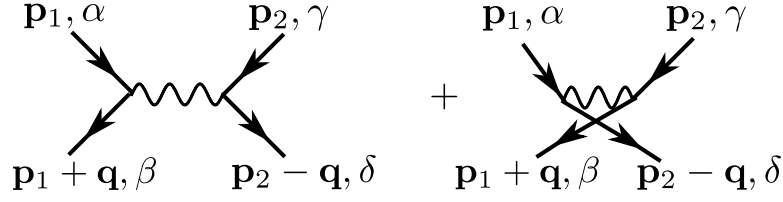


Figure 5.6.: Lowest order scattering processes of two particles with initial momenta  $\mathbf{p}_1$  ( $\mathbf{p}_2$ ) and spin  $\alpha$  ( $\gamma$ ), and final momenta  $\mathbf{p}_1 + \mathbf{q}$  ( $\mathbf{p}_2 - \mathbf{q}$ ) and spin  $\beta$  ( $\delta$ ). Since the interaction conserves spin, the left process is proportional to  $\delta_{\alpha\beta}\delta_{\gamma\delta}$  and belongs to the singlet channel, while the right process has the structure  $\delta_{\alpha\delta}\delta_{\beta\gamma} = \frac{1}{2}(\delta_{\alpha\beta}\delta_{\gamma\delta} + \sum_i \sigma_{\alpha\beta}^i \sigma_{\gamma\delta}^i)$  and therefore splits into singlet and triplet contribution.

geometry with a non-zero interaction correction is hence a double quantum dot, which was studied in Ref. [Brou 08]. We will first show, how the results of the previous Section are connected to the results of this reference. The remaining part of this section is then devoted to the interaction correction for antidot arrays, which has not been theoretically studied so far.

### 5.3.1. Double dot

We consider a double dot system, where two identical dots are connected by a ballistic contact of conductance  $G_c$ . The first (second) dot is connected to the left (right) reservoir by a ballistic contact of conductance  $G_d$ . The level density (i.e. the density of states times the dot's area) for each dot is  $N$  per spin. Within each dot, the phase space is explored uniformly during the chaotic motion. Hence we might replace the integration over phase space by a sum over the dots,

$$\int d\mathbf{X} = \sum_i \Omega_i, \quad (5.37)$$

where we weigh with the available phase space volume  $\Omega_1 = \Omega_2 = (2\pi\hbar)^2 N$  of each dot. The classical propagators are replaced by

$$P(\mathbf{X} \leftarrow \mathbf{X}'; t) = \frac{1}{\Omega_j} P(j \leftarrow i; t). \quad (5.38)$$

The probability  $P(j \leftarrow i; t)$  to be in dot  $j$  after a time  $t$ , when the particle initially started in dot  $i$ , is then calculated from the master equation

$$\partial_t P(j \leftarrow i; t) = - \sum_m \gamma_{jm} P(m \leftarrow i; t), \quad (5.39)$$

where the rate matrix  $\gamma$  has the form

$$\gamma = \begin{pmatrix} \gamma_L + \gamma_{12} & -\gamma_{12} \\ -\gamma_{12} & \gamma_R + \gamma_{12} \end{pmatrix}. \quad (5.40)$$



Here,  $\gamma_{12} = G_c/2Ne^2$  is the rate for transitions between the dots, and  $\gamma_L = \gamma_R = G_d/2Ne^2$  is the rate for escape to the left and right lead. The solution to Eq. (5.39) reads

$$P(j \leftarrow i; t) = (e^{-\gamma t})_{ji}. \quad (5.41)$$

The probability  $P_{\text{in}}$  ( $P_{\text{out}}$ ), that a particle in dot  $i$  has entered via the left contact (leaves the system via the right contact) is given by

$$P_{\text{in}}(i) = \gamma_L (\gamma^{-1})_{1i}, \quad P_{\text{out}}(i) = \gamma_R (\gamma^{-1})_{2i}. \quad (5.42)$$

The bare interaction of the double dot system can be described by a capacitive coupling of the dots

$$U_0 = \frac{e^2}{C}, \quad C = \begin{pmatrix} C_0 + C_c & -C_c \\ -C_c & C_0 + C_c \end{pmatrix}, \quad (5.43)$$

where  $C_0$  describes the coupling of each dot to an external gate, and  $C_c$  is the cross-capacitance between the dots. For the inclusion of screening, we make use of the polarization operator

$$\Pi_{ij}(\omega) = 2N (\delta_{ij} + \frac{i\omega}{\hbar} P(j \leftarrow i; \omega)), \quad (5.44)$$

from which we obtain the dynamically screened interaction as

$$U^{-1}(\omega) = U_0^{-1} + \Pi(\omega). \quad (5.45)$$

For the frequencies of interest one may neglect the first term in this equation, and one obtains

$$U_{ij}(\omega) = \frac{1}{2N} (1 - \frac{i\omega}{\hbar} \gamma^{-1})_{ij}. \quad (5.46)$$

Using the expressions of this paragraph and the Eqs. (5.22), (5.23), (5.25), (5.26), (5.27), and (5.28) from the last section, one obtains, after some algebra, the result from Ref. [Brou 08],

$$\begin{aligned} \delta G_{AA} = & -\frac{e^2}{2\pi\hbar} \frac{G_d G_c^2 (\tau_{D-} e^{-\tau_E/\tau_{D+}} + \tau_{D+} e^{-\tau_E/\tau_{D-}})}{(G_d + 2G_c)^3} \\ & \times \text{Im} \int \frac{d\omega}{\hbar} \frac{e^{i\omega\tau_E/\hbar} \partial_\omega (\omega \coth \frac{\omega}{2T})}{(1 - i\omega\tau_{D+}/\hbar)(1 - i\omega\tau_{D-}/\hbar)}. \end{aligned} \quad (5.47)$$

Here,  $\tau_{D+} = 2Ne^2/G_d$  and  $\tau_{D-} = 2Ne^2/(G_d + 2G_c)$  are the characteristic dwell times of the double dot system (they refer to relaxation of (anti)symmetric charge configurations). For zero Ehrenfest time, one recovers the results known from Random Matrix Theory, while for large Ehrenfest times,  $\delta G_{AA}$  is suppressed as  $e^{-\tau_E/\tau_{D\pm} - 2\pi\tau_E T/\hbar}$  (for more details, see Ref. [Brou 08], where the stated results are too large by a factor of two). We note, that the Hartree contribution is zero in this case, due to the long-range nature of interaction.

### 5.3.2. Antidot arrays

In the following, we now apply the theory developed in Section 5.2 to quasi one-dimensional and two-dimensional antidot arrays. The antidot arrays consist of a ballistic electron gas

with randomly placed disc-shaped scatterers of size much larger than the Fermi wavelength. The classical dynamics in such an antidot array is chaotic, and diffusive on length scales much larger than the disc size  $a$  or the distance between discs. In particular, since the Ehrenfest time  $\tau_E = \lambda^{-1} \ln(a/\lambda_F) \gg \lambda^{-1}$  because of the large logarithm, and since  $\lambda^{-1}$  is comparable to the transport time  $\tau$ , the diffusive dynamics applies for timescales down to  $\tau_E$ .

A diffusively moving particle quickly loses its memory about the direction of motion, so that the classical propagators  $P(\mathbf{X}, \mathbf{X}'; t)$  depend on the positions  $\mathbf{r}$  and  $\mathbf{r}'$  associated with the phase space points  $\mathbf{X}$  and  $\mathbf{X}'$  only. This leads to significant simplifications of the general semiclassical expressions for the interaction correction  $\delta G_{AA}$ . In order to evaluate  $\delta G_{AA}$  in this limit, we start by expressing the integration over momentum at fixed energy as an integration over the corresponding angle  $\phi$ ,

$$d\mathbf{p}_\xi = (2\pi\hbar)^2 \nu \frac{d\phi}{2\pi}, \quad (5.48)$$

where  $\nu$  is the density of states per spin. We then find

$$P(\mathbf{X}, \mathbf{X}'; t) = \frac{1}{(2\pi\hbar)^2 \nu} P(\mathbf{r}, \mathbf{r}'; t), \quad (5.49)$$

where  $P(\mathbf{r} \rightarrow \mathbf{r}'; t)$  depends on the positions only and satisfies a diffusion equation,

$$(\partial_t - D\Delta_{\mathbf{r}})P(\mathbf{r}, \mathbf{r}'; t) = \delta(t)\delta(\mathbf{r} - \mathbf{r}'), \quad (5.50)$$

with diffusion coefficient  $D$ . For a rectangular sample of dimension  $L \times W$ , coupled to ideal leads at  $x = 0$  and  $x = L$  and with insulating boundaries at  $y = 0$  and  $y = W$ , the solution of Eq. (5.50) reads

$$P(\mathbf{r}, \mathbf{r}'; t) = \theta(t) \sum_{\mathbf{q}} \psi_{\mathbf{q}}(\mathbf{r}) \psi_{\mathbf{q}}(\mathbf{r}') e^{-D\mathbf{q}^2 t}, \quad (5.51)$$

with the function

$$\psi_{\mathbf{q}}(\mathbf{r}) = \sqrt{\frac{4}{LW}} \sin(q_x x) \times \begin{cases} 1/\sqrt{2} & \text{if } q_y = 0, \\ \cos(q_y y) & \text{if } q_y \neq 0. \end{cases} \quad (5.52)$$

The sum over  $\mathbf{q}$  runs over  $q_x = \frac{n\pi}{L}$  with  $n = 1, 2, \dots$  and  $q_y = \frac{m\pi}{W}$  with  $m = 0, 1, \dots$ . We also use the Fourier-transformed diffusion propagator,

$$P(\mathbf{r}, \mathbf{r}'; \omega) = \sum_{\mathbf{q}} \frac{\psi_{\mathbf{q}}(\mathbf{r}) \psi_{\mathbf{q}}(\mathbf{r}')}{D\mathbf{q}^2 - i\omega/\hbar}. \quad (5.53)$$

Finally, the probabilities  $P_{\text{in}}(\mathbf{r})$  and  $P_{\text{out}}(\mathbf{r})$  that a trajectory originating at position  $\mathbf{r}$  exits the sample on the left or on the right, respectively, are

$$P_{\text{out}}(\mathbf{r}) = \frac{x}{L}, \quad P_{\text{in}}(\mathbf{r}) = \frac{L-x}{L}, \quad (5.54)$$

which may be derived from the diffusive flux

$$j_x(\mathbf{r}, \mathbf{r}'; t) = -D \partial_x P(\mathbf{r}, \mathbf{r}'; t), \quad (5.55)$$

at position  $\mathbf{r}$  and time  $t$ , for a particle starting from  $\mathbf{r}'$  at time  $t = 0$ . The Drude conductance (Eq. (5.15)) is then expressed as

$$G_0 = \frac{e^2}{2\pi^2 \hbar^2} \int dy \int d\mathbf{p}_\xi [-D \partial_x P_{\text{in}}(x)]_{x=L} \quad (5.56)$$

which gives the familiar result

$$G_0 = 2e^2 \nu D \frac{W}{L}. \quad (5.57)$$

Let us now turn to the interaction. For the inclusion of screening effects we need the polarization operator, which, for the low frequencies at which the electron dynamics is effectively diffusive, can be expressed through the diffusion propagator,

$$\Pi(\mathbf{r}, \mathbf{r}'; \omega) = 2\nu \left[ \delta(\mathbf{r} - \mathbf{r}') + \frac{i\omega}{\hbar} P(\mathbf{r}, \mathbf{r}'; \omega) \right], \quad (5.58)$$

Using Eqs. (5.34), (5.35), (5.36), we then find, that the effective interaction can be written as

$$U^{\text{R}}(\mathbf{r}_1, \mathbf{r}_2; \omega) = \sum_{\mathbf{q}} \psi_{\mathbf{q}}(\mathbf{r}) \psi_{\mathbf{q}}(\mathbf{r}') U^{\text{R}}(\mathbf{q}, \omega) \quad (5.59)$$

where  $U^{\text{R}}(\mathbf{q}, \omega) = U^{\text{R},(j=0)}(\mathbf{q}; \omega) + 3U^{\text{R},(j=1)}(\mathbf{q}; \omega)$  is given by

$$U^{\text{R},(j=0)}(\mathbf{q}; \omega) = \frac{1}{2\nu} \frac{D\mathbf{q}^2 - i\omega/\hbar}{D\mathbf{q}^2} \quad (5.60)$$

$$U^{\text{R},(j=1)}(\mathbf{q}; \omega) = \frac{F_0^\sigma}{2\nu} \frac{D\mathbf{q}^2 - i\omega/\hbar}{D\mathbf{q}^2(1 + F_0^\sigma) - i\omega/\hbar} \quad (5.61)$$

in the singlet and triplet channel, respectively. Due to the divergence of the bare Coulomb interaction at small momenta, the interaction in the singlet channel is set by the polarization operator solely. In the triplet channel, the interaction depends on the zero angular harmonic of  $F^\sigma$ , which is the only free parameter controlling the interaction strength.

For the further calculations, it is convenient to make use of the diffusion equation, to write

$$\frac{\partial}{\partial \tau_{\text{E}}} [P(\mathbf{r}, \mathbf{r}'; \tau_{\text{E}}) e^{i\omega \tau_{\text{E}}/\hbar}] = \left( D\Delta + \frac{i\omega}{\hbar} \right) P(\mathbf{r}, \mathbf{r}'; \tau_{\text{E}}) e^{i\omega \tau_{\text{E}}/\hbar}. \quad (5.62)$$

With the help of additional spatial integrations over delta functions, which we then replace using Eq. (5.53), the interaction correction to the conductance then takes the form

$$\delta G_{\text{AA}} = \frac{\nu e^2}{\pi \hbar^2} \int d\omega \partial_\omega \left( \omega \coth \frac{\omega}{2T} \right) \text{Im} \left\{ \int d\mathbf{r}_1 d\mathbf{r}_2 U^{\text{R}}(\mathbf{r}_1, \mathbf{r}_2; \omega) K(\mathbf{r}_1, \mathbf{r}_2; \omega) \right\}, \quad (5.63)$$

where the function  $K(\mathbf{r}_1, \mathbf{r}_2; \omega)$  reads

$$\begin{aligned}
 K(\mathbf{r}_1, \mathbf{r}_2; \omega) = & \int d\mathbf{r} d\mathbf{r}' P_{in}(\mathbf{r}) P_{out}(\mathbf{r}') \\
 & \times \left\{ \mathcal{D}_\omega P(\mathbf{r}, \mathbf{r}_1; \omega) \mathcal{D}'_\omega P(\mathbf{r}_2, \mathbf{r}'; \omega) \int_{\tau_E}^\infty dt P(\mathbf{r}', \mathbf{r}; t) e^{i\omega t/\hbar} \right. \\
 & - P(\mathbf{r}, \mathbf{r}_1; \omega) P(\mathbf{r}_2, \mathbf{r}'; \omega) \mathcal{D}_\omega P(\mathbf{r}', \mathbf{r}; \tau_E) e^{i\omega \tau_E/\hbar} \\
 & + \mathcal{D}_\omega P(\mathbf{r}, \mathbf{r}_1; \omega) P(\mathbf{r}_2, \mathbf{r}'; \omega) P(\mathbf{r}', \mathbf{r}; \tau_E) e^{i\omega \tau_E/\hbar} \\
 & \left. + P(\mathbf{r}, \mathbf{r}_1; \omega) \mathcal{D}'_\omega P(\mathbf{r}_2, \mathbf{r}'; \omega) P(\mathbf{r}', \mathbf{r}; \tau_E) e^{i\omega \tau_E/\hbar} \right\}, \quad (5.64)
 \end{aligned}$$

with the short-hand notations  $\mathcal{D}_\omega = (D\Delta_{\mathbf{r}} + i\omega/\hbar)$  and  $\mathcal{D}'_\omega = (D\Delta_{\mathbf{r}'} + i\omega/\hbar)$ . The technical advantage of the structure of Eq. (5.64) is that each term contains the same diffusive propagators. Performing several partial integrations, using  $\Delta P_{in}(\mathbf{r}) = \Delta P_{out}(\mathbf{r}) = 0$ ,  $\nabla P_{in}(\mathbf{r}) = -\nabla P_{out}(\mathbf{r}) = -\frac{1}{L}\mathbf{e}_x$ , as well as  $\mathcal{D}_\omega \int_{\tau_E}^\infty dt P(\mathbf{r}', \mathbf{r}; t) e^{i\omega t/\hbar} = -P(\mathbf{r}', \mathbf{r}; \tau_E) e^{i\omega \tau_E/\hbar}$ , we are able to simplify the expression and finally obtain

$$K(\mathbf{r}_1, \mathbf{r}_2; \omega) = -\frac{4D^2}{L^2} \int d\mathbf{r} d\mathbf{r}' P(\mathbf{r}, \mathbf{r}_1; \omega) P(\mathbf{r}_2, \mathbf{r}'; \omega) \partial_x \partial_{x'} \int_{\tau_E}^\infty dt P(\mathbf{r}', \mathbf{r}; t) e^{i\omega t/\hbar}. \quad (5.65)$$

Together, Eq. (5.63) and (5.65) represent the main result for the interaction correction in antidot arrays. For zero Ehrenfest time, the time integral of Eq. (5.65) equals  $P(\mathbf{r}', \mathbf{r}; \omega)$  and one recovers the results for quantum impurities, obtained by standard diagrammatic perturbation theory (see Ref. [Alts 84], where the symbol  $F$  of this reference equals  $F/2 = -F_0^\sigma/(1 + F_0^\sigma)$  and the reference misses a factor two for the triplet contribution). If the Ehrenfest time is finite, it poses a short-time threshold and only electrons with a travel time larger than  $\tau_E$  contribute to the interaction correction. We now discuss Ehrenfest-time dependence of  $\delta G_{AA}$  in detail for a quasi-1d and a 2d antidot array.

### 5.3.3. Quasi-one dimensional antidot array

For a quasi-1d antidot array (width  $W$  much smaller than length  $L$ ), we may simplify the diffusion propagator by taking only the diffusion mode with zero transverse momentum into account. After insertion of the diffusion propagators and the interaction into Eqs. (5.63) and (5.65), and using the residue technique for the  $\omega$ -integration, we find

$$\delta G_{AA} = -\frac{e^2}{h} \sum_{m=1}^\infty \sum_{n=1}^\infty e^{-n\frac{\tau_E}{\tau_T}} e^{-m^2\frac{\tau_E}{\tau_D}} \left[ n \frac{\tau_E \tau_D}{\tau_T^2} g_m(n\tau_D/\tau_T) - n \frac{\tau_D^2}{\tau_T^2} g'_m(n\tau_D/\tau_T) \right], \quad (5.66)$$

where the time  $\tau_T = \hbar/2\pi T$  is the inverse temperature,  $\tau_D = L^2/D\pi^2$  is the diffusion time, and the function  $g_m(x)$  is expressed as

$$g_m(x) = \frac{128}{\pi^4} \sum_{k=1}^\infty c_{km}^2 \frac{1}{(k^2 + x)(m^2 + x)} \left\{ \frac{1}{k^2} + \frac{3F_0^\sigma}{k^2(1 + F_0^\sigma) + x} \right\}, \quad (5.67)$$

with

$$c_{km} = \begin{cases} km/(k^2 - m^2) & \text{if } k + m \text{ odd,} \\ 0 & \text{else.} \end{cases} \quad (5.68)$$

The summation over  $k$  in Eq. (5.67) can be written in a closed form (see Eq. (C.31) in the appendix). We will now discuss the dependence of  $\delta G_{AA}$  on temperature, system size and Ehrenfest time several limiting cases.

- $\tau_D \gg \tau_T, \tau_E$

We first consider the limit  $\tau_D \rightarrow \infty$  corresponding to a large antidot array. In this case, the Ehrenfest-time dependence of the interaction correction  $\delta G_{AA}$  is determined by the ratio  $\tau_E/\tau_T$ . For  $\tau_E/\tau_T \ll 1$  one finds the result

$$\delta G_{AA} = -\frac{e^2}{h} \sqrt{\frac{\tau_T}{\tau_D}} \frac{3\zeta(\frac{3}{2})}{\pi} \left[ 1 + 3 \frac{2 + F_0^\sigma - 2\sqrt{1 + F_0^\sigma}}{F_0^\sigma} \right], \quad (5.69)$$

independent of  $\tau_E$  and known from diagrammatic perturbation theory. Here  $\zeta(3/2) \approx 2.61238$  is the Riemann zeta function (see Appendix C.2 for details). On the other hand, for large Ehrenfest times or, equivalently, higher temperatures,  $\tau_E/\tau_T \gg 1$ , the interaction correction  $\delta G_{AA}$  acquires an exponential dependence on temperature  $\propto e^{-2\pi T \tau_E/\hbar}$ ,

$$\delta G_{AA} = -\frac{e^2}{h} \frac{4}{\pi^{3/2}} \sqrt{\frac{\tau_E}{\tau_D}} e^{-\frac{\tau_E}{\tau_T}}, \quad (5.70)$$

independent of  $F_0^\sigma$ . The crossover between these two limiting cases is shown in Fig. 5.7 for different values of the Fermi-Liquid interaction constant  $F_0^\sigma$ .

We emphasize the influence of the interaction constant in the triplet channel  $F_0^\sigma$ : While for small values of  $F_0^\sigma$ ,  $\delta G_{AA}$  is always negative and monotonously decaying as temperature is increased, a more interesting behaviour is observed at large interaction strength: At small Ehrenfest time and  $F_0^\sigma < -\frac{3}{4}$  the contribution from the triplet channel dominates and gives rise to a positive sign of the interaction correction. On the contrary, if the Ehrenfest time is large, the prefactor of the exponential behaviour shows no dependence on  $F_0^\sigma$  to leading order in  $\frac{\tau_T}{\tau_E}$  and is therefore always negative. Hence, at sufficiently large interaction strengths, one observes a sign change of the interaction correction, as the temperature is varied.

- $\tau_T \gg \tau_D, \tau_E$

In the limit of zero temperature  $\delta G_{AA}$  is a function of the ratio  $\tau_E/\tau_D$  only (we again refer to Appendix C.2 for details). At zero Ehrenfest time, we have

$$\delta G_{AA} = -\frac{e^2}{h} \sum_{m=1}^{\infty} \int_0^{\infty} dx g_m(x), \quad (5.71)$$

with  $g_m(x)$  defined in Eq. (5.67). For small  $F_0^\sigma$ , we have  $\delta G_{AA} \approx -(e^2/h)(0.74 + F_0^\sigma)$ . In this parameter range the singlet contribution is dominant, which leads to a negative sign of the interaction correction, and to a monotonous decay as a

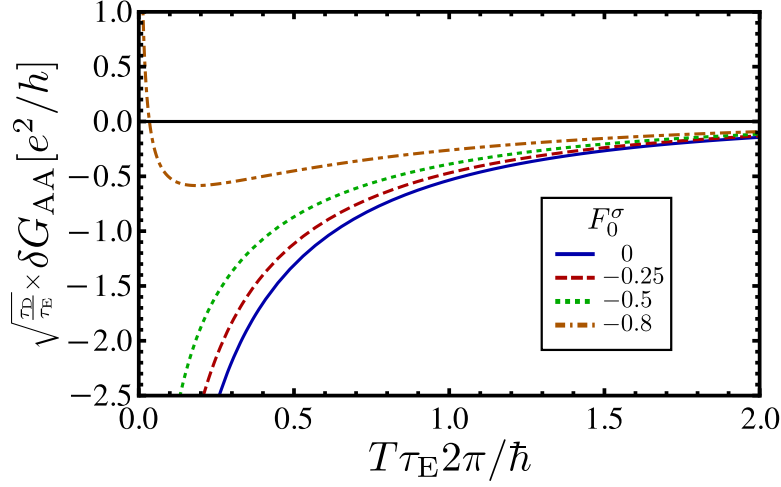


Figure 5.7.: Interaction correction to the conductance of a quasi-one dimensional antidot array in the large-system-size regime  $\tau_D \gg \tau_T, \tau_E$ .

function of  $\frac{\tau_E}{\tau_D}$ . At larger  $F_0^\sigma$  the triplet contribution competes with the singlet contribution, resulting in a sign change of the interaction correction for sufficiently strong interactions, starting at  $F_0^\sigma \approx -0.5$ . For  $\tau_E \gg \tau_D$ , we find an exponential dependence of  $\delta G_{AA}$  on  $\frac{\tau_E}{\tau_D}$

$$\delta G_{AA} = -\frac{e^2}{h} \left( 1 + \frac{3F_0^\sigma}{1 + F_0^\sigma} \right) \frac{16(5\pi^2 - 48)}{3\pi^4} \frac{\tau_D}{\tau_E} e^{-\frac{\tau_E}{\tau_D}}. \quad (5.72)$$

The crossover between the limits  $\tau_E \ll \tau_D$  and  $\tau_E \gg \tau_D$  is shown in Fig. 5.8 for several representative values of  $F_0^\sigma$ .

- $\tau_E \gg \tau_D, \tau_T$  Finally, in the “classical” limit of large Ehrenfest times, we have

$$\delta G_{AA} = -\frac{e^2}{h} \frac{\tau_E \tau_D}{\tau_T^2} e^{-\frac{\tau_E}{\tau_T}} e^{-\frac{\tau_E}{\tau_D}} g_1\left(\frac{\tau_D}{\tau_T}\right), \quad (5.73)$$

where  $g_1$  is defined in Eq. (5.67). In this parameter regime the interaction correction has the characteristic exponential suppression  $\delta G_{AA} \propto e^{-2\pi T\tau_E/\hbar - \tau_E/\tau_D}$ .

### 5.3.4. Large 2d system

We will now consider a two-dimensional antidot array of dimensions  $L \times W$ , where we restrict ourselves to the limit of large system size,  $\tau_D \gg \tau_E, \tau_T$ . In the large-size limit, the relevant quantity is the conductivity  $\sigma = GL/W$  (although we here write results for the conductivity, we formally calculate the conductance and multiply with the geometrical factor  $L/W$ , see also the discussion in Sec. 5.2.1). We may then express Eqs. (5.63) and

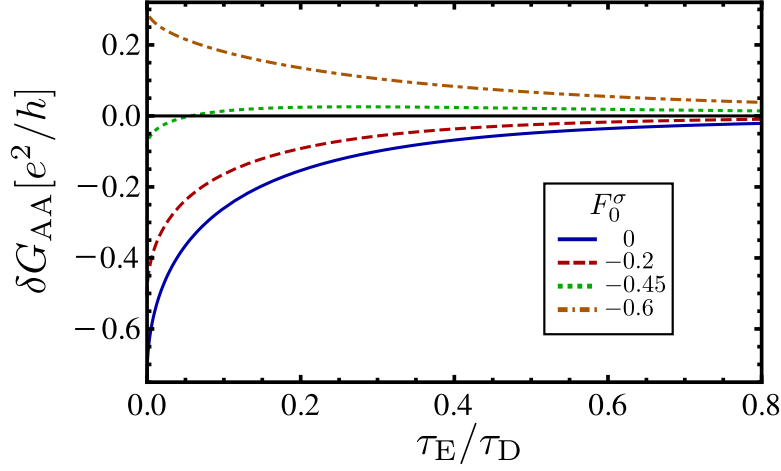


Figure 5.8.: Interaction correction to the conductance of a quasi-one dimensional antidot array in the low-temperature regime  $\tau_T \gg \tau_D, \tau_E$ .

(5.65) in momentum space,

$$\delta\sigma_{AA} = -\frac{4\nu e^2 D}{\pi\hbar^2} \int d\omega \partial_\omega \left( \omega \coth \frac{\omega}{2T} \right) \text{Im} \left\{ \int \frac{d^2\mathbf{q}}{(2\pi)^2} U^R(\mathbf{q}; \omega) \frac{Dq_x^2 e^{i\omega\tau_E} e^{-D\mathbf{q}^2\tau_E}}{(D\mathbf{q}^2 - i\omega/\hbar)^3} \right\}. \quad (5.74)$$

In the limit of zero Ehrenfest time, this expression simplifies to the well-known result of diagrammatic perturbation theory [Alej 99, Zala 01]. The full Ehrenfest-time dependence is shown in Fig. 5.9. For  $\tau_E \ll \tau_T$ , we have the asymptotic behavior

$$\delta\sigma_{AA} = -\frac{e^2}{\pi h} \left[ 1 + 3 \left( 1 - \frac{\ln(1 + F_0^\sigma)}{F_0^\sigma} \right) \right] \ln \frac{\tau_T}{\tau_E}, \quad (5.75)$$

which coincides with the well-known expression of quantum impurities, where the role of the elastic scattering time as a short-time cutoff is taken over by the Ehrenfest time. In the opposite limit  $\tau_E \gg \tau_T$ , we obtain an exponential dependence on temperature,

$$\delta\sigma_{AA} = -\frac{e^2}{\pi h} e^{-\frac{\tau_E}{\tau_T}}. \quad (5.76)$$

As in the one-dimensional situation, at small  $F_0^\sigma$  the singlet contribution dominates the interaction correction, while at larger  $F_0^\sigma$  the triplet contribution competes, and a sign change of the interaction correction as a function of  $\frac{\tau_E}{\tau_T}$  is observed if  $F_0^\sigma \lesssim -0.45$ .

## 5.4. Conclusion

In this chapter, we considered the effect of a finite Ehrenfest time on the interaction correction of a conductor in which the motion of the electrons is described by chaotic

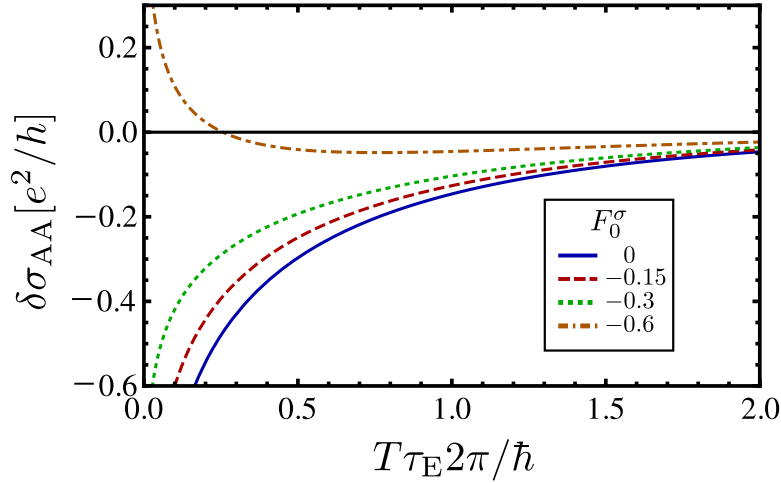


Figure 5.9.: Interaction correction to the conductivity  $\sigma$  of a two-dimensional antidot array for various values of the interaction strength  $F_0^\sigma$  in the triplet channel.

classical dynamics. Using semiclassical theory of transport, we derived an expression for the interaction correction containing only the interaction propagator and coarse-grained classical propagators of the electronic motion. We confirm the result of Ref. [Brou 08], obtained for a double ballistic quantum dot, that the Ehrenfest time enters as a short-time threshold for the interaction correction. In other words, the minimal time it takes to traverse system for trajectories responsible for the interaction corrections is the Ehrenfest time.

As a specific and experimentally relevant example we applied the formalism to antidot arrays, where the coarse-grained classical dynamics follows a diffusion equation. At zero Ehrenfest time, we recovered the well known results of the diagrammatic perturbation theory for a disordered metal [Alts 79]. If the Ehrenfest time is large, we found that the interaction correction is exponentially suppressed  $\propto e^{-\tau_E/\tau_D} e^{-2\pi T\tau_E/\hbar}$ . While the factor  $e^{-\tau_E/\tau_D}$  is also present for weak localization, the suppression with temperature is specific to the interaction correction. Unlike the dwell time  $\tau_D$ , which governs the Ehrenfest-time dependence of weak localization, temperature is a variable that can be easily controlled experimentally without changing the classical dynamics, making the interaction correction a promising experimental signature of the Ehrenfest-time dependence of quantum transport. (We note that weak localization depends on temperature implicitly via its dependence on the dephasing time. However, an independent measurement of the dephasing time that enters into the expression for the Ehrenfest-time dependence of the weak localization correction is problematic [Tian 07].)

A particular signature of the underlying classical motion is a sign change of the interaction corrections for strong enough interactions. Associated with this sign change is a non-monotonous temperature dependence of the interaction correction, in the temperature range  $T \sim \hbar/\tau_E$ . As long as only the Fock contribution is considered, the sign of the interaction correction is negative. If the Hartree contribution — more precisely, the triplet



channel of interaction — is added, there is a competition between Hartree and Fock-type corrections, and the sign of the total interaction correction at small Ehrenfest time may change as a function of the interaction strength. For large Ehrenfest time, the Fock contribution always dominates, so that the sign of the interaction correction is independent on the interaction strength in that limit.

As mentioned above, the sign change of the interaction corrections for systems with small Ehrenfest times requires a rather strong interaction in the triplet channel. In particular, in  $2d$  systems the threshold was estimated to be  $F_0^\sigma \lesssim -0.45$ , where  $F_0^\sigma$  is the corresponding Fermi liquid constant, whereas in quasi one-dimensional systems the condition reads  $F_0^\sigma \lesssim -0.75$ . Let us focus on  $2d$  systems with Coulomb interaction, for which the condition is less restrictive. Both numerical and experimental results for  $F_0^\sigma$  are available in the literature. In general,  $F_0^\sigma$  is a function of the gas parameter  $r_s = \sqrt{2}e^2/\varepsilon\hbar v_F$ , where  $\varepsilon$  is the static dielectric constant and  $v_F$  the Fermi velocity. To get an estimate for typical values of  $r_s$  to be expected in antidot array experiments, we take  $v_F \approx 3 \times 10^5 \text{ m/s}$ , which was reported in Ref. [Yevt 00] for antidot arrays fabricated from GaAs/ AlGaAs heterostructures. Together with the dielectric constant for GaAs  $\varepsilon \approx 13$  we obtain  $r_s \approx 0.8$ . In Ref. [Mink 06] the constant  $F_0^\sigma$  for a given gas parameter  $r_s$  was extracted from experimental data using the results for the interaction corrections to conductivity [Alts 85b, Fink 90, Zala 01, Gorn 04]. For systems with  $r_s \approx 1$ , typical values of  $F_0^\sigma$  were found to be of the order of  $-0.35$ . This seems consistent with numerical results obtained in Ref. [Kwon 94], where systems with moderately large  $r_s$  were analyzed. For the maximal value of  $r_s = 5$  considered in this chapter, the Fermi liquid constant decreased further down to  $F_0^\sigma = -0.5$ . Considerably larger negative values up to  $F_0^\sigma \approx -0.7$  were inferred for systems with  $r_s \approx 22$  in Ref. [Noh 03]. We take this as evidence that  $2d$  systems with sufficiently strong triplet channel interactions are realizable, provided the additional antidot structure may be superimposed. Relevant values of the gas parameter  $r_s$  are likely in the range of  $r_s \approx 3 - 5$ .



## 6. Quantum corrections to transport in graphene: a semiclassical analysis

In this chapter, we apply semiclassical methods in order to calculate quantum corrections to transport in graphene. Compared to the calculations presented in the previous chapter, in graphene we have to incorporate additionally the effect of the pseudospin, which is strongly linked to the orbital motion, and influences the results for the quantum corrections. This chapter provides an overview over semiclassical calculations of weak (anti)localization, and interaction-induced effects as the Altshuler-Aronov correction and dephasing. While for quantum disorder, the results are already known from diagrammatic perturbation theory, the semiclassical calculations provide an alternative, more intuitive approach, and allow to discuss the effect of a finite Ehrenfest time, relevant for graphene subject to a smooth disorder potential.

After an introduction, we will introduce the semiclassical propagator for graphene in Sec. 6.2. We will further discuss, how the important quantities diffusion coefficient and Lyapunov coefficient are derived from the classical chaotic dynamics (Sec. 6.3). To set the stage, we calculate the Drude conductance in Sec. 6.4, before we turn to the quantum corrections. Here, we will investigate the effect of weak (anti)localization (Sec. 6.5), and interaction-induced effects as Altshuler-Aronov correction (Sec. 6.6), and dephasing (Sec. 6.7). We conclude our results in Sec. 6.8.

The content of this chapter is based on the publication [Schn 14b].

### 6.1. Introduction

Electric properties of graphene are highly unusual, when the Fermi level is tuned to the Dirac point. When graphene is doped away from the Dirac point, its physical properties resemble those of a metal, but certain intriguing features from the Dirac spectrum remain. The reason for this lies in the “pseudospin” degree of freedom, which is connected to the two-atom basis of the two-dimensional honeycomb lattice. Sufficiently close to the Dirac point, where the electronic dispersion is still linear, the direction of the pseudospin is aligned with the momentum. This helicity of charge carriers strongly influences the electronic properties. Two important consequences are the absence of backscattering at a potential barrier (Klein tunneling) [Chei 06, Kats 06b] and the half-integral quantum Hall effect [Novo 05, Zhan 05], as discussed earlier in this thesis.

Away from the Dirac point, the conductivity of graphene can be split in the usual fashion into Drude conductivity and quantum corrections, as known from conventional metals. Soon after the initial experiments on graphene, the theory of quantum corrections in disordered metals was extended to graphene [Khve 06, McCa 06, Morp 06, Alei 06, Altl 06, Kozi 10, Jobs 12]. Of particular interest was the potential valley-mixing effect of short

range disorder (correlation length  $\xi \ll \lambda_F$ ), which leads to a transition between weak localization and weak antilocalization [Khve 06, McCa 06, Morp 06, Alei 06] and strongly affects the magnitude of the Altshuler-Aronov correction [Kozl 10, Joua 11, Jobs 12]. Such transitions were also observed experimentally [Moro 06, Tikh 08, Ki 08, Tikh 09, Cao 10, Kozl 10, Chen 10, Joua 11, Lara 11, Jobs 12]. In the present chapter, we consider the quantum corrections to the conductivity of graphene in the presence of a *long-range* impurity potential, which is smooth on the scale of the Fermi wavelength  $\lambda_F$ . Such a smooth random potential does not mix the valleys, but instead leads to a number of modifications of the quantum corrections because of its smoothness: In this situation, electrons follow well-defined classical trajectories, where the random potential ensures that the classical dynamics is chaotic. As discussed in the previous chapter, an important role in this regime is taken by the Ehrenfest time

$$\tau_E = \frac{1}{\lambda} \ln(L_c/\lambda_F), \quad (6.1)$$

where  $\lambda$  is the Lyapunov coefficient of the classical chaotic motion, and  $L_c$  is a classical reference distance (for the antidot arrays discussed in the previous chapter,  $L_c$  could be identified with the size of the antidots  $a$ ). It is known, how the Ehrenfest time influences the quantum corrections for conventional electron gases, see Refs. [Alei 96, Yevt 00, Brou 07, Altl 07] and the previous chapter. The goal of the present chapter is to extend and collect those results for the case of graphene.

The trajectory-based semiclassical calculation of quantum corrections to the conductivity of graphene differs from the same calculation for conventional metals by the additional pseudospin structure. The problem of extending the semiclassical formalism to systems with a spinor degree of freedom, such as metals with spin-orbit coupling or Dirac Hamiltonians, has received considerable attention in the literature [Rubi 63, Litt 91, Litt 92, Bolt 98, Bolt 99, Zait 05a, Zait 05b, Silv 07]. The application of the formalism to the case of graphene by Carmier and Ullmo [Carm 08] will serve as a starting point for our calculation. A key element in the trajectory-based approaches is that the pseudospin can be reconstructed along the trajectories, where it remains aligned with the momentum. Associated with the transport of the pseudospin along the trajectory is an additional phase in the semiclassical propagator, which can be identified as the Berry phase. One example where this phase plays an important role is the semiclassical calculation of the Landau levels, where the electrons acquire a Berry phase of  $\pi$  during the cyclotron motion, ultimately leading to the half-integral quantum Hall effect, see Sec. 2.2.

The semiclassical theory presented here is specifically aimed at the leading order quantum corrections (weak localization and Altshuler-Aronov correction, as well as the effect of dephasing on weak localization) for graphene in a smooth random potential. Typical systems to which the trajectory-based semiclassical method has been applied in the literature are quantum billiards, ultraballistic systems, where particles scatter only at the boundary of the sample, or antidot arrays, high mobility two-dimensional electron gases with artificially superimposed antidots, that act as classical scatterers [Rouk 89, Enss 90, Yevt 00]. While for standard semiconductor structures, quantum billiards can be shaped by means of gate potentials, such procedure is problematic for graphene, as it is a gapless material. Quantum billiards in graphene can be realized in etched structures, where the edges are atomically sharp [Pono 08, Schn 09, Mori 09, Gutt 09]. The scattering on such edges

then depends on the precise atomic configuration, and deserves a careful consideration [Wurm 11a, Wurm 11b]. The same applies to antidot arrays in graphene [Erom 09], but also here, the boundaries of the antidots are so sharp, that they lead to scattering between the valleys. Such atomically sharp boundaries invalidate a description that is solely based on classical trajectories, although for sufficiently well-defined boundaries a theoretical description involving coupled valleys is possible [Wurm 11a, Wurm 11b]. Such a limitation does not exist for the effect of an impurity potential where charged impurities in the substrate are the main source of disorder, and the graphene sheet is embedded in an insulating medium with a high dielectric constant, such as  $\text{HfO}_2$  [Jang 08, Pono 09, Newa 12]. In this case, the high dielectric constant ensures that the screening length is larger than  $\lambda_F$  at sufficiently high doping. Hence, the potential has a correlation length  $\xi \gg \lambda_F$  and classical paths are well-defined objects.

## 6.2. Semiclassical Green function

In this chapter, we consider graphene subject to a smooth disorder potential  $V(\mathbf{r})$  that does not couple the valleys. In the vicinity of the Dirac point, electrons are described by the Hamiltonian

$$H = v_F \mathbf{p} \cdot \boldsymbol{\sigma} + V(\mathbf{r}) - \mu, \quad (6.2)$$

where  $v_F$  is the Fermi velocity,  $\mu$  is the chemical potential, and  $\boldsymbol{\sigma} = (\sigma_x, \sigma_y)$  are as usual the Pauli matrices for the pseudospin degree of freedom. The eigenvalues of the kinetic energy term  $v_F \mathbf{p} \cdot \boldsymbol{\sigma}$  are  $K_{\pm} = \pm v_F |\mathbf{p}|$ . We will be interested in the case of electron-doped graphene for which the chemical potential  $\mu$  is larger than the potential  $V(\mathbf{r})$ . In this case we may restrict our attention to the conduction band and set  $K = v_F |\mathbf{p}|$ . The corresponding eigenspinor of the kinetic energy is

$$|\chi(\mathbf{p})\rangle = \frac{1}{\sqrt{2}} \begin{pmatrix} 1 \\ e^{i\phi_{\mathbf{p}}} \end{pmatrix}, \quad (6.3)$$

where the angle  $\phi_{\mathbf{p}}$  denotes the direction of the momentum  $\mathbf{p}$ , see also Eq. (2.9).

Starting point for our semiclassical analysis of transport is the semiclassical expression for the retarded Green function  $\mathcal{G}^R(\mathbf{r}, \mathbf{r}'; \varepsilon)$  at energy  $\varepsilon$  derived by Carmier and Ullmo [Carm 08],

$$\mathcal{G}^R(\mathbf{r}, \mathbf{r}'; \varepsilon) = \frac{2\pi}{(2\pi i \hbar)^{3/2}} \sum_{\alpha: \mathbf{r}' \rightarrow \mathbf{r}; \varepsilon} A_{\alpha} e^{i\mathcal{S}_{\alpha}/\hbar + i\gamma_{\alpha}} |\chi(\mathbf{p}_{\alpha})\rangle \langle \chi(\mathbf{p}'_{\alpha})|, \quad (6.4)$$

where summation is over all classical trajectories  $\alpha$  that connect the points  $\mathbf{r}$  and  $\mathbf{r}'$ ,  $\mathcal{S}_{\alpha}$  is the classical action of the trajectory,  $A_{\alpha}$  the stability amplitude (as introduced in the previous chapter in Sec. 5.2.2),  $\gamma_{\alpha}$  an additional phase shift to be defined below, and  $\mathbf{p}'_{\alpha}$  and  $\mathbf{p}_{\alpha}$  are the initial and final momenta of the trajectory  $\alpha$ , respectively. Equation (6.4) generalizes the corresponding expression for a system without spin or pseudospin degrees of freedom [Gutz 90]. (In that case the projection factor  $|\chi(\mathbf{p}_{\alpha})\rangle \langle \chi(\mathbf{p}'_{\alpha})|$  and the phase shift  $\gamma_{\alpha}$  are absent, see also Eq. (5.7)). The classical trajectories are determined by the classical Hamilton function

$$H_{\text{cl}}(\mathbf{p}, \mathbf{r}) = v_F |\mathbf{p}| + V(\mathbf{r}) - \mu. \quad (6.5)$$

Finally, the phase shift  $\gamma_\alpha$  contains the Berry phase

$$\gamma_\alpha = -\frac{1}{2} \int_0^{\tau_\alpha} dt \frac{d\phi_{\mathbf{p}_\alpha(t)}}{dt} = -\frac{1}{2} (\phi_{\mathbf{p}_\alpha} - \phi_{\mathbf{p}'_\alpha} + 2\pi n), \quad (6.6)$$

where in the second equality we chose the initial and final angles to be  $0 \leq \phi_{\mathbf{p}'_\alpha}, \phi_{\mathbf{p}_\alpha} \leq 2\pi$  and add  $2\pi n$ ,  $n$  being integer, to account for the phase winding along the path  $\alpha$ . We have not included the phase corresponding to the Maslov index [Gutz 90], which can be disregarded for the calculation of transport.

In the next Sections we also need the advanced Green function, which follows from the relation

$$\mathcal{G}^A(\mathbf{r}', \mathbf{r}; \varepsilon) = [\mathcal{G}^R(\mathbf{r}, \mathbf{r}'; \varepsilon)]^\dagger. \quad (6.7)$$

### 6.3. Diffusion coefficient and Lyapunov coefficient for a Gaussian random potential

For a random disorder potential  $V(\mathbf{r})$ , the classical dynamics, that is derived from the Hamilton function Eq. (6.5), behaves in a chaotic manner. Following Refs. [Bard 07, Adam 09], we consider a random Gaussian potential with the correlation function

$$\langle V(\mathbf{r})V(\mathbf{r}') \rangle = K_0 \frac{(\hbar v_F)^2}{2\pi\xi^2} e^{-|\mathbf{r}-\mathbf{r}'|^2/2\xi^2}, \quad (6.8)$$

where  $\xi$  is the correlation length, and  $K_0$  is the dimensionless strength of the potential. The random potential of Eq. (6.8) has been used to describe the impurity potential in experiments [Tan 07, Adam 08]. On spatial scales much longer than the correlation length, the electronic motion becomes diffusive, with a diffusion coefficient  $D$  that we will calculate in the following. Furthermore, two initially nearby classical trajectories will separate exponentially in time due to chaotic motion, at a rate given by the Lyapunov coefficient  $\lambda$ , whose value will be also calculated in the following for the Gaussian random potential.

#### 6.3.1. Diffusion constant

In order to determine the diffusion coefficient, we start by considering a particle that moves in the  $x$ -direction at time  $t = 0$  and consider how the direction of motion changes under the influence of the potential  $V(\mathbf{r})$ . Following the classical dynamics, the angle  $\phi(t)$ , at which the electron propagates at time  $t$  is given by

$$\phi(t) = -\frac{1}{\hbar k_F} \int_0^t dt' \partial_y V(\mathbf{r}(t')), \quad (6.9)$$

where  $k_F$  is the Fermi wavenumber. This equation is valid for times  $t$  short enough, such that  $|\phi(t)| \ll 1$ , so that the motion of the electron is mainly along the  $x$ -direction,  $\mathbf{r}(t) = v_F t \mathbf{e}_x$ . We then find for the mean quadratic deflection

$$\langle \phi(t)^2 \rangle = \frac{1}{(\hbar k_F v_F)^2} \int_0^{v_F t} dx dx' \langle \partial_y V(x, 0) \partial_y V(x', 0) \rangle. \quad (6.10)$$

Using the correlation function Eq. (6.8), this gives

$$\langle \phi(t)^2 \rangle = \frac{K_0 v_F t}{\xi^3 k_F^2 \sqrt{2\pi}}, \quad (6.11)$$

provided  $t$  is much longer than the “correlation time”  $t_\xi = \xi/v_F$ . Our derivation required the time  $t$  to be short enough such that the deflection is small. Such time interval exists, as long as  $K_0 \ll (k_F \xi)^2$ , which is a condition that can be met if the disorder is smooth on the scale of the Fermi wavelength ( $k_F \xi \gg 1$ ).

Equation (6.11) describes a linear-in-time increase of the quadratic deflection, a characteristic property of the diffusive motion for the angle  $\phi$ . Continuing the diffusive process beyond small angles, the validity of this equation can be extended to all times longer than the correlation time  $t_\xi$ . Further, extending the result to arbitrary starting times and arbitrary directions in the beginning of the propagation, we conclude that the angle difference  $\phi(t) - \phi(t')$  has a Gaussian distribution with zero mean and with variance

$$\langle [\phi(t) - \phi(t')]^2 \rangle = \frac{K_0 v_F}{\xi^3 k_F^2 \sqrt{2\pi}} |t - t'|. \quad (6.12)$$

Now we can calculate the electron’s mean square displacement. Since

$$\mathbf{r}(t) - \mathbf{r}(0) = v_F \int_0^t dt' [\mathbf{e}_x \cos \phi(t') + \mathbf{e}_y \sin \phi(t')], \quad (6.13)$$

the mean square displacement is given by

$$\langle |\mathbf{r}(t) - \mathbf{r}(0)|^2 \rangle = v_F^2 \int_0^t dt' dt'' \langle \cos[\phi(t') - \phi(t'')] \rangle. \quad (6.14)$$

The average can be performed using the Gaussian distribution of  $\phi(t') - \phi(t'')$  and one finds, in the long-time limit,

$$\langle [\mathbf{r}(t) - \mathbf{r}(0)]^2 \rangle = 4D|t|, \quad (6.15)$$

where the diffusion constant  $D$  is given by

$$D = \frac{\xi^3 k_F^2 v_F \sqrt{2\pi}}{K_0}. \quad (6.16)$$

The diffusion constant of Eq. (6.16) corresponds to a transport mean free path

$$l_{\text{tr}} = \tau_{\text{tr}} v_F = \frac{2\xi^3 k_F^2 \sqrt{2\pi}}{K_0}, \quad (6.17)$$

which is parametrically larger than the correlation length  $\xi$  in the limit  $k_F \xi \gg 1$  of a smooth potential.

### 6.3.2. Lyapunov coefficient

We now calculate the Lyapunov coefficient  $\lambda$  for the Gaussian-correlated disorder potential  $V(\mathbf{r})$ , specified by Eq. (6.8). Our result agrees with that of Aleiner and Larkin [Ale96], using a different method.

We consider two trajectories that are initially close in phase space, and investigate their divergence as they evolve in time. We use  $\Delta r_\perp$  and  $\Delta p_\perp$  to denote the position and momentum differences in the direction perpendicular to the propagation direction. From the classical equation of motion,

$$\dot{\mathbf{r}} = v_F \mathbf{e}_\mathbf{p}, \quad \dot{\mathbf{p}} = -\nabla V, \quad (6.18)$$

with  $\mathbf{e}_\mathbf{p}$  the unit vector in the direction of the momentum  $\mathbf{p}$ , we find that the differences  $\Delta r_\perp$  and  $\Delta p_\perp$  evolve in time as

$$\frac{\partial \Delta r_\perp}{\partial t} = v_F \frac{\Delta p_\perp}{p_F}, \quad \frac{\partial \Delta p_\perp}{\partial t} = -\frac{\partial^2 V(t)}{\partial r_\perp^2} \Delta r_\perp, \quad (6.19)$$

where  $V(t)$  is shorthand notation for  $V(\mathbf{r}(t))$ . Upon integrating the evolution equations for an infinitesimal time interval  $\delta t$  the solution may be cast in the form of a transfer matrix equation, which we write as

$$\begin{pmatrix} \frac{\Delta r_\perp(t+\delta t)}{\xi} \\ \frac{\Delta p_\perp(t+\delta t)}{z p_F} \end{pmatrix} = \mathcal{M}(t+\delta t, t) \begin{pmatrix} \frac{\Delta r_\perp(t)}{\xi} \\ \frac{\Delta p_\perp(t)}{z p_F} \end{pmatrix}, \quad (6.20)$$

where  $z^2 = \sqrt{K_0}/k_F \xi \ll 1$  and the transfer matrix  $\mathcal{M}(t, t+\delta t)$  reads

$$\mathcal{M}(t+\delta t, t) = e^{z H(t) \delta t}, \quad H(t) = \begin{pmatrix} 0 & v_F/\xi \\ f(t) & 0 \end{pmatrix}, \quad (6.21)$$

with

$$f(t) = -\frac{\xi}{z^2 p_F} \frac{\partial V(t)}{\partial r_\perp^2} \quad (6.22)$$

a stochastic function that contains all information on the random potential. The function  $f$  has zero mean, and its fluctuations in a time interval  $\Delta t$  long in comparison to the correlation time  $t_\xi = \xi/v_F$  are

$$\left\langle \int_0^{\Delta t} dt dt' f(t) f(t') \right\rangle = \frac{3}{\sqrt{2\pi}} \frac{v_F \Delta t}{\xi}. \quad (6.23)$$

(The condition  $\Delta t \gg t_\xi$  is consistent with the smallness of the parameter  $z$ .)

Sofar we have calculated the transfer matrix for an infinitesimal time interval  $\delta t$ . The result can be easily extended to calculate the transfer matrix for time intervals of arbitrary duration, via successive multiplication of transfer matrices valid for the infinitesimal segments. This results in a stochastic evolution of the transfer matrix, which can be analyzed using an explicit parameterization of the transfer matrix,

$$\mathcal{M}(t+\Delta t, t) = e^{i\varphi\sigma_2} e^{l\sigma_3} e^{i\phi\sigma_2}, \quad (6.24)$$



where  $\sigma_2$  and  $\sigma_3$  are the Pauli matrices. The exponential divergence of the trajectories follows from the radial parameter  $l$ ,

$$\lambda = \lim_{\Delta t \rightarrow \infty} \frac{l}{\Delta t}. \quad (6.25)$$

For the calculation of  $l$  it is sufficient to consider the matrix product  $\mathcal{M}^T \mathcal{M}$ , which has eigenvalues  $e^{\pm 2l}$  and no longer depends on the angular variable  $\varphi$ . The time-evolution of the remaining parameters  $l$  and  $\phi$  is given by a Langevin-type process which, for large  $l$ , reads

$$\begin{aligned} \delta l &= \frac{z}{2} \frac{v_F \delta t}{\xi} \sin 2\phi + \frac{z}{2} \sin 2\phi \int_0^{\delta t} dt' f(t') - \frac{z^2}{2} \cos 2\phi \sin^2 \phi \int_0^{\delta t} dt' dt'' f(t') f(t''), \\ \delta \cot \phi &= z \int_0^{\delta t} dt' f(t') - z \frac{v_F \delta t}{\xi} \cot^2 \phi, \end{aligned} \quad (6.26)$$

where terms of higher order than  $\delta t$  are neglected.

It is helpful to introduce the variable  $y$  via

$$y = (2\pi)^{1/6} z^{-1/3} (2/3)^{1/3} \cot \phi. \quad (6.27)$$

After averaging over fluctuations of  $f$ , we find that mean and variance of the change  $\delta y$  in an infinitesimal time interval  $\delta t$  read

$$\begin{aligned} \langle \delta y \rangle &= -(3/2)^{1/3} (2\pi)^{-1/6} z^{4/3} y^2 \frac{v_F \delta t}{\xi}, \\ \langle (\delta y)^2 \rangle &= 2^{2/3} 3^{1/3} (2\pi)^{-1/6} z^{4/3} \frac{v_F \delta t}{\xi}. \end{aligned} \quad (6.28)$$

The parameter  $y$  acquires a stationary probability distribution  $P_s(y)$ , which satisfies the equation [Kamp 07]

$$\frac{1}{2} \frac{\langle (\delta y)^2 \rangle}{\delta t} \frac{\partial P_s}{\partial y} - \frac{\langle \delta y \rangle}{\delta t} P_s = c', \quad (6.29)$$

where  $c'$  is a numerical constant. Using Eq. (6.28), we obtain

$$\frac{\partial P_s}{\partial y} + y^2 P_s = c'. \quad (6.30)$$

The only normalized solution of this equation occurs for  $1/c' = 3^{-5/6} 2^{1/3} \Gamma(1/6) \sqrt{\pi} \approx 4.976$  and reads

$$P_s(y) = c' \int_{-\infty}^y dy' e^{(y'^3 - y^3)/3}. \quad (6.31)$$

Keeping leading terms in the parameter  $z$  only, we find that the average

$$\langle \delta l \rangle = \left( \frac{3z^4}{2\sqrt{2\pi}} \right)^{1/3} y \frac{v_F \delta t}{\xi}. \quad (6.32)$$

Since the angular variable  $y$  evolves statistically independent from the radial variable  $l$  for large  $l$ , we may average  $y$  with the help of the stationary distribution (6.31), for which we find

$$\beta = \int_{-\infty}^{\infty} dy y P_s(y) = \frac{(3/2)^{1/3} \sqrt{\pi}}{\Gamma(1/6)} \approx 0.365. \quad (6.33)$$

From the definition (6.25) we then obtain the Lyapunov coefficient

$$\lambda = \beta \frac{v_F}{\xi} \left( \frac{3K_0}{2\sqrt{2\pi}(k_F\xi)^2} \right)^{1/3} = \frac{\beta}{\tau_{\text{tr}}} \left( \frac{l_{\text{tr}}\sqrt{3}}{\xi} \right)^{2/3}, \quad (6.34)$$

where, in the second equality, we inserted the transport mean free time and the mean free path of Eq. (6.17). This result agrees with the Lyapunov exponent calculated by Aleiner and Larkin [Ale96]. (One has to identify the short-length cut-off  $a$  of Ref. [Ale96] with  $\xi/\sqrt{3}$ , see the text below Eq. (A3) of Ref. [Ale96].)

## 6.4. Drude conductance

We now turn to the calculation of the conductivity. Hereto, we consider a rectangular sample of graphene of dimensions  $L \times W$ , calculate its conductance  $G$ , and obtain the conductivity  $\sigma$  from the relation  $G = \sigma W/L$ . The conductance  $G$  is calculated from the Kubo formula

$$G = \frac{e^2 d_g \hbar}{2\pi} \int dy \int dy' \int d\varepsilon \left( -\frac{\partial f(\varepsilon)}{\partial \varepsilon} \right) \text{Tr} [\hat{v}_x \mathcal{G}^R(\mathbf{r}, \mathbf{r}'; \varepsilon) \hat{v}_x' \mathcal{G}^A(\mathbf{r}', \mathbf{r}; \varepsilon)] \Big|_{x'=0}^{x=L}, \quad (6.35)$$

where  $f(\varepsilon) = 1/(e^{\varepsilon/T} + 1)$  is the Fermi function and  $d_g = 4$  denotes the degeneracy due to spin and valley. Further, the velocity operator for graphene reads

$$\hat{v}_x = v_F \sigma_x \quad (6.36)$$

and the trace indicates a summation over pseudospin indices.

For a semiclassical calculation of the conductance, we insert the semiclassical Green function (6.4) into the Kubo formula, so that  $G$  is expressed as a double sum over trajectories  $\alpha$  and  $\beta$ . Restricting the summation to diagonal terms  $\alpha = \beta$ , the so-called diagonal approximation, then gives the Drude conductance. For  $\alpha = \beta$  the semiclassical approximation Eq. (6.35) contains matrix elements of the form

$$\langle \chi(\mathbf{p}_\alpha) | \hat{v}_x | \chi(\mathbf{p}_\alpha) \rangle = v_F \cos \phi_{\mathbf{p}_\alpha} = v_x, \quad (6.37)$$

with  $v_x = \partial H_{\text{cl}} / \partial p_x$ . Apart from the factor  $d_g$ , the resulting expression is the same as in the case of a standard two-dimensional electron gas, see Eq. (5.15)

$$G_0 = d_g \frac{e^2}{(2\pi\hbar)^2} \int dy \int dy' \int d\varepsilon \left( -\frac{\partial f(\varepsilon)}{\partial \varepsilon} \right) \sum_{\alpha: (0, y') \rightarrow (L, y)} A_\alpha^2 v_x' v_x, \quad (6.38)$$

with the initial (final) classical velocity  $v_x'$  ( $v_x$ ).

The remaining summation over trajectories  $\alpha$  can be transformed to an integral over initial and final momentum and the duration of the trajectories, where the integrand contains a trajectory density, that is expressed as a  $\delta$ -function and selects the classical trajectories that connect source and drain contact. Performing the disorder average replaces the exact trajectory density by a classical propagator that is a smooth function which is a smooth function of initial and final phase space coordinates as well as time. On spatial scales much longer than the correlation length  $\xi$ , this classical propagator describes a diffusive motion. This procedure works out in precisely the same way as discussed in the previous chapter in Sec. 5.2.2 and Sec. 5.3.2, and we do not repeat it at this point.

We proceed with the result for the Drude conductivity  $\sigma_0 = G_0 L/W$ , where we then obtain the standard expression

$$\sigma_0 = d_g e^2 \nu D, \quad (6.39)$$

where the factor  $d_g = 4$  accounts for the degeneracy for spin and valley. Importantly, pseudospin does not enter as an additional degeneracy, since it is locked to the momentum. Taking the expression for the diffusion coefficient for the Gaussian random potential, Eq. (6.16), as well as the density of states at graphene,  $\nu = k_F/2\pi\hbar v_F$ , one obtains

$$\sigma_0 = \frac{4e^2}{h} \frac{(k_F \xi)^3}{K_0} \sqrt{2\pi}. \quad (6.40)$$

The same result was obtained in a quantum-mechanical calculation using the Boltzmann equation in Ref. [Adam 09].

## 6.5. Weak antilocalization

Deviations from the Drude conductance are termed quantum corrections. Without interactions and for conventional metals, the leading correction to the classical conductance results in a small reduction of the conductance, and is called “weak localization”, since it describes the onset of Anderson localization. In graphene, the Berry phase is responsible for a different sign of this quantum correction, which gives rise to an enhanced conductance (when effects of intervalley scattering and trigonal warping are neglected), and is therefore called weak *antilocalization* [Khve 06, McCa 06, Morp 06, Tikh 08, Tikh 09]. In the following, we will show how the weak antilocalization is derived in the semiclassical formalism, and discuss the effect of a finite Ehrenfest time. Again, we will give explicit results for the case of a smooth random Gaussian-correlated potential.

In the semiclassical framework, weak (anti)localization results from configurations of retarded and advanced trajectories  $\alpha$  and  $\beta$  as shown in Fig. 6.1. The trajectories can be divided into four segments: The entrance and exit segments, where the trajectories  $\alpha$  and  $\beta$  are correlated or “paired” — *i.e.*, the difference between the two trajectories is sufficiently small, that the chaotic classical dynamics can be linearized on that scale —, the loop segment, where the trajectory  $\alpha$  is paired with the time-reversed of trajectory  $\beta$ , and the encounter region (or Lyapunov region), where trajectories  $\alpha$  and  $\beta$  as well as their time-reversed are correlated. At the beginning of their first passage through the encounter region, the trajectories  $\alpha$  and  $\beta$  are located within a Fermi wavelength  $\lambda_F$ . Due to the chaotic motion, this phase-space distance increases exponentially along the

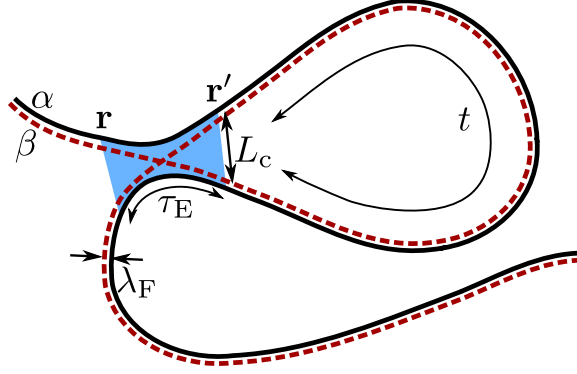


Figure 6.1.: Configurations of trajectories  $\alpha$  and  $\beta$  responsible for the weak antilocalization. We represent trajectories corresponding to retarded (advanced) Green functions as solid (dashed) lines. The trajectories consist of entrance/exit segment, a loop segment of variable duration  $t$ , and an encounter region, which allows for “pair switching” of the trajectories (indicated in blue). When trajectories are paired together, their allowed spatial separation is set by the Fermi wavelength  $\lambda_F$ . During the encounter region, this separation gets magnified to a classical size  $L_c$  beyond which the trajectories develop in an uncorrelated manner. The encounter is shown enlarged in the figure, in reality all four segments of trajectories within the encounter remain very close together, on a submacroscopic scale in phase space.

encounter region as  $d(t) = \lambda_F e^{\lambda t}$ , where  $\lambda$  is the Lyapunov coefficient characteristic of the chaotic motion. For the random Gaussian potential (6.8), the Lyapunov exponent is given by Eq. (6.34). At the end of the encounter region, the distance has reached a classical size  $L_c$ , beyond which classical motion is considered uncorrelated — *i.e.*, the classical dynamics can no longer be linearized. For the smooth random potential (6.8), we may identify  $L_c \simeq \xi$ . The duration of the encounter is set by the Ehrenfest time

$$\tau_E = \lambda^{-1} \ln(L_c/\lambda_F). \quad (6.41)$$

Our final results can be expressed in terms of Ehrenfest time only, which depends logarithmically on  $L_c$ , so that a more precise definition of the cutoff  $L_c$  is not needed.

For the calculation of the weak localization, one starts from the Kubo formula, Eq. (6.35), inserts the semiclassical expressions for the Green function, and then restricts the summation to configurations of trajectories as explained in the previous paragraph. As long as the duration of the encounter region is  $\tau_E$  or larger, the trajectories  $\alpha$  and  $\beta$  acquire an action difference  $\Delta\mathcal{S} \lesssim \hbar$  [Ale96, Rich02].

For graphene, we also have to keep track on the influence of the pseudospin, which has two effects: First, the spinor structure of the semiclassical Green function changes the velocity operator to the classical velocity, in the same way as before for the Drude conductance, see Eq. (6.37). Second, since the trajectories are no longer equal, we have to pay attention to the Berry phase collected along the trajectories  $\alpha$  and  $\beta$ . At this stage,

we can write

$$\begin{aligned} \delta G_{\text{WAL}} = & \frac{e^2 d_g}{(2\pi\hbar)^2} \int dy \int dy' \int d\varepsilon \left( -\frac{\partial f(\varepsilon)}{\partial \varepsilon} \right) \\ & \times \sum_{\alpha, \beta: (0, y') \rightarrow (L, y)} A_\alpha^2 v'_x v_x e^{i(\mathcal{S}_\alpha - \mathcal{S}_\beta)/\hbar} e^{i(\gamma_\alpha - \gamma_\beta)}, \end{aligned} \quad (6.42)$$

where the summation is restricted to the configurations of trajectories shown in Fig. 6.1, for which we have  $A_\alpha = A_\beta$ .

The difference of the Berry phase  $\Delta\gamma = \gamma_\alpha - \gamma_\beta$ , is collected in the loop segment only. (In the encounter region, the trajectories  $\alpha$  and  $\beta$  differ on a sub-macroscopic scale only, which adds a negligible contribution to the Berry phase difference.) Since the momenta of trajectory  $\alpha$  are opposite in the beginning and the end of the loop segment, we have from Eq. (6.6)

$$\gamma_{\alpha, \text{Loop}} = \pi \left( n + \frac{1}{2} \right), \quad (6.43)$$

with integer  $n$  depending on the total winding of the momentum along the trajectory. Since the Berry phase is expressed as integral along the trajectory, the Berry phase collected by trajectory  $\beta$  along the loop is just  $\gamma_{\beta, \text{Loop}} = -\gamma_{\alpha, \text{Loop}}$ . Hence, we find

$$e^{i\Delta\gamma} = -1 \quad (6.44)$$

for all configurations of trajectories contributing to the quantum correction. This minus sign is responsible for the change from weak localization (in conventional two-dimensional electron gases without spin-orbit coupling) to weak antilocalization.

The remaining calculation then proceeds as in the standard case, and we find [Brou 07]

$$\begin{aligned} \delta G_{\text{WAL}} = & -d_g \frac{e^2}{2\pi\hbar} \int d\mathbf{r} d\mathbf{r}' P_{\text{in}}(\mathbf{r}) P_{\text{out}}(\mathbf{r}) \partial_{\tau_E} P(\mathbf{r}', \mathbf{r}; \tau_E) \\ & \times \int dt P(\mathbf{r}', \mathbf{r}'; t) \end{aligned} \quad (6.45)$$

where  $P(\mathbf{r}', \mathbf{r}'; t)$  is the diffusion propagator, see Eq. (5.51), and  $P_{\text{in}}(\mathbf{r})$  and  $P_{\text{out}}(\mathbf{r})$  are defined in Eq. (5.54) in the previous chapter. For the further evaluation of Eq. (6.45), we can use the diffusion equation (5.50) to write

$$\partial_{\tau_E} P(\mathbf{r}', \mathbf{r}; \tau_E) = D \Delta_{\mathbf{r}} P(\mathbf{r}', \mathbf{r}; \tau_E) \quad (6.46)$$

and perform two partial integrations on  $\mathbf{r}$ . Making use of the explicit form of  $P_{\text{in}}(\mathbf{r})$  and  $P_{\text{out}}(\mathbf{r})$ , we arrive at

$$\delta G_{\text{WAL}} = \frac{e^2 d_g}{2\pi\hbar} \frac{2D}{L^2} \int d\mathbf{r} d\mathbf{r}' P(\mathbf{r}', \mathbf{r}; \tau_E) \int_{\tau_{\text{tr}}}^{\infty} dt P(\mathbf{r}', \mathbf{r}'; t) \quad (6.47)$$

In two dimensions, the time integral in this equation is divergent for small times, and the appropriate cutoff is set by the transport time  $\tau_{\text{tr}}$ , below which the diffusive approximation

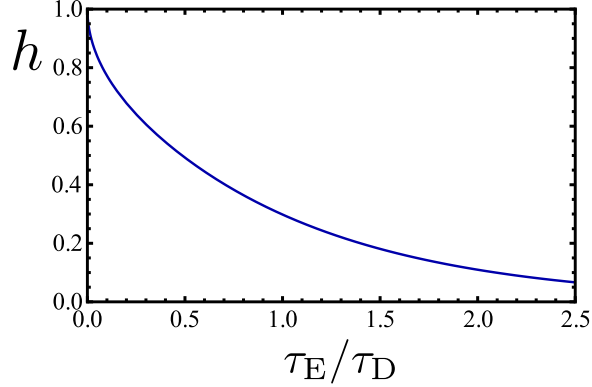


Figure 6.2.: At finite Ehrenfest time, weak antilocalization is suppressed by an additional factor  $h(\tau_E/\tau_D)$

breaks down. In the limit of large aspect ratio  $W/L$ , and small  $\tau_{\text{tr}}/\tau_D$ , where  $\tau_D = L^2/D\pi^2$  is the dwell time, we then find (see Appendix D.1)

$$\delta\sigma_{\text{WAL}} = \frac{e^2 d_g}{4\pi^2 \hbar} \ln(\tau_D/\tau_{\text{tr}}) h(\tau_E/\tau_D), \quad (6.48)$$

where the function  $h(x)$  is defined as

$$h(x) = \frac{8}{\pi^2} \sum_{\substack{n=1 \\ n \text{ odd}}}^{\infty} \frac{1}{n^2} e^{-n^2 x}. \quad (6.49)$$

It has the asymptotic behavior

$$h(x) = \begin{cases} 1 - \frac{4}{\pi^{3/2}} \sqrt{x}, & x \ll 1 \\ \frac{8}{\pi^2} e^{-x}, & x \gg 1. \end{cases} \quad (6.50)$$

At zero Ehrenfest time,  $h(0) = 1$  and we arrive at the well-known result for weak antilocalization of a symplectic metal [Hika 80]. At finite Ehrenfest time, our calculation results in a suppression of the weak antilocalization by the additional factor  $h(\tau_E/\tau_D)$ , shown in Fig. 6.2. (The same multiplicative factor  $h(\tau_E/\tau_D)$  describes the suppression of weak localization or weak antilocalization in a conventional two-dimensional electron gas. We are not aware of a calculation of the function  $h$  in this context.)

## 6.6. Altshuler-Aronov correction

We now turn to the effects of interactions on the conductivity. Interactions modify the conductivity in two physically distinct ways. First, interactions cause the so-called Altshuler-Aronov correction [Alts 79, Zala 01], which has its origin in the interference of elastic scattering off impurities and off Friedel oscillations of the electron density around an impurity.

Second, inelastic electron-electron scattering is responsible for a loss of phase coherence or “dephasing”, which sets an upper limit on the time at which weak (anti)localization can occur.

### 6.6.1. Lowest-order interaction correction

The semiclassical treatment of interaction corrections proceeds via two steps. First, one considers a specific random potential and includes interactions to first order diagrammatic perturbation theory. Such procedure is rather standard, and results in expressions in terms of Green functions  $\mathcal{G}(\mathbf{r}, \mathbf{r}'; \varepsilon)$  for the given disorder realization. The second step is to take the disorder average, where we employ the semiclassical framework. Hereto, we insert the semiclassical expressions for the Green functions and identify the relevant configurations of trajectories that contribute to the interaction corrections. Our results take into account the effects of a finite Ehrenfest time.

The calculation for the Altshuler-Aronov correction in graphene proceeds similar to the one for conventional metals presented in the previous chapter. Special attention has to be paid at the pseudospin structure. As before, explicit expressions for the Altshuler-Aronov conductance correction  $\delta G_{AA}$  are obtained from Eq. (6.35) upon replacing the retarded Green function  $\mathcal{G}^R(\mathbf{r}, \mathbf{r}'; \varepsilon)$  by  $\mathcal{G}^R(\mathbf{r}, \mathbf{r}'; \varepsilon) + \delta\mathcal{G}^{R,F}(\mathbf{r}, \mathbf{r}'; \varepsilon) + \delta\mathcal{G}^{R,H}(\mathbf{r}, \mathbf{r}'; \varepsilon)$ , and a similar replacement for the advanced Green function  $\mathcal{G}^A(\mathbf{r}, \mathbf{r}'; \varepsilon)$ , keeping terms to first order in the interaction only. The functions  $\delta\mathcal{G}^{R,F}(\mathbf{r}, \mathbf{r}'; \varepsilon)$  and  $\delta\mathcal{G}^{R,H}(\mathbf{r}, \mathbf{r}'; \varepsilon)$  are Fock and Hartree corrections to the single-particle Green function, respectively,

$$\begin{aligned} \delta\mathcal{G}_{\alpha\beta}^{R,F}(\mathbf{r}, \mathbf{r}'; \varepsilon) = & \sum_{\gamma\delta} \int \frac{d\omega}{4\pi i} \int d\mathbf{r}_1 d\mathbf{r}_2 \tanh\left(\frac{\omega - \varepsilon}{2T}\right) \mathcal{G}_{\alpha\gamma}^R(\mathbf{r}, \mathbf{r}_1; \varepsilon) \mathcal{G}_{\delta\beta}^R(\mathbf{r}_2, \mathbf{r}'; \varepsilon) \\ & \times \{U^A(\mathbf{r}_1, \mathbf{r}_2; \omega) \mathcal{G}_{\gamma\delta}^R(\mathbf{r}_1, \mathbf{r}_2; \varepsilon - \omega) - U^R(\mathbf{r}_1, \mathbf{r}_2; \omega) \mathcal{G}_{\gamma\delta}^A(\mathbf{r}_1, \mathbf{r}_2; \varepsilon - \omega)\}, \end{aligned} \quad (6.51)$$

$$\begin{aligned} \delta\mathcal{G}_{\alpha\beta}^{R,H}(\mathbf{r}, \mathbf{r}'; \varepsilon) = & -d_g \sum_{\gamma\delta} \int \frac{d\omega}{4\pi i} \int d\mathbf{r}_1 d\mathbf{r}_2 \tanh\left(\frac{\omega - \varepsilon}{2T}\right) \mathcal{G}_{\alpha\gamma}^R(\mathbf{r}, \mathbf{r}_1; \varepsilon) \mathcal{G}_{\gamma\beta}^R(\mathbf{r}_1, \mathbf{r}'; \varepsilon) \\ & \times \{U^A(\mathbf{r}_1, \mathbf{r}_2; 0) \mathcal{G}_{\delta\delta}^R(\mathbf{r}_2, \mathbf{r}_2; \varepsilon - \omega) - U^R(\mathbf{r}_1, \mathbf{r}_2; 0) \mathcal{G}_{\delta\delta}^A(\mathbf{r}_2, \mathbf{r}_2; \varepsilon - \omega)\}. \end{aligned} \quad (6.52)$$

In these expressions we wrote the pseudospin indices explicitly. We further allow for a frequency dependence of the interaction propagator  $U^R(\mathbf{r}_1, \mathbf{r}_2; \omega)$  to include the effect of dynamical screening. To first order in interaction we also obtain additional corrections to the conductance which are contributing to dephasing. These will be discussed in the next section.

Insertion of the semiclassical Green functions leads to a sum over four trajectories. Systematic contributions to  $\delta G_{AA}$  are obtained only if trajectories originating from retarded and advanced Green functions are paired up or if they undergo a small-angle encounter, as discussed in the previous chapter. We summarize the configurations of trajectories that are in line with these requirements for the Fock contribution to  $\delta G_{AA}$ , as found in the previous chapter, in Fig. 6.3. Here, configuration (a) originates from a term with three advanced Green functions and one retarded Green function. In this case, the three

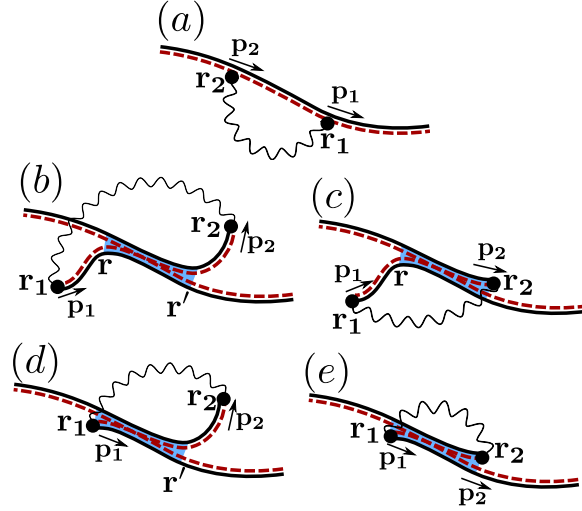


Figure 6.3.: Configurations of trajectories that contribute to the Fock contribution to the Altshuler-Aronov correction. “Retarded” and “advanced” trajectories are represented by solid and dashed lines, respectively. Encounter regions are indicated in blue.

“advanced” trajectories must join to a single trajectory that can be paired up with the “retarded” trajectory. Configurations (b)-(e) correspond to a term with two retarded and two advanced trajectories. In this situation, due to the specific requirements on start and end point of the Green functions, the trajectories cannot be paired one by one, instead the four trajectories undergo a small-angle encounter. The subdivision into configurations (b)-(e) reflects the possibilities to have none, one or both interaction points within the encounter region. For each one of the configurations shown in Fig. 6.3, there is a counterpart for which the role of retarded and advanced trajectories is interchanged.

In close analogy to the calculation for conventional electron gases, carried out in the previous chapter, we find, for a random potential with Gaussian correlations as in Eq. (6.8),

$$\delta G_{AA}^F = \frac{d_g \nu e^2}{2\pi \hbar^2} \int d\omega \frac{\partial}{\partial \omega} \left( \omega \coth \frac{\omega}{2T} \right) \int d\mathbf{r}_1 d\mathbf{r}_2 \times \text{Im} \{ U^R(\mathbf{r}_1, \mathbf{r}_2; \omega) K(\mathbf{r}_1, \mathbf{r}_2; \omega) \langle \Sigma_F(\mathbf{p}_1, \mathbf{p}_2) \rangle_{\mathbf{p}_1, \mathbf{p}_2} \}, \quad (6.53)$$

with the kernel  $K(\mathbf{r}_1, \mathbf{r}_2; \omega)$ , that contains the classical propagators, remains the same as for a conventional electron gas, derived in the previous chapter (Eq. (5.65)).

The spinor structure of the semiclassical Green function contributes the factor  $\Sigma_F(\mathbf{p}_1, \mathbf{p}_2)$ , which is not present in the calculation for the conventional two-dimensional electron gas. As explained in Fig. 6.4, it depends on the overlap of pseudospinors of the two trajectories at the interaction points. For the diffusive motion, only the quantity averaged over momenta  $\mathbf{p}_1$  and  $\mathbf{p}_2$  with  $|\mathbf{p}_1| = |\mathbf{p}_2| = p_F$  is relevant. For the Fock contribution, momentum does not change at the interaction points, see Fig. 6.3, and the spinors at the interaction



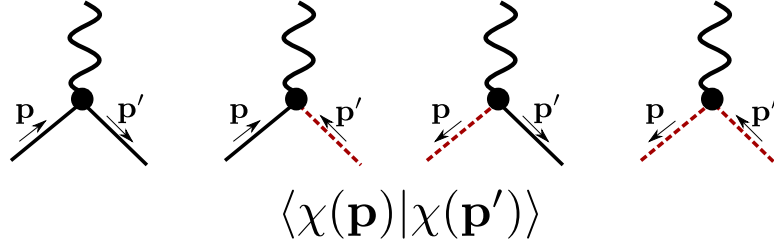


Figure 6.4.: For graphene, the pseudospin structure contributes additional factors associated with the interaction vertex. In our notation, the retarded Green function  $\mathcal{G}^R(\mathbf{r}_2, \mathbf{r}_1)$  is associated with trajectories running from  $\mathbf{r}_1$  to  $\mathbf{r}_2$ , while the advanced Green function  $\mathcal{G}^A(\mathbf{r}_2, \mathbf{r}_1)$  is associated with trajectories running from  $\mathbf{r}_2$  to  $\mathbf{r}_1$ . This amounts to the following possibilities: If the interaction vertex is associated with two Green functions of the same kind, then one trajectory is pointing towards the vertex, while the other one is pointing away. For an interaction vertex associated with one retarded and one advanced Green function, both trajectories either point towards or away from the vertex. In the figure, we show four possibilities that result in a factor  $\langle \chi(\mathbf{p}) | \chi(\mathbf{p}') \rangle$ , with the associated labelling of momenta.

points combine to a factor

$$\Sigma_F(\mathbf{p}_1, \mathbf{p}_2) = \langle \chi(\mathbf{p}_1) | \chi(\mathbf{p}_1) \rangle \langle \chi(\mathbf{p}_2) | \chi(\mathbf{p}_2) \rangle = 1. \quad (6.54)$$

Thus, up to the degeneracy  $d_g$ , the result for the Fock contribution remains unchanged as compared to the conventional metal. The spinor structure will however influence the Hartree contribution  $\delta G_{AA}^H$ , as we now show.

The relevant trajectory configurations for the Hartree correction remain the same as in the previous chapter, and are shown again in Fig. 6.5. There is a one-to-one correspondence between the trajectory configurations for the Fock and Hartree contributions. The important thing however is that, unlike for the Fock contribution, the configurations for the Hartree contribution involve a finite-angle crossing at momenta  $\mathbf{p}_1$  and  $\mathbf{p}_2$ , which has two important consequences: First, it leads to an additional difference in the classical actions of the trajectories, resulting in the fast-oscillating factor  $e^{i(\mathbf{p}_1 - \mathbf{p}_2)(\mathbf{r}_1 - \mathbf{r}_2)/\hbar}$ . Such factor also enforces the interaction points  $\mathbf{r}_1$  and  $\mathbf{r}_2$  to remain close together on a scale of the Fermi wavelength. Since the function  $K(\mathbf{r}_1, \mathbf{r}_2; \omega)$  is built from classical propagators that are smooth on the scale of Fermi wavelength, we can identify  $\mathbf{r}_1 = \mathbf{r}_2$  for this function. This effect was present also for the conventional metals. Second, the spinor structure from the interaction vertices now results in the nontrivial factor

$$\Sigma_H(\mathbf{p}_1, \mathbf{p}_2) = \langle \chi(\mathbf{p}_1) | \chi(\mathbf{p}_2) \rangle \langle \chi(\mathbf{p}_2) | \chi(\mathbf{p}_1) \rangle = \cos^2 \left( \frac{\phi_{\mathbf{p}_1} - \phi_{\mathbf{p}_2}}{2} \right). \quad (6.55)$$

This result indeed reflects the chiral nature of the charge carriers, leading to a suppression of backward scattering processes.

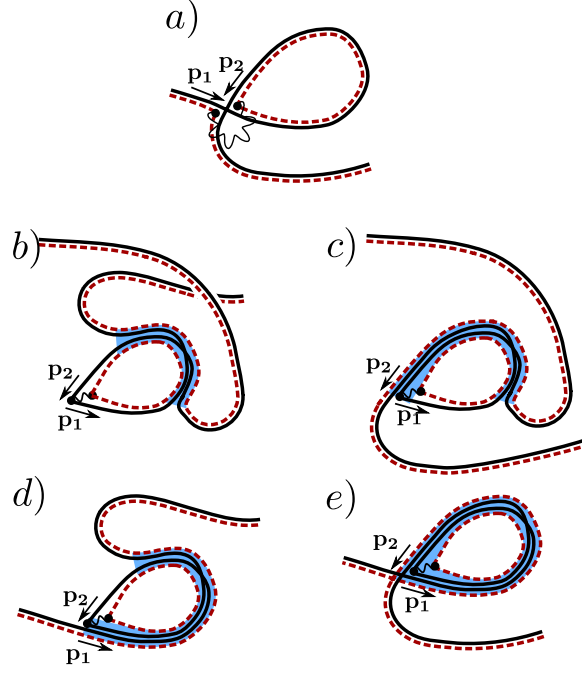


Figure 6.5.: Configurations of trajectories that contribute to the Hartree contribution to the Altshuler-Aronov correction. There is a one-to-one correspondence between the configurations for the Hartree and the Fock contribution, Fig. 6.3.

Combining everything, the Hartree contribution can be obtained from the Fock contribution by the replacement

$$U^R(\mathbf{r}_1, \mathbf{r}_2; \omega) \rightarrow -d_g \delta(\mathbf{r}_1 - \mathbf{r}_2) \langle U(\mathbf{p}_1 - \mathbf{p}_2; \omega = 0) \Sigma_H(\mathbf{p}_1, \mathbf{p}_2) \rangle_{\mathbf{p}_1, \mathbf{p}_2} \quad (6.56)$$

where the factor  $d_g$  comes from the existence of a closed trajectory-loop in the configurations of Fig. 6.5, and with the Fourier-transformed interaction

$$U^R(\mathbf{q}; \omega) = \int d\mathbf{r} e^{i\mathbf{q}\mathbf{r}/\hbar} U^R(\mathbf{r}; \omega). \quad (6.57)$$

For a short-range potential  $U(\mathbf{r}_1 - \mathbf{r}_2) \propto \delta(\mathbf{r}_1 - \mathbf{r}_2)$ , we then find  $\delta G_{AA}^H = -(d_g/2)\delta G_{AA}^F$ : The spin and valley degeneracies enhance the Hartree contribution by an extra factor  $d_g = 4$  compared to the Fock contribution, while chirality reduces it by a factor two [Kozi 10, Jobs 12].

Substituting the explicit expressions for the diffusion propagators, the final result for the interaction correction to the conductivity reads

$$\delta\sigma_{AA} = -\frac{d_g e^2 \nu D}{\pi \hbar^2} \int d\omega \frac{\partial}{\partial \omega} \left( \omega \coth \frac{\omega}{2T} \right) \text{Im} \left\{ \int \frac{d^2 \mathbf{q}}{(2\pi)^2} \mathcal{U}^R(\mathbf{q}; \omega) \frac{D q^2 e^{i\omega \tau_E} e^{-D \mathbf{q}^2 \tau_E}}{(D \mathbf{q}^2 - i\omega/\hbar)^3} \right\}, \quad (6.58)$$

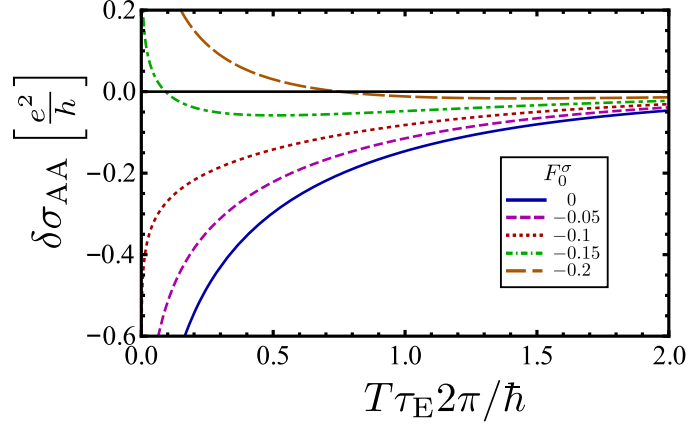


Figure 6.6.: Altshuler-Aronov correction as a function of  $T\tau_E 2\pi/\hbar$ . Different curves correspond to different values of the interaction parameter  $F_0^\sigma$ .

with the effective interaction kernel

$$\mathcal{U}^R(\mathbf{q}; \omega) = U^R(\mathbf{q}, \omega) - d_g \langle U^R(\mathbf{p}_1 - \mathbf{p}_2; 0) \Sigma_H(\mathbf{p}_1, \mathbf{p}_2) \rangle_{\mathbf{p}_1, \mathbf{p}_2}. \quad (6.59)$$

### 6.6.2. Coulomb interaction

The Coulomb interaction,  $U_C(\mathbf{r}_1, \mathbf{r}_2) = e^2/|\mathbf{r}_1 - \mathbf{r}_2|$  is long-ranged, and screening effects need to be incorporated into the results of the previous section. Similar to the case of normal metals, the structure for the result for the interaction correction remains similar, but the effective interaction kernel needs to be modified. The calculation proceeds analogous to the one presented in Sec. 5.2.5, but we have to keep track on the chiral nature of particles as well as the valley degrees of freedom. The combination of spin and valley degrees of freedom result in a total number of  $d_g \times d_g = 16$  channels for two-particle scattering processes. The long-range nature of the Coulomb interaction affects only the total singlet channel, while the remaining  $d_g^2 - 1$  channels are determined by an effective Fermi liquid parameter  $F_0^\sigma$  (which we assume to be the same in all non-singlet channels). The value of  $F_0^\sigma$  is also influenced by the chiral nature of the quasiparticles in graphene, as will be discussed below. For Coulomb interaction, the effective interaction kernel for graphene then reads

$$\mathcal{U}^R(\mathbf{q}; \omega) = \frac{1}{d_g \nu} \frac{\hbar D \mathbf{q}^2 - i\omega}{\hbar D \mathbf{q}^2} + (d_g^2 - 1) \frac{F_0^\sigma (\hbar D \mathbf{q}^2 - i\omega)}{d_g \nu [\hbar D \mathbf{q}^2 (1 + F_0^\sigma) - i\omega]}, \quad (6.60)$$

which generalizes Eqs. (5.36), (5.60), and (5.61) that were obtained for normal metals.

We plot the Altshuler-Aronov correction for various values of the interaction constant  $F_0^\sigma$  in Fig. 6.6. For small Ehrenfest time, one finds

$$\delta\sigma_{AA} = -\frac{e^2}{\pi\hbar} \left[ 1 + c \left( 1 - \frac{\ln(1 + F_0^\sigma)}{F_0^\sigma} \right) \right] \ln \frac{\hbar}{2\pi T \tau_E}, \quad (6.61)$$

with  $c = d_g^2 - 1$ . Such an expression is well-known from diagrammatic perturbation theory [Alts 85b], where in our case, the Ehrenfest time takes over the role of the elastic scattering time as a short-time cutoff. The graphene-specific physics enters the result in two ways [Kozi 10, Jobs 12]: First, the constant  $c = d_g^2 - 1$  is 15 for graphene with only smooth disorder, in contrast to  $c = 3$  for conventional metals without valley degeneracy. Second, chirality affects the interaction constant  $F_0^\sigma$ , as will be explained in more detail below. For small values of  $F_0^\sigma$ , the singlet contribution is dominant in Eq. (6.61), giving rise to a negative correction to the conductance. On the other hand, for graphene, for  $F_0^\sigma \lesssim -0.12$ , the non-singlet channels render the interaction correction positive.

For large Ehrenfest time, we find an exponential suppression

$$\delta\sigma_{AA} = -\frac{e^2}{\pi h} e^{-2\pi T\tau_E/\hbar} \quad (6.62)$$

where the prefactor of the exponential is determined by the singlet channel only to leading order in  $\hbar/T\tau_E$ , hence at large Ehrenfest times,  $\delta G_{AA}$  is negative and has a universal behavior.

A striking consequence of this asymptotics is a sign-change of the interaction correction as a function of Ehrenfest time, provided the Fermi-liquid-type interactions in the non-singlet channels are strong enough. For graphene ( $c = 15$ ) this sign change already takes place at  $F_0^\sigma \lesssim -0.12$ , in contrast to a conventional metal ( $c = 3$ ) where the sign change is observed for  $F_0^\sigma \lesssim -0.45$ . On the other hand, the values for  $F_0^\sigma$  are typically somewhat smaller in graphene, as can be seen using Thomas-Fermi approximation [Kozi 10, Jobs 12]. For conventional metals, one has

$$F_0^\sigma = -\nu \left\langle \frac{2\pi e_\star^2}{|\mathbf{p}_1 - \mathbf{p}_2| + \kappa} \right\rangle_{\mathbf{p}_1, \mathbf{p}_2}, \quad (6.63)$$

where  $e_\star$  is the charge screened by the substrate, and  $\kappa = 2 \times 2\pi\nu e_\star^2$  is the inverse screening length resulting from the metal electrons (a factor 2 accounts for spin). We then find

$$F_0^\sigma = -\nu \int_0^\pi \frac{d\theta}{\pi} \frac{2\pi e_\star^2}{2k_F \sin \frac{\theta}{2} + 4\pi\nu e_\star^2} = -\int_0^\pi \frac{d\theta}{\pi} \frac{\alpha}{2 \sin \frac{\theta}{2} + 2\alpha}, \quad (6.64)$$

where  $\theta$  is the angle between the directions of momenta  $\mathbf{p}_1$  and  $\mathbf{p}_2$ . We further used  $k_F = 2\pi\nu\hbar v_F$ , as well as the “effective fine structure constant”  $\alpha = e_\star^2/\hbar v_F$ . The gas parameter  $r_s$  is related to  $\alpha$  as  $r_s = \sqrt{2}\alpha$ . For a value  $r_s \approx 1$  we obtain  $F_0^\sigma \approx -0.28$  as a typical size for the Fermi liquid parameter.

For graphene, this calculation needs to be modified in two respects. First, the inverse screening length is twice larger, due to the valley degree of freedom. Second, chirality contributes the additional factor  $\Sigma_H(\mathbf{p}_1, \mathbf{p}_2) = \cos^2(\theta/2)$ . Both effects reduce the interaction in the non-singlet channel,

$$F_0^\sigma = -\int_0^\pi \frac{d\theta}{\pi} \frac{\alpha \cos^2 \frac{\theta}{2}}{2 \sin \frac{\theta}{2} + 4\alpha}, \quad (6.65)$$

so that now for  $r_s \approx 1$  we find  $F_0^\sigma \approx -0.1$ , which is close to the transition point for a sign-change as function of Ehrenfest time. The measurements of Ref. [Kozi 10, Joua 11,

Jobs 12] report  $F_0^\sigma$  in a range between  $-0.05$  and  $-0.15$ . However, we note that our theory requires graphene with a smooth disorder potential, but no other perturbations, as a necessary condition for the value  $c = 15$  in Eq. (6.61), since there are 16 diffusion channels. Trigonal warping or ripples, while not invalidating the semiclassical analysis, reduce the number of diffusive channels to 8, resulting in a prefactor  $c = 7$ . In case of strong intervalley scattering, only four diffusion modes are present resulting in a prefactor  $c = 3$  (see Ref. [Kech 08, Khar 08]) — although in that case the conditions for the semiclassical analysis are no longer valid. The aforementioned experiments on interaction corrections report to be in a regime where  $c = 3$  or  $c = 7$ .

## 6.7. Dephasing

We now turn to the second type of interaction correction, responsible for the dephasing. The way of calculating the dephasing in this section follows that of Ref. [Alts 82]. An alternative discussion based on perturbation theory, similar to that of the previous Section, is given in the appendix.

Because of the interactions, the electrons are subject to a time-dependent potential  $V(\mathbf{r}, t)$ . This potential affects the phase that electrons accumulate while propagating through the sample. These phase fluctuations can be included into the classical action  $\mathcal{S}_\alpha$  of the trajectory  $\alpha$  as it appears in the semiclassical expression (6.4) for the Green function by the substitution

$$\mathcal{S}_\alpha \rightarrow \mathcal{S}_\alpha + \delta\mathcal{S}_\alpha(t), \quad (6.66)$$

where the correction  $\delta\mathcal{S}_\alpha(t)$  depends on the time  $t$  at which the electron exits the sample. The shift reads [Alts 82, Alt1 07]

$$\delta\mathcal{S}_\alpha(t) = \int_{t-\tau_\alpha}^t dt' V[\mathbf{r}_\alpha(t'), t'], \quad (6.67)$$

where  $\tau_\alpha$  is the duration of the trajectory  $\alpha$ .

Such a shift of the classical actions does not affect the Drude conductivity, because the actions from the “retarded” and “advanced” trajectories cancel. It does, however, affect the weak antilocalization correction. Equation (6.42) acquires an additional factor  $e^{i(\delta\mathcal{S}_\alpha(t) - \delta\mathcal{S}_\beta(t))}$  which, when averaged over the time  $t$ , reduces the contribution from the trajectory pair  $\alpha, \beta$  by a factor

$$\left\langle e^{i(\delta\mathcal{S}_\alpha(t) - \delta\mathcal{S}_\beta(t))/\hbar} \right\rangle_t = e^{-(1/2\hbar^2)\langle(\delta\mathcal{S}_\alpha(t) - \delta\mathcal{S}_\beta(t))^2\rangle_t}. \quad (6.68)$$

The time average can be calculated using the quantum fluctuation-dissipation theorem,

$$\langle V(\mathbf{r}, t) V(\mathbf{r}', t') \rangle = \int \frac{d^2\mathbf{q} d\omega}{(2\pi)^3} \frac{\omega}{2T \sinh^2(\omega/2T)} e^{i\mathbf{q} \cdot (\mathbf{r} - \mathbf{r}') - i\omega(t - t')} \text{Im } U^R(\mathbf{q}, \omega),$$

which gives

$$\begin{aligned} \frac{1}{2} \langle ((\delta\mathcal{S}_\alpha(t) - \delta\mathcal{S}_\beta(t))^2) \rangle_t &= \int_0^{\tau_\alpha} dt_1 \int_0^{t_1} dt_2 \int \frac{d^2\mathbf{q} d\omega}{(2\pi)^3} \frac{\omega}{2T \sinh^2(\omega/2T)} \text{Im } U^R(\mathbf{q}, \omega) \\ &\times \text{Re} \left[ e^{-i\omega(t_1 - t_2)} \left( e^{i\mathbf{q} \cdot \mathbf{r}_\alpha(t_1)} - e^{i\mathbf{q} \cdot \mathbf{r}_\beta(t_1)} \right) \left( e^{-i\mathbf{q} \cdot \mathbf{r}_\alpha(t_2)} - e^{-i\mathbf{q} \cdot \mathbf{r}_\beta(t_2)} \right) \right]. \end{aligned} \quad (6.69)$$

(Note that  $\tau_\alpha = \tau_\beta$  for the trajectory pairs that contribute to weak antilocalization.) One immediately concludes that for the trajectories  $\alpha$  and  $\beta$  that contribute to the weak antilocalization correction  $\delta G_{\text{WAL}}$  only points  $\mathbf{r}_\alpha$  or  $\mathbf{r}_\beta$  in the loop or encounter segments of Fig. 6.1 contribute to  $\langle (\delta \mathcal{S}_\alpha(t) - \delta \mathcal{S}_\beta(t))^2 \rangle_t$ .

To find an explicit expression for the dephasing correction in the limit of weak dephasing, we expand the correction factor (6.68) to lowest order in the interaction  $U^R(\mathbf{q}, \omega)$  and calculate the leading interaction correction  $\delta G_{\text{deph}}$  to the weak antilocalization correction  $\delta G_{\text{WAL}}$ . We consider contributions from positions  $\mathbf{r}_{\alpha,\beta}(t_1)$  and  $\mathbf{r}_{\alpha,\beta}(t_2)$  in the loop and encounter regions separately.

The calculation for the dephasing in the loop segment is very similar to the one carried out in standard diagrammatic perturbation theory. The discussion below closely follows that of Ref. [Marq 07]. With both positions  $\mathbf{r}_{\alpha,\beta}(t_{1,2})$  in the loop region, see Fig. 6.7, we find that dephasing in the loop segment leads to the replacement  $P(\mathbf{r}', \mathbf{r}'; t) \rightarrow P(\mathbf{r}', \mathbf{r}'; t) + \delta P(\mathbf{r}', \mathbf{r}'; t)$  for the loop propagator in Eq. (6.47), with

$$\begin{aligned} \delta P(\mathbf{r}', \mathbf{r}'; t) = & -\frac{4}{\hbar^2} \int \frac{d\mathbf{q}}{(2\pi)^2} \int \frac{d\omega}{2\pi} \frac{\omega \text{Im} U^R(\mathbf{q}; \omega)}{2T \sinh^2(\omega/2T)} \\ & \times \int_0^t dt_1 \int_0^{\min(t_1, t-t_1)} dt_2 \cos[\omega(t_1 - t_2)/\hbar] \\ & \times [\mathcal{P}_{\mathbf{q}}(t_2, t_1 - t_2, t - t_1) - \mathcal{P}_{\mathbf{q}}(t_2, t - t_1 - t_2, t_1)], \end{aligned} \quad (6.70)$$

where

$$\mathcal{P}_{\mathbf{q}}(\tau_1, \tau_2, \tau_3) = \int d\mathbf{r}_1 d\mathbf{r}_2 \cos[\mathbf{q} \cdot (\mathbf{r}_1 - \mathbf{r}_2)] P(\mathbf{r}', \mathbf{r}_2, \tau_3) P(\mathbf{r}_2, \mathbf{r}_1, \tau_2) P(\mathbf{r}_1, \mathbf{r}', \tau_1). \quad (6.71)$$

Inserting the diffusion propagator  $P(\mathbf{q}, \tau) = e^{-Dq^2\tau}$ , one finds

$$\mathcal{P}_{\mathbf{q}}(\tau_1, \tau_2, \tau_3) = P(\mathbf{r}', \mathbf{r}'; t) e^{-Dq^2\tau_2(1-\tau_2/t)}, \quad (6.72)$$

with  $t = \tau_1 + \tau_2 + \tau_3$ . After insertion of the interaction (6.60) and evaluation of the integrals over time, frequency, and momentum in Eq. (6.70) (see Appendix D.3), one finds

$$\frac{\delta P(\mathbf{r}', \mathbf{r}'; t)}{P(\mathbf{r}', \mathbf{r}'; t)} = -\frac{\alpha t T}{\hbar g_0} \ln \frac{t T}{\hbar}, \quad (6.73)$$

with the dimensionless conductance  $g_0 = 2\pi\hbar d_g \nu D$ , and the constant

$$\alpha = 1 + (d_g^2 - 1) \frac{(F_0^\sigma)^2}{(1 + F_0^\sigma)(2 + F_0^\sigma)}. \quad (6.74)$$

This result signifies that at large times the loop propagator gets suppressed by interactions. Here we calculated the leading order correction, describing the onset of an exponential suppression. (In fact, in two dimensions the decay is not purely exponential [Marq 07], but contains an additional logarithm  $e^{-at \ln t}$ , as can be seen from Eq. (6.73)). We estimate the dephasing rate as the time when the leading correction becomes unity, *i.e.*,

$$\frac{1}{\tau_\varphi^{\text{loop}}} \simeq \frac{\alpha T}{g_0 \hbar} \ln \frac{g_0}{\alpha}. \quad (6.75)$$

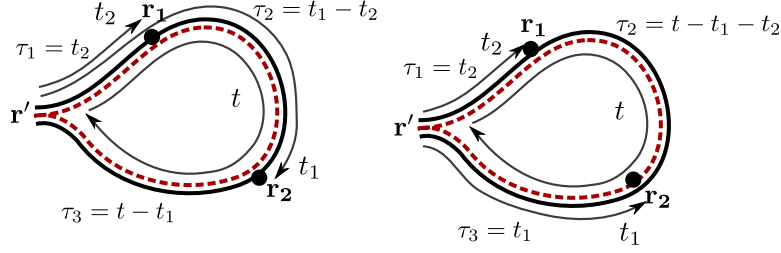


Figure 6.7.: Dephasing in the loop segment: for the calculation of the lowest-order interaction correction the propagation around the loop is split into three segments  $\mathbf{r}' \rightarrow \mathbf{r}_1$  (duration  $\tau_1$ ),  $\mathbf{r}_1 \rightarrow \mathbf{r}_2$  (duration  $\tau_2$ ), and  $\mathbf{r}_2 \rightarrow \mathbf{r}'$  (duration  $\tau_3$ ). For our figure, the trajectories  $\alpha$  (solid) and  $\beta$  (dashed) are travelled in clockwise and counterclockwise direction, respectively. The left diagram represents the contribution from the term proportional to  $e^{i\mathbf{q}\cdot\mathbf{r}_\alpha(t_1)-i\mathbf{q}\cdot\mathbf{r}_\alpha(t_2)}$  in Eq. (6.69); the right diagram represents the contribution from the term proportional to  $e^{i\mathbf{q}\cdot\mathbf{r}_\beta(t_1)-i\mathbf{q}\cdot\mathbf{r}_\alpha(t_2)}$ . The remaining two contributions, from terms proportional to  $e^{i\mathbf{q}\cdot\mathbf{r}_\alpha(t_1)-i\mathbf{q}\cdot\mathbf{r}_\beta(t_2)}$  and  $e^{i\mathbf{q}\cdot\mathbf{r}_\beta(t_1)-i\mathbf{q}\cdot\mathbf{r}_\beta(t_2)}$  are not shown. The figures have been drawn for the case that  $0 < t_2 < \min(t_1, t - t_1)$ , which is the domain of integration in Eq. (6.70).

The leading logarithmic dependence in this expression agrees with that obtained in Ref. [Naro 02] for a standard two-dimensional electron gas ( $d_g = 2$ ).

We now turn to the encounter region, where dephasing leads to an additional suppression of weak antilocalization, if the typical time for the encounter passage, the Ehrenfest time  $\tau_E$ , is sufficiently long. As discussed before, dephasing is ineffective, as long as the trajectories coincide. Within the encounter region, the trajectories  $\alpha$  and  $\beta$  are separated by a small distance, which does not exceed the classical correlation scale  $L_c$ . Dephasing then only plays a role for interaction that transfers a momentum larger than inverse mean free path, and therefore can resolve such small distance [Alt 07, Peti 07, Whit 08]. On the other hand, for low temperatures  $T\tau \ll 1$  one has  $\omega\tau \ll 1$ . In this limit, the imaginary part of the screened interaction reads [Zala 01]

$$\text{Im}U^R(\mathbf{q}; \omega) = -\frac{\beta\omega}{qd_g\hbar\nu_F}, \quad (6.76)$$

where  $\nu = k_F/2\pi\hbar\nu_F$  is the density of states and we abbreviated

$$\beta = 1 + (d_g^2 - 1)\frac{(F_0^\sigma)^2}{(1 + F_0^\sigma)^2}. \quad (6.77)$$

Note that  $\text{Im}U^R(\mathbf{q}; \omega)$  is proportional to  $q^{-1}$ , which is different from the dependence  $\text{Im}U^R(\mathbf{q}; \omega) \propto q^{-2}$  of the diffusive limit. This difference will result a different  $T$ -dependence of the dephasing rate in comparison to the loop contribution [Alt 07].

We proceed by the integration over  $\omega$ , which can be done explicitly using the known  $\omega$

dependence of  $\text{Im}U^R(\mathbf{q}; \omega)$  [Marq 07],

$$\int \frac{d\omega}{2\pi} \frac{\omega^2 e^{-i\omega(t_1-t_2)/\hbar}}{2T \sinh^2(\omega/2T)} = 2\pi T^2 w[\pi T(t_1 - t_2)/\hbar]. \quad (6.78)$$

Here the function  $w(x) = (x \coth x - 1)/\sinh^2 x$  is peaked around  $x = 0$ , normalized  $\int_{-\infty}^{\infty} dx w(x) = 1$ , and  $w(0) = 1/3$ . Hence, the times  $t_1$  and  $t_2$  need to be close together on the scale of inverse temperature. On the other hand, dephasing sets in on times much larger than  $T^{-1}$ , as we will show below. In the following, we therefore may assume that  $|t_1 - t_2| \ll \tau_E$ , when we consider encounters that are long enough to be affected by dephasing. (In fact, the calculation below will show that the main contribution stems from time differences  $|t_1 - t_2|$  much smaller than the elastic mean free time.) In particular this amounts to consider the effect of interaction during the first and second passage through the encounter separately, since they are separated by a loop of long duration. The same observation also allows us to neglect contributions where  $t_1$  is in the encounter, whereas  $t_2$  is in the loop or vice versa. We therefore focus on the first passage through the encounter region, where the trajectories  $\alpha$  and  $\beta$  are separated by a distance  $\mathbf{d}(t) = \mathbf{r}_\beta(t) - \mathbf{r}_\alpha(t)$ , with the magnitude

$$d(t) \simeq \lambda_F e^{\lambda t}, \quad (6.79)$$

where  $t$  is varying from 0 to  $\tau_E$ . We can use this to rewrite the last two factors of Eq. (6.69) as

$$\begin{aligned} & (e^{i\mathbf{q} \cdot \mathbf{r}_\alpha(t_1)} - e^{i\mathbf{q} \cdot \mathbf{r}_\beta(t_1)})(e^{-i\mathbf{q} \cdot \mathbf{r}_\alpha(t_2)} - e^{-i\mathbf{q} \cdot \mathbf{r}_\beta(t_2)}) \\ &= 4e^{i\mathbf{q} \cdot [\bar{\mathbf{r}}(t_1) - \bar{\mathbf{r}}(t_2)]} \sin[\mathbf{q} \cdot \mathbf{d}(t_1)/2] \sin[\mathbf{q} \cdot \mathbf{d}(t_2)/2], \end{aligned} \quad (6.80)$$

where  $\bar{\mathbf{r}}(t) = [\mathbf{r}_\alpha(t) + \mathbf{r}_\beta(t)]/2$  represents a trajectory intermediate between  $\alpha$  and  $\beta$ .

After performing the average over disorder configurations, we find that inclusion of the leading-order dephasing correction amounts to the replacement  $P(\mathbf{r}', \mathbf{r}; \tau_E) \rightarrow P(\mathbf{r}', \mathbf{r}; \tau_E) + 2\delta P(\mathbf{r}', \mathbf{r}; \tau_E)$  in Eq. (6.47), where the factor two accounts for the two passages through the encounter region, with

$$\begin{aligned} \delta P(\mathbf{r}', \mathbf{r}; \tau_E) &= -\frac{8\pi T^2 \beta}{\hbar^3 v_F d_g \nu} \int \frac{d^2 \mathbf{q}}{(2\pi)^2} \frac{1}{q} \int_0^{\tau_E} dt_1 \int_0^{t_1} dt_2 w(\pi T(t_1 - t_2)/\hbar) \\ &\quad \times \mathcal{P}_{\mathbf{q}}^{\text{enc}}(t_1, t_2, \tau_E - t_1 - t_2) \sin[\mathbf{q} \cdot \mathbf{d}(t_1)/2] \sin[\mathbf{q} \cdot \mathbf{d}(t_2)/2] \end{aligned} \quad (6.81)$$

and

$$\begin{aligned} \mathcal{P}_{\mathbf{q}}^{\text{enc}}(t_1, t_2, \tau_E - t_1 - t_2) &= \int d\mathbf{r}_1 d\mathbf{r}_2 \cos[\mathbf{q} \cdot (\mathbf{r}_1 - \mathbf{r}_2)] \\ &\quad \times P(\mathbf{r}', \mathbf{r}_2, \tau_E - t_1) P(\mathbf{r}_2, \mathbf{r}_1, t_1 - t_2) P(\mathbf{r}_1, \mathbf{r}, t_2), \end{aligned} \quad (6.82)$$

see Fig. 6.8. Because of the smallness of  $|t_1 - t_2|$ , the propagator  $P(\mathbf{r}_2, \mathbf{r}_1, t_1 - t_2)$  is the ballistic propagator, whereas the propagators  $P(\mathbf{r}', \mathbf{r}_2, \tau_E - t_1)$  and  $P(\mathbf{r}_1, \mathbf{r}, t_2)$  can be taken in the diffusion approximation. We change the integration variables to the mean time  $\bar{t}$  and the difference time  $t = t_1 - t_2$ . Again using the smallness of  $|t_1 - t_2|$ , we replace  $\mathbf{d}(t_1)$  and  $\mathbf{d}(t_2)$  by  $\mathbf{d}(\bar{t})$ . We neglect correlations between  $\mathbf{d}(\bar{t})$  and the direction of the velocity



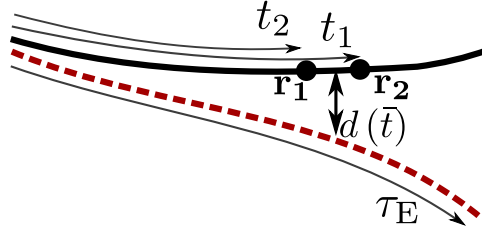


Figure 6.8.: Dephasing in the encounter segment: For the calculation, the encounter is split into three segments  $\mathbf{r}' \rightarrow \mathbf{r}_1$  (duration  $\tau_1 = t_2$ ),  $\mathbf{r}_1 \rightarrow \mathbf{r}_2$  (duration  $\tau_2 = t_1 - t_2$ ), and  $\mathbf{r}_2 \rightarrow \mathbf{r}'$  (duration  $\tau_3 = \tau_E - t_2$ ). Only configurations in which  $|t_1 - t_2| \ll \tau_E$  contribute to the interaction correction  $\delta G_{\text{deph}}$ . In the middle segment, the distance between the trajectories  $\alpha$  and  $\beta$  is  $d(\bar{t}) = \lambda_F e^{\lambda \bar{t}}$ , where  $\bar{t} = (t_1 + t_2)/2$ . The figure has been drawn for the case  $0 < t_2 < t_1$ , which is the domain of integration in Eq. (6.81)

at time  $\bar{t}$ . Using  $P(\mathbf{r}_1, \mathbf{r}, t_2) \simeq P(\mathbf{r}_2, \mathbf{r}, t_1)$ , again because of the smallness of  $|t_1 - t_2|$ , we find

$$\mathcal{P}_{\mathbf{q}}^{\text{enc}}(t_1, t_2, \tau_E - t_1 - t_2) \simeq P(\mathbf{r}', \mathbf{r}; \tau_E) J_0(v_F q |t|), \quad (6.83)$$

where we inserted the Fourier transform of the ballistic propagator. Since the integration over  $t$  converges for  $|t| \sim 1/v_F q$ , the argument of the function  $w$  may be set to zero in Eq. (6.81). Finally, the angular average over the direction of  $\mathbf{d}(\bar{t})$  gives a factor  $1 - J_0(qd(\bar{t}))$ , so that we find

$$\delta P(\mathbf{r}', \mathbf{r}; \tau_E) = -\frac{4\pi T^2 \beta}{3\hbar^3 v_F^2 d_g \nu} P(\mathbf{r}', \mathbf{r}; \tau_E) \int \frac{d^2 \mathbf{q}}{(2\pi)^2} \frac{1}{q^2} \int_0^{\tau_E} d\bar{t} [1 - J_0(qd(\bar{t}))], \quad (6.84)$$

We cut off the logarithmic divergence of the  $\mathbf{q}$  integration at large  $q$  at  $\lambda_F^{-1}$ , which gives

$$\delta P(\mathbf{r}', \mathbf{r}; \tau_E) = -\frac{2T^2 \beta}{3\hbar^3 v_F^2 d_g \nu} P(\mathbf{r}', \mathbf{r}; \tau_E) \int_0^{\tau_E} d\bar{t} \ln \frac{d(\bar{t})}{\lambda_F}.$$

The remaining time-integration is easily evaluated with the help of Eqs. (6.79), (6.41), and we obtain

$$\int_0^{\tau_E} d\bar{t} \ln \frac{d(\bar{t})}{\lambda_F} = \frac{\tau_E}{2} \ln \frac{L_c}{\lambda_F}. \quad (6.85)$$

Hence, our the final result reads

$$\frac{\delta P(\mathbf{r}', \mathbf{r}; \tau_E)}{P(\mathbf{r}', \mathbf{r}; \tau_E)} = -\frac{T^2 \beta \tau_E}{3\hbar^3 v_F^2 d_g \nu} \ln \frac{L_c}{\lambda_F}. \quad (6.86)$$

One may identify the right-hand side of Eq. (6.86) with  $\tau_E/\tau_\varphi^{\text{enc}}$ , where  $\tau_\varphi^{\text{enc}}$  is an effective dephasing time for the encounter region. With this identification, Eq. (6.86) describes the onset of an exponential suppression of the weak localization  $\propto e^{-2\tau_E/\tau_\varphi^{\text{enc}}}$  at large Ehrenfest times. Note that the time  $\tau_\varphi^{\text{enc}}$  is *twice* the dephasing time  $\tau_\varphi^{\text{ball}}$  that one finds

from dephasing in the loop region in the ballistic regime [Naro 02], consistent with the theory of Ref. [Alt1 07]. [To compare with Ref. [Naro 02], take the energy-dependent dephasing time  $\tau_\varphi(\varepsilon)$  from Eqs. (18) and (19a) of Ref. [Naro 02] in the limit  $T\tau \ll \hbar$  and calculate  $(\tau_\varphi^{\text{ball}})^{-1} = \int d\varepsilon (-\partial f / \partial \varepsilon) \tau_\varphi(\varepsilon)^{-1}$  with, for a conventional metal,  $d_g = 2$ . The low-momentum cut-off in Ref. [Naro 02] is the inverse mean free path, whereas it is the classical correlation length  $L_c$  in our case. The two lengths need not be equal, see Eq. (6.17).]

## 6.8. Conclusion

In this chapter we have presented a trajectory-based semiclassical theory of the quantum corrections to transport in graphene in the presence of a random potential that is smooth on the scale of the Fermi wavelength. A prominent role is played by the Ehrenfest time, which serves as a short-time threshold for the appearance of quantum interference effects. The Ehrenfest time also plays an important role for electrons in a conventional two-dimensional electron gas (with quadratic dispersion) if they are subject to a smooth random potential.

Compared to the conventional case, charge carriers in graphene have an additional pseudospin degree of freedom and they have an additional valley degeneracy, which leads to a few subtle modifications of the quantum corrections with respect to the conventional case. The pseudospin vector always points along the direction of motion, reflecting the chiral nature of the charge carriers in graphene. The evolution of the pseudospin along the trajectory is associated with a Berry phase of the spin transport, that additionally enters the semiclassical Green function. This Berry phase is responsible for a sign change in the weak localization correction, giving antilocalization behavior. The presence of a finite Ehrenfest time reduces the magnitude of this correction, but with a multiplicative factor that is the same for weak localization and weak antilocalization. We also considered the suppression of weak (anti)localization from dephasing at finite temperatures, and identified there, too, the role of the Ehrenfest time.

For the interaction correction there are two important differences with the case of the conventional two-dimensional electron gas: The Hartree-type processes (or, more precisely, interaction non-singlet channels) contain an additional angular dependence, as a result of chirality. Moreover, importance of screening is changed, because of the presence of the valley degeneracy. A finite Ehrenfest time suppresses the Altshuler-Aronov correction, in a similar way as for conventional metals, but unlike for weak (anti)localization the suppression is not simply a multiplicative factor. Interestingly, the interaction correction may undergo a sign change as a function of Ehrenfest time, for sufficiently strong interaction in the non-singlet channels. For graphene, the interaction strength at which this sign change takes place is smaller than in conventional electron gases, which may place it within experimental reach, as discussed in Sec. 6.6.

## 7. Conclusion

Graphene has stimulated a great deal of attraction in solid state physics in recent years. Its special electronic properties arise from a quasi-relativistic dispersion, that is characteristic for the honeycomb lattice formed by the atoms of a single layer of graphite. The relativistic nature of the electronic excitations in graphene gives rise to series of unconventional effects, that are observed in studies of the transport properties of graphene. In this thesis, we discussed various aspects of such unusual features in the electronic properties of graphene, and their relation to the peculiar bandstructure.

One part of the thesis discussed the possibility of electrostatic confinement in graphene. While it is common, to restrict the electronic motion to a quantum dot with the help of metallic gates in semiconductor structures, such procedure is problematic in graphene, due to the absence of a bandgap. The best option to create quantum dots in graphene consists of a doped region that is surrounded by an undoped graphene structure, where the Fermi level lies at the Dirac point. Although the density of states vanishes in the region outside of the dot, Klein tunneling opens a way to exit the dot, as electrons approaching the surface of the dot under normal incidence will be transmitted with unit probability. On the other hand, electrons that hit the surface away from normal incidence will be reflected back and remain inside the dot. Such angle-specific scattering suggests, that electrostatic confinement should be possible for certain geometries, that exclude normal incidence.

One way to obtain information about possible confinement in graphene, is to attach the quantum dot surrounded by undoped graphene to source and drain contacts and study the two-terminal conductance. The spatial restriction of electronic motion gives rise to discrete levels of the quantum dot, that are observed as resonances in the conductance. The structure of the resonances, as well as their behavior upon changing the coupling between dot and leads contains information about the nature of the electronic bound state and the degree of confinement. As prototypical examples, we studied a circular quantum dot with integrable classical dynamics, that should support bound states according to the arguments given above, and a stadium-shaped quantum dot, which should lack confinement in view of the classical chaotic motion.

Previous numerical studies indeed found sharp resonances for a circular graphene quantum dot, that correspond to well-confined states, while for the chaotic structure the resonances are typically broad. Further improvement has been made by linking the conductance to the scattering matrix of the quantum dot, which allows for an analytic solution for the circular quantum dot. In this thesis, we extended this machinery, in order to be able to calculate the conductance of a quantum dot of generic shape from its scattering matrix. In this way, we have been able to extract information about the structure of the bound states from the lineshape of the resonant features in the conductance. Moreover, we could easily scale to the important limit of weak coupling between dot and leads, for which the resonances become isolated. Here, we could make the distinction between features of

a regular and a chaotic dot shape rigorous, since the width of the resonances is shrinking linearly in the ratio of dot size vs. distance to the leads for a chaotic dot upon weakening the coupling to the leads, while the regular dot contains resonances that shrink at a higher power, and therefore possess a higher degree of confinement.

Remarkably, the resonances for the chaotic structure persist at a finite height close to the conductance quantum even in the limit of arbitrarily small coupling to the leads. In this thesis, we identified the Berry phase, that occurs in graphene from the pseudospin which indicates the sublattice structure, as the origin of such effect. Upon a circular motion of the electron, the pseudospin winds once around its axis, being responsible for an accumulation of a phase of  $\pi$  in the electronic wavefunction. The Berry phase is also responsible for a quantization of the angular momentum to half-integer multiples of  $\hbar$ . We could isolate the significance of such phase on possible confinement in graphene by adding an additional flux tube to the system, which contains half a flux quantum. Electrons encircling such flux tube acquire an Aharonov-Bohm phase of  $\pi$ , which is precisely cancelling the effect of a Berry phase. For this situation, the kinematic angular momentum, which is relevant for the classical argumentation, is shifted to integer values, where the state with zero angular momentum cannot be confined by means of gate potentials. Such state hence corresponds to normal incidence on the surface, where Klein tunneling prohibits confinement. Indeed we found a clear distinction between regular and chaotic shapes of the dot in the presence of the flux tube, where bound states are now only found in regular structures.

An alternative route to access information about the degree of confinement in different quantum dots is to investigate the density of states, that can also be inferred from the scattering matrix of the quantum dot. We showed, that such type of calculation provides an effective method to gain information about resonant levels of the dot, and we discussed in this thesis, how the different scenarios of quantum dots in graphene give rise to discernable features in the density of states.

To sum up, we have been able to derive a conclusive picture about which effects influence the electrostatic confinement in graphene. We remark, that the question if it is possible to confine electrons in graphene with metallic gates could not be answered a priori based on intuition, but demanded a careful study that revealed some surprising insights in the unusual Dirac physics in graphene. We believe, that the methods developed within this thesis in this context, offer valuable tools for the study of related problems. As an example, we would like to mention a possible charge trapping when the graphene sheet is deformed, for example externally with a scanning tunneling microscope tip. Electrons moving through the deformed graphene layer are affected by an effective magnetic field, that maybe able to localize the electrons. Another direction would be to drive the system out of equilibrium by changing the gate voltage of the quantum dot (or the height of the deformation of the graphene sheet) in time. Nonequilibrium phenomena are typically accompanied by rich physical effects, therefore it might be worth to extend the methods developed in this thesis and include a time-dependence.

In this thesis, we further employed semiclassical methods in order to study quantum effects in transport in disordered metals. The wave nature of electrons is confirmed by a number of features in electronic transport, such as weak localization, or the interaction correction to the conductivity. For a system where the disorder is changing on a scale much larger than the Fermi wavelength, which describes the typical extension of an elec-

---

tronic wavepacket, the electronic motion is governed by classical dynamics. The essence of semiclassical methods in quantum transport is to calculate quantum effects to the conductivity based on classical trajectories through the conductor – quantum effects arise from the interference of different trajectories. The semiclassical limit is characterized by the appearance of an additional timescale, the Ehrenfest time, not present for short-range quantum disorder, which essentially serves as a short-time threshold for the occurrence of interference effects.

One of the projects of this thesis contained the semiclassical analysis of the interaction correction to the conductance. Our study extended a previous investigation that derived a semiclassical theory for the interaction correction of a ballistic double quantum dot, the simplest system for which interaction corrections can occur. The study presented in this thesis is capable to treat a generic type of conductor that gives rise to classical electronic dynamics and allows for both short and long range type of interaction. In particular, we address the interaction correction to the conductance of antidot arrays, an experimentally relevant example for a system where electrons are following classical trajectories. We find that the Ehrenfest time is acting as a short-time threshold for the occurrence of the interaction correction, and consequently the interaction correction is strongly suppressed, once the Ehrenfest time exceeds the dwell time or inverse temperature. The sensitivity to temperature is special to the interaction correction, and maybe of importance for experimental studies, where temperature provides a well-adjustable quantity. For Coulomb interaction, there is a competition between Hartree and Fock type contributions to the conductance, which come with opposite sign. This competition may lead to a sign change of the interaction correction, as one varies Ehrenfest time, if the interaction is strong enough.

We further studied quantum corrections to transport in graphene in this thesis, based on semiclassical approximations. For the semiclassical limit to hold true, we require graphene that is doped away from the Dirac point, and subject to a smooth disorder potential, which may occur in graphene samples that are placed on a substrate with high dielectric constant. The semiclassical theory for graphene differs from the theory for conventional metals by the existence of the pseudospin, which modifies the semiclassical propagator for the electrons, such that it contains information also about the transport of the pseudospin. In this thesis, we discussed weak localization, and the interaction corrections, specifically the Altshuler-Aronov correction and dephasing, for graphene from a semiclassical point of view, based on classical trajectories. For weak localization, the Berry phase associated with the pseudospin is responsible for a change from weak localization to weak *ant*localization. We also discussed quantitatively, how such effect is suppressed by a finite Ehrenfest time. For the interaction correction, the pseudospin together with the additional valley degree of freedom is influencing the magnitude of the interaction correction. Interestingly, the sign change as a function of Ehrenfest time mentioned before appears within experimental reach for graphene.

Summarizing, in this thesis we further extended the range of applicability of semiclassical methods for the calculation of quantum transport. The usage of semiclassical methods provides several advances, it combines the highly intuitive language based on classical trajectories together with a powerful quantitative method to calculate the magnitude of the quantum corrections, and it can deal with the appearance of the Ehrenfest time in

## 7. Conclusion

---

systems with smooth “classical” disorder. We are optimistic that the developments of this thesis are useful for a further extension of the semiclassical methods to other areas in quantum transport, for instance in superconducting systems.

# Appendix





## A. Appendix to Chapter 3

### A.1. Matrix Green Function

In this appendix, we give explicit expressions for some of the matrix Green function appearing in Sec. 3.3. We follow the supplementary material of Ref. [Tito 10], but our results for the  $d$ -wave channel go beyond that reference.

Using Pauli matrices  $\tau_x$ ,  $\tau_y$ , and  $\tau_z$  for the retarded-advanced (RA) degree of freedom, and with  $\tau_0$  for the  $2 \times 2$  unit matrix in the RA grading, the explicit expression for the matrix Green function  $\check{G}_0$  is

$$\check{G}_0(x, x'; y) = \frac{1}{4\hbar v L} \check{V}(x) \check{\Lambda} \check{\Lambda}_\tau \check{\Lambda}_\sigma \check{\Lambda} \check{V}^{-1}(x') \quad (\text{A.1})$$

with  $\check{\Lambda} = \begin{pmatrix} 1 & 0 \\ 0 & 0 \end{pmatrix} \otimes \sigma_z + \begin{pmatrix} 0 & 0 \\ 0 & 1 \end{pmatrix} \otimes \sigma_0$  and

$$\check{\Lambda}_\tau = \begin{pmatrix} i \cosh(\phi y/2L) & \sinh(\phi y/2L) \\ \sinh(\phi y/2L) & -i \cosh(\phi y/2L) \end{pmatrix} \otimes \sigma_0, \quad (\text{A.2})$$

$$\check{\Lambda}_\sigma = \tau_0 \otimes \begin{pmatrix} \frac{1}{\sin[\pi(x+x'+iy)/2L]} & \frac{1}{\sin[\pi(x-x'+iy)/2L]} \\ \frac{1}{\sin[\pi(x-x'-iy)/2L]} & \frac{1}{\sin[\pi(x+x'-iy)/2L]} \end{pmatrix}, \quad (\text{A.3})$$

$$\check{V}(x) = \begin{pmatrix} \sin \frac{\phi(L-x)}{2L} & \cos \frac{\phi(L-x)}{2L} \\ i \cos \frac{\phi x}{2L} & i \sin \frac{\phi x}{2L} \end{pmatrix} \otimes \sigma_0. \quad (\text{A.4})$$

This  $s$ -wave contribution of the regularized Green function can be found as

$$\begin{aligned} \check{G}_{\text{reg}}^{ss}(x_0) &= \lim_{\substack{x' \rightarrow x_0 \\ y \rightarrow 0}} [\check{G}_0(x_0, x'; y) - g(x_0 - x', y)] \\ &= \frac{i}{4\hbar v L} \check{V}(x_0) \begin{pmatrix} \frac{1}{\sin(\pi x_0/L)} & -\sigma_x \phi / \pi \\ \sigma_x \phi / \pi & -\frac{1}{\sin(\pi x_0/L)} \end{pmatrix} \check{V}^{-1}(x_0) \end{aligned} \quad (\text{A.5})$$

Contributions from higher angular momentum modes are obtained by keeping higher terms of the Taylor series. Therefore, we write the regularized Green function as

$$\check{G}_{\text{reg}}(\mathbf{r}, \mathbf{r}') = \sum_{\mu, \nu} \frac{1}{\mu!} \frac{1}{\nu!} [(\mathbf{r} - \mathbf{r}_0) \vec{\nabla}]^\mu \check{G}_{\text{reg}}(\mathbf{r}_0, \mathbf{r}_0) [\overleftarrow{\nabla}'(\mathbf{r}' - \mathbf{r}_0)]^\nu \quad (\text{A.6})$$

Here,  $\vec{\nabla}$  acts to the right, on the first argument of the Green function, and  $\overleftarrow{\nabla}'$  acts to the left, on the second argument of the Green function. We can simplify this expression by using the equations of motion of the regularized Green function,

$$-i\sigma \vec{\nabla} \check{G}_{\text{reg}} = 0, \quad \check{G}_{\text{reg}}(-i\overleftarrow{\nabla}'\sigma) = 0 \quad (\text{A.7})$$

from which immediately follows, that

$$\partial_y \check{G}_{\text{reg}}(\mathbf{r}, \mathbf{r}') = i\sigma_z \partial_x \check{G}_{\text{reg}}(\mathbf{r}, \mathbf{r}'), \quad \partial_{y'} \check{G}_{\text{reg}}(\mathbf{r}, \mathbf{r}') = \partial_{x'} \check{G}_{\text{reg}}(\mathbf{r}, \mathbf{r}')(-i\sigma_z). \quad (\text{A.8})$$

This enables us to rewrite Eq. (A.6) as

$$\check{G}_{\text{reg}}(\mathbf{r}, \mathbf{r}') = \sum_{\mu, \nu} \frac{1}{\mu!} [(x - x_0) + i\sigma_z(y - y_0)]^\mu \check{G}_{\text{reg}}^{\mu\nu} \frac{1}{\nu!} [(x' - x_0) - i\sigma_z(y' - y_0)]^\nu, \quad (\text{A.9})$$

with

$$\check{G}_{\text{reg}}^{\mu\nu} = \partial_x^\mu \partial_{x'}^\nu \check{G}_{\text{reg}}(\mathbf{r}_0, \mathbf{r}_0). \quad (\text{A.10})$$

We now give the explicit expressions for  $\check{G}_{\text{reg}}^{\mu\nu}$  up to  $d$ -wave order. In order to keep the expressions short, we focus on the case, where the dot is placed in the middle of the sample ( $x_0 = L/2$ ),

$$\begin{aligned} \check{G}_{\text{reg}}^{sp/ps} &= \frac{i}{8\hbar v L^2} \check{V}(x_0) \begin{pmatrix} \pm \frac{\pi^2 - 3\phi^2}{6\pi} \sigma_x & -\phi \\ -\phi & \pm \frac{\pi^2 - 3\phi^2}{6\pi} \sigma_x \end{pmatrix} \check{V}^{-1}(x_0), \\ \check{G}_{\text{reg}}^{pp} &= \frac{i}{16\hbar v L^3} (\pi^2 - \phi^2) \check{V}(x_0) \begin{pmatrix} 1 & \frac{\phi}{3\pi} \sigma_x \\ -\frac{\phi}{3\pi} \sigma_x & -1 \end{pmatrix} \check{V}^{-1}(x_0), \\ \check{G}_{\text{reg}}^{sd/ds} &= \frac{i}{16\hbar v L^3} (\pi^2 - \phi^2) \check{V}(x_0) \begin{pmatrix} 1 & -\frac{\phi}{3\pi} \sigma_x \\ \frac{\phi}{3\pi} \sigma_x & -1 \end{pmatrix} \check{V}^{-1}(x_0), \\ \check{G}_{\text{reg}}^{pd/dp} &= \frac{i}{32\hbar v L^4} \check{V}(x_0) \begin{pmatrix} \mp \frac{7\pi^4 - 30\pi^2\phi^2 + 15\phi^4}{60\pi} \sigma_x & \frac{\phi(-3\pi^2 + \phi^2)}{\mp \frac{7\pi^4 - 30\pi^2\phi^2 + 15\phi^4}{60\pi} \sigma_x} \\ \phi(-3\pi^2 + \phi^2) & \mp \frac{7\pi^4 - 30\pi^2\phi^2 + 15\phi^4}{60\pi} \sigma_x \end{pmatrix} \check{V}^{-1}(x_0), \\ \check{G}_{\text{reg}}^{dd} &= \frac{i}{64\hbar v L^5} \check{V}(x_0) \begin{pmatrix} 5\pi^4 - 6\pi^2\phi^2 + \phi^4 & \frac{\phi(-7\pi^4 + 10\pi^2\phi^2 - 3\phi^4)}{15\pi} \sigma_x \\ -\phi \frac{-7\pi^4 + 10\pi^2\phi^2 - 3\phi^4}{15\pi} \sigma_x & -(5\pi^4 - 6\pi^2\phi^2 + \phi^4) \end{pmatrix} \check{V}^{-1}(x_0). \end{aligned}$$

The element  $\check{G}_{\text{reg}}^{ss}$  is given by Eq. (A.5). Since  $\check{V}(x_0)$  has no matrix structure in pseudospin space, it commutes with the  $T$ -matrix, and therefore does not play a role for the generating function.

Upon inserting (A.9) into the generating function (Eq. (3.21)), we find

$$\delta\mathcal{F} = \ln \det[1 - \mathbf{T}\check{\mathbf{G}}_{\text{reg}}], \quad (\text{A.11})$$

where  $\check{\mathbf{G}}_{\text{reg}}$  is a (infinite) matrix with entries  $G_{\text{reg}}^{\mu\nu}$  ( $\mu, \nu = 0, 1, \dots$ ) and the matrix  $\mathbf{T}$  contains the elements  $T^{\mu\nu}$

$$T^{\mu\nu} = \int d^2\mathbf{r} d^2\mathbf{r}' \frac{1}{\mu!} [(x - x_0) - i\sigma_z(y - y_0)]^\mu T(\mathbf{r}, \mathbf{r}') \frac{1}{\nu!} [(x' - x_0) + i\sigma_z(y' - y_0)]^\nu. \quad (\text{A.12})$$

This is Eq. (3.23) of the main text. In the limit that the size  $R$  of the quantum dot is much smaller than  $L$ , this expansion is convergent, and it is a good approximation to limit the number of angular momentum “channels” involved in the expansion. In the simplest case, one takes into account the  $s$ -wave contribution  $\mu = \nu = 0$  only. This limit was considered in Ref. [Tito 10]. The accuracy can be improved by including contributions

from higher angular momentum. The expressions derived above allow one to go up to the  $d$ -wave contribution.

In order to relate the object  $T^{\mu\nu}$  of Eqs. (3.23) or (A.12) to the  $T$  matrix in the partial-wave expansion, it is instructive to compare the plane-wave and circular-wave basis sets of eigenstates of the free Dirac Hamiltonian  $H_0 = -i\sigma\nabla$ . The plane wave basis consists of eigenstates, which are labeled by their wavevector  $\mathbf{k} = (k \cos \theta_k, k \sin \theta_k)$ ,

$$\psi_{\mathbf{k}}(\mathbf{r}) = \frac{e^{i\mathbf{k}\mathbf{r}}}{\sqrt{2}} \begin{pmatrix} 1 \\ e^{i\theta_k} \end{pmatrix}. \quad (\text{A.13})$$

Here and below, we restrict ourselves to positive energy solutions (conduction band) only. In the implementation, this can be achieved by choosing the gate potential of the dot to be negative. The circular-wave states are combined eigenstates of the Hamiltonian and the total angular momentum  $L_z + \frac{1}{2}\sigma_z$ , and are therefore labeled by their wavenumber  $k$  and their half-integer angular momentum quantum number  $m$ ,

$$\psi_{km}(\mathbf{r}) = \sqrt{\frac{k}{4\pi}} e^{im\theta} \begin{pmatrix} e^{-i\frac{\theta}{2}} J_{|m-\frac{1}{2}|}(kr) \\ e^{i\frac{\theta}{2}} i \text{sgn}(m) J_{|m+\frac{1}{2}|}(kr) \end{pmatrix}. \quad (\text{A.14})$$

Here,  $J_\nu$  is the Bessel function of  $\nu$ -th order. The  $2 \times 2$  matrix  $\Psi_{k\mu}$  of the main text is related to the  $\psi_{km}$  as  $\Psi_{k\mu} = (\psi_{k,\mu+1/2}, i\psi_{k,-\mu-1/2})$ . The basis change between plane waves and circular waves is expressed through the equation

$$\psi_{\mathbf{k}}(\mathbf{r}) = \sqrt{\frac{2\pi}{k}} \sum_m i^{|m-\frac{1}{2}|} e^{-i(m-\frac{1}{2})\theta_k} \psi_{km}(\mathbf{r}). \quad (\text{A.15})$$

For the scattering problem in the infinite graphene sheet, we place the center of the quantum dot at the origin. We may express the  $T$ -matrix in the plane-wave basis through the  $T$ -matrix in real space as

$$\begin{aligned} T(\mathbf{k}, \mathbf{k}') &= \frac{1}{2} \int d^2\mathbf{r} d^2\mathbf{r}' (1 \quad e^{-i\theta_k}) T(\mathbf{r}, \mathbf{r}') \begin{pmatrix} 1 \\ e^{i\theta'_k} \end{pmatrix} \\ &\quad \times \exp[ik(x' \cos \theta'_k + y' \sin \theta'_k - x \cos \theta_k - y \sin \theta_k)]. \end{aligned} \quad (\text{A.16})$$

On the other hand, the same matrix elements can be also written in spherical wave basis,

$$T(\mathbf{k}, \mathbf{k}') = \frac{2\pi}{k} \sum_{nm} (-i)^{|n-\frac{1}{2}|} i^{|m-\frac{1}{2}|} e^{i(n-\frac{1}{2})\theta_k} e^{-i(m-\frac{1}{2})\theta'_k} T_{nm}(k) \quad (\text{A.17})$$

The partial-wave  $T$  matrices  $T_{mn}$  introduced here and  $T_{\mu\nu}$  of the main text are related as

$$T_{\mu\nu} = \begin{pmatrix} T_{\mu+1/2, \nu+1/2} & iT_{\mu+1/2, -\nu-1/2} \\ -iT_{-\mu-1/2, \nu+1/2} & T_{-\mu-1/2, -\nu-1/2} \end{pmatrix}. \quad (\text{A.18})$$

Comparing Eqs. (A.16) and (A.17), we obtain a relation between the  $T$ -matrix in spherical wave basis and the  $T$ -matrix in real space. For example, for the  $s$ -wave channel we find

$$\frac{2\pi}{k} \begin{pmatrix} T_{\frac{1}{2}, \frac{1}{2}}(k) & iT_{\frac{1}{2}, -\frac{1}{2}}(k) \\ -iT_{-\frac{1}{2}, \frac{1}{2}}(k) & T_{-\frac{1}{2}, -\frac{1}{2}}(k) \end{pmatrix} = \frac{1}{2} \int d^2\mathbf{r} d^2\mathbf{r}' T(\mathbf{r}, \mathbf{r}') + \mathcal{O}(k), \quad (\text{A.19})$$

so that

$$T^{00} = \lim_{k \rightarrow 0} \frac{4\pi}{k} \begin{pmatrix} T_{\frac{1}{2}, \frac{1}{2}}(k) & iT_{\frac{1}{2}, -\frac{1}{2}}(k) \\ -iT_{-\frac{1}{2}, \frac{1}{2}}(k) & T_{-\frac{1}{2}, -\frac{1}{2}}(k) \end{pmatrix} = \lim_{k \rightarrow 0} \frac{4\pi}{k} T_{00}(k), \quad (\text{A.20})$$

where, in the last equation, we used the  $2 \times 2$  matrix notation with integer indices used in the main text. The remaining identities in Eq. (3.25) follow similarly.

## A.2. Low- $k$ -Limit of Scattering matrix

In this appendix, we present the details how to determine the low- $k$  limit of the scattering matrix. As explained in the main text, we modify the scattering problem, such that we solve the scattering problem for particles with wavenumber  $k_1 = k + k'$  in the potential  $U' = U + \hbar k'v$ . We then need to relate the scattering matrix  $S'$  for this problem, in which  $U'$  is set to zero outside a certain cut-off radius  $a$  to the scattering matrix  $S$  for the original problem, in which  $U$ , not  $U'$  is set to zero for  $r > a$ .

In order to relate these two scattering matrices, we need to calculate the scattering matrix of a potential step, in which the potential is zero for  $r > a$  and equal to  $u = \hbar k'v$  for  $r < a$ . Hereto, we expand the wavefunctions for  $r < a$  and  $r > a$  in terms of incoming and outgoing circular waves with wavenumber  $k' + k$  and  $k$ , respectively,

$$\begin{aligned} \psi_{a-}(\mathbf{r}) &= \sum_m (L_m^+ \psi_{k+k', m, +}(\mathbf{r}) + L_m^- \psi_{k+k', m, -}(\mathbf{r})), \\ \psi_{a+}(\mathbf{r}) &= \sum_m (R_m^+ \psi_{k, m, +}(\mathbf{r}) + R_m^- \psi_{k, m, -}(\mathbf{r})), \end{aligned} \quad (\text{A.21})$$

where the scattering states  $\psi_{k, m, \pm}$  are obtained from the basis states  $\psi_{km}$  in Eq. (A.14) by the replacement  $J(kr) \rightarrow H^\pm(kr)$ . The coefficients  $R_m^\pm$  and  $L_m^\pm$  are related through the transfer matrix  $\mathcal{T}$ ,

$$\begin{pmatrix} R_m^+ \\ R_m^- \end{pmatrix} = \mathcal{T}_m(k, k + k', a) \begin{pmatrix} L_m^+ \\ L_m^- \end{pmatrix}, \quad (\text{A.22})$$

which is easily calculated from continuity of the wave function at  $r = a$ ,

$$\mathcal{T}_m(k, k + k', a) = \frac{\pi a}{4i} \tilde{\mathcal{T}}_m(k, k + k', a) \sqrt{k(k + k')}, \quad (\text{A.23})$$

where the  $2 \times 2$  matrix  $\tilde{\mathcal{T}}_m(k, k + k', a)$  has entries

$$\begin{aligned} \tilde{\mathcal{T}}_m(k, k + k', a)_{11} &= H_{|m|+\frac{1}{2}}^{(-)}(ka) H_{|m|-\frac{1}{2}}^{(+)}(ka + k'a) - H_{|m|-\frac{1}{2}}^{(-)}(ka) H_{|m|+\frac{1}{2}}^{(+)}(ka + k'a), \\ \tilde{\mathcal{T}}_m(k, k + k', a)_{12} &= H_{|m|+\frac{1}{2}}^{(-)}(ka) H_{|m|-\frac{1}{2}}^{(-)}(ka + k'a) - H_{|m|-\frac{1}{2}}^{(-)}(ka) H_{|m|+\frac{1}{2}}^{(-)}(ka + k'a). \end{aligned} \quad (\text{A.24})$$

The other entries are given by the relations  $\tilde{\mathcal{T}}_m(k, k + k', a)_{21} = -\tilde{\mathcal{T}}_m(k, k + k', a)_{12}^*$ ,  $\tilde{\mathcal{T}}_m(k, k + k', a)_{22} = -\tilde{\mathcal{T}}_m(k, k + k', a)_{11}^*$ . The transfer matrix is converted into reflec-

tion/transmission coefficients using the standard relations

$$\begin{aligned}
\rho &= \mathcal{T}_{12}(\mathcal{T}_{22})^{-1}, \\
\tau &= (\mathcal{T}_{22})^{-1}, \\
\tau' &= \mathcal{T}_{11} - \mathcal{T}_{12}(\mathcal{T}_{22})^{-1}\mathcal{T}_{21}, \\
\rho' &= -(\mathcal{T}_{22})^{-1}\mathcal{T}_{21}.
\end{aligned} \tag{A.25}$$

Upon taking the limit  $k \rightarrow 0$ , we find

$$\begin{aligned}
\rho_m &= 1 + \frac{i\pi a^{2|m|}}{[(|m| - \frac{1}{2})!]^2 2^{2|m|-1}} \frac{H_{|m|+\frac{1}{2}}^{(-)}(k'a)}{H_{|m|-\frac{1}{2}}^{(-)}(k'a)} k^{2|m|} + \mathcal{O}(k^{2|m|+1}), \\
\tau_m = \tau'_m &= \frac{1}{(|m| - \frac{1}{2})! 2^{|m|-\frac{3}{2}}} \frac{a^{|m|-\frac{1}{2}}}{\sqrt{k'}} \frac{1}{H_{|m|-\frac{1}{2}}^{(-)}(k'a)} k^{|m|} + \mathcal{O}(k^{|m|+1}), \\
\rho'_m &= -\frac{H_{|m|-\frac{1}{2}}^{(+)}(k'a)}{H_{|m|-\frac{1}{2}}^{(-)}(k'a)} + \mathcal{O}(k).
\end{aligned} \tag{A.26}$$

We can now relate the scattering matrices  $S'$  for particles with energy  $k'$  in the potential  $U' = U + \hbar k'v$  and  $U' = 0$  for  $r > a$  to the scattering matrix  $S$  for particles with energy  $k$  in the potential  $U$ , with  $U = 0$  for  $r > a$ ,

$$S = \rho + \tau'(1 - S'\rho')^{-1}S'\tau. \tag{A.27}$$

Inserting the above expansions, we get an expression of the form

$$S_{nm}(k) = \delta_{nm} + S_{nm}^{(1)} k^{|n|+|m|} + \mathcal{O}(k^{|n|+|m|+1}), \tag{A.28}$$

coinciding with Eq. (3.33) in the main text. The coefficient  $S^{(1)}$  depends on  $a$ ,  $k'$  and  $S'$ .



## B. Appendix to Chapter 4

### B.1. Numerical simulation of the two-terminal transport

The numerical approach for the two-terminal transport in the presence of a  $\pi$ -flux follows Ref. [Bard 07]. The potential  $V(\mathbf{r})$  is replaced by a potential  $\sum_n V_n(y)\delta(x - x_n)$  that is nonzero at  $N$  discrete values  $-L/2 = x_0 < x_1 < x_2 < \dots < x_{N-1} < x_N = L/2$  of the  $x$  coordinate, with

$$V_n(y) = \int_{(x_{n-1}+x_n)/2}^{(x_n+x_{n+1})/2} dx V(x, y), \quad n = 1, 2, \dots, N-1.$$

Between the discrete points the wavefunction is solved from the free Dirac equation. This solution takes its simplest form after Fourier transform with respect to the transverse coordinate  $y$ , because the free Dirac equation does not couple different transverse modes. These solutions are then matched by applying the appropriate boundary conditions at the discrete points  $x = x_j$ ,  $j = 1, 2, \dots, N$ . A numerically stable method to implement this program is to express both the solution of the free Dirac equation and the matching conditions at the discrete points  $x = x_j$  in terms of scattering matrices. The scattering matrix of the entire sample is then obtained from convolution of the scattering matrices of the  $2N - 1$  individual components. The result of the calculation is the transmission matrix  $t$ , which is related to the two-terminal conductance via the Landauer formula,

$$G = \frac{4e^2}{h} \text{tr } t t^\dagger, \quad (\text{B.1})$$

where the trace is taken of the transverse Fourier modes. The number of “slices”  $N$  and the number of transverse modes  $M$  must be chosen large enough, that the conductance  $G$  no longer depends on  $N$  and  $M$ .

The vector potential (4.15) corresponds to the boundary condition

$$\lim_{x \uparrow 0} \psi(x, y) = - \lim_{x \downarrow 0} \psi(x, y) \quad \text{for } -W/2 < y < 0, \quad (\text{B.2})$$

whereas  $\psi(x, y)$  is continuous at  $x = 0$  for  $0 < y < W/2$ . In the approach described above, this boundary condition is expressed in terms of a scattering matrix relating incoming and outgoing waves at  $x \uparrow 0$  and  $x \downarrow 0$ . This scattering matrix has no reflective part, whereas the transmission matrix is

$$t_{mn} = \begin{cases} 0 & \text{if } m - n \text{ even,} \\ -4i/[(k_m - k_n)W] & \text{if } m - n \text{ odd,} \end{cases} \quad (\text{B.3})$$

where the integers  $m$  and  $n$  label the transverse modes and  $k_n = 2\pi n/W$ . This transmission matrix has the special properties that  $t = t^\dagger$  and  $t^2 = 1$ .

In order to ensure numerical stability, unitarity must be preserved while restricting to a finite number of transverse modes  $M$ . For the transmission matrix (B.3) this can be achieved using the following trick: One first builds the hermitian matrix  $h = i(e^{i\phi} - t)/(t + e^{i\phi}) = \cot \phi - t/\sin \phi$  out of the transmission matrix, where  $\phi$  is a phase that can be chosen arbitrarily, then truncates  $h$ , which can be done straightforwardly without compromising hermiticity, and then uses the inverse relation  $t = e^{i\phi}(1 + ih)/(1 - ih)$  to obtain a finite-dimensional transmission matrix. In our numerical calculation we set  $\phi = \pi/2$ . We verified that the elements of the resulting finite-dimensional transmission matrix approach the elements of the exact transmission matrix (B.3) in the limit that the number of transverse mode  $M \rightarrow \infty$ .

## B.2. Numerical simulation of the density of states

In this appendix, we provide details concerning the numerical calculation of the density of states out of the scattering matrix for a gate-defined dot or arbitrary shape. We first choose a disc of radius  $R$  that fully covers the quantum dot. Inside this disc, *i.e.*, for  $r < R$ , the scattering matrix needs to be determined numerically; outside the disc the Dirac equation can be solved analytically, see Sec. 4.4.1.

For  $r < R$  we rewrite the Dirac equation as

$$[v_F \mathbf{p} \cdot \boldsymbol{\sigma} + U(\mathbf{r})] \psi = \hbar v_F k_{\text{ref}} \psi, \quad (\text{B.4})$$

where  $k_{\text{ref}}$  is a reference wavenumber that can in principle be chosen arbitrarily and the potential  $U(\mathbf{r})$  is defined as

$$U(\mathbf{r}) = V(\mathbf{r}) - \varepsilon + \hbar v_F k_{\text{ref}}. \quad (\text{B.5})$$

We regard Eq. (B.4) as a scattering problem of an electron with wavenumber  $k_{\text{ref}}$  on the potential  $U(\mathbf{r})$ . For the solution of this scattering problem, we divide the disc of radius  $R$  in  $N$  circular slices  $r_i < |\mathbf{r}| < r_{i+1}$ , where  $0 \equiv r_0 < r_1 < r_2 < \dots < r_{N-1} < r_N \equiv R$ . We first calculate the scattering matrix  $\mathcal{S}^{(i)}$  of the  $i$ th slice, which is defined for a scattering problem for which the potential  $U(\mathbf{r})$  is set to zero everywhere except for  $r_{i-1} < r < r_i$ . The scattering matrix  $\mathcal{S}^{(i)}$  is defined with respect to flux-normalized scattering states defined for  $r < r_{i-1}$  and  $r > r_i$ , taken at wavenumber  $k_{\text{ref}}$ . If we choose the slices thin enough, a treatment of the scattering problem in the Born approximation is sufficient. The wavenumber  $k_{\text{ref}}$  should be chosen large enough, that these scattering states are well defined. A too small value of  $k_{\text{ref}}$  disturbs the numerical procedure, since the Hankel function are divergent at small arguments. On the other hand, too large values for  $k_{\text{ref}}$  require a finer slicing. After the calculation of the scattering matrices  $\mathcal{S}^{(i)}$  for the individual slices, concatenation of those yields the full scattering matrix  $\mathcal{S}_R(\varepsilon)$  for the potential  $U(\mathbf{r})$  inside the disc of radius  $R$ . This procedure is very similar to the calculation in Ch. 3

For the further calculation, we only need the scattering matrix at small energies. We thus expand

$$S_R(\varepsilon) = S_R^{(0)} + S_R^{(1)}\varepsilon + O(\varepsilon^2), \quad (\text{B.6})$$

where the matrices  $S_R^{(0)}$  and  $S_R^{(1)}$  are obtained from the numerics by setting the energy  $\varepsilon$  in the potential  $U(\mathbf{r})$  (Eq. (B.5)) first to zero, and then to a very small value.



To calculate the density of states, we need the full scattering matrix  $\mathcal{S}$ , that relates in- and outgoing states in the metallic lead, *i.e.* we still need to account for the undoped graphene region  $R < r < L$ . Since the problem is circularly symmetric outside the disc of radius  $R$ , one can establish an explicit connection between  $\mathcal{S}$  and  $\mathcal{S}_R$ . For  $r > L$  the wavefunction for an electron incident in angular momentum channel  $m$  has the form

$$\psi_\varepsilon(\mathbf{r}) = \psi_{k_\infty, m}^{(-)}(\mathbf{r}) + \sum_n \mathcal{S}_{nm}(\varepsilon) \psi_{k_\infty, n}^{(+)}(\mathbf{r}), \quad (\text{B.7})$$

which defines the scattering matrix  $\mathcal{S}_{nm}$  in the general case that angular momentum is not conserved. For  $R < r < L$  we may expand the solution of the Dirac equation as

$$\psi_\varepsilon(\mathbf{r}) = \sum_n \left[ a_{nm} \psi_{k, n}^{(-)}(\mathbf{r}) + b_{nm} \psi_{k, n}^{(+)}(\mathbf{r}) \right], \quad (\text{B.8})$$

with  $k = \varepsilon/\hbar v_F$ , whereas for the limit  $r \uparrow R$  the wavefunction may be written as

$$\psi_\varepsilon(\mathbf{r}) = \sum_n c_{nm} \left[ \psi_{k_{\text{ref}}, n}^{(-)}(\mathbf{r}) + \sum_p \mathcal{S}_{R, pn}(\varepsilon) \psi_{k_{\text{ref}}, p}^{(+)}(\mathbf{r}) \right], \quad (\text{B.9})$$

with the scattering matrix  $\mathcal{S}_R(\varepsilon)$  as defined above. By imposing continuity of the wavefunction at  $r = R$  and  $r = L$ , we can eliminate the coefficients  $a_{nm}$ ,  $b_{nm}$  and  $c_{nm}$  and express  $\mathcal{S}(\varepsilon)$  in terms of  $\mathcal{S}_R(\varepsilon)$ . This program can be carried out analytically, including the expansion in  $k$  relevant for the application of Eq. (4.31) of the main text. The resulting equations can be obtained in a straightforward manner, but they are too lengthy to be reported here.

We checked that our results do not depend on the choice of  $R$  and  $k_{\text{ref}}$  that were introduced into the numerical procedure as auxiliary parameters.



## C. Appendix to Chapter 5

### C.1. Details of the semiclassical calculation

#### C.1.1. Sum rule

Here we show how to derive the sum rule Eq. (5.11). We start by noticing that

$$A_\alpha^2 = \left| \det \begin{pmatrix} \frac{\partial^2 S_\alpha}{\partial \mathbf{r}' \partial \mathbf{r}} & \frac{\partial^2 S_\alpha}{\partial \mathbf{r}' \partial \xi} \\ \frac{\partial^2 S_\alpha}{\partial \xi \partial \mathbf{r}} & \frac{\partial^2 S_\alpha}{\partial \xi \partial \xi} \end{pmatrix} \right| = \left| \det \begin{pmatrix} \frac{\partial \mathbf{p}'_\alpha}{\partial \mathbf{r}} & \frac{\partial \mathbf{p}'_\alpha}{\partial \xi} \\ \frac{\partial \tau_\alpha}{\partial \mathbf{r}} & \frac{\partial \tau_\alpha}{\partial \xi} \end{pmatrix} \right|. \quad (\text{C.1})$$

Hence we may write

$$\begin{aligned} & \sum_{\alpha: \mathbf{r}' \rightarrow \mathbf{r}; \xi} A_\alpha^2 f(\mathbf{p}'_\alpha, \mathbf{p}_\alpha, \tau_\alpha) \\ &= \int_0^\infty dt \int d\mathbf{p}' \sum_{\alpha: \mathbf{r}' \rightarrow \mathbf{r}; \xi} \delta(t - \tau_\alpha) \delta(\mathbf{p}' - \mathbf{p}'_\alpha) f(\mathbf{p}', \mathbf{p}_\alpha, t) \left| \det \begin{pmatrix} \frac{\partial \mathbf{r}}{\partial \mathbf{p}'} & \frac{\partial \xi}{\partial \mathbf{p}'} \\ \frac{\partial \mathbf{r}}{\partial t} & \frac{\partial \xi}{\partial t} \end{pmatrix} \right|^{-1}. \end{aligned} \quad (\text{C.2})$$

The determinant serves as a Jacobian for the transformation  $(t, \mathbf{p}') \rightarrow (\xi, \mathbf{r})$ ,

$$\begin{aligned} & \sum_{\alpha: \mathbf{r}' \rightarrow \mathbf{r}; \xi} \delta(t - \tau_\alpha) \delta(\mathbf{p}' - \mathbf{p}'_\alpha) f(\mathbf{p}', \mathbf{p}_\alpha, t) \left| \det \begin{pmatrix} \frac{\partial \mathbf{r}}{\partial \mathbf{p}'} & \frac{\partial \xi}{\partial \mathbf{p}'} \\ \frac{\partial \mathbf{r}}{\partial t} & \frac{\partial \xi}{\partial t} \end{pmatrix} \right|^{-1} \\ &= \delta[\xi - H(\mathbf{r}, \mathbf{p}(\mathbf{r}', \mathbf{p}'; t))] \delta[\mathbf{r} - \mathbf{r}(\mathbf{r}', \mathbf{p}'; t)] f[\mathbf{p}', \mathbf{p}(\mathbf{r}', \mathbf{p}'; t), t], \end{aligned} \quad (\text{C.3})$$

where  $(\mathbf{r}(\mathbf{r}', \mathbf{p}'; t), \mathbf{p}(\mathbf{r}', \mathbf{p}'; t))$  is the phase space point that a trajectory originating from  $(\mathbf{r}', \mathbf{p}')$  reaches after time  $t$ . After insertion of  $\int d\mathbf{p} \delta(\mathbf{p} - \mathbf{p}(\mathbf{r}', \mathbf{p}'; t))$  we finally arrive at Eq. (5.11).

#### C.1.2. Convolution rule

In this appendix we derive the convolution rule

$$\begin{aligned} & \int d\mathbf{r}_1 d\mathbf{r}_2 \mathcal{G}^A(\mathbf{r}', \mathbf{r}_2; \xi) \mathcal{G}^A(\mathbf{r}_2, \mathbf{r}_1; \xi - \omega) \mathcal{G}^A(\mathbf{r}_1, \mathbf{r}; \xi) f(\mathbf{r}_1 - \mathbf{r}_2) \\ &= -\frac{1}{\hbar^2} \frac{2\pi}{(-2\pi i \hbar)^{3/2}} \sum_{\alpha: \mathbf{r}' \rightarrow \mathbf{r}; \xi} A_\alpha e^{-iS_\alpha/\hbar} \int_0^{\tau_\alpha} dt \int_0^t dt' f(\mathbf{r}_\alpha(t) - \mathbf{r}_\alpha(t')) e^{i\omega(t-t')/\hbar}, \end{aligned} \quad (\text{C.4})$$

where  $f(\mathbf{r})$  is an arbitrary function. (Here we omitted contributions from stationary configurations of trajectories, that cannot be connected to a single trajectory. For the

calculation of the interaction correction, such contributions drop out upon pairing with the retarded trajectory.)

To this end, we first prove an auxiliary identity for the stability amplitudes. Hereto we consider a trajectory  $\alpha$  that connects  $\mathbf{r}'$  with  $\mathbf{r}$ . Further, let  $\mathbf{r}_1$  be a point on trajectory  $\alpha$ , and  $\alpha'$  ( $\alpha''$ ) be the part of trajectory  $\alpha$  connecting  $\mathbf{r}'$  with  $\mathbf{r}_1$  ( $\mathbf{r}_1$  with  $\mathbf{r}$ ). The stability amplitude  $A_\alpha$  can be then written as [Gutz 90]

$$A_\alpha^2 = \frac{1}{v_F^2} \left| \frac{\partial^2 \mathcal{S}_\alpha(\mathbf{r}, \mathbf{r}')}{\partial r_\perp \partial r'_\perp} \right| = \frac{1}{v_F^2} \left| \frac{\partial p'_{\perp\alpha}}{\partial r_\perp} \right|, \quad p'_{\perp\alpha}(\mathbf{r}, \mathbf{r}') = -\frac{\partial \mathcal{S}_\alpha(\mathbf{r}, \mathbf{r}')}{\partial r'_\perp}, \quad (\text{C.5})$$

where  $v_F$  is the Fermi velocity and  $r_\perp$  ( $r'_\perp$ ) denote displacements perpendicular to the trajectory  $\alpha$ . The last equation implicitly defines  $r_{\perp\alpha}(r'_\perp, p'_\perp)$ . We then introduce

$$B_\alpha = -\left( \frac{\partial r_{\perp\alpha}}{\partial p'_{\perp\alpha}} \right)_{r'_\perp}, \quad B_{\alpha'} = -\left( \frac{\partial r_{\perp1\alpha'}}{\partial p'_{\perp\alpha'}} \right)_{r'_\perp}, \quad B_{\alpha''} = -\left( \frac{\partial r_{\perp1\alpha''}}{\partial p_{\perp1\alpha''}} \right)_{r_{\perp1}}, \quad (\text{C.6})$$

such that  $A_\alpha^2 = v_F^{-2} |B_\alpha^{-1}|$ ,  $A_{\alpha'}^2 = v_F^{-2} |B_{\alpha'}^{-1}|$ ,  $A_{\alpha''}^2 = v_F^{-2} |B_{\alpha''}^{-1}|$ . Then the following identity holds:

$$B_\alpha = B_{\alpha'} B_{\alpha''} \left( \frac{\partial^2 \mathcal{S}_{\alpha'}(\mathbf{r}_1, \mathbf{r}')}{\partial r_{\perp1}^2} + \frac{\partial^2 \mathcal{S}_{\alpha''}(\mathbf{r}, \mathbf{r}_1)}{\partial r_{\perp1}^2} \right). \quad (\text{C.7})$$

For the proof of Eq. (C.7), we note that  $B_\alpha$  measures the change of the final coordinate of  $\alpha$  induced by a small change of the initial momentum. When we consider  $\alpha$  to be composed by  $\alpha'$  and  $\alpha''$ , a small change of the initial momentum leads to a change of the intermediate coordinate and momentum, which results in a change of the final coordinate,

$$\begin{aligned} & \left( \frac{\partial r_{\perp\alpha}}{\partial p'_{\perp\alpha}} \right)_{r'_\perp} \\ &= \left( \frac{\partial r_{\perp\alpha''}}{\partial p_{\perp1\alpha''}} \right)_{r_{\perp1}} \left( \frac{\partial p_{\perp1\alpha'}}{\partial p'_{\perp\alpha'}} \right)_{r'_\perp} + \left( \frac{\partial r_{\perp\alpha''}}{\partial r_{\perp1\alpha''}} \right)_{p_{\perp1}} \left( \frac{\partial r_{\perp1\alpha'}}{\partial p'_{\perp\alpha'}} \right)_{r'_\perp} \\ &= \left( \frac{\partial r_{\perp\alpha''}}{\partial p_{\perp1\alpha''}} \right)_{r_{\perp1}} \left( \frac{\partial r_{\perp1\alpha'}}{\partial p'_{\perp\alpha'}} \right)_{r'_\perp} \left[ \left( \frac{\partial p'_{\perp\alpha'}}{\partial r_{\perp1\alpha'}} \right)_{r'_\perp} \left( \frac{\partial p_{\perp1\alpha'}}{\partial p'_{\perp\alpha'}} \right)_{r'_\perp} + \left( \frac{\partial r_{\perp\alpha''}}{\partial r_{\perp1\alpha''}} \right)_{p_{\perp1}} \left( \frac{\partial p_{\perp1\alpha''}}{\partial r_{\perp1\alpha''}} \right)_{r_{\perp1}} \right] \\ &= \left( \frac{\partial r_{\perp\alpha''}}{\partial p_{\perp1\alpha''}} \right)_{r_{\perp1}} \left( \frac{\partial r_{\perp1\alpha'}}{\partial p'_{\perp\alpha'}} \right)_{r'_\perp} \left[ \left( \frac{\partial p_{\perp1\alpha'}}{\partial r_{\perp1\alpha'}} \right)_{r'_\perp} - \left( \frac{\partial p_{\perp1\alpha''}}{\partial r_{\perp1\alpha''}} \right)_{r_{\perp1}} \right] \end{aligned} \quad (\text{C.8})$$

The last line yields Eq. (C.7).

In a similar fashion, one verifies that

$$B_{\alpha'} = B_\alpha B_{\alpha''} \left( \frac{\partial^2 \mathcal{S}_{\alpha''}(\mathbf{r}, \mathbf{r}_1)}{\partial r_\perp^2} - \frac{\partial^2 \mathcal{S}_\alpha(\mathbf{r}, \mathbf{r}')}{\partial r_\perp^2} \right). \quad (\text{C.9})$$

The identity we need for the derivation of the convolution rule (C.4) involves the partitioning of a single trajectory  $\alpha$  into three trajectories  $\alpha'$  ( $\mathbf{r}' \rightarrow \mathbf{r}_1$ ),  $\alpha''$  ( $\mathbf{r}_1 \rightarrow \mathbf{r}_2$ ) and  $\alpha'''$  ( $\mathbf{r}_2 \rightarrow \mathbf{r}$ ). In this case, we have

$$B_\alpha = B_{\alpha'} B_{\alpha''} B_{\alpha'''} \left[ \left( \frac{\partial^2 \mathcal{S}_{\alpha'}}{\partial r_{\perp1}^2} + \frac{\partial^2 \mathcal{S}_{\alpha''}}{\partial r_{\perp1}^2} \right) \left( \frac{\partial^2 \mathcal{S}_{\alpha''}}{\partial r_{\perp2}^2} + \frac{\partial^2 \mathcal{S}_{\alpha'''}}{\partial r_{\perp2}^2} \right) - \left( \frac{\partial^2 \mathcal{S}_{\alpha''}}{\partial r_{\perp1} \partial r_{\perp2}} \right)^2 \right]. \quad (\text{C.10})$$

To see this, one introduces the trajectory  $\tilde{\alpha}$  as connection of  $\alpha$  and  $\alpha'$  and makes use of Eqs. (C.7) and (C.9).

We now turn to the proof of the convolution rule (C.4). Hereto, we define

$$K(\mathbf{r}, \mathbf{r}'; \omega) = \int d\mathbf{r}_1 d\mathbf{r}_2 \delta(\mathbf{r}_1 - \mathbf{r}_2 - \mathbf{a}) \mathcal{G}^A(\mathbf{r}', \mathbf{r}_2; \xi) \mathcal{G}^A(\mathbf{r}_2, \mathbf{r}_1; \xi - \omega) \mathcal{G}^A(\mathbf{r}_1, \mathbf{r}; \xi), \quad (\text{C.11})$$

where  $\mathbf{a}$  is arbitrary, but fixed. With the abbreviation  $\tilde{\mathbf{r}}_1 = \mathbf{r}_1 - \mathbf{a}$  we write

$$K(\mathbf{r}, \mathbf{r}'; \omega) = \int d\mathbf{r}_1 \mathcal{G}^A(\mathbf{r}', \tilde{\mathbf{r}}_1; \xi) \mathcal{G}^A(\tilde{\mathbf{r}}_1, \mathbf{r}_1; \xi - \omega) \mathcal{G}^A(\mathbf{r}_1, \mathbf{r}; \xi). \quad (\text{C.12})$$

We then insert the semiclassical expressions for the Green functions which expresses the former equation as a sum over trajectories  $\alpha'$  (from  $\mathbf{r}'$  to  $\tilde{\mathbf{r}}_1$ ),  $\alpha''$  (from  $\tilde{\mathbf{r}}_1$  to  $\mathbf{r}_1$ ), and  $\alpha'''$  (from  $\mathbf{r}_1$  to  $\mathbf{r}$ ).

The integration over  $\mathbf{r}_1$  is carried out within stationary phase approximation. Here we only take into account stationary phase configurations, where  $\alpha'$ ,  $\alpha''$  and  $\alpha'''$  are connected to a single trajectory. Other configurations play no role for the calculation of the conductance, since the three advanced trajectories are paired with a single retarded trajectory. Hence the convolution  $K$  may be written as a sum over trajectories  $\alpha$  connecting  $\mathbf{r}'$  with  $\mathbf{r}$  and a sum over points  $\mathbf{r}_1^{(0)}$ , for which  $\alpha$  first passes through  $\tilde{\mathbf{r}}_1^{(0)} = \mathbf{r}_1^{(0)} - \mathbf{a}$  and then through  $\mathbf{r}_1^{(0)}$ . Deviations  $\Delta\mathbf{r}_1 = (\Delta x_1, \Delta y_1)$  from  $\mathbf{r}_1^{(0)}$  may be parametrized as

$$\begin{aligned} \Delta r_{\perp 1} &= -\sin(\theta) \Delta x_1 + \cos(\theta) \Delta y_1 \\ \Delta \tilde{r}_{\perp 1} &= -\sin(\tilde{\theta}) \Delta x_1 + \cos(\tilde{\theta}) \Delta y_1 \end{aligned} \quad (\text{C.13})$$

where  $\theta$  ( $\tilde{\theta}$ ) is the angle of the momentum of trajectory  $\alpha$  at  $\mathbf{r}_1^{(0)}$  ( $\tilde{\mathbf{r}}_1^{(0)}$ ), and in turns  $\Delta r_{\perp 1}$  ( $\Delta \tilde{r}_{\perp 1}$ ) represent perpendicular displacements of trajectory  $\alpha$  at  $\mathbf{r}_1^{(0)}$  ( $\tilde{\mathbf{r}}_1^{(0)}$ ). We then expand the sum of the actions of trajectories  $\alpha'$ ,  $\alpha''$  and  $\alpha'''$  up to second order in  $\Delta\mathbf{r}_1$ :

$$\mathcal{S}_{\alpha'}(\tilde{\mathbf{r}}_1, \mathbf{r}'; \xi) + \mathcal{S}_{\alpha''}(\mathbf{r}_1, \tilde{\mathbf{r}}_1; \xi - \omega) + \mathcal{S}_{\alpha'''}(\mathbf{r}, \mathbf{r}_1; \xi) = \mathcal{S}_{\alpha}(\mathbf{r}, \mathbf{r}'; \xi) - \omega\tau + \Delta\mathcal{S}(\Delta\mathbf{r}_1), \quad (\text{C.14})$$

where  $\tau$  is the duration of  $\alpha$  between  $\tilde{\mathbf{r}}_1^{(0)}$  and  $\mathbf{r}_1^{(0)}$ , and  $\Delta\mathcal{S}(\Delta\mathbf{r}_1)$  is given by

$$\begin{aligned} \Delta\mathcal{S}(\Delta\mathbf{r}_1) &= \frac{1}{2} \left[ \frac{\partial^2 \mathcal{S}_{\alpha'}(\tilde{\mathbf{r}}_1^{(0)}, \mathbf{r}')}{\partial \tilde{r}_{\perp 1}^2} + \frac{\partial^2 \mathcal{S}_{\alpha''}(\mathbf{r}_1^{(0)}, \tilde{\mathbf{r}}_1^{(0)})}{\partial \tilde{r}_{\perp 1}^2} \right] \Delta \tilde{r}_{\perp 1}^2 \\ &\quad + \frac{1}{2} \left[ \frac{\partial^2 \mathcal{S}_{\alpha''}(\mathbf{r}_1^{(0)}, \tilde{\mathbf{r}}_1^{(0)})}{\partial r_{\perp 1}^2} + \frac{\partial^2 \mathcal{S}_{\alpha'''}(\mathbf{r}, \mathbf{r}_1^{(0)})}{\partial r_{\perp 1}^2} \right] \Delta r_{\perp 1}^2 \\ &\quad + \left[ \frac{\partial^2 \mathcal{S}_{\alpha''}(\mathbf{r}_1^{(0)}, \tilde{\mathbf{r}}_1^{(0)})}{\partial \tilde{r}_{\perp 1} \partial r_{\perp 1}} \right] \Delta r_{\perp 1} \Delta \tilde{r}_{\perp 1}, \end{aligned} \quad (\text{C.15})$$

where as a consequence of energy conservation only perpendicular displacements need to be considered. The integration over  $\Delta\mathbf{r}_1$  can then be accomplished and using Eq. (C.10) we get

$$K(\mathbf{r}, \mathbf{r}'; \omega) = \left( \frac{2\pi}{(2\pi i \hbar)^{3/2}} \right)^3 (2\pi i \hbar) \sum_{\alpha: \mathbf{r}' \rightarrow \mathbf{r}; \xi} \sum_{\{\mathbf{r}_1^{(0)}\}} \frac{1}{v_F^2} \frac{1}{|\sin(\theta - \tilde{\theta})|} A_{\alpha} e^{-i(\mathcal{S}_{\alpha} - \omega\tau)/\hbar}$$

where the factor  $|\sin(\theta - \tilde{\theta})|^{-1}$  originates from the Jacobian of the transformation (C.13). (A possible phase shift from taking the squareroot of Eq. (C.10) is needed to restore the correct Maslov index. For our calculation however, the Maslov index plays no role and we drop it in our expressions.)

On the other hand, we have

$$\int_0^{\tau_\alpha} dt \int_0^t dt' \delta^{(2)}(\mathbf{r}_\alpha(t) - \mathbf{r}_\alpha(t') - \mathbf{a}) = \sum_{\{\mathbf{r}_1^{(0)}\}} \frac{1}{v_F^2} \frac{1}{|\sin(\theta - \tilde{\theta})|}.$$

With that, we finally obtain

$$K(\mathbf{r}, \mathbf{r}', \omega) = -\frac{1}{\hbar^2} \frac{2\pi}{(2\pi i \hbar)^{3/2}} \sum_{\alpha: \mathbf{r}' \rightarrow \mathbf{r}; \xi} A_\alpha e^{-i\mathcal{S}_\alpha/\hbar} \int_0^{\tau_\alpha} dt \int_0^t dt' \delta^{(2)}(\mathbf{r}_\alpha(t) - \mathbf{r}_\alpha(t') - \mathbf{a}) e^{i\omega(t-t')}. \quad (\text{C.16})$$

Multiplying with  $f(\mathbf{a})$  and integrating over  $\mathbf{a}$  then yields Eq. (C.4).

### C.1.3. Summation over classical trajectories involving a small-angle encounter

The summation over classical trajectories with a small-angle encounter as given in Fig. 5.4 is performed using the procedure of Refs. [Mull 07, Brou 07]. We here outline the main points of this calculation.

The four trajectories  $\alpha$  (from  $\mathbf{r}'$  to  $\mathbf{r}_2$ ),  $\beta$  (from  $\mathbf{r}_1$  to  $\mathbf{r}$ ),  $\gamma$  (from  $\mathbf{r}'$  to  $\mathbf{r}$ ), and  $\delta$  (from  $\mathbf{r}_1$  to  $\mathbf{r}_2$ ) are piecewise paired as shown in Fig. C.1. We start by noting that the choice of the retarded trajectories  $\alpha$  and  $\beta$  fully specifies the advanced trajectories  $\gamma$  and  $\delta$ , since the linearized chaotic dynamics allows for precisely one unique solution of a trajectory that satisfies the initial and final conditions required for the pairing shown in Fig. C.1. Moreover, the products of the stability amplitudes are equal,  $A_\alpha A_\beta = A_\gamma A_\delta$ , so that the product of four Green functions required for the calculation of  $\delta G_{\text{AA}}$  can be written as

$$\begin{aligned} & \mathcal{G}^{\text{R}}(\mathbf{r}, \mathbf{r}_1; \xi) \mathcal{G}^{\text{A}}(\mathbf{r}_1, \mathbf{r}_2, \xi - \omega) \mathcal{G}^{\text{R}}(\mathbf{r}_2, \mathbf{r}'; \xi) \mathcal{G}^{\text{A}}(\mathbf{r}', \mathbf{r}; \xi) \\ &= \frac{1}{2\pi \hbar^3} \sum_{\alpha: \mathbf{r}' \rightarrow \mathbf{r}_2; \xi} \sum_{\beta: \mathbf{r}_1 \rightarrow \mathbf{r}; \xi} A_\alpha^2 A_\beta^2 e^{i\Delta\mathcal{S}/\hbar} e^{i\omega\tau_\delta/\hbar}, \end{aligned} \quad (\text{C.17})$$

where  $\Delta\mathcal{S}$  is the action difference  $\mathcal{S}_\alpha + \mathcal{S}_\beta - \mathcal{S}_\gamma - \mathcal{S}_\delta$ . The summation over trajectories  $\alpha$  and  $\beta$  is restricted to those trajectories that undergo (at least) one small-angle encounter.

The action difference  $\Delta\mathcal{S}$  has two contributions: One contribution from the length difference of the retarded trajectories  $\alpha$  and  $\beta$  vs. the advanced trajectories  $\gamma$  and  $\delta$ , and one contribution from the different energy  $\xi - \omega$  associated with the trajectory  $\delta$ . The former contribution has been calculated in Refs. [Ture 03, Speh 03] and equals  $s_e u_e$ ; the latter contribution equals  $\omega\tau_\delta$ , where  $\tau_\delta$  is the duration of the trajectory  $\delta$ . Note that the product  $s_e u_e$  is independent of the position of the phase space point  $\mathbf{X}_e$  along the encounter.

The trajectories  $\alpha$  and  $\beta$  are enumerated by first picking a phase space point  $\mathbf{X}_e$  on the trajectory  $\alpha$ . The Poincaré surface of section at this point may be parameterized with

stable and unstable phase space coordinates, which are denoted  $s_e$  and  $u_e$  respectively. Moving the Poincaré surface of section along the trajectory, the unstable (stable) coordinate grows (shrinks) as  $e^{\pm\lambda t}$ , where  $\lambda$  is the Lyapunov coefficient. We choose the origin of the coordinate system such that the trajectory  $\alpha$  pierces the Poincaré surface of section at coordinates  $(s_e, u_e) = (0, 0)$ . The point  $\mathbf{X}_e$  is part of an encounter formed by trajectories  $\alpha$  and  $\beta$ , if  $\beta$  passes through the Poincaré surface of section at phase-space distance  $|s_e| < c$  and  $|u_e| < c$ , where  $c$  is a cutoff scale, below which the chaotic classical motion can be linearized. (One can always simultaneously rescale the coordinates  $s$  and  $u$ , such that the cut-off scale is the same for both coordinates.) The cut-off scale  $c$  enters the final results in the combination  $\ln(c^2/\hbar)$  only, so that the precise value of  $c$  is unimportant, as long as  $c$  represents a scale characteristic of the *classical* dynamics. One verifies that the choice of the phase space point  $\mathbf{X}_e$  on the trajectory  $\alpha$  and of the phase space coordinates for the trajectory  $\beta$  also specify the two remaining trajectories  $\gamma$  and  $\delta$ . Indeed, since  $\gamma$  is paired with  $\alpha$  before the encounter, and with  $\beta$  after the encounter, it pierces through the Poincaré surface of section at the same unstable coordinate as  $\beta$  and the same stable coordinate as  $\alpha$ . Similar considerations apply to the trajectory  $\delta$ . The summation over trajectories  $\alpha$  and  $\beta$  is then written as

$$\begin{aligned} \sum_{\alpha: \mathbf{r}' \rightarrow \mathbf{r}_2; \xi} \sum_{\beta: \mathbf{r}_1 \rightarrow \mathbf{r}; \xi} A_\alpha^2 A_\beta^2 \dots = & \int d\mathbf{p}_\xi d\mathbf{p}'_\xi d\mathbf{p}_{1,\xi} d\mathbf{p}_{2,\xi} \int d\mathbf{X}_e \int_{-c}^c ds_e du_e \\ & \times \int_0^\infty d\tau_\alpha \int_0^\infty d\tau_\beta \int_0^{\tau_\alpha} dt_\alpha \int_0^{\tau_\beta} dt_\beta \frac{1}{t_{\text{enc}}} \\ & \times \rho_\xi(\mathbf{r}', \mathbf{p}' \rightarrow \mathbf{X}_e; \tau_\alpha - t_\alpha) \rho_\xi(\mathbf{X}_e \rightarrow \mathbf{r}_2, \mathbf{p}_2; t_\alpha) \\ & \times \rho_\xi(\mathbf{r}_1, \mathbf{p}_1 \rightarrow \mathbf{X}_e^*; t_\beta) \rho_\xi(\mathbf{X}_e^* \rightarrow \mathbf{r}, \mathbf{p}; \tau_\beta - t_\beta) \dots, \end{aligned} \quad (\text{C.18})$$

where  $\mathbf{X}_e^*$  is the phase space point located at phase-space displacement  $(s_e, u_e)$  from  $\mathbf{X}$  and the dots indicate an arbitrary function of the end-point coordinates of the trajectories  $\alpha$  and  $\beta$ . The time  $t_{\text{enc}}$  denotes the duration of the encounter. The factor  $t_{\text{enc}}$  in the denominator accounts for the fact, that  $\mathbf{X}_e$  can be chosen anywhere along the encounter. The ends of the encounter are determined by the condition that  $\max(|s|, |u|) = c$ , or that one of the trajectories involved ends, whichever occurs first. Since the phase space coordinates  $s$  and  $u$  decreases/increases exponentially upon proceeding along the trajectories  $\alpha$  and  $\beta$ , with a rate given by the Lyapunov exponent  $\lambda$ , one finds that  $t_{\text{enc}}$  is given by the expression

$$t_{\text{enc}} = \min[\lambda^{-1} \ln(c/|s_e|), t_\beta] + \min[\lambda^{-1} \ln(c/|u_e|), t_\alpha]. \quad (\text{C.19})$$

The four different scenarios, depending on whether  $t_\beta$  and  $t_\alpha$  are larger or smaller than  $\lambda^{-1} \ln(c/|s_e|)$  and  $\lambda^{-1} \ln(c/|u_e|)$ , respectively, correspond to the four contributions to  $\delta G_{\text{AA}}^{\text{F},2a} - \delta G_{\text{AA}}^{\text{F},2d}$  to  $\delta G_{\text{AA}}^{\text{F},2}$ . The same situation also occurs in the calculation of the shot noise, see Ref. [Whit 06, Brou 06].

The next step in the calculation is to replace the exact trajectory densities  $\rho_\xi$  by the coarse-grained ones. In order to account for correlations inside the encounter, we introduce phase space points  $\mathbf{X}$  and  $\mathbf{X}'$  at the beginning and end of the encounter — if the phase-space points  $\mathbf{X}_1$  and  $\mathbf{X}_2$  associated with the interaction position are not inside the

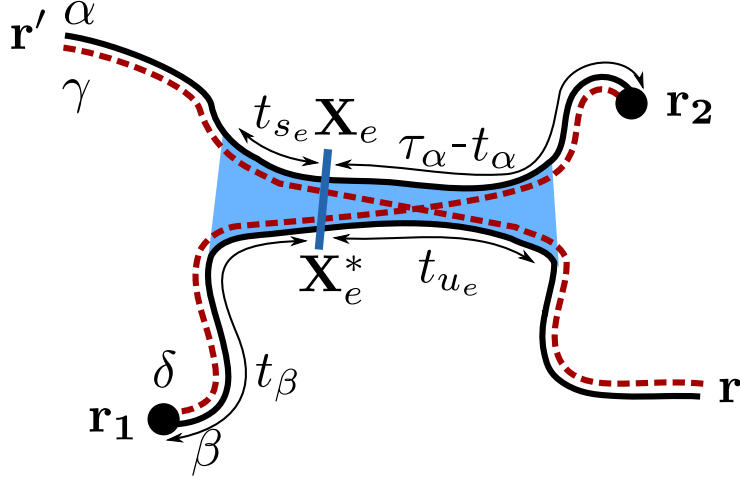


Figure C.1.: Schematic drawing of an encounter, formed by the trajectories  $\alpha$ ,  $\beta$ ,  $\gamma$ , and  $\delta$ , with timescales and phase-space points as described in the main text.

encounter. Outside the encounter region we may replace the product of the exact trajectory densities by the product of the classical propagators, whereas inside the encounter only a single classical propagator remains. After coarse graining the classical propagators are insensitive to small phase-space difference between  $\mathbf{X}_e$  and  $\mathbf{X}_e^*$ , so that we may replace  $\mathbf{X}_e^*$  by  $\mathbf{X}_e$ . As a result, the integration over  $s_e$  and  $u_e$  and the integration over  $\mathbf{X}_e$  can be performed separately. The integration over  $\mathbf{X}_e$  can be performed using a convolution rule for the classical propagators,

$$\int d\mathbf{X}_e P(\mathbf{X}_2, \mathbf{X}_e; t_2) P(\mathbf{X}_e, \mathbf{X}_1; t_1) = P(\mathbf{X}_2, \mathbf{X}_1; t_1 + t_2). \quad (\text{C.20})$$

The contribution  $\delta G_{AA}^{\text{F}, 2a}$  is then expressed as Eq. (5.22) with  $K^1$  replaced by

$$\begin{aligned} K^{2a}(\mathbf{X}_1, \mathbf{X}_2; \omega) = & - \int d\mathbf{X} d\mathbf{X}' P_{\text{in}}(\mathbf{X}) P(\mathbf{X}, \mathbf{X}_1; \omega) P(\mathbf{X}_2, \mathbf{X}'; \omega) P_{\text{out}}(\mathbf{X}') \\ & \times \frac{1}{2\pi\hbar} \int_{-c}^c ds du P(\mathbf{X}', \mathbf{X}; t_{\text{enc}}) e^{i\omega t_{\text{enc}}/\hbar} \frac{e^{isu/\hbar}}{t_{\text{enc}}}, \end{aligned} \quad (\text{C.21})$$

where  $P(\mathbf{X}, \mathbf{X}'; \omega)$  is the Fourier transform of  $P(\mathbf{X}, \mathbf{X}'; t)$ , see Eq. (5.29). The encounter time for this contribution is given by  $t_{\text{enc}} = \lambda^{-1} \ln(c^2/|su|)$ . In order to perform the integration over the phase-space coordinate  $s$  and  $u$  we make use of the integral identity

$$\frac{1}{2\pi\hbar} \int_{-c}^c ds du \frac{e^{isu/\hbar}}{t_{\text{enc}}} f(t_{\text{enc}}) = \frac{\partial}{\partial \tau_E} f(\tau_E), \quad (\text{C.22})$$

which holds for an arbitrary function  $f(t)$  which is a slow function of its argument on the time scale  $\lambda^{-1}$ . In this equation, the Ehrenfest time is defined as

$$\tau_E = \lambda^{-1} \ln(c^2/\hbar). \quad (\text{C.23})$$



One notes that this definition is consistent with Eq. (5.1) of the main text, since  $c^2$  is a classical action characteristic of the classical motion, which can also be expressed as  $c^2 = p_F a$ , where  $a$  is a length scale characteristic of the classical motion. The equivalence to Eq. (5.1) then follows since  $p_F = 2\pi\hbar/\lambda_F$ . With the equality (C.22) the result (5.25) of the main text follows immediately.

To prove Eq. (C.22), one makes use of the identity

$$\frac{2}{\pi} \int_0^{e^{-\lambda t}} dx \frac{\sin x}{x} = \theta(-t), \quad (\text{C.24})$$

where the Heaviside step function  $\theta(t)$  is broadened on the scale  $\lambda^{-1}$ . Taking derivatives on each side, we obtain

$$\frac{2\lambda}{\pi} \sin(e^{-\lambda t}) = \delta(t), \quad (\text{C.25})$$

$$\frac{2\lambda^2}{\pi} e^{-\lambda(t)} \cos(e^{-\lambda t}) = -\frac{\partial}{\partial t} \delta(t). \quad (\text{C.26})$$

These equations can be applied to the left hand side of Eq. (C.22) after writing the integration in terms of positive  $s$  and  $u$  and after a variable change that uses  $t_{\text{enc}}$  and  $v = s/c$  as the integration variables,

$$\begin{aligned} \frac{1}{2\pi\hbar} \int_{-c}^c ds du \frac{e^{isu/\hbar}}{t_s + t_u} f(t_s + t_u) &= \frac{2}{\pi} \int_0^\infty dt_{\text{enc}} \int_{e^{-\lambda t_{\text{enc}}}}^1 dv \frac{\lambda e^{-\lambda(t_{\text{enc}} - \tau_E)} \cos(e^{-\lambda(t_{\text{enc}} - \tau_E)})}{v t_{\text{enc}}} f(t_{\text{enc}}) \\ &= \frac{2\lambda^2}{\pi} \int_0^\infty dt_{\text{enc}} e^{-\lambda(t_{\text{enc}} - \tau_E)} \cos(e^{-\lambda(t_{\text{enc}} - \tau_E)}) f(t_{\text{enc}}) \\ &= \frac{\partial}{\partial \tau_E} f(\tau_E), \end{aligned} \quad (\text{C.27})$$

where we used Eq. (C.26) in the last line.

For the contribution  $\delta G_{AA}^{\text{F},2b}$ , the encounter is bounded to the right by the phase space point  $\mathbf{X}_2$  of the interaction. In this case, the encounter time is given by  $t_{\text{enc}} = \lambda^{-1} \ln(c/|s|) + t_\alpha$ , where  $t_\alpha$  can take values between zero and  $\lambda^{-1} \ln(c/|u|)$ . The expression for  $\delta G_{AA}^{\text{F},2b}$  is again of the form (5.22), with  $K^1$  replaced by

$$\begin{aligned} K^{2b}(\mathbf{X}_1, \mathbf{X}_2; \omega) &= - \int d\mathbf{X} P_{\text{in}}(\mathbf{X}) P(\mathbf{X}, \mathbf{X}_1; \omega) P_{\text{out}}(\mathbf{X}_2) \frac{1}{2\pi\hbar} \\ &\times \int_{-c}^c ds du \int_0^{\lambda^{-1} \ln(c/|u|)} dt_\alpha P(\mathbf{X}_2, \mathbf{X}; t_{\text{enc}}) e^{i\omega t_{\text{enc}}/\hbar} \frac{e^{isu/\hbar}}{t_{\text{enc}}}. \end{aligned} \quad (\text{C.28})$$

The integration over  $s$  and  $u$  in Eq. (C.28) is done with the help of the identity

$$\frac{1}{2\pi\hbar} \int_{-c}^c ds du \int_0^{\lambda^{-1} \ln(c/|u|)} dt_\alpha \frac{e^{isu/\hbar}}{t_{\text{enc}}} f(t_{\text{enc}}) = f(\tau_E), \quad (\text{C.29})$$

which is proven by first performing the integrations over  $s$  and  $u$ , and then using the identity (C.25). The final result is Eq. (5.26) of the main text. The derivation of Eq. (5.27) of the main text is similar.

Finally, for the fourth and last contribution  $\delta G_{AA}^{F,2d}$ , the encounter is bounded by both phase space points  $\mathbf{X}_1$  and  $\mathbf{X}_2$  of the interaction vertices. The encounter time is here given by  $t_{\text{enc}} = t_\alpha + t_\beta$ , where  $t_\alpha$  and  $t_\beta$  vary between 0 and  $\lambda^{-1} \ln(c/|u|)$  and between 0 and  $\lambda^{-1} \ln(c/|s|)$ , respectively. The expression for  $\delta G_{AA}^{F,2d}$  takes the form (5.22), with  $K^1$  replaced by

$$K^{2d}(\mathbf{X}_1, \mathbf{X}_2; \omega) = - \int d\mathbf{X} P_{\text{in}}(\mathbf{X}_1) P_{\text{out}}(\mathbf{X}_2) \frac{1}{2\pi\hbar} \int_{-c}^c ds du \\ \times \int_0^{\lambda^{-1} \ln(c/|s|)} dt_\beta \int_0^{\lambda^{-1} \ln(c/|u|)} dt_\alpha P(\mathbf{X}_2, \mathbf{X}; t_{\text{enc}}) e^{i\omega(t_{\text{enc}})/\hbar} \frac{e^{isu/\hbar}}{t_{\text{enc}}}. \quad (\text{C.30})$$

The integrations over  $s$  and  $u$  can be performed with the help of Eq. (C.24) and yield Eq. (5.28) of the main text.

## C.2. Details of the discussion

In this appendix we add some technical details to the discussion of Sec. 5.3. The function  $g_m(x)$  of Eq. (5.67) can be cast in the following closed analytic expression

$$g_m(x) = \frac{8}{\pi^2 (m^2 + x)^2} + \frac{32m^2 a \tanh^s \left( a \frac{\pi\sqrt{x}}{2} \right)}{\pi^3 \sqrt{x} (m^2 + x) (m^2 + ax)^2} \Bigg|_{a \rightarrow 0}^{a=1} \\ + \frac{24F_0^\sigma m^2}{\pi^2 (m^2 + x)^2 ((1 + F_0^\sigma)m^2 + x)} \\ - \frac{96b^{3/2} m^2 \tanh^s \left( \frac{\pi\sqrt{x}}{2\sqrt{b}} \right)}{\pi^3 \sqrt{x} (m^2 + x) (bm^2 + x)^2} \Bigg|_{b=1}^{b=1+F_0^\sigma}, \quad (\text{C.31})$$

where  $s = \pm 1$  for  $m$  even (odd). In the regime  $\tau_D \gg \tau_T, \tau_E$ , we may write this as

$$g_m(n\tau_D/\tau_T) = \frac{8}{\pi^2} \frac{\tau_T^2}{\tau_D^2} \frac{1}{(m^2 \frac{\tau_T}{\tau_D} + n)^2} \left[ 1 + \frac{3F_0^\sigma}{m^2 \frac{\tau_T}{\tau_D} (1 + F_0^\sigma) + n} \right] \left( 1 + \mathcal{O}(\sqrt{\frac{\tau_T}{\tau_D}}) \right), \quad (\text{C.32})$$

where terms with an additional factor  $\sqrt{\tau_T/\tau_D} \propto \frac{1}{L}$  correspond to finite size corrections and will be neglected.

After replacing the summation over  $m$  in Eq. (5.66) by an integration, we obtain

$$\delta G_{AA} = -\frac{4e^2}{\pi\hbar} \sqrt{\frac{\tau_T}{\tau_D}} \sum_{n=1}^{\infty} e^{-n \frac{\tau_E}{\tau_T}} n \left( \frac{\tau_E}{\tau_T} \right)^{5/2} \left[ f_1(n \frac{\tau_E}{\tau_T}) - f_1'(n \frac{\tau_E}{\tau_T}) \right], \quad (\text{C.33})$$

with

$$f_1(x) = \int_0^\infty dz \frac{1}{\sqrt{z}} \frac{1}{(z+x)^2} \left[ 1 + \frac{3F_0^\sigma z}{z(1+F_0^\sigma) + x} \right] e^{-z}. \quad (\text{C.34})$$

Apart from the prefactor  $\sqrt{\tau_T/\tau_D}$ , the interaction correction  $\delta G_{AA}$  is a function of the ratio  $\tau_E/\tau_T$  only. The limiting behavior for small and large ratios  $\tau_E/\tau_T$  is given in the main text.

For the case  $\tau_T \gg \tau_E, \tau_D$ , we replace the summation over  $n$  in Eq. (5.66) by an integration and find

$$\delta G_{AA} = -\frac{e^2}{h} \sum_{m=1}^{\infty} e^{-m^2 \frac{\tau_E}{\tau_D}} \int_0^{\infty} dx \left(1 + \frac{\tau_E}{\tau_D} x\right) g_m(x) e^{-x \frac{\tau_E}{\tau_D}}. \quad (\text{C.35})$$

This is a function of the ratio  $\tau_E/\tau_D$  only.

For the case of a large two-dimensional antidot array we use the residue technique to perform the  $\omega$  integration of Eq. (5.74), and obtain

$$\delta G_{AA} = -\frac{e^2}{h} \frac{W}{L} \frac{1}{\pi} \sum_{n=1}^{\infty} e^{-n \frac{\tau_E}{\tau_T}} n \frac{\tau_E^2}{\tau_T^2} \left[ f_2 \left( n \frac{\tau_E}{\tau_T} \right) - f_2' \left( n \frac{\tau_E}{\tau_T} \right) \right], \quad (\text{C.36})$$

with

$$f_2(x) = \int_0^{\infty} dz \frac{1}{(z+x)^2} \left[ 1 + \frac{3F_0^\sigma z}{z(1+F_0^\sigma) + x} \right] e^{-z}. \quad (\text{C.37})$$



## D. Appendix to Chapter 6

### D.1. Weak antilocalization

Here we present some details of the calculation to the weak antilocalization. We start from Eq. (6.47) and insert the diffusion propagators Eq. (5.51). After performing the spatial integrals, we find

$$\delta G_{\text{WAL}} = \frac{e^2 d_g}{2\pi\hbar} \frac{64}{\pi^4} \sum_{\substack{n=1 \\ n \text{ odd}}}^{\infty} \sum_{l=1}^{\infty} \sum_{k=0}^{\infty} \frac{e^{-(l^2+k^2/r^2)\frac{\tau_{\text{tr}}}{\tau_{\text{D}}}}}{l^2 + k^2/r^2} \frac{l^2 e^{-n^2 \frac{\tau_{\text{E}}}{\tau_{\text{D}}}}}{n^2(4l^2 - n^2)} \quad (\text{D.1})$$

where  $\tau_{\text{D}} = L^2/D\pi^2$  is the dwell time, and  $r = W/L$  is the aspect ratio. For large aspect ratios  $r$ , the summation over  $k$  can be replaced by an integration,

$$\sum_{k=0}^{\infty} \frac{1}{l^2 + k^2/r^2} e^{-(k^2/r^2)\frac{\tau_{\text{tr}}}{\tau_{\text{D}}}} \approx r \int_0^{\infty} dx \frac{1}{l^2 + x^2} e^{-x^2 \frac{\tau_{\text{tr}}}{\tau_{\text{D}}}} = r \frac{\pi}{2l} + O\left(\sqrt{\frac{\tau_{\text{tr}}}{\tau_{\text{D}}}}\right). \quad (\text{D.2})$$

We are interested in leading terms in the small parameter  $\tau_{\text{tr}}/\tau_{\text{D}}$  only, for which one finds

$$\delta G_{\text{WAL}} = \frac{e^2 d_g}{2\pi\hbar} \frac{W}{L} \frac{32}{\pi^3} \sum_{\substack{n=1 \\ n \text{ odd}}}^{\infty} \sum_{l=1}^{\infty} \frac{l e^{-n^2 \frac{\tau_{\text{E}}}{\tau_{\text{D}}}} e^{-l^2 \frac{\tau_{\text{tr}}}{\tau_{\text{D}}}}}{n^2(4l^2 - n^2)} \quad (\text{D.3})$$

In the limit of small  $\tau_{\text{tr}}/\tau_{\text{D}}$ , the behavior of the summand for large  $l$  is relevant. We then may simplify the summation over  $n$  as follows: The main contributions arise for  $n \approx 0$  and  $n \approx 2l$ , where the summand has poles. If  $l$  is large, the poles are well separated, and the dominant contribution comes from the pole at  $n \approx 0$ ,

$$\sum_{\substack{n=1 \\ n \text{ odd}}}^{\infty} \frac{1}{n^2(4l^2 - n^2)} e^{-n^2 \frac{\tau_{\text{E}}}{\tau_{\text{D}}}} \approx \frac{1}{4l^2} \sum_{\substack{n=1 \\ n \text{ odd}}}^{\infty} \frac{1}{n^2} e^{-n^2 \frac{\tau_{\text{E}}}{\tau_{\text{D}}}}, \quad (\text{D.4})$$

which results in the expression

$$\delta G_{\text{WAL}} = g \frac{e^2}{2\pi\hbar} \frac{W}{L} \frac{8}{\pi^3} \sum_{\substack{n=1 \\ n \text{ odd}}}^{\infty} \frac{1}{n^2} e^{-n^2 \frac{\tau_{\text{E}}}{\tau_{\text{D}}}} \sum_l \frac{1}{l} e^{-l^2 \frac{\tau_{\text{tr}}}{\tau_{\text{D}}}}. \quad (\text{D.5})$$

For small  $l$ , this expression is not accurate, hence this summation has a lower cutoff, which is not relevant for small  $\tau_{\text{tr}}/\tau_{\text{D}}$ , however, where the  $l$ -summation results in  $\ln \sqrt{\tau_{\text{D}}/\tau_{\text{tr}}}$ . Hence, we find Eq. (6.48) from the main text.

## D.2. Dephasing: Perturbation theory

An alternative derivation of the dephasing correction to weak antilocalization can be obtained directly from perturbation theory in the interaction. Following Ref. [Ale99], to leading order in interaction, one finds two corrections to the conductance. The first one of these corresponds to the Altshuler-Aronov correction and was considered in Sec. 6.6. The second correction reads

$$\begin{aligned} \delta G_{\text{deph}} = & -d_g \frac{e^2 \hbar}{2\pi} \int dy \int dy' \int d\varepsilon \left( -\frac{\partial f(\varepsilon)}{\partial \varepsilon} \right) \int \frac{d\omega}{2\pi} \left[ \coth\left(\frac{\omega}{2T}\right) - \tanh\left(\frac{\omega - \varepsilon}{2T}\right) \right] \\ & \times \int d\mathbf{r}_1 d\mathbf{r}_2 \text{Im} [U^R(\mathbf{r}_1, \mathbf{r}_2; \omega)] \\ & \times \text{tr} \left[ \hat{v}_x \mathcal{G}^R(\mathbf{r}, \mathbf{r}_1; \varepsilon) \mathcal{G}^R(\mathbf{r}_1, \mathbf{r}_2; \varepsilon - \omega) \mathcal{G}^R(\mathbf{r}_2, \mathbf{r}'; \varepsilon) \hat{v}'_x \mathcal{G}^A(\mathbf{r}', \mathbf{r}; \varepsilon) \right. \\ & + \hat{v}_x \mathcal{G}^R(\mathbf{r}, \mathbf{r}'; \varepsilon) \hat{v}'_x \mathcal{G}^A(\mathbf{r}', \mathbf{r}_2; \varepsilon) \mathcal{G}^A(\mathbf{r}_2, \mathbf{r}_1; \varepsilon - \omega) \mathcal{G}^A(\mathbf{r}_1, \mathbf{r}; \varepsilon) \\ & \left. + \hat{v}_x \mathcal{G}^R(\mathbf{r}, \mathbf{r}_1; \varepsilon) \mathcal{G}^R(\mathbf{r}_1, \mathbf{r}'; \varepsilon - \omega) \hat{v}'_x \mathcal{G}^A(\mathbf{r}', \mathbf{r}_2; \varepsilon - \omega) \mathcal{G}^A(\mathbf{r}_2, \mathbf{r}; \varepsilon) \right]_{x'=0}^{x=L}. \quad (\text{D.6}) \end{aligned}$$

The calculation proceeds by inserting the semiclassical expressions for the Green functions and identify the relevant configurations of trajectories. Only configurations where “advanced” and “retarded” trajectories are paired up (where we also allow for small angle encounters or pairing of time-reversed trajectories) contribute systematically to the conductance. For the first term inside the trace in Eq. (D.6), this is only possible, if the three “retarded” trajectories join together to a single trajectory connecting the points  $\mathbf{r}'$  with  $\mathbf{r}$ , that can be paired up with the advanced trajectory. In the semiclassical approximation, we then evaluate the integration over  $\mathbf{r}_1$  and  $\mathbf{r}_2$  within stationary phase approximation, where we keep only stationary configurations that join to a single trajectory. The result of such a calculation is

$$\begin{aligned} & \int d\mathbf{r}_1 d\mathbf{r}_2 \mathcal{G}^R(\mathbf{r}, \mathbf{r}_1; \varepsilon) \mathcal{G}^R(\mathbf{r}_1, \mathbf{r}_2; \varepsilon - \omega) \mathcal{G}^R(\mathbf{r}_2, \mathbf{r}'; \varepsilon) \text{Im} [U^R(\mathbf{r}_1, \mathbf{r}_2; \omega)] \\ = & -\frac{1}{\hbar^2} \frac{2\pi}{(2\pi i \hbar)^{3/2}} \sum_{\alpha: \mathbf{r}' \rightarrow \mathbf{r}; \varepsilon} A_\alpha e^{i\mathcal{S}_\alpha/\hbar} |\chi(\mathbf{p}_\alpha)\rangle \langle \chi(\mathbf{p}'_\alpha)| e^{i\gamma_\alpha} \\ & \times \int_0^{\tau_\alpha} dt \int_0^t dt' \text{Im} [U^R(\mathbf{r}_\alpha(t), \mathbf{r}_\alpha(t'); \omega)] e^{-i\omega(t-t')/\hbar}, \quad (\text{D.7}) \end{aligned}$$

We here restrict ourselves to explain, how the structure of this result can be understood, and refer to Appendix C.1.2 for the detailed calculation. The first step is to identify points  $\mathbf{r}_1$  and  $\mathbf{r}_2$ , which make the total phase of the integrand stationary. Such configurations are obtained, whenever there exists a single classical trajectory  $\alpha$  the connects the points  $\mathbf{r}'$  and  $\mathbf{r}$  via  $\mathbf{r}_2$  and  $\mathbf{r}_1$ . Since the position of the intermediate points can be anywhere along the trajectory  $\alpha$ , the summation over stationary configurations of the intermediate points is expressed a summation over trajectories  $\alpha$  as well as two time integrations along the trajectory  $\alpha$ . The Green function connecting the intermediate points is taken at a different energy, resulting in the additional factor  $e^{-i\omega(t-t')/\hbar}$ , as follows from Eq. (5.9). Furthermore, the actions of the three subpaths sum up to the action  $\mathcal{S}_\alpha$  of the joined path. Similarly, the individual Berry phases for the subpaths combine to the Berry phase of the

joined path  $\gamma_\alpha$ , as the Berry phase is expressed as integral along the trajectory. Since the momenta are smoothly connected at the intermediate points, the intermediate spinors match together, and only the spinors at the endpoints remain in the final expression. The second step in the evaluation of the integral is to integrate over quadratic fluctuations around the stationary configurations. This, in turns, renders the proper stability amplitude  $A_\alpha$  and the prefactor, see Appendix C.1.2.

Similar considerations apply to the second and third term of the trace of Eq. (D.6). Therefore, we can write Eq. (D.6) as a sum over one “retarded” trajectory  $\alpha$  and one “advanced” trajectory  $\beta$ , connecting source and drain. Since only paired trajectories are of relevance, we may simplify  $A_\alpha = A_\beta$  and  $\tau_\alpha = \tau_\beta$ . Since the only dependence on the propagation energy  $\varepsilon$  is in the factor between square brackets on the first line of Eq. (D.6), we may perform the integration over  $\varepsilon$  and find

$$\int d\varepsilon \left( -\frac{\partial f(\varepsilon)}{\partial \varepsilon} \right) \left[ \coth \left( \frac{\omega}{2T} \right) - \tanh \left( \frac{\omega - \varepsilon}{2T} \right) \right] = \frac{\frac{\omega}{2T}}{\sinh^2 \frac{\omega}{2T}}. \quad (\text{D.8})$$

Inserting the Fourier transformed interaction we then obtain

$$\begin{aligned} \delta G_{\text{deph}} = & \frac{e^2 d_g}{(2\pi\hbar)^2} \int dy \int dy' \sum_{\alpha, \beta} A_\alpha^2 v'_x v_x e^{i(\mathcal{S}_\alpha - \mathcal{S}_\beta)} e^{i(\gamma_\alpha - \gamma_\beta)} \\ & \times \int \frac{d\omega}{2\pi} \frac{\frac{\omega}{2T}}{\sinh^2 \frac{\omega}{2T}} \int \frac{d\mathbf{q}}{(2\pi)^2} \text{Im} U^R(\mathbf{q}; \omega) \frac{1}{2\hbar^2} \int_0^{\tau_\alpha} dt_1 dt_2 e^{-i\omega(t_1 - t_2)/\hbar} \\ & \times \left[ e^{i\mathbf{q}[\mathbf{r}_\alpha(t_1) - \mathbf{r}_\alpha(t_2)]} + e^{i\mathbf{q}[\mathbf{r}_\beta(t_1) - \mathbf{r}_\beta(t_2)]} - e^{i\mathbf{q}[\mathbf{r}_\alpha(t_1) - \mathbf{r}_\beta(t_2)]} - e^{i\mathbf{q}[\mathbf{r}_\beta(t_1) - \mathbf{r}_\alpha(t_2)]} \right], \end{aligned} \quad (\text{D.9})$$

which is consistent with the expressions of Sec. 6.7.

### D.3. Dephasing: Loop segment

In this appendix we add some details to the calculation of the dephasing for the loop segment. The imaginary part of the screened interaction in the diffusive limit, Eq. (6.60), evaluates to

$$\text{Im} U^R(\mathbf{q}, \omega) = \text{Im} U^{R,s}(\mathbf{q}, \omega) + (d_g^2 - 1) \text{Im} U^{R,t}(\mathbf{q}, \omega), \quad (\text{D.10})$$

with

$$\begin{aligned} \text{Im} U^{R,s}(\mathbf{q}, \omega) &= -\frac{1}{d_g \hbar \nu} \frac{\omega}{Dq^2}, \\ \text{Im} U^{R,t}(\mathbf{q}, \omega) &= -\frac{1}{d_g \hbar \nu} \frac{(F_0^\sigma)^2 \omega Dq^2}{(1 + F_0^\sigma)^2 (Dq^2)^2 + (\omega/\hbar)^2}. \end{aligned} \quad (\text{D.11})$$

Accordingly, we split Eq. (6.70) as

$$\delta P(\mathbf{r}', \mathbf{r}'; t) = \delta P^s(\mathbf{r}', \mathbf{r}'; t) + (d_g^2 - 1) \delta P^t(\mathbf{r}', \mathbf{r}'; t) \quad (\text{D.12})$$

Using Eq. (6.72), we are lead to the temporal integral

$$\mathcal{I}(\omega, \mathbf{q}, t) = \int_0^t dt_1 dt_2 e^{-i\omega(t_1-t_2)/\hbar} \left[ e^{-Dq^2\tau_2(1-\tau_2/t)} - e^{-Dq^2\bar{\tau}_2(1-\bar{\tau}_2/t)} \right], \quad (\text{D.13})$$

where  $\tau_2 = |t_1 - t_2|$  and  $\bar{\tau}_2 = |t - t_1 - t_2|$ . We evaluate this integral in the long-time limit  $t \gg \max(\hbar/\omega, 1/Dq^2)$  (which is sufficient for the present analysis),

$$\mathcal{I}(\omega, \mathbf{q}, t) \simeq 2t \frac{Dq^2}{(Dq^2)^2 + (\omega/\hbar)^2}, \quad (\text{D.14})$$

*i.e.*, we find a linear-in- $t$  behavior.

For the  $\mathbf{q}$ -integration we consider the non-singlet part of the interaction first,

$$\int \frac{d\mathbf{q}}{(2\pi)^2} \frac{Dq^2 \text{Im} U^{R,t}(\mathbf{q}, \omega)}{(Dq^2)^2 + (\omega/\hbar)^2} = -\frac{\pi\hbar(F_0^\sigma)^2}{4g_0(1+F_0^\sigma)(2+F_0^\sigma)}.$$

Here we introduced the dimensionless conductance  $g_0 = 2\pi\hbar d_g \nu D$ . Our expression now reads

$$\delta P^t(\mathbf{r}', \mathbf{r}'; t) = -\frac{\pi t}{2g_0\hbar} \frac{(F_0^\sigma)^2}{(1+F_0^\sigma)(2+F_0^\sigma)} \int \frac{d\omega}{2\pi} \mathcal{F}\left(\frac{\omega}{2T}\right). \quad (\text{D.15})$$

For small  $\omega/T$ , we may expand the function  $\mathcal{F}(x) \approx 1/x$ , which gives a logarithmic divergent  $\omega$ -integral. This integral should be cut at high energies by temperature, and at small energies by  $\hbar/t$ , where Eq. (D.14) ceases to be valid. So we find

$$\delta P^t(\mathbf{r}', \mathbf{r}'; t) = -\frac{(F_0^\sigma)^2}{(1+F_0^\sigma)(2+F_0^\sigma)} \frac{Tt}{g_0\hbar} \ln \frac{Tt}{\hbar}. \quad (\text{D.16})$$

The result for the singlet channel can be obtained from the latter equation by formally sending  $F_0^\sigma \rightarrow \infty$ .



# Bibliography

- [Adag 03] I. Adagideli, “*Ehrenfest-time-dependent suppression of weak localization*”, Phys. Rev. B **68**, 233308 (2003).
- [Adam 08] S. Adam, S. Cho, M. S. Fuhrer, and S. Das Sarma, “*Density Inhomogeneity Driven Percolation Metal-Insulator Transition and Dimensional Crossover in Graphene Nanoribbons*”, Phys. Rev. Lett. **101**, 046404 (2008).
- [Adam 09] S. Adam, P. W. Brouwer, and S. Das Sarma, “*Crossover from quantum to Boltzmann transport in graphene*”, Phys. Rev. B **79**, 201404 (2009).
- [Akke 07] E. Akkermans and G. Montambaux. *Mesoscopic Physics of Electrons and Photons*. Cambridge University Press, Cambridge, UK (2007).
- [Alel 06] I. L. Aleiner and K. B. Efetov, “*Effect of Disorder on Transport in Graphene*”, Phys. Rev. Lett. **97**, 236801 (2006).
- [Alel 96] I. L. Aleiner and A. I. Larkin, “*Divergence of classical trajectories and weak localization*”, Phys. Rev. B **54**, 14423 (1996).
- [Alel 99] I. L. Aleiner, B. L. Altshuler, and M. E. Gershenson, “*Interaction effects and phase relaxation in disordered systems*”, Waves Random Media **9**, 201 (1999).
- [Alt1 06] A. Altland, “*Low-Energy Theory of Disordered Graphene*”, Phys. Rev. Lett. **97**, 236802 (2006).
- [Alt1 07] A. Altland, P. W. Brouwer, and C. Tian, “*Interplay of Ehrenfest time and dephasing time in ballistic conductors*”, Phys. Rev. Lett. **99**, 036804 (2007).
- [Alts 79] B. L. Altshuler and A. G. Aronov, Zh. Eksp. Teor. Fiz. **77**, 2028 (1979). [Sov. Phys. JETP **50**, 968 (1979)].
- [Alts 82] B. L. Altshuler, A. G. Aronov, and D. E. Khmelnitsky, “*Effects of electron-electron collisions with small energy transfers on quantum localisation*”, J. Phys. C **15**, 7367 (1982).
- [Alts 83] B. L. Altshuler and A. G. Aronov, “*Fermi-liquid theory of the electron-electron interaction effects in disordered metals*”, Solid State Commun. **46**, 429 (1983).
- [Alts 84] B. L. Altshuler, A. G. Aronov, and A. Y. Zyuzin, “*Size effects in disordered conductors*”, Zh. Eksp. Teor. Fiz. **86**, 709 (1984). [Sov. Phys. JETP **59**, 415 (1984)].

- [Alts 85a] B. L. Altshuler, “*Fluctuations in the extrinsic conductivity of disordered conductors*”, JETP Lett. **41**, 648 (1985).
- [Alts 85b] B. L. Altshuler and A. G. Aronov. *Electron–Electron Interaction in Disordered Conductors*, Chap. 1, 1 – 153. Vol. 10 of *Modern Problems in Condensed Matter Sciences*, North–Holland, Amsterdam, (1985).
- [Ande 79] P. W. Anderson, E. Abrahams, and T. V. Ramakrishnan, Phys. Rev. Lett. **43**, 718 (1979).
- [Arga 93] N. Argaman, Y. Imry, and U. Smilansky, “*Semiclassical analysis of spectral correlations in mesoscopic systems*”, Phys. Rev. B **47**, 4440 (1993).
- [Arga 95] N. Argaman, “*Semiclassical Analysis of the Conductance of Mesoscopic Systems*”, Phys. Rev. Lett. **75**, 2750 (1995).
- [Arga 96] N. Argaman, “*Semiclassical analysis of the quantum interference corrections to the conductance of mesoscopic systems*”, Phys. Rev. B **53**, 7035 (1996).
- [Bara 93] H. U. Baranger, R. A. Jalabert, and A. D. Stone, “*Quantum-chaotic scattering effects in semiconductor microstructures*”, Chaos **3**, 665 (1993).
- [Bard 07] J. H. Bardarson, J. Tworzydło, P. W. Brouwer, and C. W. J. Beenakker, “*Demonstration of one-parameter scaling at the Dirac point in graphene*”, Phys. Rev. Lett. **99**, 106801 (2007).
- [Bard 09] J. H. Bardarson, M. Titov, and P. W. Brouwer, “*Electrostatic Confinement of Electrons in an Integrable Graphene Quantum Dot*”, Phys. Rev. Lett. **102**, 226803 (2009).
- [Been 08] C. W. J. Beenakker, “*Colloquium: Andreev reflection and Klein tunneling in graphene*”, Rev. Mod. Phys. **80**, 1337 (2008).
- [Belo 03] I. S. Beloborodov, K. B. Efetov, A. V. Lopatin, and V. M. Vinokur, “*Transport Properties of Granular Metals at Low Temperatures*”, Phys. Rev. Lett. **91**, 246801 (2003).
- [Bolt 98] J. Bolte and S. Keppeler, “*Semiclassical Time Evolution and Trace Formula for Relativistic Spin-1/2 Particles*”, Phys. Rev. Lett. **81**, 1987 (1998).
- [Bolt 99] J. Bolte and S. Keppeler, “*A Semiclassical Approach to the Dirac Equation*”, Ann. Phys. **274**, 125 (1999).
- [Boot 08] T. J. Booth, P. Blake, R. R. Nair, D. Jiang, E. W. Hill, U. Bangert, A. Bleloch, M. Gass, K. S. Novoselov, M. I. Katsnelson, and A. K. Geim, “*Macroscopic Graphene Membranes and Their Extraordinary Stiffness*”, Nano Lett. **8**, 2442 (2008).
- [Brou 06] P. W. Brouwer and S. Rahav, “*Semiclassical theory of the Ehrenfest-time dependence of quantum transport in ballistic quantum dots*”, Phys. Rev. B **74**, 075322 (2006).

- [Brou 07] P. W. Brouwer, “*Semiclassical theory of the Ehrenfest-time dependence of quantum transport*”, Phys. Rev. B **76**, 165313 (2007).
- [Brou 08] P. W. Brouwer and J. N. Kupferschmidt, “*Interaction Correction to the Conductance of a Ballistic Conductor*”, Phys. Rev. Lett. **100**, 246805 (2008).
- [Bunc 05] J. S. Bunch, Y. Yaish, M. Brink, K. Bolotin, and P. L. McEuen, “*Coulomb Oscillations and Hall Effect in Quasi-2D Graphite Quantum Dots*”, Nano Lett. **5**, 287 (2005).
- [Butt 00] M. Büttiker, “*Time-dependent transport in mesoscopic structures*”, J. Low. Temp. Phys. **118**, 519 (2000).
- [Butt 93] M. Büttiker, “*Capacitance, admittance, and rectification properties of small conductors*”, J. Phys. Condens. Matter **5**, 9361 (1993).
- [Butt 94] M. Büttiker, H. Thomas, and A. Prêtre, “*Current partition in multiprobe conductors in the presence of slowly oscillating external potentials*”, Z. Phys. B **94**, 133 (1994).
- [Cao 10] H. Cao, Q. Yu, L. A. Jauregui, J. Tian, W. Wu, Z. Liu, R. Jalilian, D. K. Benjamin, Z. Jiang, J. Bao, S. S. Pei, and Y. P. Chen, “*Electronic transport in chemical vapor deposited graphene synthesized on Cu: Quantum Hall effect and weak localization*”, Appl. Phys. Lett. **96**, 122106, (2010).
- [Carm 08] P. Carmier and D. Ullmo, “*Berry phase in graphene: Semiclassical perspective*”, Phys. Rev. B **77**, 245413 (2008).
- [Cast 09] A. H. Castro Neto, F. Guinea, N. M. R. Peres, K. S. Novoselov, and A. K. Geim, “*The electronic properties of graphene*”, Rev. Mod. Phys. **81**, 109 (2009).
- [Cast 84] C. Castellani, C. Di Castro, P. A. Lee, and M. Ma, “*Interaction-driven metal-insulator transitions in disordered fermion systems*”, Phys. Rev. B **30**, 527 (1984).
- [Chak 86] S. Chakravarty and A. Schmid, “*Weak localization: The quasiclassical theory of electrons in a random potential*”, Physics Reports **140**, 193 (1986).
- [Chei 06] V. V. Cheianov and V. I. Falko, “*Selective transmission of Dirac electrons and ballistic magnetoresistance of n-p junctions in graphene*”, Phys. Rev. B **74**, 041403(R) (2006).
- [Chen 10] Y.-F. Chen, M.-H. Bae, C. Chialvo, T. Dirks, A. Bezryadin, and N. Mason, “*Magnetoresistance in single-layer graphene: weak localization and universal conductance fluctuation studies*”, Journal of Physics: Condensed Matter **22**, 205301 (2010).
- [Das 11] S. Das Sarma, S. Adam, E. H. Hwang, and E. Rossi, “*Electronic transport in two-dimensional graphene*”, Rev. Mod. Phys. **83**, 407 (2011).

- [Das 99] S. Das Sarma and E. H. Hwang, “*Charged Impurity-Scattering-Limited Low-Temperature Resistivity of Low-Density Silicon Inversion Layers*”, Phys. Rev. Lett. **83**, 164 (1999).
- [Datt 95] S. Datta. *Electronic transport in mesoscopic systems*. Cambridge University Press, (1995).
- [Down 11] C. A. Downing, D. A. Stone, and M. E. Portnoi, “*Zero-energy states in graphene quantum dots and rings*”, Phys. Rev. B **84**, 155437 (2011).
- [Dros 10] S. Dröscher, P. Roulleau, F. Molitor, P. Studerus, C. Stampfer, K. Ensslin, and T. Ihn, “*Quantum capacitance and density of states of graphene*”, Appl. Phys. Lett. **96**, 152104 (2010).
- [Drud 00] P. Drude, “*Zur Elektronentheorie der Metalle*”, Annalen der Physik **306**, 566 (1900).
- [Enss 90] K. Ensslin and P. M. Petroff, “*Magnetotransport through an antidot lattice in GaAs-Al<sub>x</sub>Ga<sub>1-x</sub>As heterostructures*”, Phys. Rev. B **41**, 12307 (1990).
- [Erom 09] J. Eroms and D. Weiss, “*Semiclassical Approach to Chaotic Quantum Transport*”, New. J. Phys. **11**, 095021 (2009).
- [Fano 61] U. Fano, “*Effects of Configuration Interaction on Intensities and Phase Shifts*”, Phys. Rev. **124**, 1866 (1961).
- [Fink 83] A. M. Finkel’shtein, Zh. Eksp. Teor. Fiz. **84**, 168 (1983). [Sov. Phys. JETP **57**, 97 (1983)].
- [Fink 90] A. M. Finkel’shtein, “*Electron liquid in disordered conductors.*”, Sov. Sci. Rev. A **14**, 1 (1990).
- [Frad 86] E. Fradkin, “*Critical behavior of disordered degenerate semiconductors. I. Models, symmetries, and formalism*”, Phys. Rev. B **33**, 3257 (1986).
- [Geim 07] A. K. Geim and K. S. Novoselov, “*The rise of graphene*”, Nat. Mater. **6**, 138 (2007).
- [Geim 09] A. K. Geim, “*Graphene: Status and Prospects*”, Science **324**, 1530 (2009).
- [Gian 09] F. Giannazzo, S. Sonde, V. Raineri, and E. Rimini, “*Screening Length and Quantum Capacitance in Graphene by Scanning Probe Microscopy*”, Nano Lett. **9**, 23 (2009).
- [Gold 86] A. Gold and V. T. Dolgoplov, “*Temperature dependence of the conductivity for the two-dimensional electron gas: Analytical results for low temperatures*”, Phys. Rev. B **33**, 1076 (1986).
- [Golu 04] D. S. Golubev and A. D. Zaikin, “*Transport of interacting electrons in arrays of quantum dots and diffusive wires*”, Phys. Rev. B **70**, 165423 (2004).

- 
- [Gork 79] L. P. Gorkov, A. I. Larkin, and D. E. Khmel'nitskii, *Pis'ma Zh. Eksp. Teor. Fiz.* **30**, 248 (1979). [*JETP Lett.* **30**, 228 (1979)].
- [Gorn 04] I. V. Gornyi and A. D. Mirlin, "*Interaction-induced magnetoresistance in a two-dimensional electron gas*", *Phys. Rev. B* **69**, 045313 (2004).
- [Grus 13] A. L. Grushina, D.-K. Ki, and A. F. Morpurgo, "*A ballistic pn junction in suspended graphene with split bottom gates*", *Appl. Phys. Lett.* **102**, 223102 (2013).
- [Gutt 09] J. Güttinger, C. Stampfer, F. Libisch, T. Frey, J. Burgdörfer, T. Ihn, and K. Ensslin, "*Electron-Hole Crossover in Graphene Quantum Dots*", *Phys. Rev. Lett.* **103**, 046810 (2009).
- [Gutt 12] J. Güttinger, F. Molitor, C. Stampfer, S. Schnez, A. Jacobsen, S. Dröscher, T. Ihn, and K. Ensslin, "*Transport through graphene quantum dots*", *Rep. Prog. Phys.* **75**, 126502 (2012).
- [Gutz 90] M. Gutzwiller. *Chaos in Classical and Quantum Mechanics*. Springer, New York (1990).
- [Hart 12] T. Hartmann, J. Michl, C. Petitjean, T. Wellens, J.-D. Urbina, K. Richter, and P. Schlagheck, "*Weak localization with nonlinear bosonic matter waves*", *Annals of Physics* **327**, 1998 (2012).
- [Hein 13] J. Heini, M. Schneider, and P. W. Brouwer, "*Interplay of Aharonov-Bohm and Berry phases in gate-defined graphene quantum dots*", *Phys. Rev. B* **87**, 245426 (2013).
- [Hika 80] S. Hikami, A. I. Larkin, and Y. Nagaoka, "*Spin-Orbit Interaction and Magnetoresistance in the Two Dimensional Random System*", *Prog. Theor. Phys.* **63**, 707 (1980).
- [Ishi 07] M. Ishigami, J. H. Chen, W. G. Cullen, M. S. Fuhrer, and E. D. Williams, "*Atomic Structure of Graphene on SiO<sub>2</sub>*", *Nano Lett.* **7**, 1643 (2007).
- [Jaco 12] A. Jacobsen, P. Simonet, K. Ensslin, and T. Ihn, "*Transport in a three-terminal graphene quantum dot in the multi-level regime*", *New J. Phys.* **14**, 023052 (2012).
- [Jacq 04] P. Jacquod and E. V. Sukhorukov, "*Breakdown of Universality in Quantum Chaotic Transport: The Two-Phase Dynamical Fluid Model*", *Phys. Rev. Lett.* **92**, 116801 (2004).
- [Jala 90] R. A. Jalabert, H. U. Baranger, and A. D. Stone, "*Conductance fluctuations in the ballistic regime: A probe of quantum chaos?*", *Phys. Rev. Lett.* **65**, 2442 (1990).
-

- [Jang 08] C. Jang, S. Adam, J.-H. Chen, E. D. Williams, S. Das Sarma, and M. S. Fuhrer, “*Tuning the Effective Fine Structure Constant in Graphene: Opposing Effects of Dielectric Screening on Short- and Long-Range Potential Scattering*”, Phys. Rev. Lett. **101**, 146805 (2008).
- [Jobs 12] J. Jobst, D. Waldmann, I. V. Gornyi, A. D. Mirlin, and H. B. Weber, “*Electron-Electron Interaction in the Magnetoresistance of Graphene*”, Phys. Rev. Lett. **108**, 106601 (2012).
- [Joua 11] B. Jouault, B. Jabakhanji, N. Camara, W. Desrat, C. Consejo, and J. Camassel, “*Interplay between interferences and electron-electron interactions in epitaxial graphene*”, Phys. Rev. B **83**, 195417 (2011).
- [Kamp 07] N. G. van Kampen. *Stochastic Processes in Physics and Chemistry*. North-Holland, (2007).
- [Kane 88] C. L. Kane, R. A. Serota, and P. A. Lee, “*Long-range correlations in disordered metals*”, Phys. Rev. B **37**, 6701 (1988).
- [Kats 06a] M. I. Katsnelson, “*Zitterbewegung, chirality, and minimal conductivity in graphene*”, Eur. Phys. J. B **51**, 1434 (2006).
- [Kats 06b] M. I. Katsnelson, K. S. Novoselov, and A. K. Geim, “*Chiral tunnelling and the Klein paradox in graphene*”, Nature Physics **2**, 620 (2006).
- [Kech 08] K. Kechedzhi, O. Kashuba, and V. I. Fal’ko, “*Quantum kinetic equation and universal conductance fluctuations in graphene*”, Phys. Rev. B **77**, 193403 (2008).
- [Khar 08] M. Y. Kharitonov and K. B. Efetov, “*Universal conductance fluctuations in graphene*”, Phys. Rev. B **78**, 033404 (2008).
- [Khve 06] D. V. Khveshchenko, “*Electron Localization Properties in Graphene*”, Phys. Rev. Lett. **97**, 036802 (2006).
- [Ki 08] D.-K. Ki, D. Jeong, J.-H. Choi, H.-J. Lee, and K.-S. Park, “*Inelastic scattering in a monolayer graphene sheet: A weak-localization study*”, Phys. Rev. B **78**, 125409 (2008).
- [Kozi 10] A. A. Kozikov, A. K. Savchenko, B. N. Narozhny, and A. V. Shytov, “*Electron-electron interactions in the conductivity of graphene*”, Phys. Rev. B **82**, 075424 (2010).
- [Kupf 08] J. N. Kupferschmidt and P. W. Brouwer, “*Temperature and magnetic-field dependence of the quantum corrections to the conductance of a network of quantum dots*”, Phys. Rev. B **78**, 125313 (2008).
- [Kwon 94] Y. Kwon, D. M. Ceperley, and R. M. Martin, “*Quantum Monte Carlo calculation of the Fermi-liquid parameters in the two-dimensional electron gas*”, Phys. Rev. B **50**, 1684 (1994).

- [Land 77] L. D. Landau and E. M. Lifshitz. *Quantum mechanics*. Vol. 3 of *Course in Theoretical Physics*, Pergamon, Oxford (1977).
- [Lang 61] J. S. Langer and V. Ambegaokar, “Friedel Sum Rule for a System of Interacting Electrons”, *Phys. Rev.* **121**, 1090 (1961).
- [Lara 11] S. Lara-Avila, A. Tzalenchuk, S. Kubatkin, R. Yakimova, T. J. B. M. Janssen, K. Cedergren, T. Bergsten, and V. Fal’ko, “Disordered Fermi Liquid in Epitaxial Graphene from Quantum Transport Measurements”, *Phys. Rev. Lett.* **107**, 166602 (2011).
- [Lee 85] P. A. Lee and A. D. Stone, “Universal Conductance Fluctuations in Metals”, *Phys. Rev. Lett.* **55**, 1622 (1985).
- [Li 07] G. Li and E. Y. Andrei, “Observation of Landau levels of Dirac fermions in graphite”, *Nature Phys.* **3**, 623 (2007).
- [Litt 91] R. G. Littlejohn and W. G. Flynn, “Geometric phases in the asymptotic theory of coupled wave equations”, *Phys. Rev. A* **44**, 5239 (1991).
- [Litt 92] R. G. Littlejohn and W. G. Flynn, “Semiclassical theory of spin-orbit coupling”, *Phys. Rev. A* **45**, 7697 (1992).
- [Ludw 94] A. W. W. Ludwig, M. P. A. Fisher, R. Shankar, and G. Grinstein, “Integer quantum Hall transition: An alternative approach and exact results”, *Phys. Rev. B* **50**, 7526 (1994).
- [Marq 07] F. Marquardt, J. von Delft, R. A. Smith, and V. Ambegaokar, “Decoherence in weak localization. I. Pauli principle in influence functional”, *Phys. Rev. B* **76**, 195331 (2007).
- [Mart 08] J. Martin, N. Akerman, G. Ulbricht, T. Lohmann, J. H. Smet, K. von Klitzing, and A. Yacoby, “Observation of electron-hole puddles in graphene using a scanning single-electron transistor”, *Nature Phys.* **4**, 144 (2008).
- [McCa 06] E. McCann, K. Kechedzhi, V. I. Fal’ko, H. Suzuura, T. Ando, and B. L. Altshuler, “Weak-Localization Magnetoresistance and Valley Symmetry in Graphene”, *Phys. Rev. Lett.* **97**, 146805 (2006).
- [Mess 61] A. Messiah. *Quantum Mechanics*. North-Holland (1961).
- [Mink 06] G. M. Minkov, A. V. Germanenko, O. E. Rut, A. A. Sherstobitov, V. A. Larionova, A. K. Bakarov, and B. N. Zvonkov, “Diffusion and ballistic contributions of the interaction correction to the conductivity of a two-dimensional electron gas”, *Phys. Rev. B* **74**, 045314 (2006).
- [Mkhi 12] V. V. Mkhitarian and E. G. Mishchenko, “Resonant finite-size impurities in graphene, unitary limit, and Friedel oscillations”, *Phys. Rev. B* **86**, 115442 (2012).

- [Mori 09] S. Moriyama, D. Tsuya, E. Watanabe, S. Uji, M. Shimizu, T. Mori, T. Yamaguchi, and K. Ishibashi, “*Coupled Quantum Dots in a Graphene-Based Two-Dimensional Semimetal*”, Nano Letters **9**, 2891 (2009).
- [Moro 06] S. V. Morozov, K. S. Novoselov, M. I. Katsnelson, F. Schedin, L. A. Ponomarenko, D. Jiang, and A. K. Geim, “*Strong Suppression of Weak Localization in Graphene*”, Phys. Rev. Lett. **97**, 016801 (2006).
- [Morp 06] A. F. Morpurgo and F. Guinea, “*Intervalley Scattering, Long-Range Disorder, and Effective Time-Reversal Symmetry Breaking in Graphene*”, Phys. Rev. Lett. **97**, 196804 (2006).
- [Mull 07] S. Müller, S. Heusler, P. Braun, and F. Haake, “*Semiclassical Approach to Chaotic Quantum Transport*”, New. J. Phys. **9**, 12 (2007).
- [Naro 02] B. N. Narozhny, G. Zala, and I. L. Aleiner, “*Interaction corrections at intermediate temperatures: Dephasing time*”, Phys. Rev. B **65**, 180202 (2002).
- [Naza 94] Y. V. Nazarov, “*Limits of universality in disordered conductors*”, Phys. Rev. Lett. **73**, 134 (1994).
- [Newa 12] A. Newaz, Y. S. Puzyrev, B. Wang, S. T. Pantelides, and K. I. Bolotin, “*Probing charge scattering mechanisms in suspended graphene by varying its dielectric environment*”, Nature Comm. **3**, 734 (2012).
- [Noh 03] H. Noh, M. P. Lilly, D. C. Tsui, J. A. Simmons, E. H. Hwang, S. Das Sarma, L. N. Pfeiffer, and K. W. West, “*Interaction corrections to two-dimensional hole transport in the large  $-r_s$  limit*”, Phys. Rev. B **68**, 165308 (2003).
- [Nomu 07] K. Nomura, M. Koshino, and S. Ryu, “*Topological Delocalization of Two-Dimensional Massless Dirac Fermions*”, Phys. Rev. Lett. **99**, 146806 (2007).
- [Novo 04] K. S. Novoselov, A. K. Geim, S. V. Morozov, D. Jiang, Y. Zhang, S. V. Dubonos, I. V. Grigorieva, and A. A. Firsov, “*Electric Field Effect in Atomically Thin Carbon Films*”, Science **306**, 666 (2004).
- [Novo 05] K. S. Novoselov, A. K. Geim, S. V. Morozov, D. Jiang, M. I. Katsnelson, I. V. Grigorieva, S. V. Dubonos, and A. A. Firsov, “*Two-dimensional gas of massless Dirac fermions in graphene*”, Nature **438**, 197 (2005).
- [Ostr 07] P. M. Ostrovsky, I. V. Gornyi, and A. D. Mirlin, “*Quantum criticality and minimal conductivity in graphene with long-range disorder*”, Phys. Rev. Lett. **98**, 256801 (2007).
- [Pere 06] N. M. R. Peres, F. Guinea, and A. H. C. Neto, “*Electronic properties of disordered two-dimensional carbon*”, Phys. Rev. B **73**, 125411 (2006).
- [Peti 07] C. Petitjean, P. Jacquod, and R. S. Whitney, JETP Lett. **86**, 763 (2007).



- 
- [Pono 08] L. A. Ponomarenko, F. Schedin, M. I. Katsnelson, R. Yang, E. W. Hill, K. S. Novoselov, and A. K. Geim, “*Chaotic Dirac Billiard in Graphene Quantum Dots*”, Science **320**, 356 (2008).
- [Pono 09] L. A. Ponomarenko, R. Yang, T. M. Mohiuddin, M. I. Katsnelson, K. S. Novoselov, S. V. Morozov, A. A. Zhukov, F. Schedin, E. W. Hill, and A. K. Geim, “*Effect of a High- $\kappa$  Environment on Charge Carrier Mobility in Graphene*”, Phys. Rev. Lett. **102**, 206603 (2009).
- [Pono 10] L. A. Ponomarenko, R. Yang, R. V. Gorbachev, P. Blake, A. S. Mayorov, K. S. Novoselov, M. I. Katsnelson, and A. K. Geim, “*Density of States and Zero Landau Level Probed through Capacitance of Graphene*”, Phys. Rev. Lett. **105**, 136801 (2010).
- [Ramm 98] J. Rammer. *Quantum Transport Theory*. Perseus Books (1998).
- [Rich 02] K. Richter and M. Sieber, “*Semiclassical Theory of Chaotic Quantum Transport*”, Phys. Rev. Lett. **89**, 206801 (2002).
- [Rick 13] P. Rickhaus, R. Maurand, M.-H. Liu, M. Weiss, and K. R. C. Schönenberger, “*Ballistic interferences in suspended graphene*”, Nature Comm. **4**, 2342 (2013).
- [Rouk 89] M. L. Roukes and A. Scherer, Bull. Am. Phys. Soc **34**, 633 (1989).
- [Rubi 63] S. I. Rubinow and J. B. Keller, “*Asymptotic Solution of the Dirac Equation*”, Phys. Rev. **131**, 2789 (1963).
- [Rudi 97] A. M. Rudin, I. L. Aleiner, and L. I. Glazman, “*Tunneling zero-bias anomaly in the quasiballistic regime*”, Phys. Rev. B **55**, 9322 (1997).
- [Schn 09] S. Schnetz, F. Molitor, C. Stampfer, J. Güttinger, I. Shorubalko, T. Ihn, and K. Ensslin, “*Observation of excited states in a graphene quantum dot*”, Applied Physics Letters **94**, 012107 (2009).
- [Schn 11] M. Schneider and P. W. Brouwer, “*Resonant scattering in graphene with a gate-defined chaotic quantum dot*”, Phys. Rev. B **84**, 115440 (2011).
- [Schn 13] M. Schneider, G. Schwiete, and P. W. Brouwer, “*Semiclassical theory of the interaction correction to the conductance of antidot arrays*”, Phys. Rev. B **87**, 195406 (2013).
- [Schn 14a] M. Schneider and P. W. Brouwer, “*Density of states as a probe of electrostatic confinement in graphene*”, arXiv:1404.2135 (2014).
- [Schn 14b] M. Schneider and P. W. Brouwer, “*Quantum corrections to transport in graphene: a trajectory-based semiclassical analysis*”, arXiv:1404.2129 (2014).
- [Shon 98] N. H. Shon and T. Ando, “*Quantum Transport in Two-Dimensional Graphite System*”, J. Phys. Soc. Jpn. **67**, 2421 (1998).
-

- [Silv 07] P. G. Silvestrov and K. B. Efetov, “*Quantum Dots in Graphene*”, Phys. Rev. Lett. **98**, 016802 (2007).
- [Smil 92] U. Smilansky, S. Tomsovic, and O. Bohigas, “*Spectral fluctuations and transport in phase space*”, J. Phys. A: Math. Gen. **25**, 3261 (1992).
- [Smit 60] F. T. Smith, Phys. Rev. **118**, 349 (1960).
- [Speh 03] D. Spehner, “*Spectral form factor of hyperbolic systems: leading off-diagonal approximation*”, J. Phys. A **36**, 7269 (2003).
- [Stam 08] C. Stampfer, E. Schurtenberger, F. Molitor, J. Güttinger, T. Ihn, and K. Ensslin, “*Tunable Graphene Single Electron Transistor*”, Nano Lett. **8**, 2378 (2008).
- [Stol 11] M. D. Stoller, C. W. Magnuson, Y. Zhu, S. Murali, J. W. Suk, R. Piner, and R. S. Ruoff, “*Interfacial capacitance of single layer graphene*”, Energy Environ. Sci. **4**, 4685 (2011).
- [Tan 07] Y.-W. Tan, Y. Zhang, K. Bolotin, Y. Zhao, S. Adam, E. H. Hwang, S. Das Sarma, H. L. Stormer, and P. Kim, “*Measurement of Scattering Rate and Minimum Conductivity in Graphene*”, Phys. Rev. Lett. **99**, 246803 (2007).
- [Tian 07] C. Tian, A. Altland, and P. W. Brouwer, “*Interplay of Ehrenfest and Dephasing times in ballistic conductors*”, Phys. Rev. Lett. **99**, 036804 (2007).
- [Tikh 08] F. V. Tikhonenko, D. W. Horsell, R. V. Gorbachev, and A. K. Savchenko, “*Weak Localization in Graphene Flakes*”, Phys. Rev. Lett. **100**, 056802 (2008).
- [Tikh 09] F. V. Tikhonenko, A. A. Kozikov, A. K. Savchenko, and R. V. Gorbachev, “*Transition between Electron Localization and Antilocalization in Graphene*”, Phys. Rev. Lett. **103**, 226801 (2009).
- [Tito 10] M. Titov, P. M. Ostrovsky, I. V. Gornyi, A. Schuessler, and A. D. Mirlin, “*Charge Transport in Graphene with Resonant Scatterers*”, Phys. Rev. Lett. **104**, 076802 (2010).
- [Ture 03] M. Turek and K. Richter, “*Leading off-diagonal contribution to the spectral form factor of chaotic quantum systems*”, J. Phys. A **36**, L455 (2003).
- [Twor 04] J. Tworzydło, A. Tajic, and C. W. J. Beenakker, “*Quantum-to-classical crossover of mesoscopic conductance fluctuations*”, Phys. Rev. B **69**, 165318 (2004).
- [Twor 06] J. Tworzydło, B. Trauzettel, M. Titov, A. Rycerz, and C. W. J. Beenakker, “*Sub-Poissonian Shot Noise in Graphene*”, Phys. Rev. Lett. **96**, 246802 (2006).

- [Wall 47] P. R. Wallace, “*The Band Theory of Graphite*”, Phys. Rev. **71**, 622 (1947).
- [Whit 06] R. S. Whitney and P. Jacquod, “*Shot Noise in Semiclassical Chaotic Cavities*”, Phys. Rev. Lett. **96**, 206804 (2006).
- [Whit 08] R. S. Whitney, P. Jacquod, and C. Petitjean, “*Dephasing in quantum chaotic transport: A semiclassical approach*”, Phys. Rev. B **77**, 045315 (2008).
- [Wign 55] E. P. Wigner, Phys. Rev. **98**, 145 (1955).
- [Wurm 11a] J. Wurm, K. Richter, and I. Adagideli, “*Edge effects in graphene nanostructures: From multiple reflection expansion to density of states*”, Phys. Rev. B **84**, 075468 (2011).
- [Wurm 11b] J. Wurm, K. Richter, and I. Adagideli, “*Edge effects in graphene nanostructures: Semiclassical theory of spectral fluctuations and quantum transport*”, Phys. Rev. B **84**, 205421 (2011).
- [Xia 09] J. Xia, F. Chen, J. Li, and N. Tao, “*Measurement of the quantum capacitance of graphene*”, Nature Nanotech. **4**, 505 (2009).
- [Yevt 00] O. Yevtushenko, G. Lütjering, D. Weiss, and K. Richter, “*Weak Localization in Antidot Arrays: Signature of Classical Chaos*”, Phys. Rev. Lett. **84**, 542 (2000).
- [Zait 05a] O. Zaitsev, D. Frustaglia, and K. Richter, “*Role of Orbital Dynamics in Spin Relaxation and Weak Antilocalization in Quantum Dots*”, Phys. Rev. Lett. **94**, 026809 (2005).
- [Zait 05b] O. Zaitsev, D. Frustaglia, and K. Richter, “*Semiclassical theory of weak antilocalization and spin relaxation in ballistic quantum dots*”, Phys. Rev. B **72**, 155325 (2005).
- [Zala 01] G. Zala, B. N. Narozhny, and I. L. Aleiner, “*Interaction corrections at intermediate temperatures: Longitudinal conductivity and kinetic equation*”, Phys. Rev. B **64**, 214204 (2001).
- [Zhan 05] Y. Zhang, Y.-W. Tan, H. L. Stormer, and P. Kim, “*Experimental observation of the quantum Hall effect and Berry’s phase in graphene*”, Nature **438**, 201 (2005).
- [Zieg 98] K. Ziegler, “*Delocalization of 2D Dirac Fermions: The Role of a Broken Supersymmetry*”, Phys. Rev. Lett. **80**, 3113 (1998).



# Acknowledgements

The successful completion of this thesis would not have been possible without the support of many people. At the end of this thesis, I would like to take the opportunity to say thank you.

First of all, I would like to thank my advisor Piet Brouwer, who offered me the possibility to write the thesis in a truly unique and outstanding group. I am deeply grateful for his enduring guidance through my work, for his great support, whenever I got stuck, and for giving me enough freedom to work on my own. All in all it is hard to imagine a better place to write a PhD thesis.

I would like to thank Felix von Oppen for co-refereeing this thesis, and I am grateful to Piet and Felix for creating this inspiring atmosphere in the Dahlem Center for Complex Quantum Systems.

Moreover, I am very much indebted to all members of the Dahlem Center for Complex Quantum Systems, who made the period of the PhD a great time in my life. In particular, I would like to thank Jörg Behrmann, Emil Bergholtz, Niels Bode, Jeroen Danon, Matthias Duckheim, Friedrich Gethmann, Matthias Lüsche, Torsten Karzig, Tobias Micklitz, Falko Pientka, Maresa Rieder, Björn Sbierski, Peter Silvestrov and Silvia Viola Kusminski for the support in all kinds of scientific and non-scientific problems. I also would like to deeply thank my collaborator Georg Schwiete, and I am grateful for the beneficial times when I was working with my students Julia Heintz, Max Hering, and Johannes Jünemann. A great thanks also to Ehud Amitai, Farhad Arbabzadah, Christian Krumnow, Alessandro Ricottone, Maresa Rieder, and Hristo Velkov for making the times in my office very enjoyable. Moreover, I would like to thank Gabriele Herrmann for administrative support.

Furthermore, I acknowledge financial support by the German Research foundation (DFG) in the priority program SPP 1459 “Graphene”, and by the Alexander von Humboldt foundation.

Finally, my deepest gratitude goes to my family, for the great support throughout my life, and for making me the person that I am.



# Curriculum Vitae

For reasons of data protection,  
the *curriculum vitae* is not included in the online version of this thesis.





# Publications

Publications, that constitute the content of this thesis:

- Martin Schneider and Piet W. Brouwer,  
“*Resonant scattering in graphene with a gate-defined chaotic quantum dot*”,  
Phys. Rev. B **84**, 115440 (2011), <http://dx.doi.org/10.1103/PhysRevB.84.115440>  
[Ch. 3].
- Martin Schneider, Georg Schwiete, and Piet W. Brouwer,  
“*Semiclassical theory of the interaction correction to the conductance of antidot arrays*”,  
Phys. Rev. B **87**, 195406 (2013), <http://dx.doi.org/10.1103/PhysRevB.87.195406>  
[Ch. 5].
- Julia Heinl, Martin Schneider and Piet W. Brouwer,  
“*Interplay of Aharonov-Bohm and Berry phases in gate-defined graphene quantum dots*”,  
Phys. Rev. B **87**, 245426 (2013), <http://dx.doi.org/10.1103/PhysRevB.87.245426>  
[Ch. 4].
- Martin Schneider and Piet W. Brouwer,  
“*Quantum corrections to transport in graphene: a trajectory-based semiclassical analysis*”,  
arXiv:1404.2129 (2014), accepted for publication in New. J. Phys. [Ch. 6].
- Martin Schneider and Piet W. Brouwer,  
“*Density of states as a probe of electrostatic confinement in graphene*”,  
Phys. Rev. B **89**, 205437 (2014), <http://dx.doi.org/10.1103/PhysRevB.89.205437>  
[Ch. 4].

Publications, that have been completed in parallel to this thesis:

- Martin Schneider, Dmitry A. Bagrets, and Alexander D. Mirlin,  
“*Theory of the nonequilibrium electronic Mach-Zehnder interferometer*”,  
Phys. Rev. B **84**, 075401 (2011).
- Christian F. Hermanns, Matthias Bernien, Alex Krüger, Christian Schmidt, Sören T. Waßerroth, Gelavizh Ahmadi, Benjamin W. Heinrich, Martin Schneider, Piet W. Brouwer, Katharina J. Franke, Eugen Weschke, and Wolfgang Kuch,  
“*Magnetic Coupling of  $Gd_3N@C_{80}$  Endohedral Fullerenes to a Substrate*”,  
Phys. Rev. Lett. **111**, 167203 (2013).